

## University of Southampton Research Repository

Copyright © and Moral Rights for this thesis and, where applicable, any accompanying data are retained by the author and/or other copyright owners. A copy can be downloaded for personal non-commercial research or study, without prior permission or charge. This thesis and the accompanying data cannot be reproduced or quoted extensively from without first obtaining permission in writing from the copyright holder/s. The content of the thesis and accompanying research data (where applicable) must not be changed in any way or sold commercially in any format or medium without the formal permission of the copyright holder/s.

When referring to this thesis and any accompanying data, full bibliographic details must be given, e.g.

Thesis: Author (Year of Submission) "Full thesis title", University of Southampton, name of the University Faculty or School or Department, PhD Thesis, pagination.

Data: Author (Year) Title. URI [dataset]

UNIVERSITY OF SOUTHAMPTON

FACULTY OF SCIENCE

PHYSICS

RHENIUM, TANTALUM AND GOLD SURFACES:  
AN INVESTIGATION INTO THE ORIGINS OF PEAKS IN THE LOW ENERGY  
SECONDARY ELECTRON SPECTRUM

by  
Sylvia Croxall  
(nee Knowles B.Sc.)

A thesis submitted for the degree of  
Doctor of Philosophy  
at the University of Southampton

The Department of Physics  
The University  
Highfield  
Southampton  
SO9 5NH

September 1983

To my husband

and parents

When you have eliminated the impossible,  
whatever remains, 'however improbable',  
must be the truth.

Sir Arthur Conan Doyle.

## CONTENTS

	Page
ABSTRACT	
LIST OF FIGURES AND TABLES	
CHAPTER 1 INTRODUCTION	1
CHAPTER 2 THEORY OF AUGER ELECTRON SPECTROSCOPY	4
2.1 The Secondary Electron Spectrum	4
2.2 The Auger Process	4
2.3 Auger Electron Energies	8
2.4 Auger Yields and Intensities	12
2.5 Auger Line Widths and Shapes	14
2.6 Origins of Other Peaks in the Secondary Electron Spectrum	17
2.7 Principles of Secondary Electron Detection	18
CHAPTER 3 EXPERIMENTAL EQUIPMENT AND PROCEDURES	22
3.1 Vacuum Equipment	22
3.2 Sample Mount and Manipulator	24
3.3 Auger Electron Spectroscopy Instrumentation	26
3.3.1 Hardware	26
3.3.2 Software	28
3.3.3 High Temperature A.E.S.	30
3.4 Sample Preparation	38
3.4.1 Tungsten	38
3.4.2 Rhenium	38
3.4.3 Tantalum	39
3.4.4 Gold	39
3.5 Experimental Procedure	40
3.5.1 Energy Calibration of Spectra	40
3.5.2 Yield Curves	41
3.5.3 High Temperature Experiments	43
CHAPTER 4 SIMULATION OF EXPERIMENTAL SPECTRA	48
4.1 The Second Derivative Spectrum	48
4.2 Simulation of Experimental Spectrum	50
4.3 Effect of a Large Modulation Voltage	54

4.4 Simulation of Experimental Spectrum using Broadened Lorentzians	62
4.5 Conclusions	63
CHAPTER 5 PREVIOUS WORK	70
5.1 Trends Across the Series	70
5.2 Conflicting Reports on Gold	72
5.3 Work on Tungsten Performed in this Laboratory	74
5.3.1 Previous work	74
5.3.2 Present work	78
5.4 Summary	78
CHAPTER 6 THE RHENIUM AUGER TRANSITIONS: 150-200eV	82
6.1 Results	82
6.2 Discussion	92
6.3 Conclusions	103
CHAPTER 7 MINOR PEAKS IN THE RHENIUM SECONDARY ELECTRON SPECTRUM	104
7.1 The Peaks at 216eV and 229eV	104
7.1.1 Results	104
7.1.2 Discussion	104
7.2 The 241eV Peak	111
7.2.1 Results	111
7.2.2 Discussion	114
7.3 The 187.8eV Peak	114
7.3.1 Results	114
7.3.2 Discussion	115
7.4 The 350eV and 361eV Peaks	115
7.4.1 Results	115
7.4.2 Discussion	116
7.5 Conclusion	116
CHAPTER 8 PRELIMINARY RESULTS FROM TANTALUM AND GOLD	119
8.1 Tantalum	119
8.1.1 Results	119
8.1.2 Discussion	127
8.1.2.1 160eV to 190eV	130
8.1.2.2 190eV to 200eV	132
8.1.2.3 200eV to 215eV	133
8.1.2.4 215eV to 230eV	134

8.1.3 Conclusion	134
8.2 Gold	135
8.2.1 Results	135
8.2.2 Discussion	144
8.2.2.1 140eV to 170eV	144
8.2.2.2 170eV to 220eV	145
8.2.2.3 220eV to 290eV	145
8.2.2.4 A cascade process	145
8.2.3 Conclusion	147
CHAPTER 9 COMPARISON OF RESULTS	148
9.1 The $N_{4,5}N_{6,7}N_{6,7}$ Super Coster-Kronig Transitions?	148
9.1.1 Change in Peak Position with Atomic Number	149
9.1.2 Comparison with Larkins' Theoretical Line Energies	152
9.1.3 Comparison with Empirical Line Energy Calculations	154
9.1.4 Widths of Peaks	156
9.2 The $N_{4,5}N_{6,7}O_{2,3}$ Coster-Kronig Transitions	158
9.3 The $N_{4,5}N_{6,7}O_{4,5}$ Coster-Kronig Transitions	159
9.4 Conclusion	160
CHAPTER 10 SUMMARY AND CONCLUSIONS	161
APPENDIX I EXPERIMENTAL CONTROL LANGUAGE INTERPRETER (E.C.L.I.)	165
I.a Energy window calculations	165
I.b How E.C.L.I. works	165
I.c Summary of all possible user commands	167
APPENDIX II	168
REFERENCES	170
ACKNOWLEDGEMENTS	177

UNIVERSITY OF SOUTHAMPTON

ABSTRACT

FACULTY OF SCIENCE

PHYSICS

Doctor of Philosophy

RHENIUM, TANTALUM AND GOLD SURFACES:  
AN INVESTIGATION INTO THE ORIGINS OF PEAKS IN THE LOW ENERGY  
SECONDARY ELECTRON SPECTRUM

by Sylvia Croxall B.Sc.

This thesis reports an investigation into the origins of peaks in the low energy secondary electron spectra of 5d transition metal surfaces. The rhenium spectrum was studied in detail, followed by preliminary studies of tantalum and gold.

Spectra were recorded in ultra high vacuum using a cylindrical mirror analyser connected to a microcomputer. An experimental control language interpreter was developed for the data logging. Computer programs were also written for analysis. This included the curve fitting of second derivative experimental spectra with both Lorentzian peaks and Lorentzian peaks broadened by the detecting voltage modulation technique. The program was able to determine peak positions, relative intensities and widths of overlapping peaks from noisy spectra. Such peaks are difficult to resolve by eye.

The main peaks in the spectra were due to Auger emission as predicted. However, unexpectedly, peaks were also found which were due to Auger 'cascade' processes and diffraction effects. These overlap the Auger peaks and will distort any measurements taken in quantitative experiments if peaks are assumed to be entirely due to Auger emission.

The most intense group of peaks in the spectra (140 to 190eV) were identified as mainly due to  $N_{4,5}N_{6,7}N_{6,7}$  super Coster-Kronig transitions, in agreement with current theoretical intensity calculations. However, there is a discrepancy of 10eV between theoretical  $N_{4,5}N_{6,7}N_{6,7}$  line energies and the rhenium experimental peak energies. The discrepancy between experiment and theory is small at each end of the 5d transition metal series and rises to a maximum at rhenium (which has a half full 5d shell). 30% of  $N_4$  initial holes were found to decay to an  $N_5V$  final state rather than the  $N_{6,7}N_{6,7}$  final state in rhenium. This compares with the theoretical value of only 1%. The widths of rhenium peaks in this area varied from 5.0eV to 7.6eV which is slightly below the 8eV predicted.

## LIST OF FIGURES AND TABLES

<u>FIGURE</u>	<u>page</u>
2.1 The secondary electron energy spectrum	5
2.2 The Auger process	6
2.3 Cylindrical mirror analyser, schematic diagram	19
3.1 Schematic of experimental chamber	23
3.2 The sample mounting	25
3.3 Auger Electron Spectroscopy detection system	27
3.4 Block diagram of the computer system	29
3.5 User program to produce the spectra in figures 3.6, 3.7 and 3.8	31
3.6 Rhenium 'Auger' spectrum induced by 2500eV primary electrons	32
3.7 Rhenium 'Auger' spectrum induced by 2500eV primary electrons	33
3.8 Rhenium 'Auger' spectrum, integral of figure 3.7	34
3.9 STATUS for spectrum in figure 3.6a	35
3.10 Schematic diagram of pulsed heater	37

3.11	Electron energies involved in measurements with a C.M.A	42
3.12	(a) Experimental measurement of beam current using a 69V bias (b) Proportion of total current measured (c) Calibration of collected current v. primary beam energy for constant beam current	44
3.13	Appearance of satellite 'ghost' peak at high temperatures	45
3.14	Mechanism for production of satellite peak	47
4.1	Comparison of resolutions of $N(E)$ , $dN(E)/dE$ and $d^2N(E)/dE^2$ spectra	49
4.2	Simulation of rhenium spectrum by (a) 3 Lorentzian peaks and (b) 6 Lorentzian peaks	55
4.3	Contribution of each term in equation 4.5 to the intensity of the centre of a peak as a function of modulation voltage	57
4.4	Normalised f.w.h.m. of an elastic peak as a function of modulation voltage	59
4.5	f.w.h.m. v. modulation voltage for five Lorentzian peaks fitted to the rhenium spectrum	60
4.6	Simulation of rhenium spectrum, recorded using a large modulation voltage, by 3 Lorentzian peaks	61
4.7	Fit of a Lorentzian peak to a broadened Lorentzian peak	64

4.8	Simulation of rhenium spectrum (shown in figure 4.2) by 6 broadened Lorentzian peaks	65
4.9	f.w.h.m. v. modulation voltage for five broadened Lorentzian peaks fitted to the rhenium spectrum	66
4.10	Simulation of rhenium spectrum in figure 4.8 without the contributions from modulation broadening	67
5.1	Temperature dependence of tungsten 222eV and 232eV peaks	79
5.2	Temperature dependence of tungsten 222eV and 232eV peaks logarithmic scale	80
6.1	Rhenium secondary electron spectrum induced by 1400eV primary electrons	83
6.2	Rhenium secondary electron spectrum induced by 400eV primary electrons	84
6.3	Second derivative rhenium secondary electron spectrum	85
6.4	Second derivative spectrum of a 177eV elastic peak from a rhenium surface	87
6.5	Yield curves for rhenium peaks at 164, 171 and 178eV	88
6.6	Yield curve for rhenium 350eV peak	91
6.7	Best fit of $N_5$ and $N_3$ yield curves to the rhenium 164eV peak's yield curve	96

6.8	Best fit of $N_4$ and $N_3$ yield curves to the rhenium 178eV peak's yield curve	98
6.9	Comparison of Larkins' theoretical line energies and rhenium experimental line energies	102
7.1	Yield curves for rhenium peaks at 216 and 229eV	105
7.2	Best fit of $N_5$ and $N_3$ yield curves to the rhenium 216eV peak's yield.	107
7.3	Best fit of $N_4$ and $N_3$ yield curves to the rhenium 229eV peak's yield	108
7.4	Yield curve for rhenium 241eV peak	112
7.5	Temperature dependence of rhenium 241eV peak	113
7.6	Best fit of $N_3$ and $N_1$ yield curves to the rhenium 361eV peak's yield	117
8.1	First derivative tantalum secondary electron spectrum induced by 2500eV primary electrons	120
8.2	Second derivative tantalum secondary electron spectrum induced by 2500eV primary electrons	121
8.3	Second derivative tantalum secondary electron spectrum	123
8.4	Second derivative tantalum secondary electron spectrum	126
8.5	Simulation of tantalum spectrum by 4 Lorentzian peaks	128

8.6	Simulation of tantalum spectrum (shown in figure 8.5) by 7 Lorentzian peaks	129
8.7	Comparison of Larkins' theoretical line energies and tantalum experimental line energies	131
8.8	First derivative gold secondary electron spectrum induced by 2500eV primary electrons	136
8.9	Second derivative gold secondary electron spectrum induced by 1700eV primary electrons	139
8.10	Second derivative gold secondary electron spectrum 140 to 170eV	141
8.11	Second derivative gold secondary electron spectrum 220 to 290eV	142
8.12	Approximate comparison of sulphur $L_{2,3}$ and gold $N_{4,5}$ yield curves (yield curves approximated by rhenium yield curve in figure 6.5)	143
8.13	Comparison of Larkins' theoretical line energies and gold experimental line energies	146
9.1	Change in experimental peak position with atomic number	151
9.2	Examples of Larkins' theoretical line energies v. atomic number	153
9.3	Discrepancy between experimental and Larkins' theoretical line energies v. atomic number	155

9.4	Comparison of experimental peak positions with theoretical line energies calculated using an empirical equation (equation 2.4)	157
II.1	The Newton-Raphson method for $f(x)=0$ when $f(x)$ crosses zero	169
II.2	The Newton-Raphson method for $f(x)=0$ when $f(x)$ does not reach zero	169

## TABLE

## Page

5.1	Summary of results and conclusions found by Rawlings et al. (1980b) for some minor peaks in the tungsten spectrum	77
6.1a	Results from fit of 6 Lorentzian peaks to rhenium spectrum, figure 4.2b	90
6.1b	Results from fit of 6 broadened Lorentzian peaks to rhenium spectrum, figure 4.8	90
6.2	Theoretical super Coster-Kronig, Coster-Kronig and Auger line energies for rhenium in the region 90eV-260eV	93
6.3	Theoretical super Coster-Kronig and Coster-Kronig line energies for rhenium	100
8.1	Theoretical super Coster-Kronig, Coster-Kronig and Auger line energies for tantalum in the region 100eV-260eV	124
8.2	Theoretical super Coster-Kronig, Coster-Kronig and Auger line energies for gold in the region 110eV-290eV	137
9.1	Comparison of the positions of equivalent experimental peaks	150

## CHAPTER 1

### INTRODUCTION

Solids interact with their surroundings through their surfaces. The structure and composition of a surface affects many physical and chemical processes. For example, in electronics metal-oxide-semiconductor transistor devices depend on surface effects and devices such as diodes rely on the interface between dissimilar areas. Other examples are catalysis, optical reflection, adhesion, corrosion, thermionic and photoelectric emission. The production of surfaces of known chemical purity is important in industry for the fabrication of integrated circuits, the production of catalysts and the prevention of corrosion. Thus to assure the quality and reproducibility of surfaces, reliable methods of measuring surface composition are necessary.

There are many methods of examining surfaces. Among them Auger Electron Spectroscopy (A.E.S.) is popular in both academic research and in industry. It is used mainly as a tool to identify the elements present on a surface. Elements are identified on a spectrum by their 'fingerprint': each element has a unique characteristic Auger Electron Spectrum with well defined peak energies and relative intensities. To aid in identification standard spectra are published for most elements.

However there are problems with A.E.S. Auger electrons are 'secondary' electrons emitted by ionised atoms relaxing to a state of lower energy. Thus the Auger Electron Spectrum is obtained by collecting secondary electrons. Unfortunately the Auger process is not the only process resulting in secondary electrons. So the secondary electron spectrum contains many peaks that are due to other processes as well as those due to the Auger process. In addition, the theoretical predictions of Auger peak positions and intensities are not always very accurate. So it may not be easy to decide which peaks are Auger peaks and which are not. When a peak is incorrectly assumed to be an Auger peak

and used in calculations to determine the quantity of an element on the surface, inevitably the answers will be wrong. The confusion is greatest for elements with high atomic numbers. For example Rawlings et al. (1978) used a tungsten 'Auger' peak as a tool in some quantitative experiments, but later found that the peak had a more complicated origin (Rawlings et al., 1979). The only way to determine the origin of peaks is to play an elaborate game of 'who-done-it'.

There is an increasing need to solve this problem because more and more people with little experience of A.E.S. are using it solely as a tool to study other phenomena. For example there are now far more publications describing the use of A.E.S. as a tool than about the study of A.E.S. itself. Someone needs to take a closer look at these 'Auger' peaks so that other workers can use A.E.S. with confidence.

To this end the author has investigated the origins of peaks in the low energy secondary electron spectra of some 5d transition metal surfaces. The 5d transition metals (tantalum, tungsten, rhenium, osmium, iridium, platinum, and gold) are of particular interest to the catalysis industry. The present work was built on an investigation of tungsten that had already been performed in this laboratory (Rawlings et al. 1980a, 1979, 1980b).

The author has made a detailed study of the low energy secondary electron spectrum of a rhenium surface and preliminary studies of tantalum and gold surfaces. Particular attention was paid to the most intense peaks which had been previously associated with theoretically predicted Auger peaks. Although other workers have studied gold (Larkins and Lubenfeld, 1977 and Matthew et al., 1980) their contradictory conclusions show that more work is needed.

This thesis is organised as follows. Chapter 2 outlines the theoretical background to the study. Chapter 3 describes the experimental equipment and procedures, including the

installation of a microcomputer for data logging and analysis. Chapter 4 discusses the problem of overlapping peaks in the spectrum. A 'curve fitting' computer program was able to resolve some overlapping peaks that could not be resolved by eye. Chapter 5 looks at relevant previous experimental and theoretical work. Chapter 6 describes the investigation of the most intense group of peaks in the rhenium low energy secondary electron spectrum. This included use of the curve fitting program and analysis of the variation of a peak's intensity with the energy of the primary beam of electrons. Several less intense rhenium peaks are discussed in chapter 7. The preliminary investigation of the tantalum and gold spectra is covered in chapter 8, concentrating on the most intense groups of peaks. In chapter 9 the present results, previous work and theories are compared with each other. The author found trends in the results across the transition metal series particularly useful in the analysis. Finally chapter 10 summarises the investigation, presents conclusions and suggests relevant further work.

## CHAPTER 2

### THEORY OF AUGER ELECTRON SPECTROSCOPY

This chapter includes a basic description of the Auger process, the theories predicting the energy positions, intensities and shapes of Auger peaks, and the principles of secondary electron detection.

#### 2.1 The Secondary Electron Spectrum

When a beam of electrons of energy  $E_p$  is fired at a solid surface, the resulting 'secondary' electron spectrum has the general form shown in figure 2.1. Region I in the diagram contains a broad peak of low energy electrons which have undergone many collisions in the bulk in a cascade process. Region II has small peaks of well defined energy superimposed on a slowly varying background. Some of the peaks result from Auger transitions and are characteristic of the elements on the surface. Other peaks consist of electrons that have lost discrete amounts of energy in exciting plasmons or interband transitions. The electrons in regions I and II have been inelastically scattered from the surface. Region III contains the elastically reflected electrons of energy  $E_p$  which are used for electron diffraction studies (L.E.E.D. and R.H.E.E.D.). There is some fine detail in Region III due to excitation of lattice vibrations. These phonons have energies of several hundredths of an electron volt.

#### 2.2 The Auger Process

The radiationless de-excitation of atoms was predicted by Rosseland (1923) and first experimentally established by Auger (1923). If, for example, an initial vacancy is created in the W-shell of an atom, (figure 2.2a), the filling of the vacancy by an electron will result in the emission of either

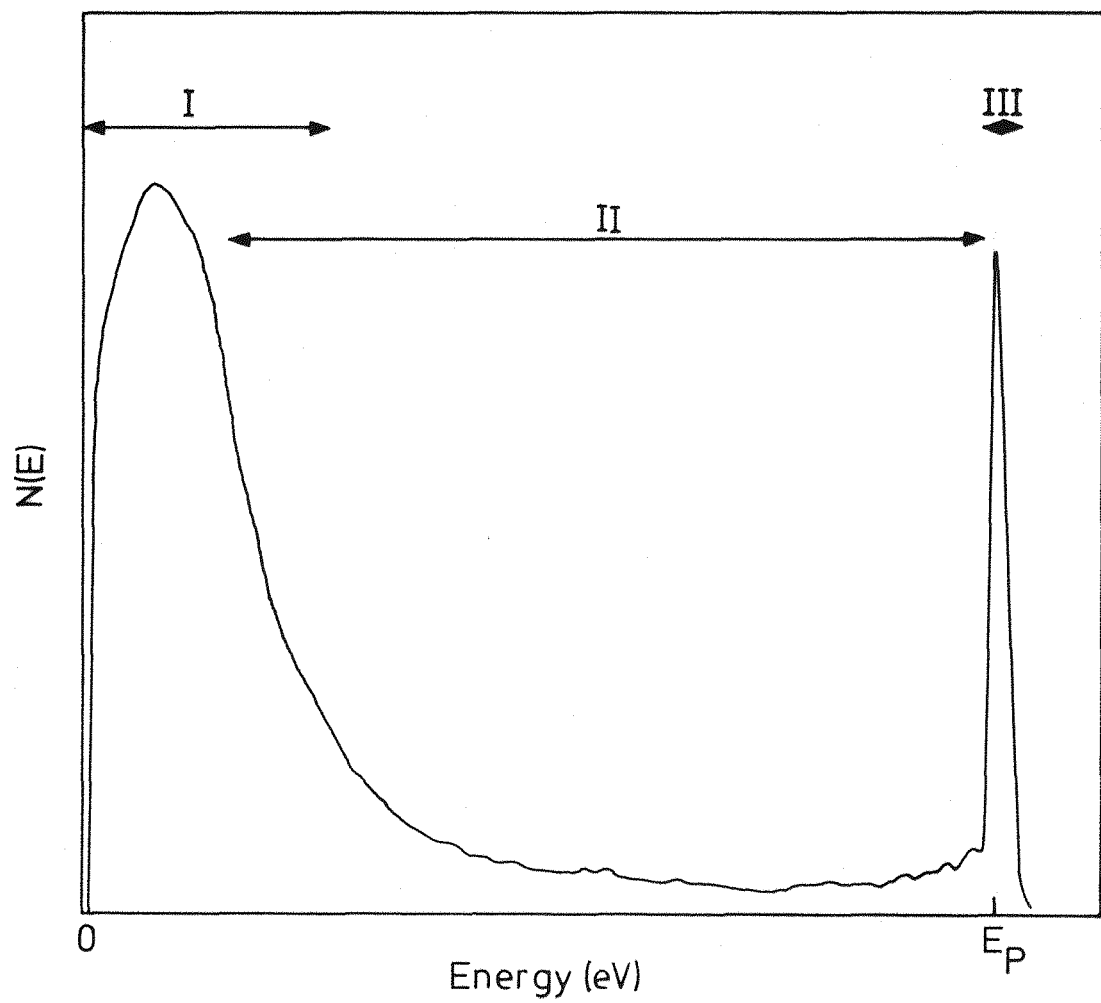
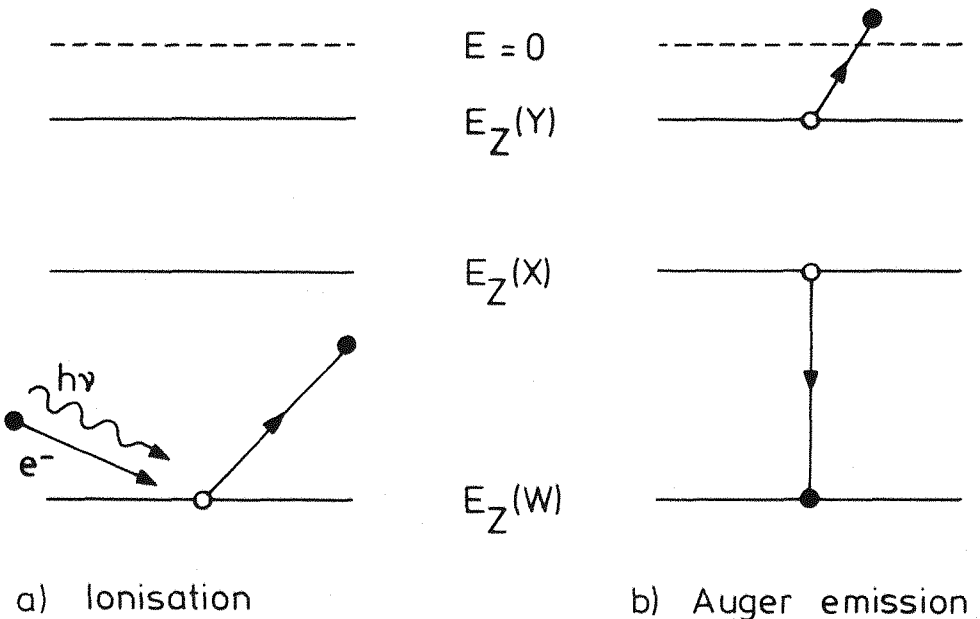


Figure 2.1 The secondary electron energy spectrum.



The atom is ionised leaving a hole at energy  $E_Z(W)$ . An electron from an energy level  $E_Z(X)$  fills the hole and the energy  $E_Z(W) - E_Z(X)$  is transferred to another electron. After overcoming the binding energy  $E_Z(Y)$ , this electron leaves with kinetic energy  $\simeq E_Z(W) - E_Z(X) - E_Z(Y)$ .

Figure 2.2 The Auger process.

an X-ray or an Auger electron. When energetically possible an Auger electron is usually emitted (Bishop and Rivière, 1969). The initial hole is filled within  $10^{-17}$  to  $10^{-12}$  second by an electron from an outer orbital, and the excess energy used to eject a third electron (the Auger electron) from the atom (figure 2.2b). The atom is left in a doubly ionised state and may undergo further Auger transitions until it is neutralised by the capture of free electrons.

If an initial vacancy in the K-shell is filled by an  $L_1$  electron with the expulsion of an  $L_2$  electron, the emitted electron is referred to as a  $KL_1L_2$  Auger electron. If it is not necessary to distinguish between subshells reference is made to the KLL Auger group. If the initial electron transition is between two subshells, as for the  $L_1L_2M_1$  electron, the process is called a Coster-Kronig transition (Coster and Kronig, 1935). When all three shells are members of the same subshell, e.g. the  $L_1L_2L_3$  electron, it is a super Coster-Kronig process (McGuire, 1972). Finally if the Auger transition involves valence electrons  $V$  is often used in the label, e.g.  $M_2VV$ .

It was initially thought that the Auger process was a two step process. In the first step the initial vacancy was filled by an outer electron with the emission of an X-ray. This X-ray was then absorbed by the same atom and another electron emitted in the second step. The  $KL_1L_1$  Auger electron would then have to be a result of the internal conversion of a  $KL_1$  X-ray. This X-ray transition is always forbidden by the selection rule  $\Delta l = \pm 1$  for radiative dipole transitions and so the Auger process must be one of radiationless reorganisation of an excited atom. The idea of a 'virtual' photon being exchanged in the interaction is however used both as a conceptual aid and in the mathematics (Chattarji, 1976).

### 2.3 Auger Electron Energies

Experimental Auger electron energies provide information on the energy difference between the initial (one hole) and final (two hole) electronic states of a system. Theoretically this entails finding the total energy  $E$  of the atomic system in each of the two electronic states. In principle these can be found by the exact solution of the quantum mechanical equation

$$H\Psi = E\Psi \quad (2.1)$$

where  $H$  is the generalised Hamiltonian operator and  $\Psi$  is the many particle wave function describing the chosen electronic state (Larkins, 1975). This equation is the time independent Schrödinger equation in a nonrelativistic framework, and Dirac's equation when relativity is included. Its exact solution has not been accomplished for atoms with more than one electron so approximate methods must be used.

An approximate Hamiltonian,  $H_{\text{eff}}$ , that satisfies Schrödinger's equation is often used (Larkins, 1975)

$$H_{\text{eff}} = H_0 + H_{\text{coul}} + H_{\text{so}}.$$

$H_0 + H_{\text{coul}}$  is the nonrelativistic Hamiltonian with  $H_0$  representing the one electron part and  $H_{\text{coul}}$  the Coulomb interaction between electron pairs, and  $H_{\text{so}}$  is the one electron spin orbit correction.

In the limit when  $H_{\text{coul}} \gg H_{\text{so}}$ , the atomic states can be classified using a Russell-Saunders or LS coupling scheme for the vector coupling of spin and orbital angular momenta. The energy state of the system (referred to as a term) is characterised by the quantum numbers  $n$  and  $l$ , the total orbital angular momentum  $L$  and the total spin angular momentum  $S$ . A term is identified by the symbol  $^{2S+1}L$ . In the absence of spin-orbit interaction and magnetic effects, a term has  $(2S+1)(2L+1)$  degenerate energy components. The LS

scheme closely represents the coupling in atoms of low atomic number. When the spin-orbit interaction effect dominates,  $H_{SO} \gg H_{coul}$ , a jj coupling scheme is applied. Here energy states are characterised by the quantum numbers  $n, l$  and  $j$  and the total angular momentum  $J$ . This limit is approached for atoms of high atomic number. For most atoms the vector coupling lies between the two extremes. For  $H_{coul} \sim H_{SO}$  intermediate coupling is used. The energy levels are characterised by  $n, l$  and  $j$ , and  $L, S$  and  $J$ , because the spin-orbit interaction term lifts the degeneracy of energy levels in LS coupling. These levels are identified by the symbol  $^{2S+1}L_J$ , where  $|L - S| \leq J \leq |L + S|$ . These coupling schemes are discussed by Condon and Shortly (1935).

Equation 2.1 is often solved using the self-consistent field Hartree-Fock method (Hartree, 1927; Fock, 1930a,b). The solution is summarised by Larkins (1975) for non relativistic, intermediate coupling and relativistic systems.

Once the total energies of the initial and final electronic states have been calculated, the transition energy (kinetic energy of the Auger electron) is found by conservation of energy to be

$$E(\text{trans}) = E(\text{initial}) - E(\text{final}).$$

From figure 2.2, for the general Auger-type process WXY, the transition energy is

$$E(WXY) = E(W) - E(XY) \quad (2.2)$$

where  $E(W)$  and  $E(XY)$  represent the energies of the initial and final states. In principle, with a knowledge of the atomic state energies  $E(\text{initial})$  and  $E(\text{final})$  the transition energies can be calculated. However, because of the approximations required to solve equation 2.1 several semi-empirical methods have evolved to calculate Auger electron energies.

Larkins (1977) has calculated Auger electron energies for the elements  $10 \leq Z \leq 100$  using a semi-empirical method (Larkins, 1976) developed within an intermediate coupling framework. The Auger electron energy for the  $W_i X_j Y_k, {}^{2S+1}L_J$  process is determined with the expression

$$E(W_i X_j Y_k, {}^{2S+1}L_J) = E_Z(W_i) - E_Z(X_j) - E_Z(Y_k) - \Delta({}^{2S+1}L_J)$$

where  $E_Z(W_i)$  is the binding energy of an electron in a selected subshell  $W_i$  of an atom with atomic number  $Z$  and  $\Delta({}^{2S+1}L_J)$  is a correction term evaluated for the  ${}^{2S+1}L_J$  final state configuration of the system. For vapour phase systems

$$\Delta({}^{2S+1}L_J) = \langle X_j Y_k \rangle {}^{2S+1}L_J - K(X_1 Y_1)$$

while for solid phase systems

$$\Delta({}^{2S+1}L_J) = \langle X_j Y_k \rangle {}^{2S+1}L_J - K(X_1 Y_1) - S(Z).$$

$\langle X_j Y_k \rangle {}^{2S+1}L_J$  is the interaction energy of a pair of holes in the orbitals  $X_j$  and  $Y_k$  of an atom in the  ${}^{2S+1}L_J$  multiplet state. Larkins expresses this as a combination of Slater integrals (Slater, 1960) and the appropriate spin orbit coupling parameters, assuming frozen orbitals from the initial to the final state. In the frozen orbital approximation the transition from initial to final state is assumed to be so rapid that the 'spectator' electrons do not have time to adjust to the changing electronic environment within the lifetime of the process. The same wavefunction can then be used for both the initial and final states.  $K(X_1 Y_1)$  is the adiabatic relaxation correction which accounts for the adjustment of the 'spectator' electrons within the transition lifetime. This correction is often called 'intra-atomic relaxation' (Shirley, 1973; Matthew, 1973).  $S(Z)$  is the solid state correction term which accounts for the partial screening of core holes by the

valence band electrons in the solid system. This 'extra-atomic relaxation' (Kowalczyk et al., 1974 and 1973) reduces the total energy of the excited state.  $S(Z)$  is derived using an atomic Hartree-Fock screening model.

Larkins uses experimental binding energies compiled by Sevier (1972) and states that the accuracy of his results depends largely on the accuracy of the binding energies. Where the binding energies are known to a high accuracy he suggests that his Auger electron energies are within 1 to 2eV of the experimental values with the maximum discrepancies near 5eV. Larkins' energies are for the solid phase and referenced to the Fermi level (Larkins, 1977). These results are compared with the Auger line energies found in the present experimental work.

There are also several empirical methods for solving equation 2.2. The simplest method is to neglect the change in binding energy of an electron due to the presence of a hole in another shell and write

$$E_Z(WXY) = E_Z(W) - E_Z(X) - E_Z(Y).$$

Often the binding energy of the ejected electron is taken to be that of the atom of the next higher atomic number as it 'feels' a greater nuclear charge due to the reduced screening of the inner electrons because of the inner vacancy. This gives

$$E_Z(WXY) = E_Z(W) - E_Z(X) - E_{Z+1}(Y).$$

Bergström and Hill (1954) suggested the equation

$$E_Z(WXY) = E_Z(W) - E_Z(X) - E_Z(Y) - \Delta Z(E_{Z+1}(Y) - E_Z(Y)) \quad (2.3)$$

where  $\Delta Z$  is determined by fitting to experimental results. Since there is no difference between the WXY and WYX Auger

electrons Albridge and Hollander (1961) made equation 2.3 symmetric, and Chung and Jenkins (1970) set  $\Delta Z=1$  to give

$$E_Z(WXY) = E_Z(W) - \frac{1}{2}(E_Z(X) + E_{Z+1}(X) + E_Z(Y) + E_{Z+1}(Y)) \quad (2.4)$$

This formula has a typical accuracy of the order of 5eV.

#### 2.4 Auger Yields and Intensities

The experimentally measured current from an Auger peak for a solid specimen is  $\sim 10^{-5} i_p$ . Hence a primary electron beam current  $i_p \sim 10^{-6} A$ , gives an Auger current of  $\sim 10^{-11} A$ . The observed Auger current is taken as a measure of the Auger line intensity. For initial atom ionisation by electrons this current depends on (a) the cross-section for ionisation  $\sigma_W$  and (b) the Auger yield per initial vacancy  $a_{WXY}$ .

$\sigma_W$  depends mainly on the primary beam energy and the binding energy  $E_W$  of the shell  $W$ . Various methods have been used to calculate the variation of  $\sigma_W$  as a function of the primary beam energy  $E_p$  but the general trend follows the equation (Chattarji, 1976)

$$\sigma_W = \frac{\gamma}{E_W^2} \frac{\ln U}{U} \quad (2.5)$$

where  $U = E_p/E_W$  and  $\gamma$  is a constant depending on the number of electrons in the shell  $W$ .  $\sigma_W$  is a maximum when  $U \sim 2.72$ , that is for  $E_p \sim 2.72 E_W$ .  $\gamma$  ranges from 600 to 1100 (Bauer, 1975).

The variation of the intensity of a peak with primary beam energy  $E_p$  was plotted for several peaks in the present experimental work. The intersection of this distribution with the  $E_p$  axis indicates the minimum primary beam energy necessary for ionisation and therefore identifies the initial core level leading to Auger (or other) decay. The

shape shows whether the peak is the result of an Auger process, (similar to equation 2.5), from a different origin, or the sum of two or more separate processes (see Rawlings et al. (1980b) for examples of composite peaks).

$a_{WXY}$  is the probability that a vacancy  $W$  is filled by an Auger transition involving the levels  $X$  and  $Y$ . Wentzel (1927) gave the first derivation of the Auger transition probability for the non-relativistic situation. The Coulomb interaction between the two electrons involved is considered to be the perturbation that causes one electron to undergo a transition from its initial bound state to a final state in the positive energy continuum, and the second electron to fill the initial atomic vacancy. Perturbation theory gives (Mott and Massey, 1965)

$$a_{if} = \left(\frac{2\pi}{\hbar}\right) \left| \langle i | \frac{e^2}{|\mathbf{r}_1 - \mathbf{r}_2|} | f \rangle \right|^2$$

which must be summed over all possible final states (depending on the coupling scheme). Møller (1931) derived a relativistic formula for the probability amplitude. He assumed that one electron acted as a source of virtual photons and a second electron interacted with these photons. The derivation is shown by Chattarji (1976). The formula includes both the Coulomb repulsion between the two electrons and the relativistic current-current (spin-spin) interaction. It reduces to Wentzel's equation in the non-relativistic limit.

There are two different methods used to solve these equations; screened hydrogenic and Hartree-Fock-Slater. The screened hydrogenic calculations differ in the choice of screening constants and are not very accurate. Three types of Hartree-Fock-Slater methods are used (McGuire, 1975a).

McGuire (1974) uses one of these Hartree-Fock-Slater methods (McGuire, 1969) to calculate N-shell Auger transition rates, yields and level widths (see next section) for  $38 \leq Z \leq 103$ . His calculations use j-j coupling apart from decay for initial f holes ( $N_{6,7}$  holes) which use LS coupling. He estimated the energy of the Auger electron using equation 2.4 and found that his calculations of transition rate for ejection of NNX and NNN (where X represents other shells apart from N) Auger electrons were sensitive to the estimate of Auger electron energy. McGuire's calculations (McGuire, 1974 and 1975b) will be compared to the present experimental work in later chapters.

In view of the complications introduced by the solid-state environment, Auger yields and intensities in free atoms can only act as a very rough guideline for atoms in a solid.

The electron current from an Auger transition in a solid depends on the primary beam current, the cross-section for ionisation, the Auger yield per initial vacancy, the backscattering factor (enhancement of Auger line due to backscattered primary electrons and energetic secondary electrons), the escape probability for an Auger electron in a certain direction (depending on the mean free path), and the atomic concentration of the element (Palmberg, 1976).

## 2.5 Auger Line Widths and Shapes

The shape of an X-ray emission line can be calculated using the Dirac quantum theory of the radiation field (Weisskopf and Wigner, 1930; F. Hoyt, 1930; A. Hoyt, 1932) or in terms of a classical model by treating the radiating atom as a damped harmonic oscillator (Sevier, 1972). Both methods give the intensity  $|a_\gamma|^2$  of emitted radiation of frequency

$$J(\gamma) d\gamma = |a_\gamma|^2 d\gamma = \frac{\Gamma}{2\pi} \frac{d\gamma}{2\pi(\gamma_0 - \gamma)^2 + (\Gamma/2)^2} .$$

The transition line width  $\Gamma$  (f.w.h.m.) is equal to the sum of the widths of the initial and final states. The frequency distribution is a Lorentzian profile. When two Lorentzian distributions are 'folded' together (Sevier, 1972) the resulting distribution is also Lorentzian with the width equal to the sum of the widths of the original two curves.

If a free ion with a vacancy in an inner shell is considered, the lifetime of the state is determined by the sum of all possible decay processes. These are either radiative with the probability  $\omega_R$  or radiationless (i.e. Auger (A) or Coster-Kronig (CK))

$$\omega_R + \omega_A + \omega_{CK} = 1. \quad (2.6)$$

According to Heisenberg's uncertainty principle the natural width of a level  $\Gamma$  is inversely proportional to the lifetime of a vacancy in that level  $\tau$ ,

$$\Gamma = \frac{\hbar}{\tau}, \quad (2.7)$$

and, due to folding, equal to the sum of the partial widths

$$\Gamma = \Gamma_R + \Gamma_A + \Gamma_{CK} \quad (2.8)$$

because the energy distribution is Lorentzian. It follows that the partial widths are proportional to the respective transition rates: from equations 2.7 and 2.8

$$\frac{1}{\tau} = \frac{1}{\tau_A} + \frac{1}{\tau_R} + \frac{1}{\tau_{CK}}$$

and then using equations 2.6 and 2.8

$$\omega_R = \frac{\Gamma_R}{\Gamma}, \quad \omega_A = \frac{\Gamma_A}{\Gamma}, \quad \omega_{CK} = \frac{\Gamma_{CK}}{\Gamma}.$$

The lifetime is often governed by Coster-Kronig transitions which have a high transition probability when they are energetically possible.

Auger transition line widths arise from the width contributions of the three atomic levels participating in the transition. Width value estimates assuming that the Auger line width is equal to the sum of the atomic levels agree well with measured widths after correcting for instrumental broadening (e.g. Erman et al., 1965).

In the solid state the electronic energy levels are broadened by the mutual interaction of the atoms. The inner levels have negligible broadening compared to their natural linewidth but the weakly bound electrons form the valence bands which are described by their density of states. The Auger lines of a solid state sample are broadened compared to the gaseous state because of the changes in lifetime broadening. The core level (initial state) lifetime will not be changed much (Shaw and Thomas, 1972) but the lifetime broadening of the final state will increase (Gallon and Nuttall, 1975). After an Auger transition in a gas, further de-excitation is often not energetically allowed giving a long lived final state. In solids, however, there are many electrons available in the valence band which can take part in further transitions giving the final state a short lifetime and thus producing broader peaks. The solid state is also responsible for the characteristic tailing structure which is sometimes seen on the low energy side of the Auger peak. This is produced by escaping electrons that have suffered small energy losses ionising weakly bound electrons (Matthew and Komninos, 1975).

The experimental line shape is a mixture of the Auger line shape and the instrumental width contribution. The Auger line shape is Lorentzian and the instrumental line shape is usually approximated by a Gaussian line shape. If two Lorentzians are folded together the widths are added:

$$\Gamma_{ab} = \Gamma_a + \Gamma_b$$

whereas for two Gaussians

$$\Gamma_{ab}^2 = \Gamma_a^2 + \Gamma_b^2.$$

Thus the measured width is neither the sum of the Auger width and instrumental width nor the root of the sum of the squares. To obtain the natural width, the measured line shape is often matched with the Voigt integrals; a function representing the folding of a Gaussian G line shape and Lorentzian L profile.

$$S(x) = \int_{-\infty}^{+\infty} G(x - \delta) \cdot L(\delta) d\delta. \quad (2.9)$$

Normalised S shapes for several values of G/L ratios are shown by Krause (1975).

There is further broadening relevant in the present experimental work which results from the method of detection. This will be discussed in chapter 4.

## 2.6 Origins of Other Peaks in the Secondary Electron Spectrum

In the secondary electron spectrum there are many other ways of producing peaks in the same region as the Auger peaks under study. These peaks can easily be mistakenly attributed to an Auger transition and so care must be taken in analysing the spectrum.

The most important non-Auger peaks are loss peaks and diffraction features. There is also the possibility of the Auger process occurring in a doubly ionised atom.

Energy loss peaks are due to primary electrons that have lost discrete amounts of energy by exciting collective oscillations of the valence electrons in the solid (plasma oscillations) or interband transitions. The energies of the loss peaks are well defined with respect to the primary energy. Thus a shift in the primary energy causes a corresponding shift of the energy loss spectra.

In Auger spectra from single crystal surfaces peaks have been observed which are strongly temperature dependent. They can be explained by the assumption of a slightly different mean free path for electrons of certain energy, emitted into certain directions of the crystal. These diffraction features depend on the degree of perfection of the crystal surface and on the aperture of the analyser. (McDonnell et al., 1973; Becker and Hagstrum, 1974).

## 2.7 Principles of Secondary Electron Detection

The analyser used in the present work is a cylindrical mirror analyser (C.M.A.). It is a window device or 'band-pass filter' which only collects electrons in a narrow energy range  $\Delta E$  at  $E$  (Palmberg et al., 1969). The arrangement consists of two coaxial cylinders with the sample placed normal to and on the axis of the cylinders (figure 2.3). The inner cylinder and sample are grounded. The outer cylinder has a negative voltage  $V_a$  applied to it so that secondary electrons leaving the sample and passing through a gridded aperture in the inner cylinder are reflected towards a second aperture in the inner cylinder. The ratio  $E/eV_a$  depends on the geometry of the analyser (including the position of the specimen) and lies between 1 and 2. An annular slit at the focal position allows only electrons with energy values in a narrow region  $\Delta E$  around the energy  $E$  to reach the collector. The current reaching the collector is

$$I(E) \approx K \Delta E N(E) = K R E N(E) \quad (2.10)$$

where  $K$  is a constant for the geometry used and  $R = \Delta E/E$  is the resolution which is a constant in the absence of stray magnetic fields.

Being superimposed on a variable background where the total secondary current is much larger than the Auger current, the Auger peaks are very small and need to be

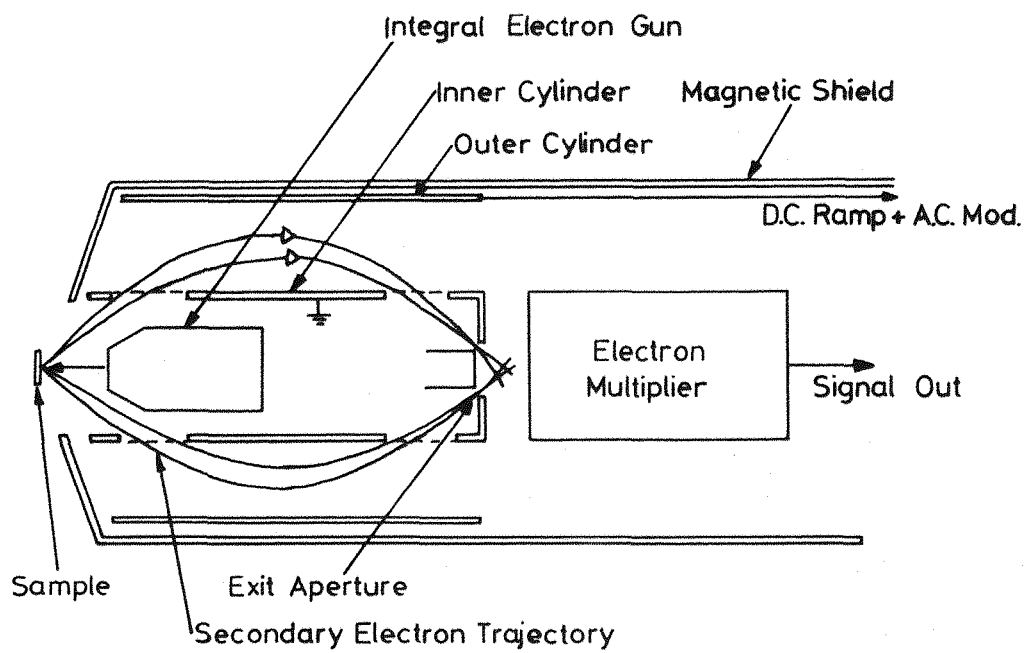


Figure 2.3 Cylindrical mirror analyser, schematic diagram.

accentuated. This is accomplished by differentiating the energy distribution to remove a large proportion of the background. Close or overlapping peaks are also better resolved in the differentiated spectrum (see chapter 4).

In the C.M.A. the current  $I$  is electronically differentiated by applying a small modulation voltage  $V_0 \cos \omega t$  to the outer cylinder and detecting the required harmonic of the output current. By Maclaurin's theorem

$$I(E+eV_0 \cos \omega t) = I(E) + e \frac{dI}{dE} V_0 \cos \omega t + e^2 \frac{d^2 I}{dE^2} \frac{V_0^2 \cos^2 \omega t}{2!} + \dots \quad (2.11)$$

Using the half angle formula  $(\cos \omega t)^2 = \frac{1}{2}(1 + \cos 2\omega t)$  this becomes

$$I(E+eV_0 \cos \omega t) = I(E) + e \frac{dI}{dE} V_0 \cos \omega t + \frac{d^2 I}{dE^2} \frac{e^2 V_0^2}{4} (1 + \cos 2\omega t) + \dots \quad (2.12)$$

Neglecting higher order terms the  $dI/dE$  term corresponds to the first harmonic. The amplitude of this first harmonic current is

$$\begin{aligned} I(\omega) &= eV_0 \frac{dI}{dE} = eV_0 K \frac{d}{dE} (R E N(E)) \\ &= eV_0 K R (N(E) + E \frac{dN(E)}{dE}) \end{aligned}$$

The first harmonic contains  $N(E)$  as well as  $dN(E)/dE$  but the  $N(E)$  term is negligible (providing  $E \gtrsim 50$  eV) because the  $dN(E)/dE$  term is multiplied by  $E$ . Thus detection at the frequency  $\omega$  will yield the  $dN(E)/dE$  spectrum (the electronics is described in chapter 3).

Similarly the  $d^2I/dE^2$  term corresponds to the second harmonic.

$$\begin{aligned}
 I(2\omega) &= \frac{e^2 v_0^2 d^2 I}{4 dE^2} = \frac{e^2 v_0^2}{4} K \frac{d^2}{dE^2} (R E N(E)) \\
 &= \frac{e^2 v_0^2}{4} K R \left( 2 \frac{dN(E)}{dE} + E \frac{d^2N(E)}{dE^2} \right) \\
 &\approx \frac{e^2 v_0^2}{4} K R \left( E \frac{d^2N(E)}{dE^2} \right). \tag{2.13}
 \end{aligned}$$

The  $d^2N(E)/dE^2$  term dominates because it is multiplied by  $E$ , and the  $d^2N(E)/dE^2$  spectrum is plotted by detecting at twice the frequency of the modulation voltage.

## CHAPTER 3

### EXPERIMENTAL EQUIPMENT AND PROCEDURES

#### 3.1 Vacuum Equipment

To investigate clean surface properties all surface contaminants must be removed, and the rate at which re-contamination takes place must be reduced. At a pressure of  $1 \times 10^{-7}$  torr gas molecules collide with surfaces at rates that deposit about one atomic monolayer ( $\sim 10^{15}$  atoms.cm $^{-2}$ ) in 25 seconds (Dushman and Lafferty, 1962) if all the molecules stick to the surface. So at this pressure there is little time to perform an experiment before contamination becomes significant. Ideally, a pressure in the low  $10^{-10}$  torr range or below (ultra-high vacuum (u.h.v.)) should be used: then it takes about two hours for a monolayer to condense on a surface.

The u.h.v. chamber used in the present work (figure 3.1) is made of stainless steel and was built in the Physics department workshop. Experimental equipment is attached to the chamber via standard bolt-on 'conflat' flanges and includes a cylindrical mirror analyser, an ion gauge to measure the pressure, a quadrupole mass spectrometer, LEED optics and a sample manipulator assembly. The main pump is a standard Varian 140 litre.s $^{-1}$  sputter ion pump. To activate this pump a pressure of  $< 10^{-3}$  torr is required and provided by a 'Vacsorb' sorption roughing pump. The sorption pump is connected to the main chamber via the backing line which can be completely isolated from the main chamber and main ion pump. The backing line has its own 8 litre.s $^{-1}$  ion pump and has three gas inlet valves allowing three different gases to be available. Oxygen was used in the present work for cleaning the samples.

To reach u.h.v. the rate of influx of gas into the chamber must be reduced. The most common source of gas is from gases which have been adsorbed onto the surfaces inside the chamber during exposure to the atmosphere: these desorb

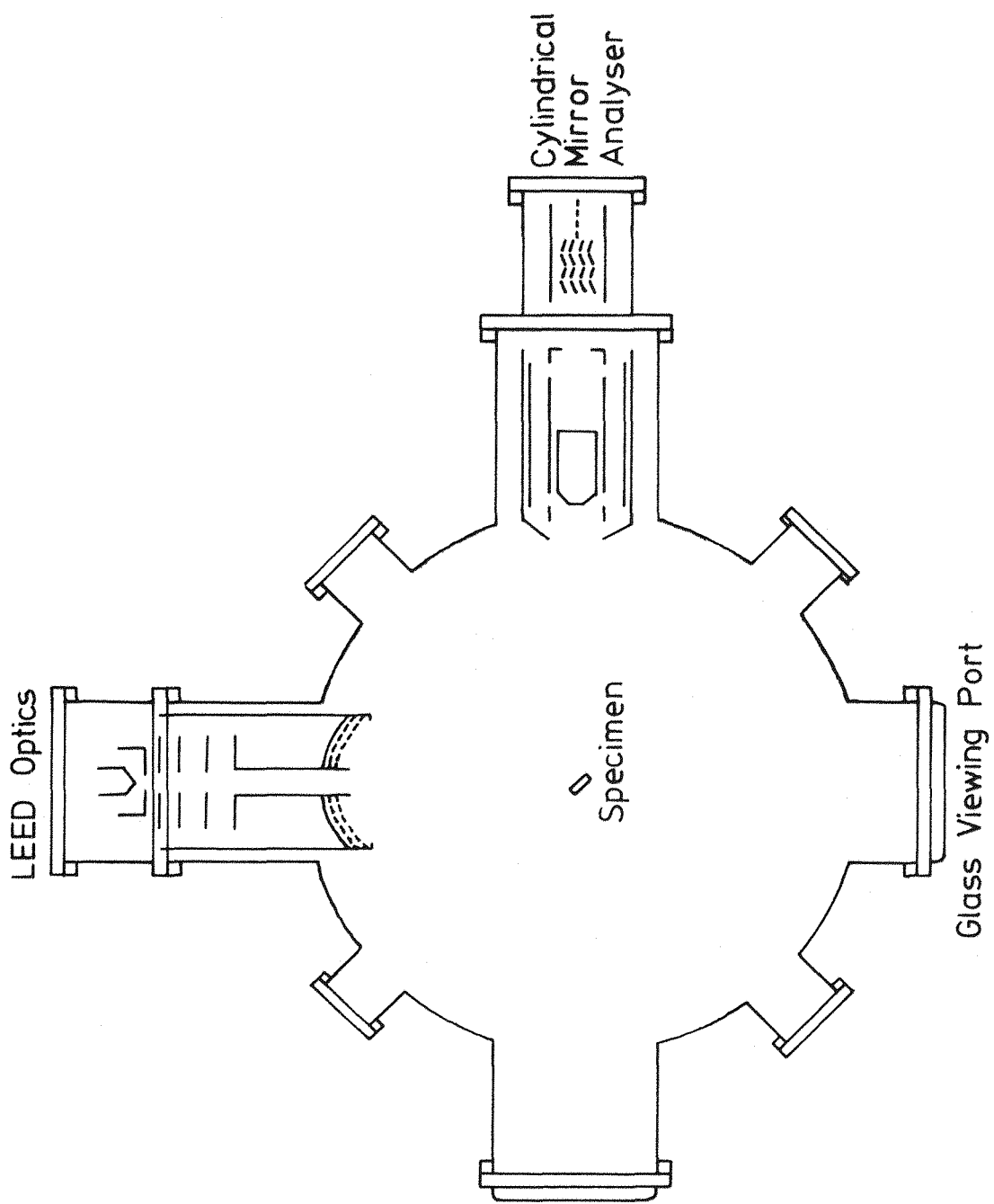


Figure 3.1 Schematic of experimental chamber.

as the pressure in the chamber is reduced. After initial pump down, with the sorption pump and ion pump to about  $10^{-8}$  torr, a preliminary outgas of the specimen and all gauges and filaments was carried out. Then the entire system, including the ion pumps and backing line, was baked at  $\sim 200^{\circ}\text{C}$  for  $\sim 48$  hours to desorb gases from the surfaces inside the chamber (for details see Jones, 1976). An ultimate pressure of  $2 \times 10^{-10}$  torr could be recorded after further outgassing of the specimen, gauges and filaments.

Pressures were measured using two commercial Bayard-Alpert type ionisation gauge heads. One was in a glass envelope out of line of site of the rest of the equipment and the other was a 'nude' gauge inside the main chamber.

### 3.2 Sample Mount and Manipulator

The sample mount is shown in figure 3.2. It was designed for use in gas adsorption experiments (Jones, 1976) and therefore incorporates both efficient Joule heating and liquid nitrogen cooling of the sample (the facility for cooling was not used in the present work). The ribbon sample was wedged in tungsten foil which was spot welded to tantalum foil strips attached to the sample cooler. The copper heating leads running from the sample cooler to the electrical feed-throughs were covered with fibreglass insulation to prevent shorting as the sample was rotated. A tungsten-tungsten 26% rhenium thermocouple was used to measure the temperature of the sample. The thermocouple leads were sprung against the back of the sample and the thermocouple voltage calibrated against an optical pyrometer.

Manipulation of the sample was achieved by a rotary drive (Torvac Ltd.) mounted on flexible bellows (Palatine Precision Ltd.) which allowed rotation, vertical translation and tilt in the vertical plane.

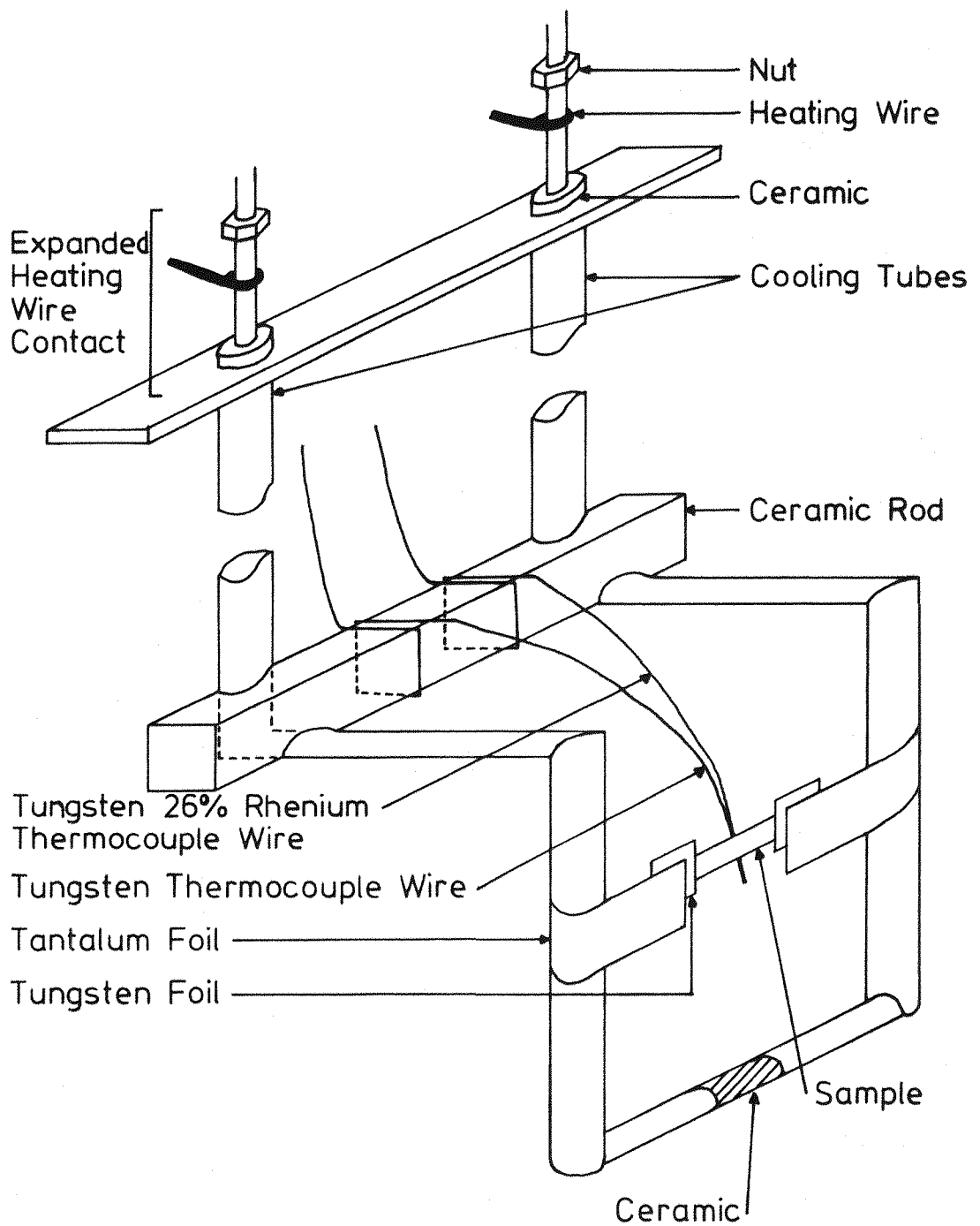


Figure 3.2 The sample mounting.

### 3.3 Auger Electron Spectroscopy Instrumentation

#### 3.3.1 Hardware

The electron energy analyser is a standard Varian cylindrical mirror analyser (C.M.A.) (Model No. 981-260) with an integral electron gun (figure 2.3). The principle of detecting an Auger spectrum is described in section 2.7. A block diagram of the original A. E. S. detection system is shown in figure 3.3. The selection of the desired harmonic is accomplished by amplifying the A.C. signal from the electron multiplier with a tuned pre amplifier (Nathan and Hopkins, 1973) which selects the required component of the series (equation 2.10) and provides a voltage output which is proportional to the current input at the resonant frequency. This signal is fed to a coherent detector synchronised by a signal derived from the modulation oscillator, and a smoothed D.C. output is obtained which is proportional to the input. The Nicolet 1072 instrument computer controlled the period of the ramp (though not the setting of the energy 'window') and recorded the spectra. It could be used as a signal averager, and also to smooth, add, subtract, multiply by a constant and integrate spectra. The  $N(E)$  spectra were obtained by integrating recorded  $\frac{dN(E)}{dE}$  spectra.

For most of the experimental work the instrument computer was replaced by a Cromemco Z-20 microcomputer. This microcomputer is based on the Z-80 microprocessor, has 64Kbytes of RAM (Random Access Memory) and two  $5\frac{1}{4}$  inch floppy disk drives. It was chosen because it combined the low cost of a microcomputer with the versatility provided by its S-100 bus and CP/M compatible disk operating system (see next section). The S-100 bus has become a de facto standard and there are therefore many different interface boards made by several manufacturers which can plug into this bus. The best interface board can thus be chosen for each

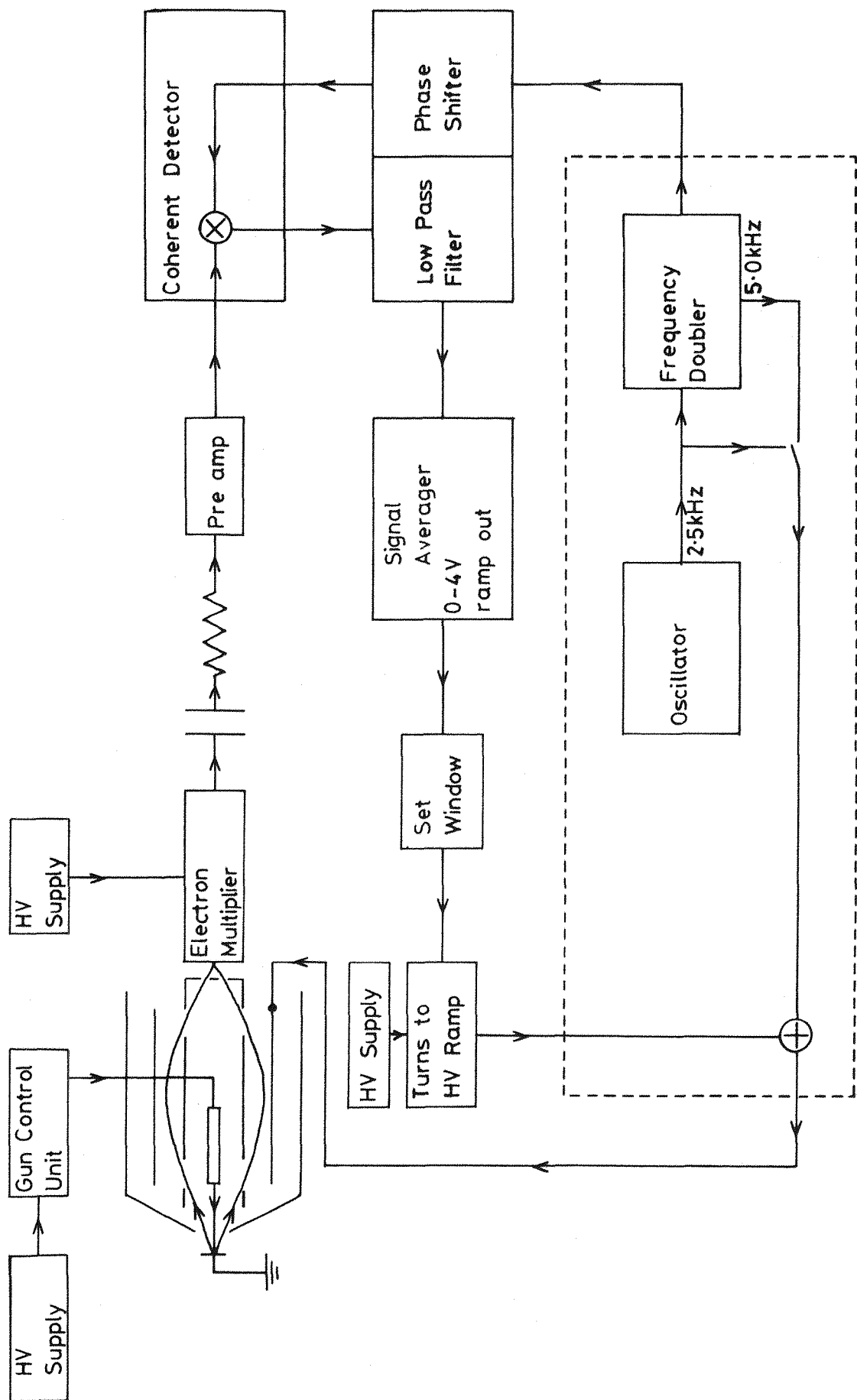


Figure 3.3 Auger Electron Spectroscopy detection system.

application. The S-100 bus in the Cromemco has 22 sockets permitting easy future expansion of the system.

The computer was interfaced to the experiment as shown in figure 3.4 via 12-bit and 8-bit analogue I/O boards. The experimental spectra were displayed on an oscilloscope; the display being updated as the data was logged. Though the data was collected and plotted with 12-bit accuracy (1 part in 4096) the 8-bit accuracy display (1 part in 256) with 256 x 256 points was adequate visually.

The total energy range required for the ramp was provided by amplifying a 0 to 10 volt ramp from the 12-bit DAC to 0 to 400 volts. Sub energy ranges (energy 'windows') were then produced by scanning the relevant part of the 0 to 10 volt ramp (Appendix Ia). The rate of data collection was also controlled by the computer.

### 3.3.2 Software

The Cromemco Z-2D is provided with the Cromemco Disk Operating System (CDOS) which is compatible with the industry standard Z80 operating system CP/M. Thus there is a large choice of software available which does not necessarily have to be provided by Cromemco. A large proportion of the software to control data logging and later data analysis was written in Pascal using the Pascal/Z compiler provided by Ithaca Intersystems. The device drivers (I/O software) had to be written in assembly for speed.

There are three main methods of controlling equipment by computer. These are menu selection, fill-in-the-blank and parametric methods (Shneiderman, 1980; Martin, 1973). In menu methods the user selects one of a set of numbered choices for each decision that has to be made. For fill-in-the-blank methods the user provides a word, number, or phrase in response to a question from the computer. Both these methods are computer initiated and very easy to use but become repetitious and time consuming in frequent use. Parametric methods, however, are user initiated; the user

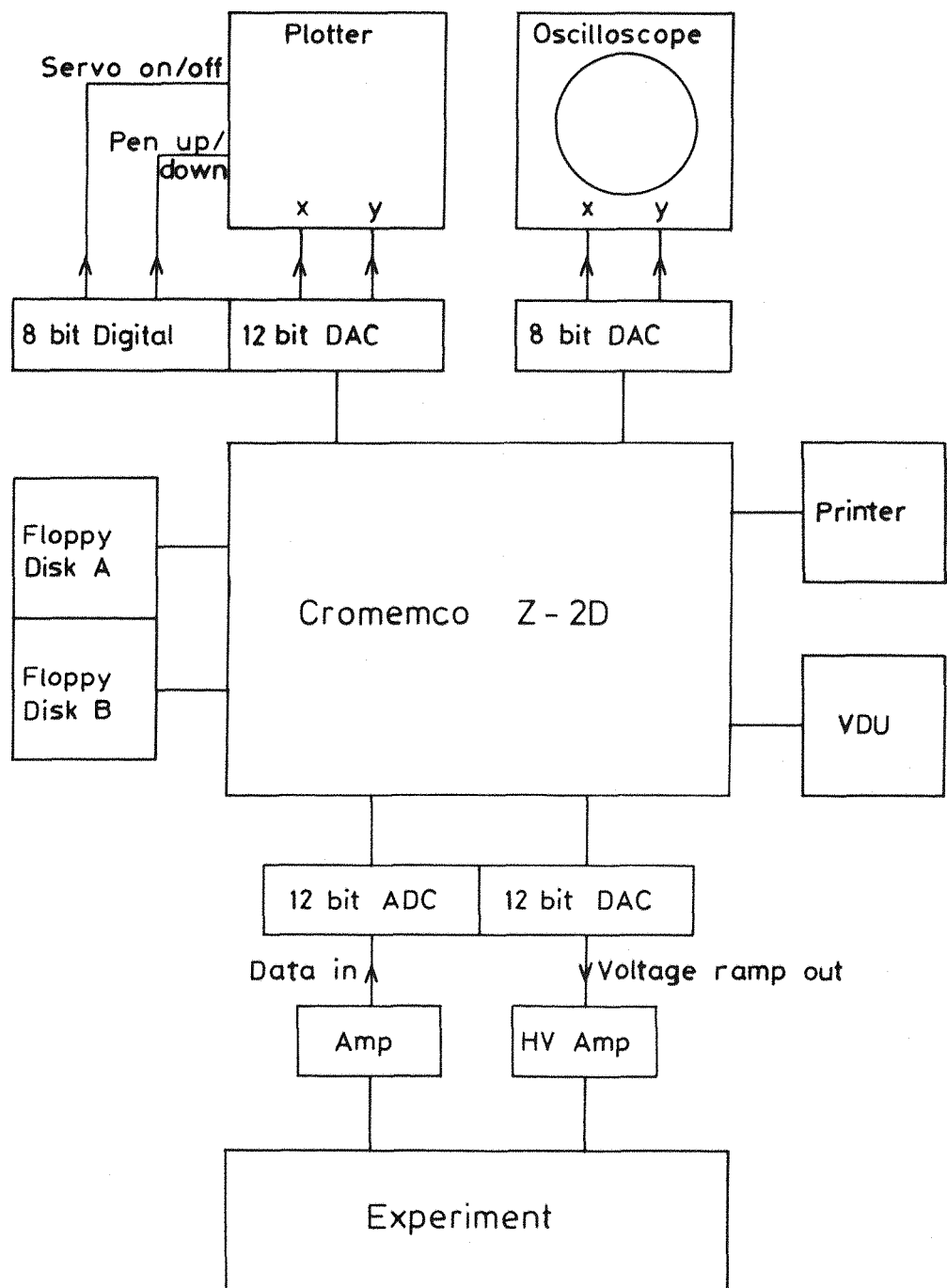


Figure 3.4 Block diagram of the computer system.

provides a formatted set of numbers, codes or words which the computer obeys. These systems require more training but are faster to use. Good error checking and handling is important with parametric methods because they are user initiated.

For this application a parametric method was used in the form of a special language interpreter (Knowles, Croxall and Hopkins, 1982). Interpreters allow greater flexibility than other methods as they can deal with both immediate execution of a single command and deferred execution of a set of commands (called the user program). For a description of how the 'Experimental Control Language Interpreter' works see Appendix Ib.

An example of a typical user program is listed in figure 3.5. This program was used to produce the spectra in figures 3.6, 3.7 and 3.8. The program is largely self explanatory. SET commands are used to change values stored in the STATUS. The status in figure 3.9 was for the spectrum in figure 3.6a. When a spectrum is saved on a floppy disk its STATUS is permanently stored with it so that it can be accurately identified in the future. There are six 'memory boxes' in which spectra can be stored denoted as @1 etc. in the user program. As in the instrument computer, spectra stored in these 'boxes' can be added, subtracted, smoothed, integrated etc. An advantage of the present system is that data can be saved on disk for later analysis. The allowed user commands are listed in Appendix Ic.

### 3.3.3 High Temperature A.E.S.

In order to identify diffraction features it was necessary to record the secondary electron spectrum at different temperatures. The original method of heating the sample was resistively with an A.C. current. If the A.C. was left on during an Auger spectrum scan, the alternating magnetic fields set up affected both the primary electron beam and the secondary electrons: thus no sensible

```

10      (FIRST DO SECOND DIFFERENTIAL SPECTRUM)
20      SET ORDER = 2
30      SET GAIN = 32 (THIS IS GAIN OF AMPLIFIER
                      IN FIGURE 3.4)
40      SET EL = 40
50      SET EH = 195
60      PRINT "SWITCH ON BEAM AND CHECK BEAM CURRENT"
70      PAUSE
80      SWEEP @1,4
90      SET EL = 190
100     SET EH = 345
110     SWEEP @2,4
120     (NOW DO FIRST DIFFERENTIAL SPECTRUM)
130     SET ORDER = 1
140     SET GAIN = 8
150     SET EL = 40
160     SET EH = 195
170     PRINT "SWITCH TO FIRST DIFFERENTIAL"
180     PAUSE
190     SWEEP @3,4
200     SET EL = 190
210     SET EH = 345
220     SWEEP @4,4
230     PRINT "SWITCH OFF BEAM"
240     (NOW INTEGRATE TO GET N(E))
250     (ADD AN OFFSET TO GIVE THE FLAT BACKGROUND)
260     LET @3 = @3+400
270     (AND INTEGRATE AFTER DIVIDING BY 2x2x2x2x2)
280     LET @5 = INTEGRAL (@3↑-5)
290     (DISPLAY SPECTRA ON SCOPE WITH SUITABLE
      MULTIPLICATION FACTORS)
300     DISPLAY @1↑-5
310     DISPLAY @2↑-5
320     DISPLAY @3↑-5
330     DISPLAY @4↑-5
340     DISPLAY @5↑-5
350     END

```

Figure 3.5 User Program to Produce the Spectra in figures 3.6, 3.7 and 3.8.

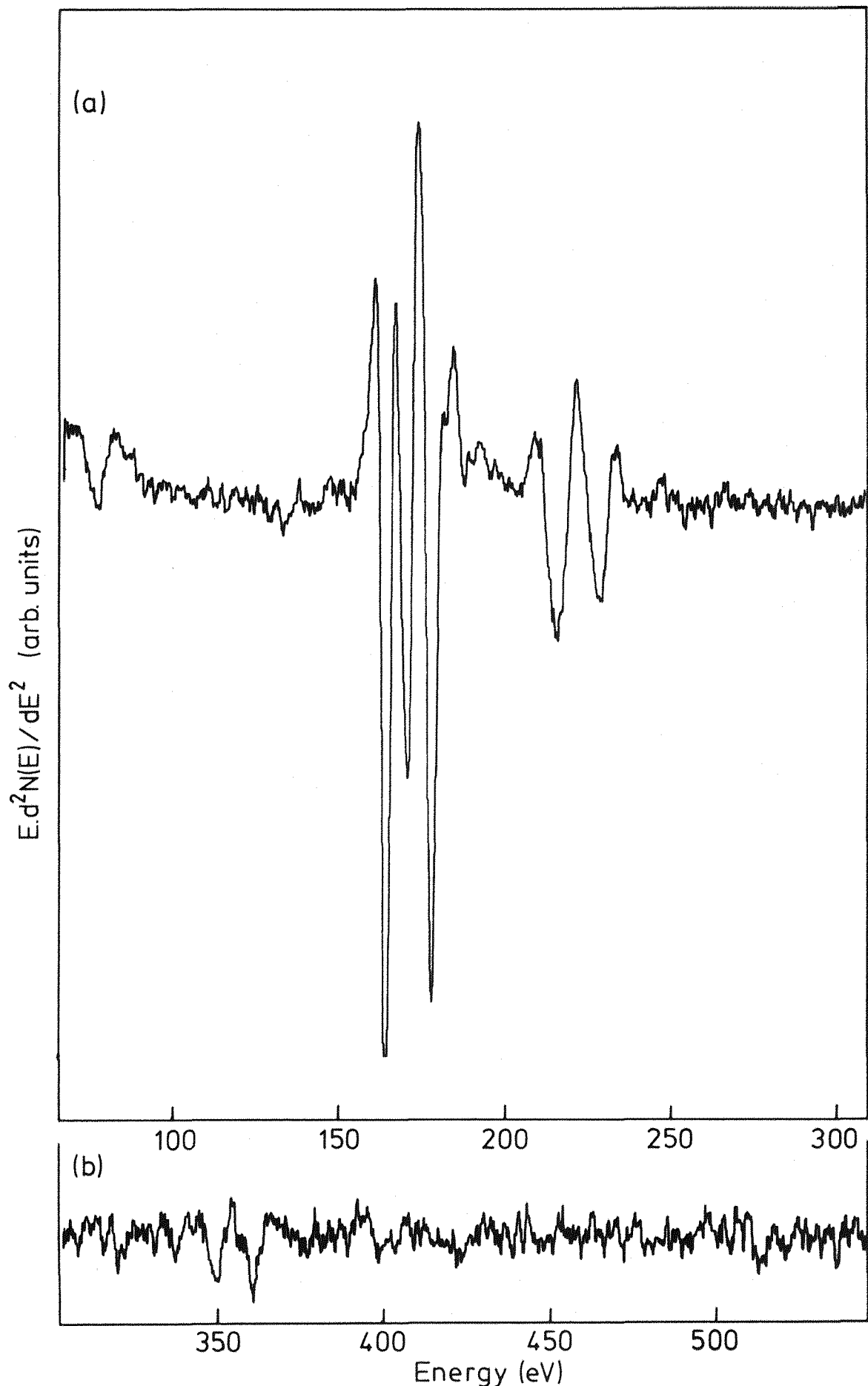


Figure 3.6 Rhenium 'Auger' spectrum induced by 2500 eV primary electrons ( $I_b = 5 \mu A$ ,  $v_m = 2.5 V_{ptp}$ ,  $\tau = 0.3 s$ , scan  $1 eV \cdot s^{-1}$ ).

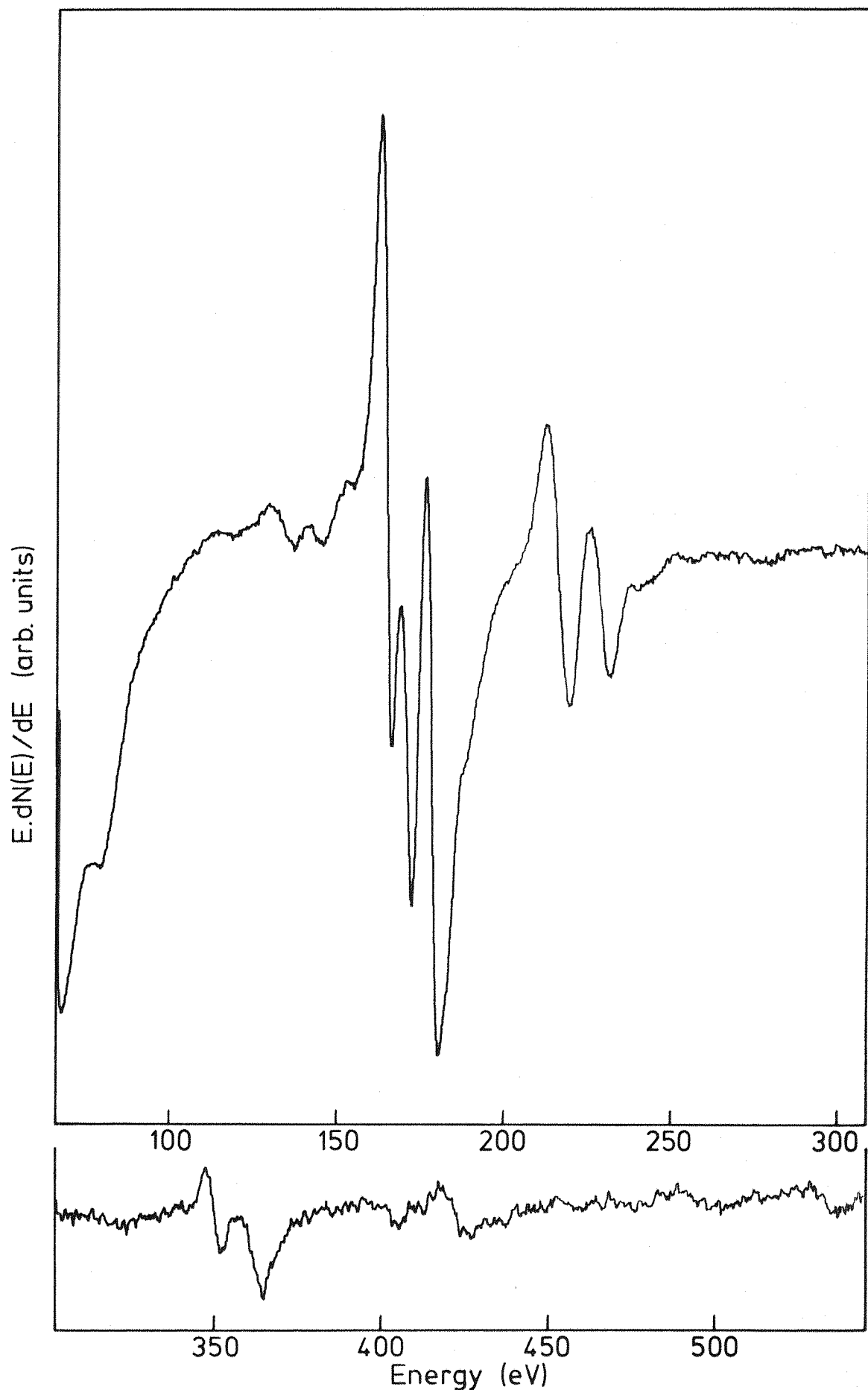


Figure 3.7 Rhenium 'Auger' spectrum induced by 2500 eV primary electrons ( $I_b = 2\mu A$ ,  $v_m = 3.1V_{ptp}$ ,  $\tau = 0.3s$ , scan  $1eV.s^{-1}$ ).

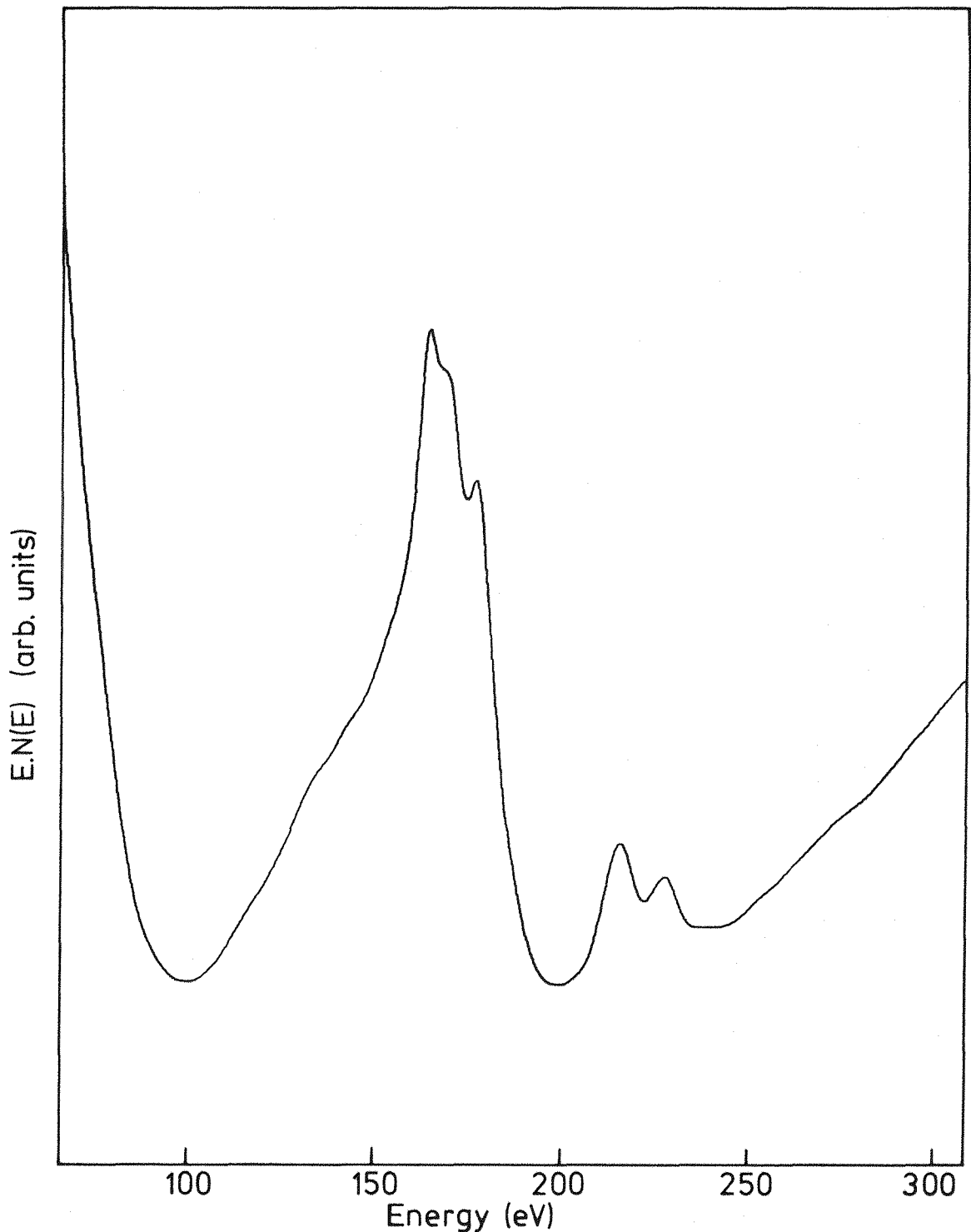


Figure 3.8 Rhenium 'Auger' spectrum, integral of figure 3.7.

on 1/8/81 at 12:00:00

ME = SYLVIA KNOWLES  
STRUCT = POLYCRYSTALLINE  
MODE = CLEAN AUGER  
REF = BOOK 3, PAGE 40  
NB = FOR THESIS  
METAL = RHENIUM  
GAS = AS LITTLE AS POSS.  
CRYSTAL PLANE <000>  
ORDER = 2 =  $d^2N/dE^2$   
GAIN = 32  
T = 293 Kelvin  
EL = 40.0 eV  
EH = 193.4499 eV  
EXP = 0.000000E+00 Langmuir  
RATE = 1.000000E+00 eV/sec  
IB = 4.999998E-06 amps  
EP = 2.500000E+03 eV  
VM = 5.439997E-01 volts

4 scans with version 1-a

Figure 3.9 STATUS for Spectrum in figure 3.6a

measurements could be taken. A better method of heating the sample was necessary.

Many people, including Burton et al. (1976) use an electron beam to heat the sample. This eliminates any magnetic effects due to resistive heating. Others, Shelton et al. (1974), pass a D.C. current through the crystal and deflect the primary electron beam back to its room temperature position. It is extremely difficult to adjust the primary beam to hit exactly the same spot on the crystal at all temperatures. Also, the constant magnetic field will deflect all the secondary electrons being detected. A third method has been used by Tu and Blakely (1976) for use with a C.M.A., and Hamilton (1978) for a retarding field analyser. They switch the sample heating current on and off at  $\sim 200\text{Hz}$  and only collect secondary electrons during the 'off' periods. To do this Tu and Blakely arrange that the incident beam is deflected off the sample during the 'on' periods. In this way the Auger electrons are collected under field-free conditions.

A method similar to that of Tu and Blakely was used for the present experiments based on a pulsed heater. The final design is shown in figure 3.10. The circuit is designed so that the D.C. heating current is on during up to half of a 200Hz cycle, and Auger electrons are detected in the other half of the cycle. The heating pulse has a constant amplitude of 40A at the crystal; in order to change the temperature of the crystal the width of the pulse is varied between zero and the maximum of half the total cycle. The pulse width can be set either manually or via a feedback circuit which keeps the mean voltage across the crystal constant. The Auger electron detection circuit is controlled via a monostable and opto. isolator which switches the pre amplifier off during the heating half of the cycle.

In this way Auger electrons can be collected from a hot crystal without problems due to magnetic fields.

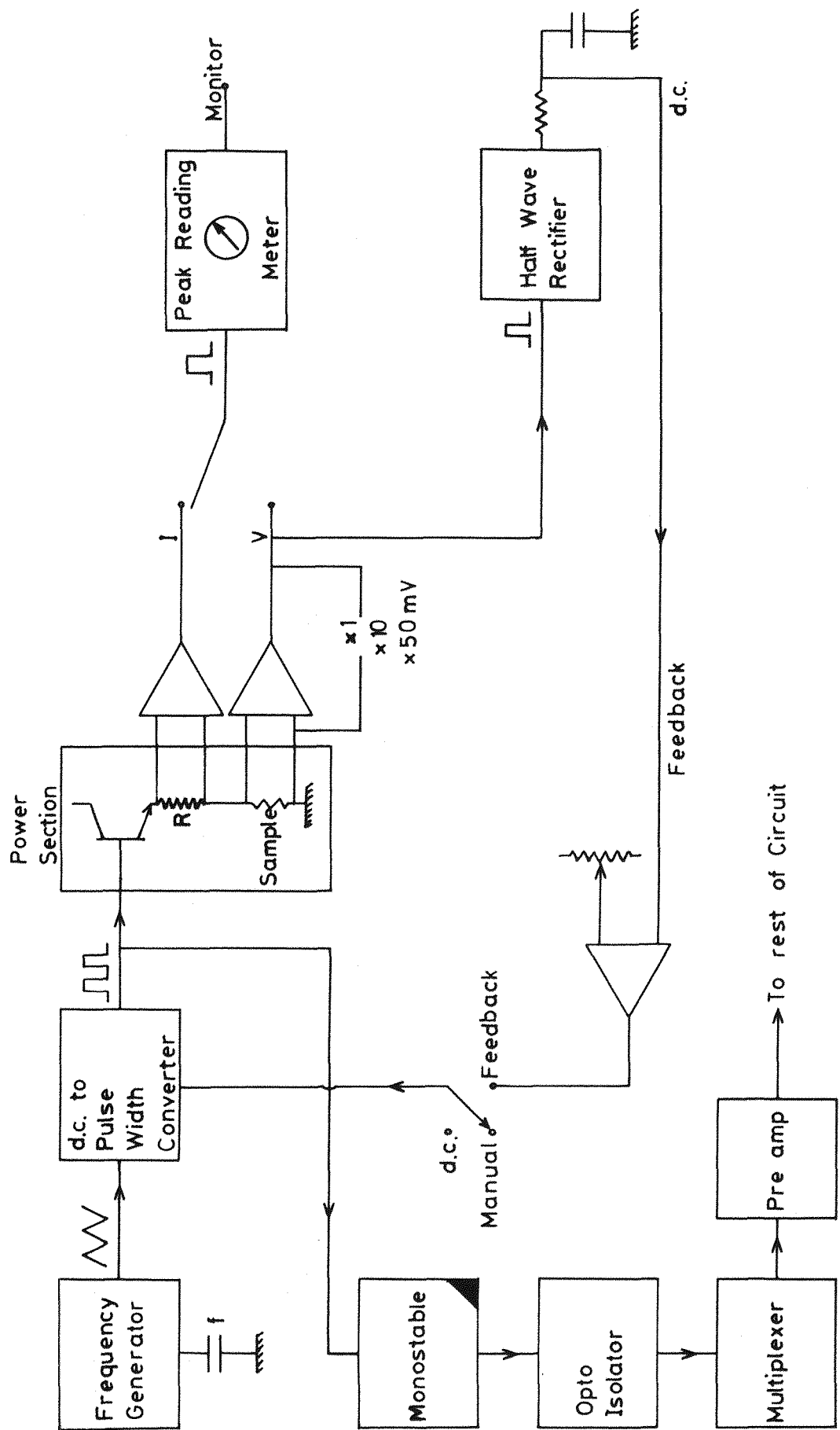


Figure 3.10 Schematic diagram of pulsed heater.

### 3.4. Sample Preparation

#### 3.4.1 Tungsten (B.C.C.)

The tungsten sample was a W(110) single crystal ribbon of dimensions 9mm x 3mm x 0.13mm. It was originally used for gas adsorption experiments by Rawlings et al. (e.g. 1978) and Foulias (1982).

It had been spark cut, mechanically polished and chemically etched before being mounted in the vacuum chamber. Cleaning in vacuo (mainly to remove carbon) was achieved by repeated cycles of 1500K heating in  $5 \times 10^{-8}$  torr of oxygen followed by flashing to 2000K in  $2 \times 10^{-10}$  torr to remove the oxide layer and allow more carbon to segregate to the surface. This was repeated until the surface was clean (Foulias, 1982). The surface was flashed to  $\sim 2000$ K frequently during the present experiments to remove any oxygen and deplete the surface of carbon (carbon segregates into the bulk at high temperatures (Foulias, 1982)).

#### 3.4.2. Rhenium (H.C.P.)

The rhenium surface used in the present experiments was that of a polycrystalline ribbon 10mm x 3mm x 0.125mm supplied by Goodfellow metals (99.99% purity). The ribbon was electropolished in concentrated  $H_2SO_4$  (Dooley and Haas, 1970) and finally cleaned in vacuo by adsorbing oxygen onto the surface and then 'flash' heating the sample to  $\sim 2000$ K to drive off the surface contamination and oxide layer. The main contaminant before this treatment was carbon. When the ribbon was left overnight in the vacuum both carbon and oxygen were found on the surface and this was removed easily by 'flash' heating. The surface was 'flashed' clean frequently during experiments so that all the readings were taken on a surface from which no Auger signal, apart from that of rhenium, could be seen.

A polycrystalline sample was used in an effort to reduce directional effects of emission from the surface which would be found with a <sup>single</sup> crystalline surface. This was a partial success but diffraction features appeared in the secondary electron spectrum due to the local ordering. X-ray diffraction scans of the surface before and after the experiments showed that the long periods of heating during the experiments had caused ordering with the 0001 face parallel to the surface. Alnot et al. (1979) found that a 30 $\mu$ m thick polycrystalline ribbon became preferentially oriented in the (0001) direction after prolonged annealing at ~2200K.

#### 3.4.3 Tantalum (B.C.C.)

The tantalum surface used was part of the sample support shown in figure 3.2. The main contaminants found on this surface by A.E.S. were sulphur, carbon and oxygen. Cleaning of tantalum samples is often just by prolonged heating at ~2800K (Chesters et al, 1974) but the tantalum support could not be heated to that temperature with the present arrangement because of its large cross-sectional area. With as much heating as possible the 'cleanest' obtained had a significant amount of sulphur and oxygen on the surface. It was thought, however, that some meaningful preliminary results could be obtained from this surface. The effects of contamination and correction for them are discussed in chapter 8.

#### 3.4.4 Gold (F.C.C.)

The gold sample was a polycrystalline ribbon 10mm x 3mm x 0.025mm supplied by Goodfellow Metals (99.99% purity). It was given no special treatment prior to mounting in the vacuum chamber. Before cleaning the secondary electron spectrum contained Auger peaks due to carbon, oxygen, chlorine, sulphur and nitrogen. Larkins and Lubenfeld (1977)

cleaned their gold foil sample by heating it at 200°C for 2 hours in vacuum. The only remaining contaminant after this treatment was the carbon KLL Auger spectrum which was estimated to be only 4% of the total intensity in that region. Matthew et al. (1980) cleaned their gold (100) single crystal surface by cycles of argon-ion bombardment and heating in oxygen and in vacuum. There was however a small carbon Auger peak in their 'clean' gold spectrum.

For this work the surface was first heated at 800K for 5 minutes. This removed all the contaminants detectable on the Auger spectrum apart from the carbon. Further heating at 800K for 7 hours did not affect the carbon Auger intensity. Heating at 800K in a pressure of  $10^{-7}$  torr oxygen for 30 minutes had no impact on the carbon signal. Similar treatment with hydrogen was no better. Argon-ion bombardment was not used in the cleaning process as no argon-ion gun was available on the experimental system.

In order to do some preliminary experiments the sample was heated to 800K for 5 minutes to remove all but the carbon from the surface, and the carbon contaminated surface was used for the experiments.

### 3.5 Experimental Procedure

#### 3.5.1 Energy Calibration of Spectra

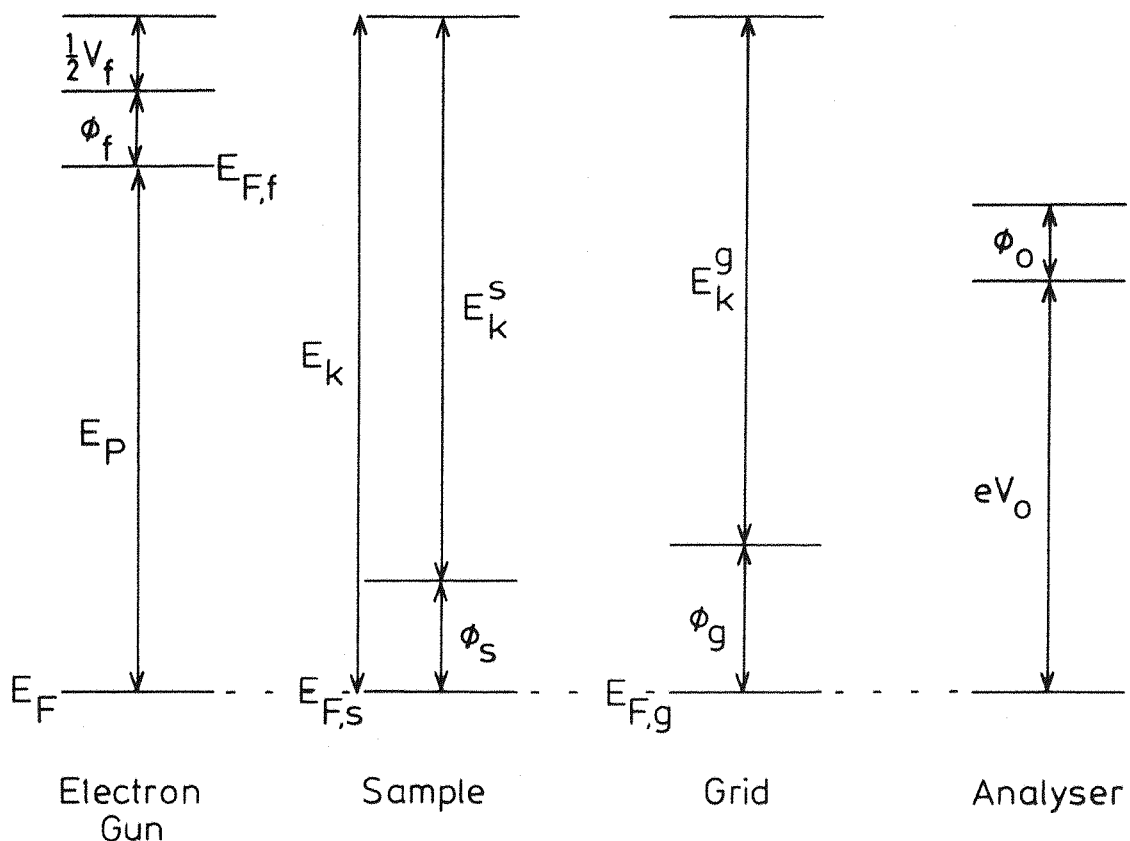
As explained in chapter 2 the voltage applied to the outer cylinder of the C.M.A. is not the same as the energy of the electrons being analysed but depends on the geometry of the analyser and the position of the sample with respect to the analyser. For this reason the spectra were calibrated by superimposing the second derivative of elastic peaks of known energy  $E_p$  in the experimental energy windows. The elastic peak energy relative to the system Fermi energy ( $E_F$ ) is then equal to the applied gun potential ( $E_p$ ), plus 4.5eV for the polycrystalline tungsten filament work function, plus half the potential difference across the D.C. heated

filament (1 to 1.5eV) (figure 3.11). Each time the sample was repositioned, the energy scale was recalibrated. The energy scale is expected to be accurate to  $\pm 0.5\text{eV}$  relative to  $E_F$ .

### 3.5.2 Yield Curves

To plot a yield curve the primary beam energy had to be reduced to as near the binding energy of the initial vacancy as possible. This led to problems with loss peaks from the primary beam overlapping with the peak under study. To eliminate loss peaks using the present equipment Rawlings et al. (1980a) applied the voltage modulation to the specimen which should suppress all peaks referenced to the primary beam, including loss peaks. Unfortunately they found that  $\sim 5\%$  of the loss peak intensity could still be seen. This was presumed to be due to inadequate screening of the analyser and distortion of the electron trajectories by the modulating potential. The alternative is to identify the positions of the loss peaks and then not use the values of  $E_p$  that produce loss peaks which will overlap the peak under study. The energy positions of the loss peaks were determined by modulating the primary electron beam energy and therefore eliminating peaks referenced to the sample, including Auger peaks. The presence of loss peaks can be checked when modulating the analyser by putting a small bias voltage on the sample. This will shift peaks in the spectrum referenced to the primary beam, but not those referenced to the sample. The 'gaps' in the yield curves in later chapters indicate the values of  $E_p$  where losses interfered with the peak being studied. These gaps did not cause problems when interpreting the data.

From section 2.4, the yield of an Auger emission depends on the primary beam current  $I_b$  as well as the primary beam energy  $E_p$  and so  $I_b$  must be kept constant for all values of  $E_p$  while plotting a yield curve. During the experiments the beam current was measured by putting a bias



$E_k$  = energy to be measured e.g. energy of Auger electron.

$V_0$  = voltage applied to outer cylinder of C.M.A.

For calibration of spectra with the elastic peak

$$E_k = E_p + \phi_f + \frac{1}{2}V_f$$

Figure 3.11 Electron energies involved in measurement with a C.M.A.

of 69V on the sample and measuring the current with an electrometer as shown in figure 3.12a. This measures the flow of secondary electrons with energy less than  $V=69V$  (Figure 3.12b). Thus the electrons between  $eV$  and  $E_p + eV$  will escape and the measured current  $I_{coll}$  is less than the true beam current  $I_b$ . The proportion of 'lost' current increases approximately linearly as  $E_p$  increases. To keep  $I_b$  constant,  $I_{coll}$  was calibrated against  $E_p$  for a constant value of  $I_b$ , and  $I_{coll}$  adjusted in the yield curve experiments. The calibration was achieved by putting an electrometer in the electron gun earth line to measure  $I_b$  (by conservation of charge). Figure 3.12c shows the calibration for the tungsten sample. This graph was used for all the experiments. Any small errors introduced (e.g. if the relationship is not quite linear between  $E_p = 500eV$  and  $2500eV$ ) will affect all the yield curves similarly. As the analysis involved comparing yield curves and ratios of yields at different primary beam energies, any calibration errors should not significantly affect the conclusions.

### 3.5.3 High Temperature Experiments

Auger spectra were recorded above room temperature with the sample pulse heated as already described (section 3.3.3). Unfortunately, with the sample in its optimum position with respect to the analyser, a satellite appeared on the high energy side of each peak which increased with increasing temperature. The effect is best seen by looking at the elastic peak in figure 3.13. The satellite is present at room temperature but is negligibly small. Froitzheim et al. (1975) noticed high and low energy satellites of an elastic peak using a  $127^\circ$  cylindrical type analyser. They deduced that these 'ghost' lines were due to electron reflections occurring on the walls of the inner and outer cylinders.

The high energy satellite seen in the present work could similarly have been caused by reflection from the

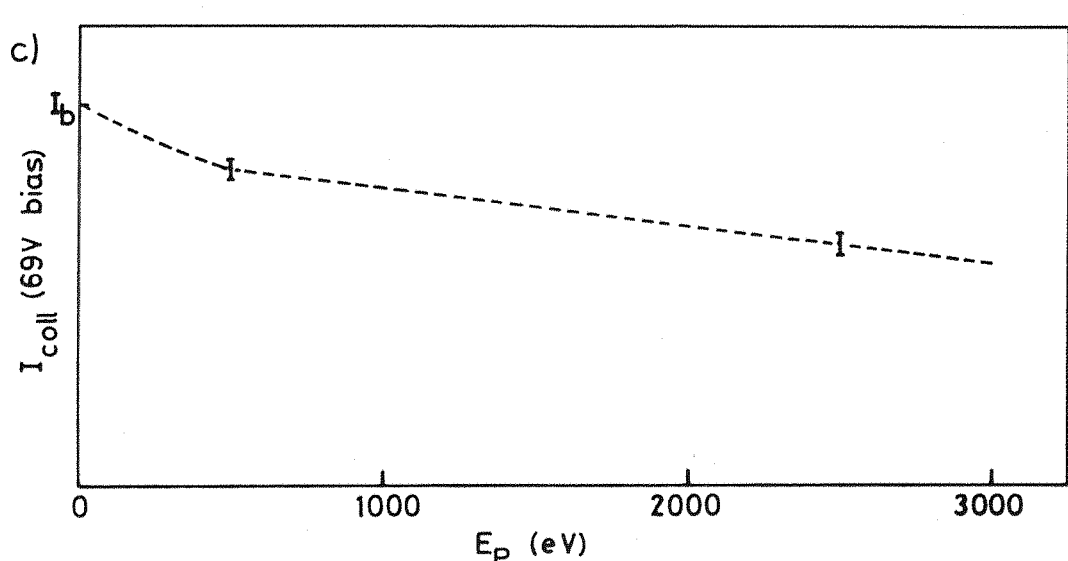
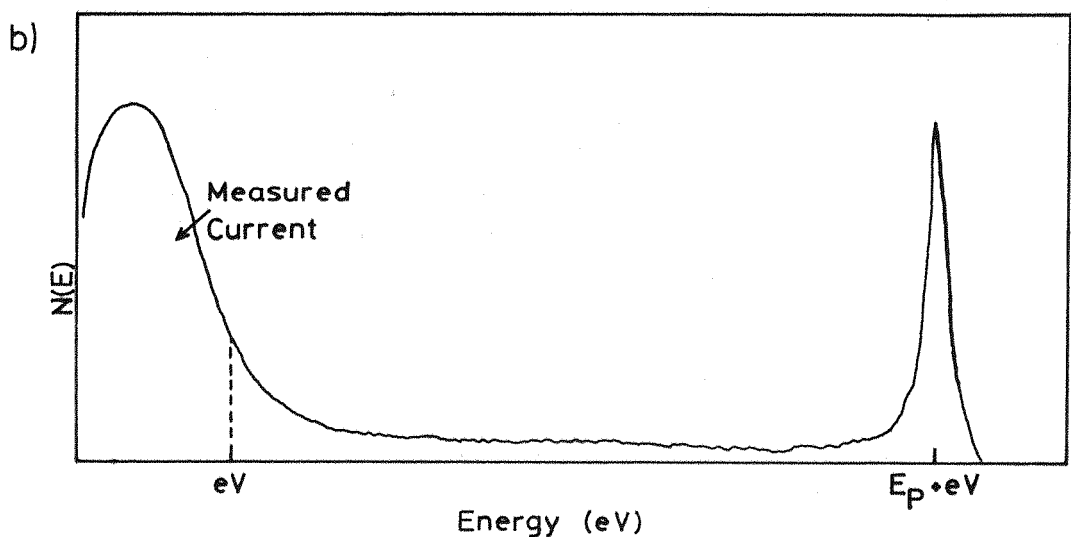
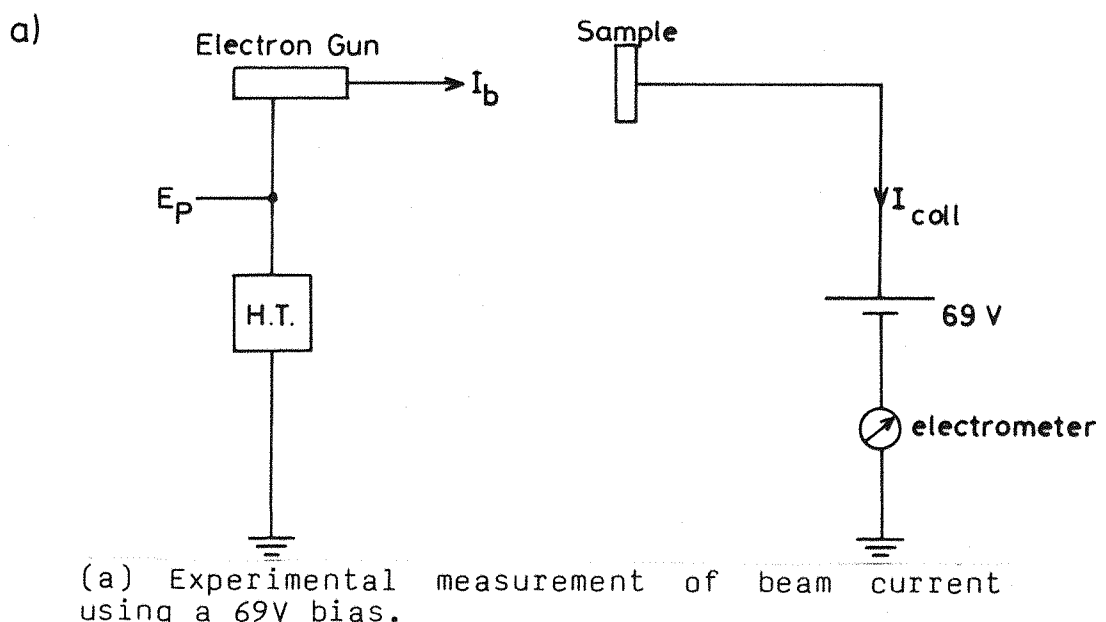


Figure 3.12 (c) Calibration of collected current v. primary beam energy for constant beam current.

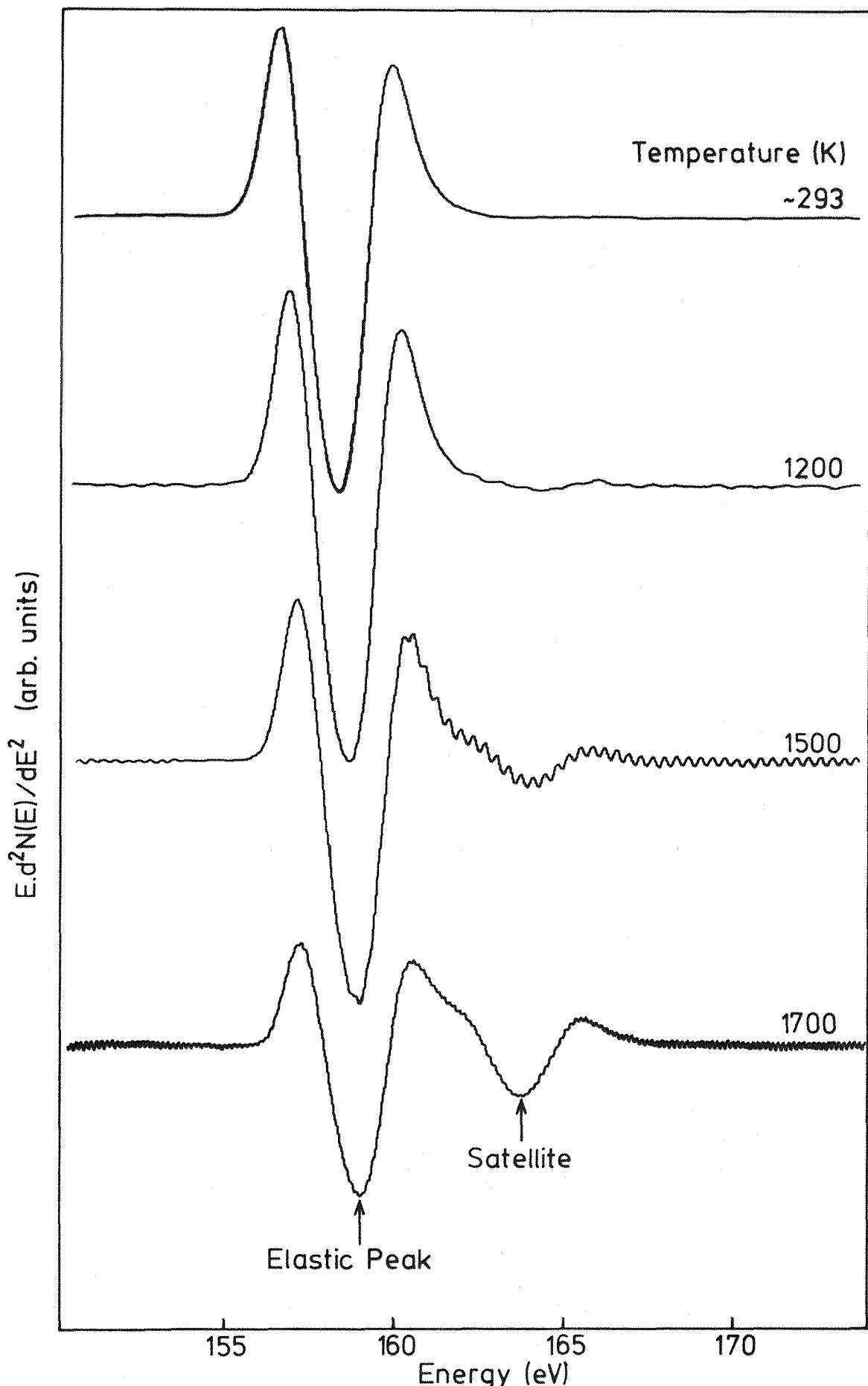


Figure 3.13 Appearance of satellite 'ghost' peak at high temperatures ( $E_p = 158.5$  eV,  $I_b = 0.5 \mu\text{A}$ ,  $v_m = 3.55 \text{ V}_{\text{pp}}$ ,  $\tau = 0.3$  s, scan  $1 \text{ eV.s}^{-1}$ ).

inner cylinder as shown in figure 3.14. When the sample was moved towards the analyser the 'ghost' peak intensity increased with respect to the elastic peak, and when the sample was move further away from the analyser the ghost decreased relative to the elastic peak. This suggests that heating the sample holder and sample causes the sample holder to bend towards the analyser. Thus to take high temperature spectra the sample was moved until the ghost intensity at 1700K was negligible. With the sample in this position the intensity of the peaks was reduced and the energy scale had to be recalibrated but 'real' temperature dependent effects could be identified.

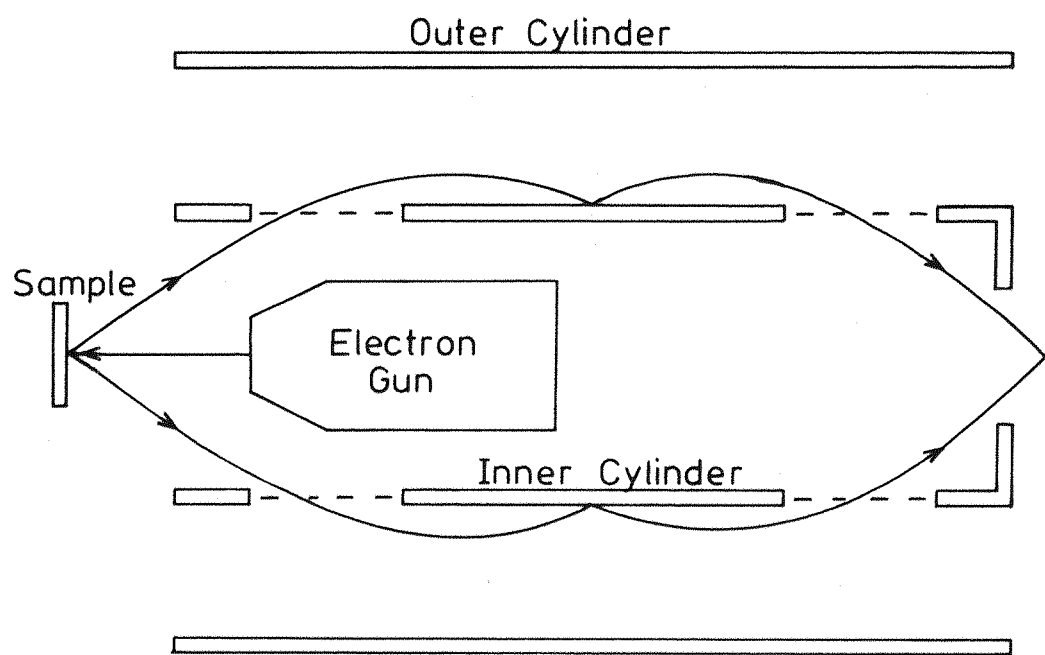


Figure 3.14 Mechanism for production of satellite peak.

## CHAPTER 4

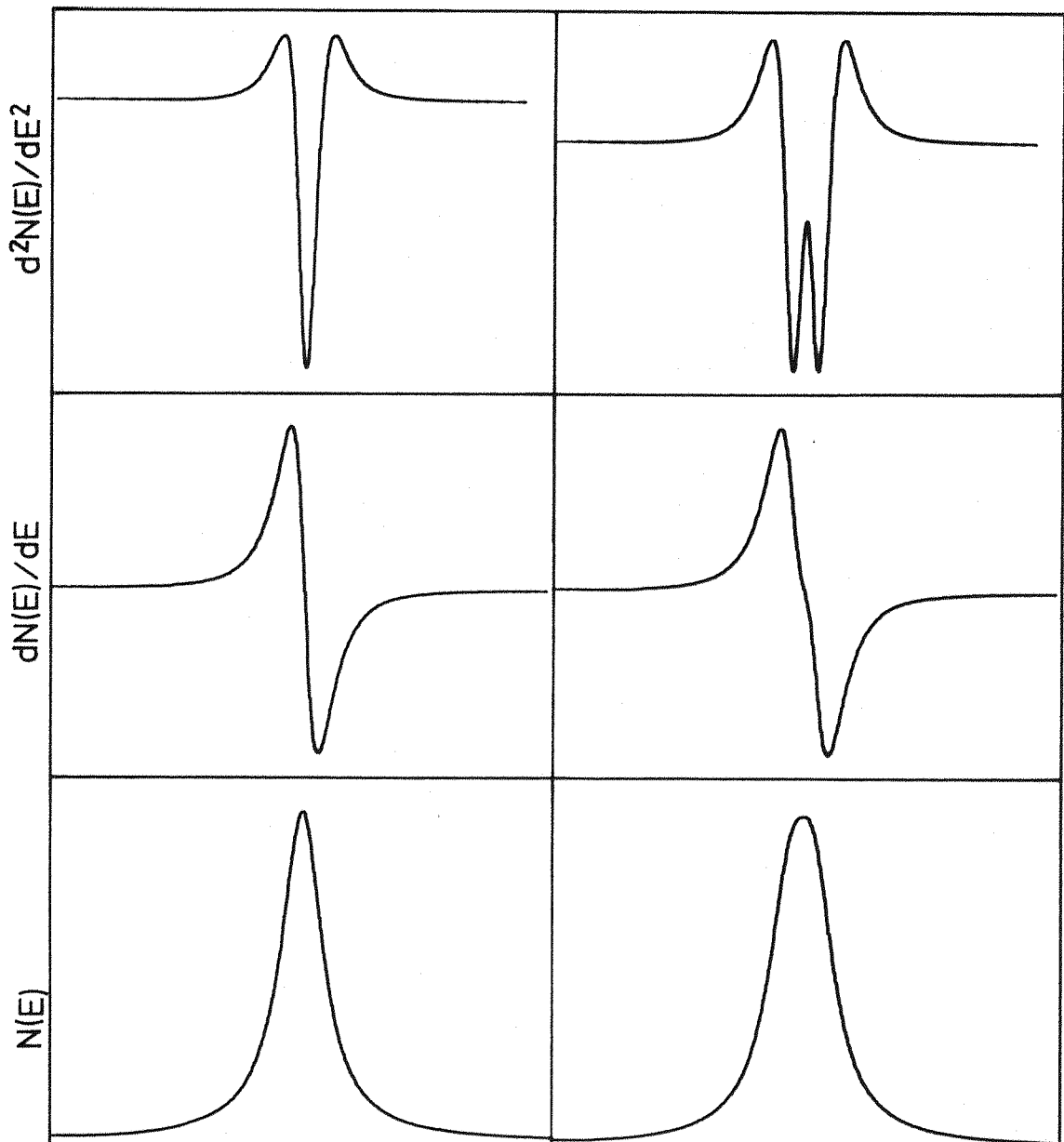
### SIMULATION OF EXPERIMENTAL SPECTRA

#### 4.1 The Second Derivative Spectrum

If a spectrum is recorded in  $N(E)$  form the small Auger peaks are buried in a large background current (figure 2.1). The effects of this background may be reduced in several different ways (Kirschner, 1977) each of which produces slightly different Auger spectra from the same data. However, many experimenters record instead the first derivative spectra  $dN(E)/dE$  which eliminates the effects of a first order polynomial background (straight line) and thus accentuates the Auger peaks. If second derivative spectra  $d^2N(E)/dE^2$  are recorded the effect of a second order polynomial background (parabola) is eliminated from the spectra.

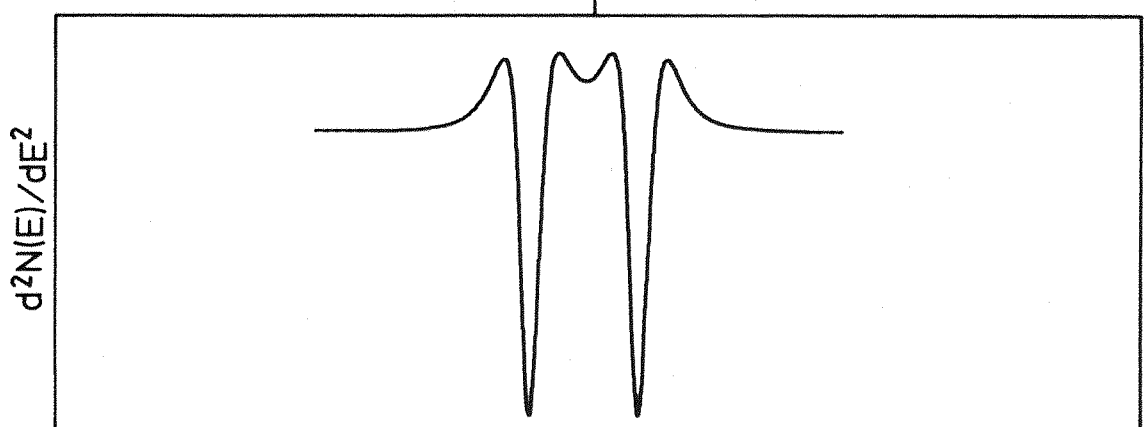
Another advantage of recording the second derivative is that the resolution is improved. One of the problems in the present work was determining the number of peaks present in an area including several very close peaks. Figure 4.1a shows a Lorentzian peak shape, its first derivative and its second derivative. The second derivative peak is much narrower than the  $N(E)$  curve. To demonstrate the difference in resolution figure 4.1b shows the sum of two identical Lorentzians of f.w.h.m. 4eV and separation 2eV in  $N(E)$ ,  $dN/dE$  and  $d^2N/dE^2$  form. The sum in  $N(E)$  gives little indication of the presence of two peaks whereas there are obviously two distinct peaks in the  $d^2N/dE^2$  curve. The second derivative mode of recording spectra was used in the present work because of the better resolution.

However there are disadvantages in the use of second derivative detection of the spectrum. One of these is that, for the same beam current, a smaller signal is collected than for lower order detection. This is only of concern in experiments where the beam current must be kept small (e.g.



a) Lorentzian peak  
f.w.h.m.=4eV

b) Two Lorentzians 2eV  
apart, each f.w.h.m.=4eV



c) Two Lorentzians 8eV apart, each f.w.h.m.=4eV.

Figure 4.1 Comparison of resolutions of  $N(E)$ ,  $dN(E)/dE$  and  $d^2N(E)/dE^2$  spectra.

gas adsorption). A second possible disadvantage was pointed out by Henrich (1980). If two second derivative peaks are close together the overlapping of the side wings may be mistaken for a small peak in between (figure 4.1c). This problem may be overcome by fitting a simulated spectrum to the experimental spectrum. The first simulation of a spectrum must include only the obvious intense peaks. Then any peaks that are not due to overlapping side wings can be indentified. Extra peaks may then be added to the simulated spectrum until it is an acceptable fit to the experimental spectrum.

#### 4.2 Simulation of Experimental Spectrum

There have been several approaches to the simulation of N(E) spectra. Weightman et al. (1976) used Lorentzian line shapes with a characteristic loss tail and included an instrument function but constrained the peaks to have the same widths. Antonides et al. (1977) theoretically predicted the line intensities and constrained their peaks to these intensities and the same width but varied the positions and proportion of Lorentzian (Auger) plus Gaussian (instrument) peak shape (equation 2.9). Since part of the present work was to compare theory with experiment the latter method was not used.

As the present experiments were on solid state specimens the Auger peaks were quite broad and so the instrument broadening was assumed to be small in comparison. The detecting modulation voltage was also assumed to be small enough so that higher terms in the series of equation 2.12 could be neglected. The experimental spectrum was therefore simulated by a number of Lorentzian shaped peaks.

Unfortunately analytic techniques could not be used to calculate a best fit to the experimental spectrum. So an iterative method was used to improve the fit of a simulated spectrum to the experimental spectrum. For the purposes of the computation a function must be defined which describes

the quality of the fit. The objective of the computation is then to iteratively reduce the value of this function by altering the simulated spectrum. This function, called the objective function, must be well behaved; i.e. it must have continuous first and second derivatives.

The objective function was chosen to be

$$D = \int_{E_1}^{E_2} (S(E, \underline{P}) - C(E))^2 \cdot dE$$

where  $C(E)$  is the experimental spectrum,  $S(E, \underline{P})$  is the simulated spectrum and  $\underline{P}$  is a vector of the parameters which determine the simulated spectrum. In practice the experimental data was collected at discrete energies with equal energy steps  $\Delta E$  between them. Thus  $D$  cannot be calculated exactly as above; instead the integral must be approximated by a summation. The following simple approximation was chosen for the objective function

$$D \approx \sum_{i=1}^{\frac{E_2 - E_1}{\Delta E} + 1} (S(E_i, \underline{P}) - C(E_i))^2 \Delta E. \quad (4.1)$$

One iterative method of solving equations of the form  $f(x)=0$  is the Newton-Raphson method. However if the first derivative of the function  $f(x)$  is too small at the root then the method fails (see appendix II). The chosen objective function  $D$  does not cross the zero line so the first derivative would be zero at the root. In addition if there is any random noise or distortion on the experimental spectrum then the objective function can never even reach zero. Since the objective function  $D$  cannot reach zero, a more practical aim is to find its minimum value, i.e. the closest possible fit to the experimental spectrum. This is easily found by using the Newton-Raphson technique to find the root of the first derivative of  $D$ :

$$\frac{\partial D}{\partial \underline{P}} = 0.$$

This presents no numerical problems because the second derivative  $\frac{\partial^2 D}{\partial P^2}$  does not become small at the minimum of  $D$ .

The multi dimensional form of the Newton-Raphson method is now derived from first principles: if  $\underline{P}^{(j)}$  is a rough approximation to a root of the  $n$  dimensional function

$$\frac{\partial D}{\partial P} = 0$$

then a closer approximation to the root is  $\underline{P}^{(j+1)} = \underline{P}^{(j)} + \underline{h}$  where  $\underline{h}$  is a small step in  $n$  space given by Taylor's expansion

$$\frac{\partial D(P)}{\partial P} \Big|_{P=\underline{P}^{(j)} + \underline{h}} = 0 = \frac{\partial D(P)}{\partial P} \Big|_{P=\underline{P}^{(j)}} + \frac{\partial^2 D(P)}{\partial P \partial P} \Big|_{P=\underline{P}^{(j)}} \cdot \underline{h} + \dots$$

Neglecting the smaller terms,  $\underline{h}$  can be calculated from

$$\frac{\partial^2 D(P)}{\partial P \partial P} \Big|_{P=\underline{P}^{(j)}} \cdot \underline{h} = - \frac{\partial D(P)}{\partial P} \Big|_{P=\underline{P}^{(j)}} \quad (4.2)$$

$\underline{h}$  is used to calculate  $\underline{P}^{(j+1)}$  which is then used to calculate  $\underline{P}^{(j+2)}$  etc. until the root is of the required accuracy.

Equation 4.2 can be solved using Gaussian elimination including row pivoting.

Each peak in the simulated spectrum is assumed to be a second differential Lorentzian peak. The Lorentzian function is (Sickafus, 1974)

$$N(E) = \frac{A \cdot \Gamma}{(E - E_0)^2 + \Gamma^2/4}$$

where  $\Gamma$  is the f.w.h.m. of the peak,  $E_0$  is the position of the peak and  $4A/\Gamma$  is the height of the peak. Differentiated twice this becomes

$$\frac{\partial^2 N(E)}{\partial E^2} = \frac{32A\Gamma(12(E-E_0)^2 - \Gamma^2)}{(4(E-E_0)^2 + \Gamma^2)^3} = L(E). \quad (4.3)$$

Thus the simulated spectrum at energy  $E_i$  is  
no of peaks

$$S(E_i, P) = \text{zero} + (\text{slope}.E_i) + \sum_{k=1}^{\text{no of peaks}} L(E_i, A_k, E_{0k}, \Gamma_k). \quad (4.4)$$

A first guess is taken for the background parameters (zero level and slope) and the parameters for each peak ( $A$ ,  $E_0$  and  $\Gamma$ ). All the equations required for the iterative solution are derived analytically from equations 4.3, 4.4 and 4.1.

The experimental spectra are logged by the computer as 1024 points. These points are reduced to 65 (by adding together groups of 16 original data points to form a single new point with the special provision to add only 8 points to form each end point) to reduce the time taken to fit a curve to an acceptable level. The curvefitting program was written in Pascal to run on the Cromemco Z-2D microcomputer, and this meant that real numbers could only be represented to an accuracy of about  $6\frac{1}{2}$  significant figures. In practice the full Gaussian elimination method of solving equation 4.2 would not work with this limited accuracy because the level of noise made the equations ill conditioned. A relaxed method (Kowalik and Osborne, 1968) was therefore used where the non diagonal elements of the matrix  $\frac{\partial^2 D}{\partial P \partial P}$  were set to zero. There were no numerical problems with this method though it took considerably more steps than necessary. Each step in this relaxed method reduced the difference between the experimental and simulated spectra until the minimum was reached. The Gaussian method would have been faster had it worked in spite of the greater calculation time per step. It was possible to fit a peak to a simple low noise spectrum

such as an elastic peak using both methods and it was found that both methods reached the same solution.

As an example, figure 4.2 shows simulations of the low energy (150-190eV) secondary electron spectrum from a rhenium surface. Figure 4.2a shows the best fit with three Lorentzian shaped peaks and 4.2b the better fit using six Lorentzian peaks.

#### 4.3 Effect of a Large Modulation Voltage

In the previous section it was assumed that  $V_0$  in equation 2.11 was small enough that higher terms in that series could be neglected. If  $V_0$  is not small the higher terms make a significant contribution to the experimental secondary electron spectrum. Extending equation 2.11 further to include more higher order terms gives

$$I(E+eV_0 \cos \omega t) = I(E) + e \cdot \frac{dI}{dE} V_0 \cos \omega t + e^2 \cdot \frac{d^2 I}{dE^2} \frac{V_0^2 \cos^2 \omega t}{2!} + e^3 \cdot \frac{d^3 I}{dE^3} \frac{V_0^3 \cos^3 \omega t}{3!} + e^4 \cdot \frac{d^4 I}{dE^4} \frac{V_0^4 \cos^4 \omega t}{4!} + \dots$$

The electronic detection of the second differential involves multiplying this function by  $\cos 2\omega t$  and averaging over  $\omega t = 0$  to  $\pi$  (Houston and Park, 1972):

$$\begin{aligned} \frac{2}{\pi} \int_0^{\pi} I(E+eV_0 \cos \omega t) \cos 2\omega t d\omega t &= \frac{2}{\pi} \int_0^{\pi} (I(E) + e \cdot \frac{dI}{dE} V_0 \cos \omega t \\ &+ e^2 \cdot \frac{d^2 I}{dE^2} \frac{V_0^2}{4} (1 + \cos 2\omega t) + e^3 \cdot \frac{d^3 I}{dE^3} \frac{V_0^3}{6} \cos^3 \omega t \\ &+ e^4 \cdot \frac{d^4 I}{dE^4} \frac{V_0^4}{96} (\cos 2\omega t + 1)^2 + \dots) \cos 2\omega t d\omega t. \end{aligned}$$

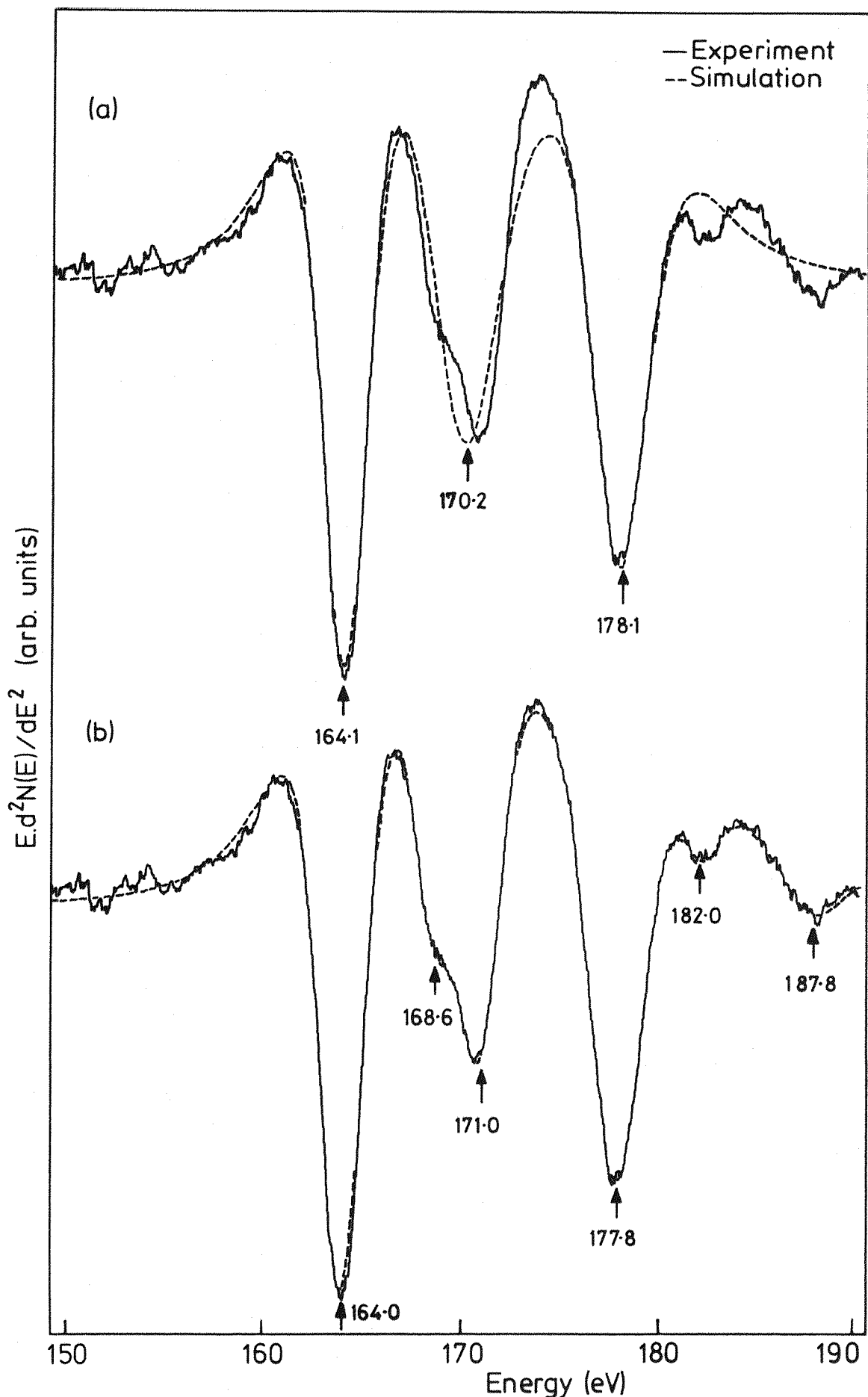


Figure 4.2 Simulation of rhenium spectrum by (a) 3 Lorentzian peaks and (b) 6 Lorentzian peaks ( $E_p = 1400$  eV,  $I_b = 5 \mu\text{A}$ ,  $v_m = 2.1 \text{ V}_{\text{ptp}}$ ,  $\tau = 0.3$  s, scan  $0.5 \text{ eV} \cdot \text{s}^{-1}$ ).

When the right hand side of this equation is integrated only terms in  $\cos 2\omega t$  are non zero, giving

$$\begin{aligned}
 & \frac{2}{\pi} \int_0^{\pi} I(E + eV_0 \cos \omega t) \cos 2\omega t \, d\omega t \\
 &= \frac{e^2 V_0^2}{4} \left( \frac{d^2 I}{dE^2} + \frac{e^2 V_0^2}{12} \frac{d^4 I}{dE^4} + \frac{e^4 V_0^4}{384} \frac{d^6 I}{dE^6} \right. \\
 & \quad \left. + \frac{e^6 V_0^6}{23040} \frac{d^8 I}{dE^8} + \frac{e^8 V_0^8}{2211840} \frac{d^{10} I}{dE^{10}} + \dots \right) .
 \end{aligned}$$

Using equation 2.10 and approximations such as that in equation 2.13 the detected second differential spectrum becomes

$$\begin{aligned}
 &= \frac{e^2 V_0^2}{2} E.K.R \left( \frac{d^2 N}{dE^2} + \frac{e^2 V_0^2 d^4 N}{12 dE^4} + \frac{e^4 V_0^4}{384} \frac{d^6 N}{dE^6} \right. \\
 & \quad \left. + \frac{e^6 V_0^6}{23040} \frac{d^8 N}{dE^8} + \frac{e^8 V_0^8}{2211840} \frac{d^{10} N}{dE^{10}} + \dots \right) .
 \end{aligned}$$

As the fitted spectra were for energy windows of approximately 40eV width, multiplying the spectrum by  $E$  has a negligible effect on the shape of the spectrum. Therefore

$$\begin{aligned}
 \frac{\text{spectrum}}{e^2 V_0^2} \cdot \text{constant} &= \frac{d^2 N}{dE^2} + \frac{e^2 V_0^2 d^4 N}{12 dE^4} + \frac{e^4 V_0^4}{384} \frac{d^6 N}{dE^6} \\
 & \quad + \frac{e^6 V_0^6}{23040} \frac{d^8 N}{dE^8} + \frac{e^8 V_0^8}{2211840} \frac{d^{10} N}{dE^{10}} + \dots \quad (4.5)
 \end{aligned}$$

As an indication of the relative intensities of the terms in this equation as a function of the modulation voltage see figure 4.3.

This figure shows the contribution of each term to the intensity of the centre of a peak (at  $E=E_0$ ) (plotted as a

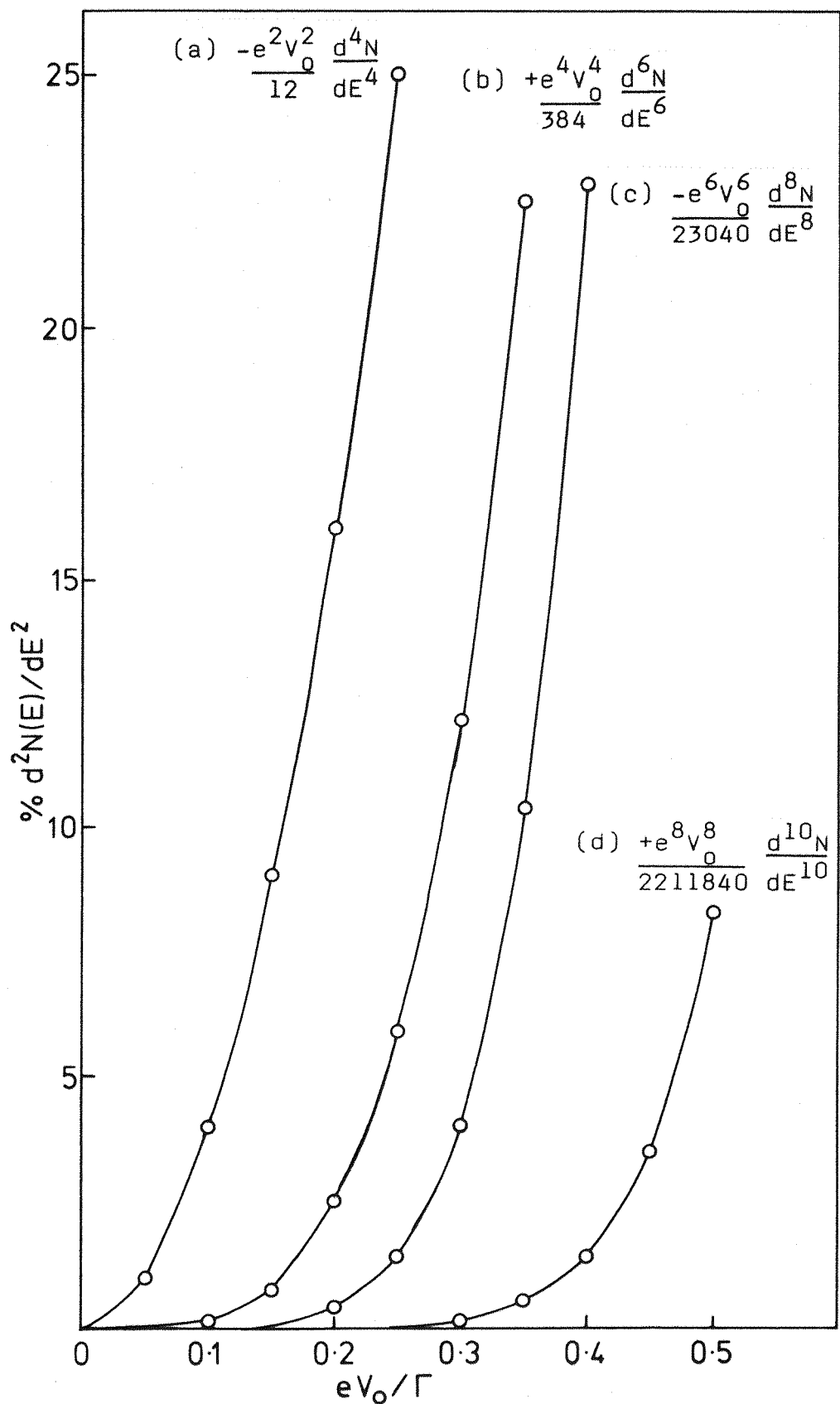


Figure 4.3 Contribution of each term in equation 4.5 to the intensity of the centre of a peak as a function of modulation voltage.

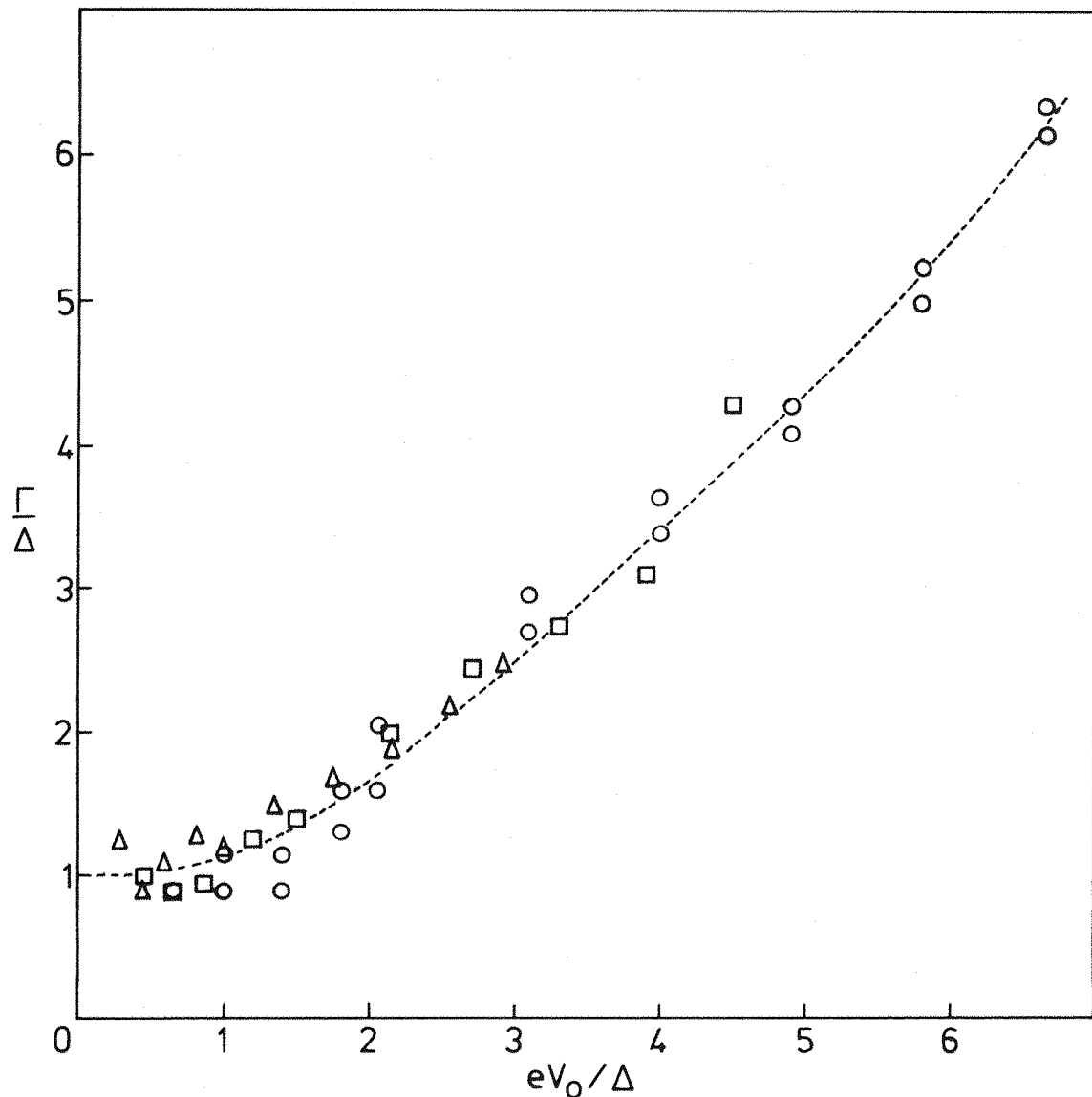
percentage of the  $d^2N/dE^2$  intensity) as a function of modulation voltage. The terms are alternately positive and negative. For example when the modulation voltage is 10% of the f.w.h.m. of the peak, the  $d^4N/dE^4$  term contributes intensity equal to 4% of the  $d^2N/dE^2$  intensity. There is negligible intensity from higher terms in the series. However as the modulation voltage increases with respect to the f.w.h.m. of the peak, intensity from the higher terms becomes significant. With a modulation voltage 30% of the f.w.h.m. of the peak the relative contributions of the

$$\frac{d^4N}{dE^4}, \frac{d^6N}{dE^6}, \frac{d^8N}{dE^8} \text{ and } \frac{d^{10}N}{dE^{10}}$$

terms as a percentage of the  $d^2N/dE^2$  intensity are -36%, +12%, -4% and +0.1% respectively.

The empirical effect of the modulation voltage on the width of a peak was seen by measuring the variation of the f.w.h.m. of an elastic peak, figure 4.4. The modulation voltage also affects the apparent width of peaks obtained from curve fitting. Figure 4.5 shows this effect for Lorentzian peaks fitted to a rhenium spectrum (such as figure 4.2b) for a range of modulation voltages. Because large modulation voltages also affect the shape of peaks so that they are no longer Lorentzian, attempting to fit Lorentzian peaks to spectra obtained using large modulation voltages is theoretically suspect.

When large modulation voltages are used resolution is lost. For example when the modulation voltage exceeded  $\sim 5V_{ptp}$  only one peak could be fitted to the central peak at 171eV in the spectrum (see figure 4.2b). When two peaks were suggested the iterative procedure moved them both to the same central position. A fit of just three Lorentzian peaks to the spectrum with  $V_0 = 6.8$  volts<sub>ptp</sub> (figure 4.6) gives no hint of the presence of two peaks in the 171eV peak. Thus great care must be taken in the choice of  $V_0$  for experimental work as, though a larger modulation voltage



- $E_p = 160$  eV
- $E_p = 300$  eV
- △  $E_p = 500$  eV
- $\Delta$   $= \Gamma$  without modulation broadening (at  $V_0=0$ )
- For  $E_p = 160$  eV,  $\Delta = 1.22$  eV
- For  $E_p = 300$  eV,  $\Delta = 1.80$  eV
- For  $E_p = 500$  eV,  $\Delta = 2.77$  eV

Figure 4.4 Normalised f.w.h.m. of an elastic peak as a function of modulation voltage.

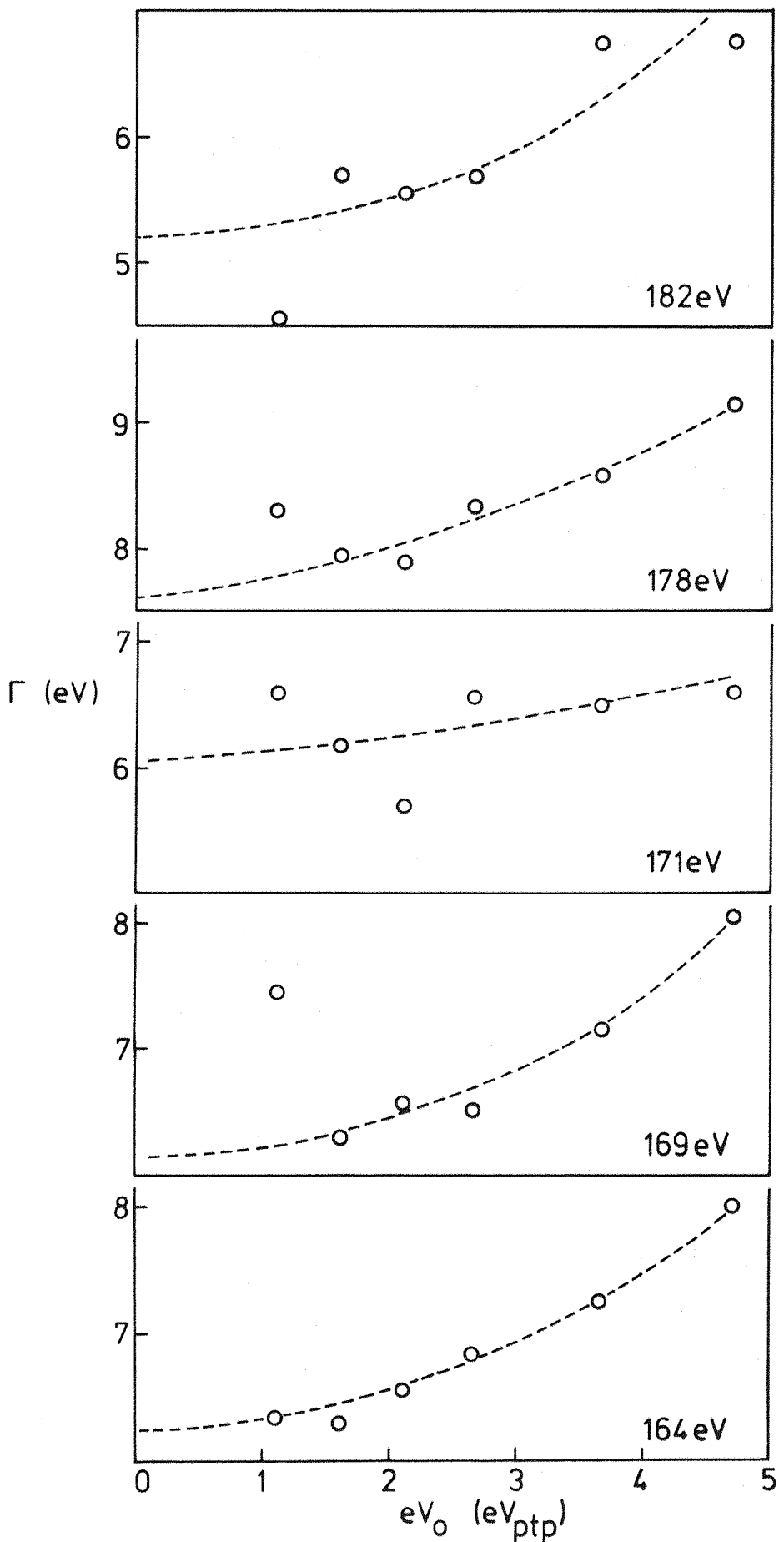


Figure 4.5 f.w.h.m. v. modulation voltage for five Lorentzian peaks fitted to the rhenium spectrum.

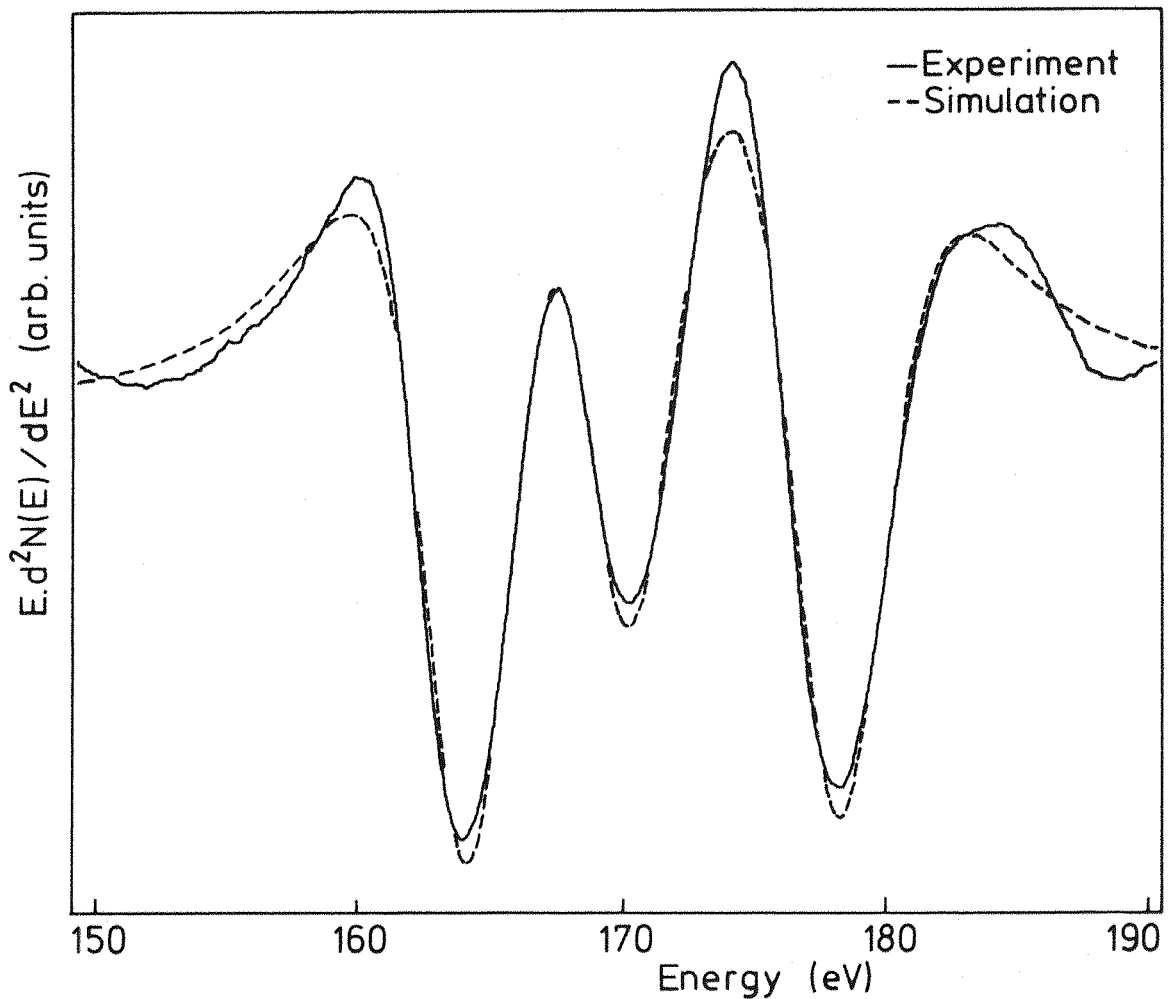


Figure 4.6 Simulation of rhenium spectrum, recorded using a large modulation voltage, by 3 Lorentzian peaks ( $E_p = 1400$  eV,  $I_b = 5 \mu\text{A}$ ,  $v_m = 6.8$  V ptp,  $\tau = 0.3$  s, scan  $0.5$  eV.s $^{-1}$ ).

gives a larger signal, it also reduces resolution and may merge overlapping peaks into a single peak.

The natural width of a peak (i.e. without modulation broadening) can be estimated from the asymptote to the f.w.h.m. v. modulation broadening curve in figure 4.5 or may be found by simulating the experimental curve with 'broadened' Lorentzian peaks.

#### 4.4 Simulation of Experimental Spectrum using Broadened Lorentzians

As was previously stated, it is theoretically suspect to fit Lorentzians to curves significantly distorted by modulation broadening. Thus some attention was paid to fitting broadened Lorentzians to the broadened spectra.

From equation 4.5, the modulation broadened simulated spectrum is

$$\begin{aligned}
 S(E_i, P) = & \text{zero} + (\text{slope. } E_i) + \sum_{k=1}^{\text{no of peaks}} L(E_i, A_k, E_{ok}, \Gamma_k) \\
 & + \frac{e^2 V^2}{120} \sum_k \frac{d^2 L}{dE_i^2}(E_i, A_k, E_{ok}, \Gamma_k) \\
 & + \frac{e^4 V^4}{384} \sum_k \frac{d^4 L}{dE_i^4}(E_i, A_k, E_{ok}, \Gamma_k) \\
 & + \frac{e^6 V^6}{23040} \sum_k \frac{d^6 L}{dE_i^6}(E_i, A_k, E_{ok}, \Gamma_k) \\
 & + \frac{e^8 V^8}{2211840k} \sum_k \frac{d^8 L}{dE_i^8}(E_i, A_k, E_{ok}, \Gamma_k)
 \end{aligned}$$

with the derivatives calculated analytically from equation 4.3. Ten terms were considered to give sufficient accuracy for the experimental modulation voltages used. The simulated spectrum was fitted to the experimental spectrum by the Newton-Raphson method already described. Because of the extra calculations the curve fitting process now took too long using the microcomputer (up to three weeks) and so the program was transferred to run on an ICL 2970 mainframe computer (where it only took thirty minutes).

The difference in shape between a Lorentzian peak and a modulation broadened Lorentzian can be seen in figure 4.7 where a Lorentzian has been fitted to a broadened Lorentzian.

Figure 4.8 shows a fit of six broadened Lorentzian peaks to the same experimental spectrum as before (shown in figure 4.2). There is little visual difference between the fit with broadened Lorentzians and that with just Lorentzian peaks. The 'broadened' fit however is expected to give a much better indication of the width of the peaks. To test this, the f.w.h.m. of the fitted peaks was plotted as a function of the modulation voltage (figure 4.9). The points for each peak are scattered about a horizontal average. The scatter is greater for the less intense peaks as these are more affected by noise. The average width for each peak compare well with the estimated intersects with the  $\Gamma$  axis in figure 4.5 for the Lorentzian peak fits. This supports the reliability of the broadened fit data.

Figure 4.10 shows the fitted spectrum in figure 4.8 without the contributions from modulation broadening.

#### 4.5 Conclusions

Ordinary Lorentzian peaks and modulation broadened Lorentzian peaks have been used to simulate experimental peaks. When fitted to the same experimental spectrum both methods adjust the fitted peaks to virtually the same energy positions and similar relative intensities (height  $\times$  width).

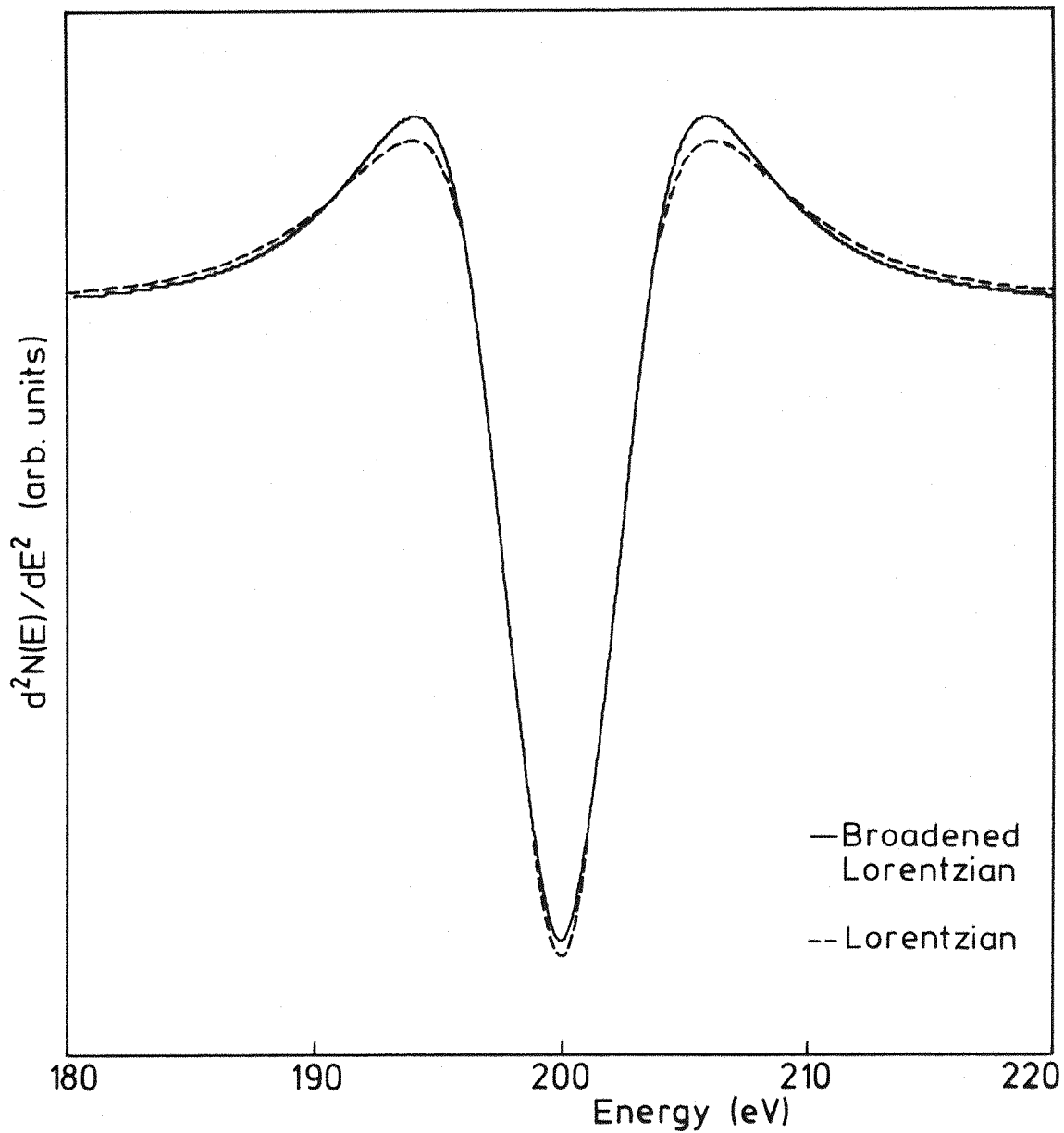


Figure 4.7 Fit of a Lorentzian peak to a broadened Lorentzian peak. The broadened peak is a Lorentzian peak centred at 200eV with a f.w.h.m. of 10eV, broadened using a modulation voltage of 3.33eV. The Lorentzian fitted to this broadened peak has a f.w.h.m. of 12eV.

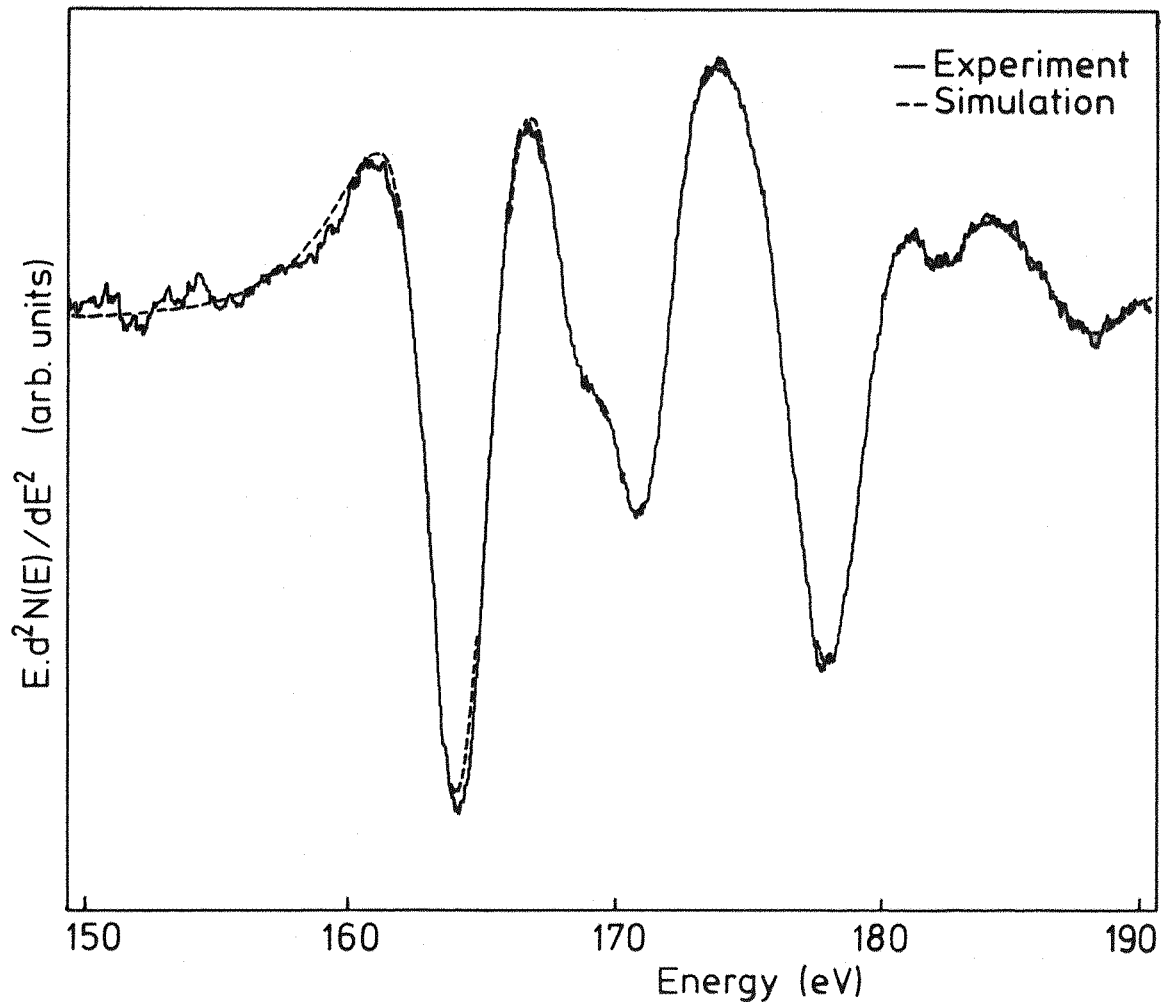


Figure 4.8 Simulation of rhenium spectrum (shown in figure 4.2) by 6 broadened Lorentzian peaks ( $E_p=1400\text{eV}$ ,  $I_b=5\mu\text{A}$ ,  $v_m=2.1\text{V}_{\text{ptp}}$ ,  $\tau=0.3\text{s}$ , scan  $0.5\text{eV}\cdot\text{s}^{-1}$ ).

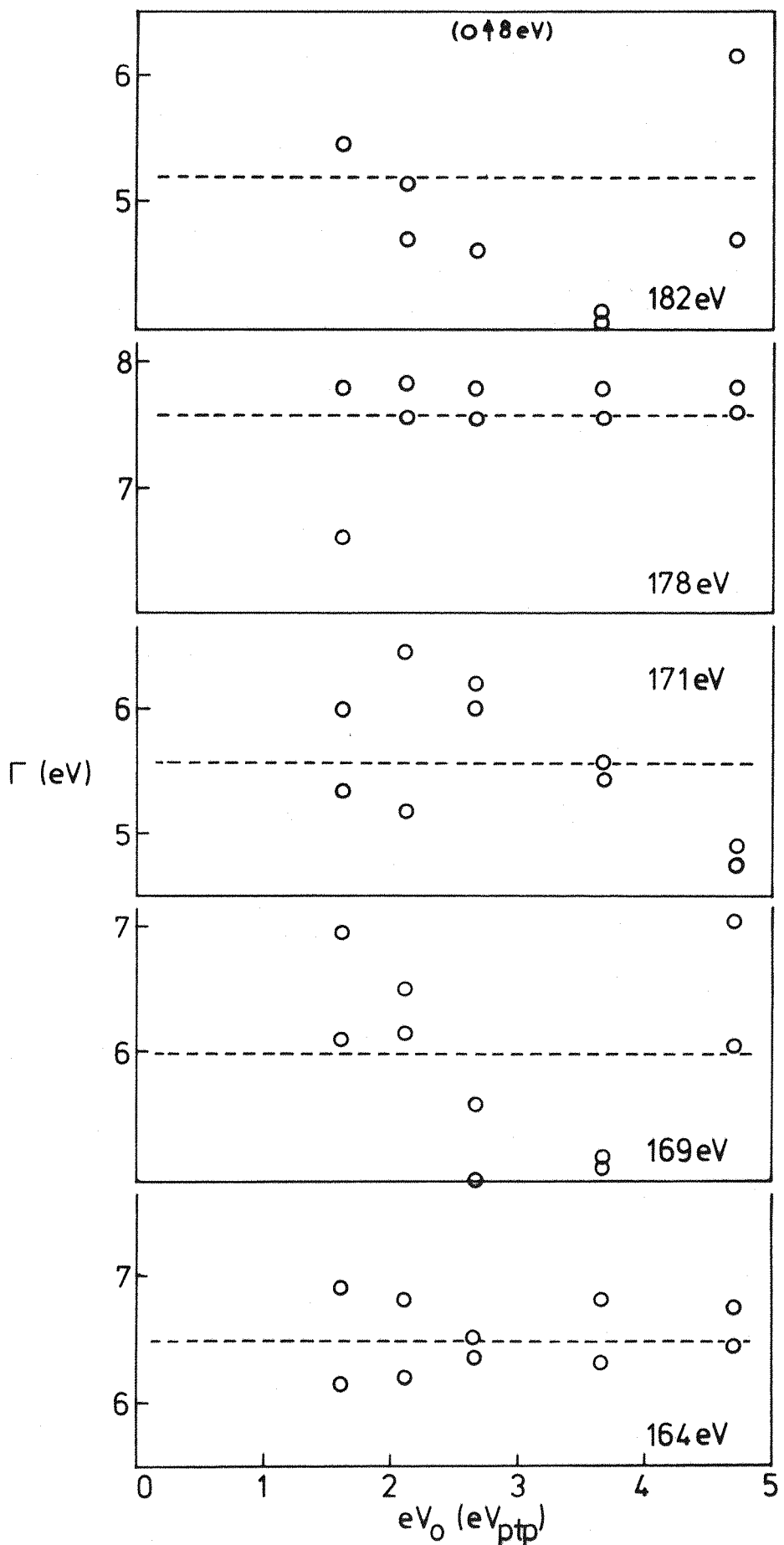


Figure 4.9 f.w.h.m. v. modulation voltage for five broadened Lorentzian peaks fitted to the rhenium spectrum.

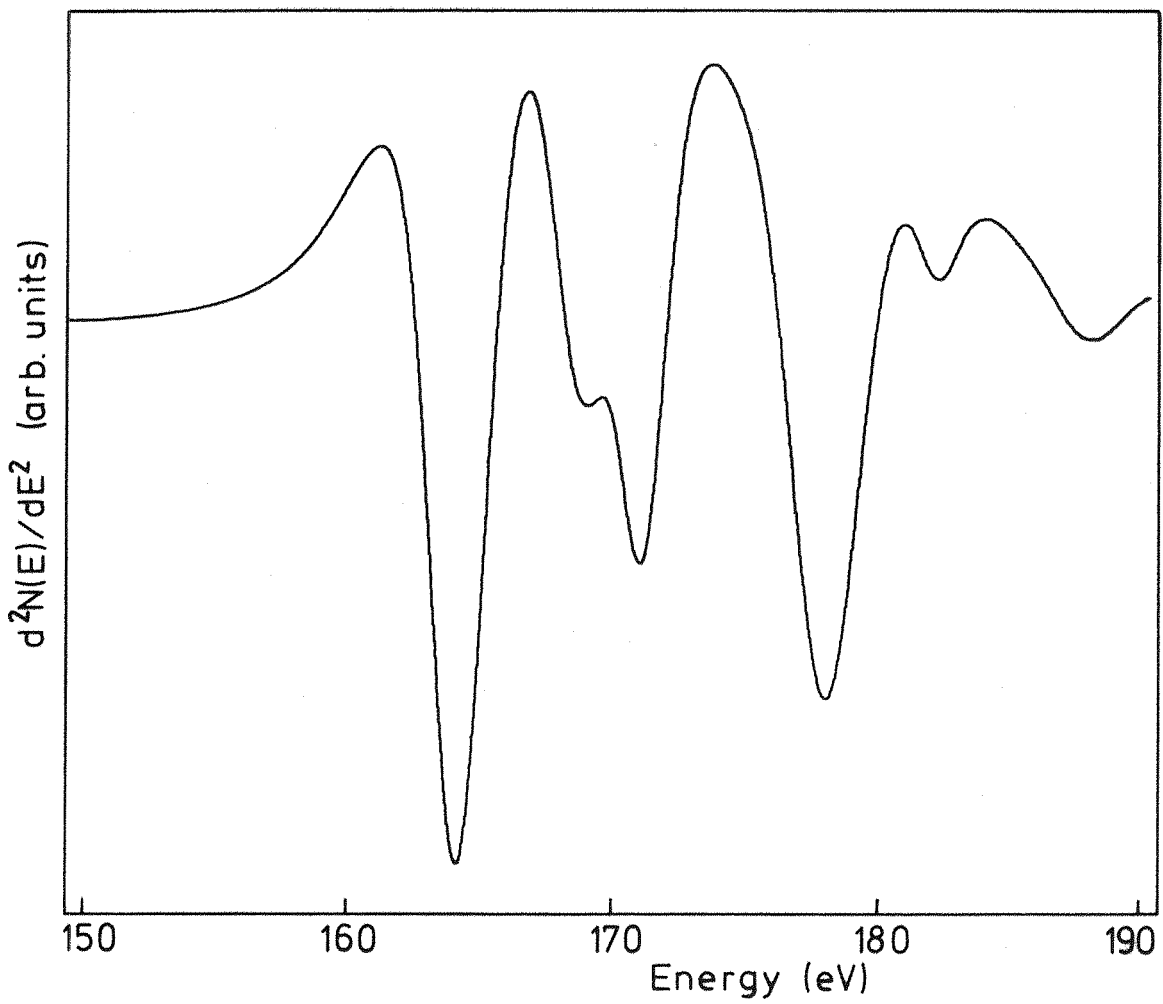


Figure 4.10 Simulation of rhenium spectrum in figure 4.8 without the contributions from modulation broadening.

The broadened peak fit appears to give an accurate value for the width of a peak independent of modulation broadening. A mean width can be calculated from several 'broadened' fits performed on the same part of a spectrum taken at different modulation voltages. A mean makes no sense for the widths of peaks obtained using the ordinary Lorentzian peak fit.

In chapter 2 the various contributions to the shape of an experimentally detected Auger peak were discussed. The original Lorentzian shaped Auger peak is affected by several effects including an instrument function (probably Gaussian), the modulation broadening and a loss tail on the low energy side of the peak (due to the solid state environment). The curve fitting program only took account of the basic Lorentzian line shape plus the modulation broadening as these appeared to be the major contributions to the peaks. This view is supported by the 'visual' accuracy of the simulated spectra and the consistency of the peak positions, relative intensities and widths for spectra recorded with different modulation voltages.

It would be difficult to define an accurate analytic function to represent the loss tail. Accurate addition of a Gaussian instrument function would be easier. This would involve convoluting the Lorentzian and Gaussian line shapes before adding the modulation broadening. This is possible but far from trivial. The resolution of the cylindrical mirror analyser was used to estimate the effect of instrument broadening on the width of the peaks. The resolution is quoted as being better than 1% and was measured to be  $\Delta E/E = 0.5\%$  using figure 4.4: assuming that the natural width of an elastic peak is negligible, the asymptote to the graph gives the width  $\Delta E$  added by instrument broadening. This analysis assumes that addition is an adequate approximation for convolution. A resolution of 0.5% would account for  $\sim 0.8\text{eV}$  of the  $6.5\text{eV}$  f.w.h.m. of the  $164\text{eV}$  peak (figure 4.10). The instrument broadening was therefore not expected to significantly alter the basic Lorentzian shape of the Auger peaks.

The results of the rhenium spectra simulations presented in this chapter are discussed in chapter 6. Other simulations were performed for parts of the tantalum spectrum (chapter 8).

## CHAPTER 5

### PREVIOUS WORK

The aim of the present investigation was to determine the Auger transitions contributing to the low energy spectra of some 5d transition metals. This was achieved by identifying the initial states of the Auger processes and then using theoretical calculations of line energies and relative intensities to assign the correct final states.

The early work on Auger spectra was performed on the K-Auger series, particularly the KLL series as it is the most intense group and completely isolated from other K-Auger groups. Studies on the other groups were more difficult as the component subgroups overlap. Sevier (1972) reviews and compares these studies on both gases and solids. L-, M- and N- Auger and Coster-Kronig spectra have been studied less for two main reasons: firstly the collection of 'low' energy electron spectra gave experimental problems, and secondly, these spectra were more complex and therefore more difficult to analyse.

The theories (e.g. McGuire, 1974) predict that the  $N_{4,5}N_{6,7}X$  (where  $X = N_{6,7}, O_{2,3}$  and  $O_{4,5}$ ) Auger transitions will contribute the most intensity to the low energy electron spectra of the 5d metals. Many workers have used Auger Electron Spectroscopy to identify the elements adsorbed on 5d transition metal surfaces, for example in gas adsorption experiments. However only papers concerned with correctly assigning the substrate Auger transitions are presented here. Others that may be helpful in the analysis of non-Auger peaks are discussed elsewhere in the text.

#### 5.1 Trends Across the Series

The first systematic study of the low energy ( $\sim 140\text{eV}$  to  $190\text{eV}$ ) secondary electron spectra of several 5d transition metal surfaces was undertaken by Haas et al. (1970). They

presented spectra for hafnium, tantalum, tungsten, rhenium, iridium, platinum and gold, only missing osmium in the series. They were struck by the similarity of the spectra obtained from these metals and therefore assumed that they resulted from the same transitions. A monotonic decrease in the energy at which the three major peaks appeared was observed as the atomic number increased. No chemical changes were seen so they assumed that most of the transitions involved core electrons. Haas et al. (1970) plotted the yield of the major tantalum peaks as a function of incident beam voltage to determine the critical ionisation energy. Inspection of the binding energies for tantalum showed that the initial ionisation must come from the  $N_4$  or  $N_5$  levels. Using the equation (see chapter 2)

$$E_Z(WXY) = E_Z(W) - E_Z(X) - E_{Z+1}(Y)$$

they calculated all the possible Auger line energies. For only one group of transitions did they find the required behaviour that the Auger energy decreased in energy with increase in atomic number. This was the  $N_5N_6N_6$ ,  $N_5N_6N_7$ ,  $N_5N_7N_7$  group. They noted that there were three peaks in the first derivative spectra and so assigned the three  $N_5$  based transitions to these three peaks. They also noted that the experimental shift in energy with atomic number was smallest for the elements Hf, Ta and W and greatest for Ir, Pt and Au. Their calculated energy shifts followed the same trend, thus confirming their assignment.

Two later catalogues, the Handbook of Auger Electron Spectroscopy (1976) and McGuire (1979), show similar spectra to Haas et al.'s from which the same trend can be seen.

Red'kin et al. (1971) studied the Auger electron spectrum of osmium (which Haas et al. did not include) up to 300eV. On the basis of Haas et al.'s results for the other metals in the 5d series, they assigned their three equivalent osmium peaks to the  $N_5N_6N_6$ ,  $N_5N_6N_7$ , and  $N_5N_7N_7$  Coster-Kronig transitions.

Chung and Jenkins (1970) compared Haas et al.'s (1970) experimental Auger line energies from 5d metal surfaces with their empirical formula (equation 2.4). Their formula produced almost identical line energies to those calculated by Haas et al.. However Chung and Jenkins felt that the three major experimental peaks should have been attributed to  $N_{4,6,7}N_{6,7}$  as well as  $N_{5,6,7}N_{6,7}$  transitions. The highest energy peak was in the calculated  $N_{4,6,7}N_{6,7}$  region whilst the two lower peaks were in the  $N_{5,6,7}N_{6,7}$  region.

McGuire (1974) has calculated the atomic N-shell Coster-Kronig and Auger rates for the 5d series using j-j coupling for all transitions apart from those involving initial f holes for which he used LS coupling (see chapter 2). The calculations predict that the decay of N-shell holes is dominated by Coster-Kronig transitions of the form NNX and super Coster-Kronig transitions of the form NNN. Moreover the  $N_{4,6,7}N_{6,7}$  transitions are expected to be comparable in strength to the  $N_{5,6,7}N_{6,7}$  transitions. McGuire therefore suggested that the peaks seen by Red'kin et al. for osmium were due to  $N_{4,6,7}N_{6,7}$  transitions as well as  $N_{5,6,7}N_{6,7}$  as the calculated energy positions of the  $N_{4,6,7}N_{6,7}$  peaks are also in the correct region.

## 5.2 Conflicting Reports on Gold

Larkins and Lubenfeld (1977) reported their study of the low energy secondary electron spectrum of gold, induced by ( $Al K_{\alpha}$ ) X-rays. They compared their results with Larkins' (1977) line energy predictions and McGuire's (1974) transition probability calculations (see chapter 2 for discussion of these theories). The background in their  $N(E)$  spectrum was 'removed' by assuming a linear background over the lower energy region (where the  $N_{4,5}N_{6,7}N_{6,7}$  transitions are predicted) and a fourth order polynomial background over the higher energy region (the  $N_{4,5}N_{6,7}O_{4,5}$  area). They estimated that 4% of the total intensity in this region was due to the presence of carbon on the surface though it was

difficult to estimate this figure as the carbon Auger peaks overlap the gold  $N_{4,5}N_{6,7}O_{4,5}$  peaks.

There were several overlapping peaks between 140 and 170eV which agreed well with Larkins' line energy calculations of the  $N_{4,5}N_{6,7}N_{6,7}$  Auger energies. A second group of peaks between 210 and 290eV were in the energy region predicted for the  $N_{4,5}N_{6,7}O_{4,5}$  transitions. The total area under the peaks between 210 and 290eV was about seven times as large as that between 140 and 170eV. There was little intensity in comparison between 170 and 210eV. Larkins and Lubenfeld (1977) therefore concluded that the dominant decay processes for  $N_{4,5}$  vacancies in solid gold were the  $N_{4,5}N_{6,7}O_{4,5}$  Coster-Kronig series rather than the  $N_{4,5}N_{6,7}N_{6,7}$  super Coster-Kronig series as predicted by McGuire. As McGuire's calculations are for free atoms and not those in the solid state, they are expected to be most reliable in predicting the relative transition probabilities for processes not involving conduction band electrons. Larkins and Lubenfeld's results suggest that transition rate data based upon an atomic model cannot be relied upon when conduction band levels are involved.

Matthew, Netzer and Bertel (1980) studied the  $N_{4,5}N_{6,7}N_{6,7}N_{4,5}N_{6,7}O_{2,3}$  and  $N_{4,5}N_{6,7}O_{4,5}$  Auger transitions of gold, platinum and iridium. They used electron bombardment of their single crystal specimens and a hemispherical analyser to record the secondary electron spectra in the region 100 to 300eV. Like Larkins and Lubenfeld they found a small amount of carbon on their gold surface despite cleaning. The background on the N(E) spectra was 'removed' as two separate polynomial sections. On the gold spectrum they found a 1:1 correspondence between the features observed by Larkins and Lubenfeld and their own; there was good agreement on energy values for the peaks but dramatic differences in the relative intensities of peaks in the range 130 to 170eV and 220 to 270eV. For all three metals Larkins' line energy predictions agreed well with the assumption that the main intensity in the region 140 to

170eV was due to  $N_{4,5}N_{6,7}N_{6,7}$  super Coster-Kronig transitions. The intensity between 210 and 270eV was attributed to  $N_{4,5}N_{6,7}O_{4,5}$  transitions using an empirical formula because Larkins does not predict energies for transitions involving the valence band.

Two small peaks were observed in the gold spectrum between 170 and 210eV, and assigned to the  $N_{4,5}N_{6,7}O_{2,3}$  transitions. In platinum the lower energy peak begins to overlap with the  $N_{4,5}N_{6,7}N_{6,7}$  group and the iridium spectrum shows even more overlap.

For all three metals the ratio of yields of the transitions  $N_{4,5}N_{6,7}O_{4,5}$  to  $N_{4,5}N_{6,7}N_{6,7}$  was less than one, though not as small as McGuire's theory predicts, showing that the  $N_{4,5}N_{6,7}N_{6,7}$  group was the more intense. The ratio increased rapidly with atomic number.

Because of their different conclusions Matthew et al. suggest that Larkins and Lubenfeld did not remove all of the background signal in the  $N_{4,5}N_{6,7}O_{4,5}$  portion of their N(E) spectrum.

### 5.3 Work on Tungsten Performed in this Laboratory

#### 5.3.1 Previous work

Rawlings et al. (1980a) studied the low energy tungsten Auger transitions (150-200eV) from a (110) single crystal surface. They plotted the yield of the three largest peaks in the second derivative spectrum as a function of primary beam energy and found the ratios of the yield below the  $N_3$  threshold to the maximum yield to be

$$\begin{aligned} R_{166} &= 0.407(\pm 0.003) \\ R_{172} &= 0.454(\pm 0.006) \\ \text{and } R_{179} &= 0.380(\pm 0.006). \end{aligned}$$

A curve synthesis exercise performed by the author on the latter peaks at 172eV and 179eV showed that they were each

composed of at least two peaks. For comparison the yield curve from the  $N_3$  based peak at 354eV was also plotted.

From the difference in the yield curves the three lower energy peaks appeared to result from three different initial hole states. Rawlings et al. used the three yield ratios with Larkins' line energy theory and McGuire's intensity theory to analyse the experimental spectrum. They concluded that the intensity of the 166eV peak resulted mostly from  $N_5N_{6,7}X$  though when energetically allowed there was an  $N_3N_5V$  contribution. The 172eV peak was due to  $N_5N_{6,7}X$ , the 179eV peak was due to  $N_4N_{6,7}X$  and the 354eV peak due to  $N_3N_{6,7}X$  (where  $X = N_{6,7}$  or  $O_{2,3}$ ). They had difficulty in determining the final states ( $X$ ) as Larkins' (1977) line energy calculations predict that the  $N_{4,5}N_{6,7}N_{6,7}$  series overlaps the  $N_{4,5}N_{6,7}O_{2,3}$  series. McGuire (1974) expects the  $N_{4,5}N_{6,7}N_{6,7}$  group to dominate the spectrum. Unfortunately if his results are correct, Larkins'  $N_{4,5}N_{6,7}N_{6,7}$  calculated energies have to be increased by 5eV to obtain reasonable term assignments to the experimental peaks. However no energy shift was required to match the experimental peaks with the  $N_{4,5}N_{6,7}O_{2,3}$  theoretical line energies. Because of this conflict between the two theories and experimental evidence Rawlings et al. could not be certain of the final state.

There were also two very low intensity peaks in their spectrum which were still visible below the  $N_3$  threshold level. The empirical formula for Auger line positions (equation 2.4) predicts that the  $N_{4,5}N_{6,7}O_{4,5}$  peaks should be found in these positions. (Larkins does not present line energies for transitions involving the conduction band).

Finally the total areas of the peaks (including those from the simulated peaks) were used to estimate the ratio of  $N_5$  to  $N_4$  initial hole states. If  $N_4$  and  $N_5$  initial holes decay to all the same states then this ratio would be 3:2. The only decay route available to  $N_4$  initial holes but not to  $N_5$  initial holes is the  $N_4N_5V$  Coster-Kronig transition. McGuire's (1974) calculations suggest 1.2%  $N_4 \rightarrow N_5$  compared to

$N_4 \rightarrow N_{6,7}$  decay, though this figure may not be correct as a conduction band electron is involved. The experimental ratio was 2.4:1 suggesting an appreciable rate for the  $N_4 N_5 V$  transition.

Rawlings et al. (1979) continued (though publication dates indicate the contrary) with a study of the tungsten 210eV peak. The yield curve for this peak was compared to the  $N_3, N_4$  and  $N_5$  initial state yield curves plotted in their previous study. For a primary beam energy of 1200eV, the 210eV peak could be adequately described by considering ~23% of the intensity to be due to  $N_4$  initial holes and the rest from  $N_3$  initial holes. The  $N_4$  based intensity was accounted for by the  $N_4 N_{6,7} V$  Coster-Kronig processes but there were no  $N_3$  initial hole transitions predicted in this energy region. Rawlings et al. rejected autoionisation and direct double ionisation as possible causes for the extra intensity in favour of a two step cascade process. Using an empirical formula to estimate the energy position, the first step  $N_3 \rightarrow N_5 V$  followed by the second step  $N_5 V \rightarrow X V V$  (where  $X = N_{6,7}$  or  $O_{2,3}$ ) gave intensity in the correct position. Thus the 210eV peak may be explained by  $N_4 N_{6,7} V$  emission plus intensity from the second step of the cascade  $N_3 \rightarrow N_5 V \rightarrow X V V$ .

Further work by Rawlings et al. (1980b) looked at five of the less intense peaks in the tungsten spectrum at 142eV, 131eV, 116eV, 219eV and 229eV. Rawlings et al. investigated the temperature dependence and energy dependence of the yields for each of the five peaks. They used the pulsed heater described in chapter 3 to enable the sample to be heated at the same time as measurements were taken. The 142eV peak was not temperature dependent. All of the other peaks showed some temperature dependence which was though to arise from the diffraction of secondary electrons. The results and conclusions are summarised in Table 5.1.

Energy position of peak (eV)	Analysis of Yield Curve	Analysis of temperature dependence	Conclusions: processes contributing to the peak
142	2 contributions to the peak.	none	major process: $N_3N_5N_7$ , minor process: $N_4N_7O_1$
131	3 contributions to the peak	Slightly temperature dependent	a temperature dependent process, $N_4N_6O_1$ ,
229	1 contribution: yield curve rose steeply from threshold to maximum at lower energy than Auger yield curve	In graph of yield v. temperature gave straight line up to 11200K.	a temperature dependent process: Kikuchi mechanism $N_3N_5N_6,7$
219	2 contributions: one similar to the 229eV peak yield curve.	slightly less dependent on temperature than the 229eV peak.	a temperature dependent process (probably same as 229eV peak), $N_4N_6,7O_4,5$
116	1 contribution: yield curve not the same as an Auger yield curve or the 229eV peak yield curve.	most temperature dependent	a temperature dependent process but not the same as the 229eV peak.

Table 5.1  
Summary of results and conclusions found by Rawlings et al. (1980b) for some minor peaks in the tungsten spectrum.

### 5.3.2 Present work

Further investigation of the 219eV and 229eV tungsten peaks threw doubt on Rawlings et al.'s conclusions. The author plotted the temperature dependence of these peaks up to 2000K, 800K higher than Rawlings et al.. The same experimental procedure was used with the first derivative spectra recorded using the pulsed heater. Spectra were adjusted to look horizontal by subtracting a straight line approximation to the background. The yield was taken as the peak to peak heights of the peaks in the residual spectrum.

Graphs of the temperature dependence are shown in figures 5.1 (linear scale) and 5.2 (logarithmic scale). On logarithmic scales the graphs for both peaks form three straight line sections; up to 1200K, 1200K to 1500K and above 1500K. The first part of the graph for the 229eV peak was suggested to be a Kukuchi mechanism by Rawlings et al. (section 5.3.1) but it is difficult to find a mechanism that explains the rest of the graph.

### 5.4 Summary

Early work on the low energy Auger electron spectra of 5d transition metal surfaces was by Haas et al. (1970). They looked at several metals and noticed trends in the series. More recently work has concentrated on detailed analyses of individual metals. Two groups, Larkins and Lubenfeld (1977) and Matthew et al. (1980) have made a study of gold, and Rawlings et al. have investigated the tungsten spectrum.

The broad aim of the present investigation was to determine the Auger transitions contributing to the low energy electron spectra of the 5d metals. This involves separating the Auger peaks from other peaks, shown to be necessary by Rawlings et al., and comparing the experimental results with theory. An important part of this work is to look for trends in the results from several different metals.

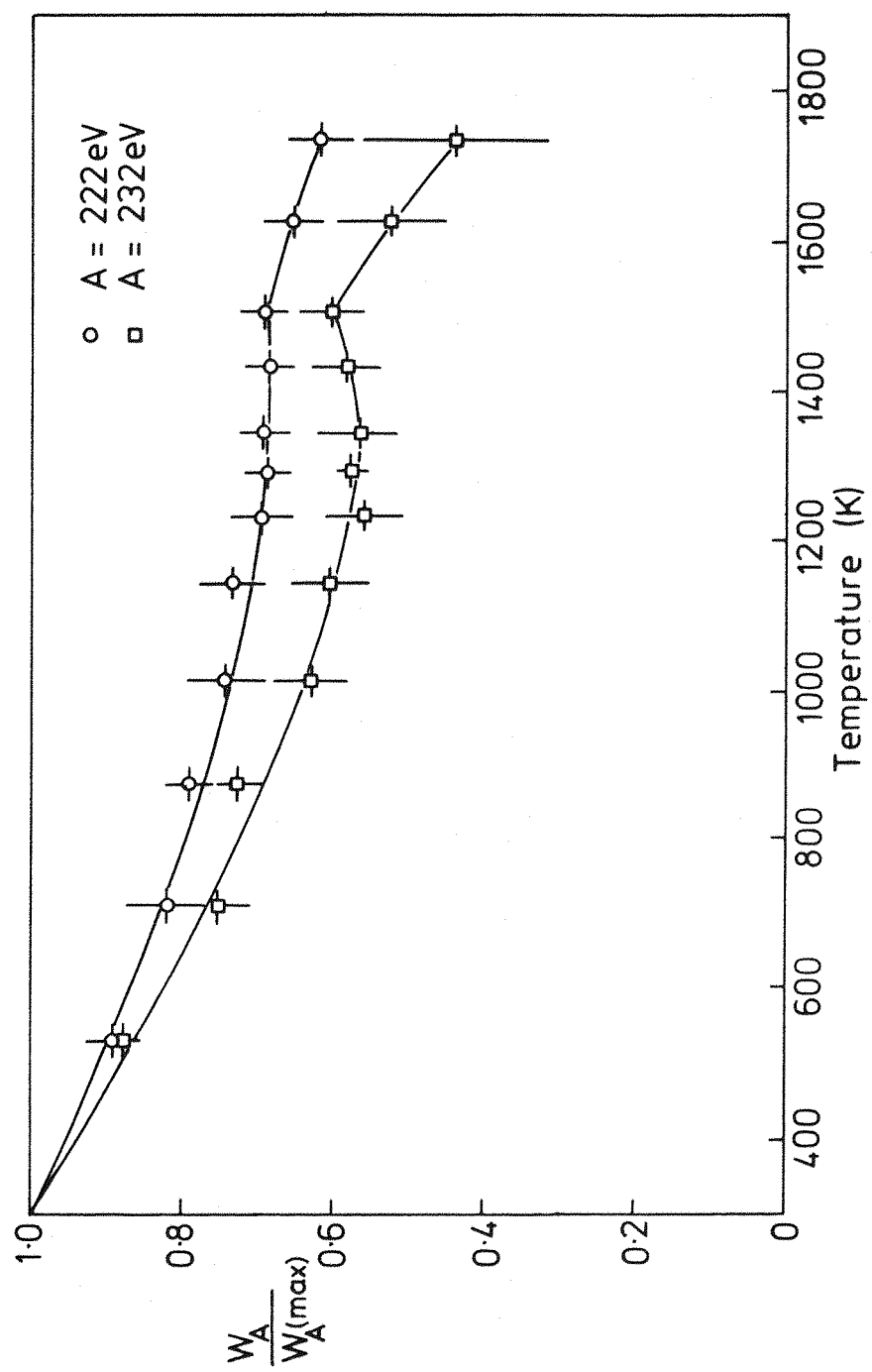


Figure 5.1 Temperature dependence of tungsten 222eV and 232eV peaks.

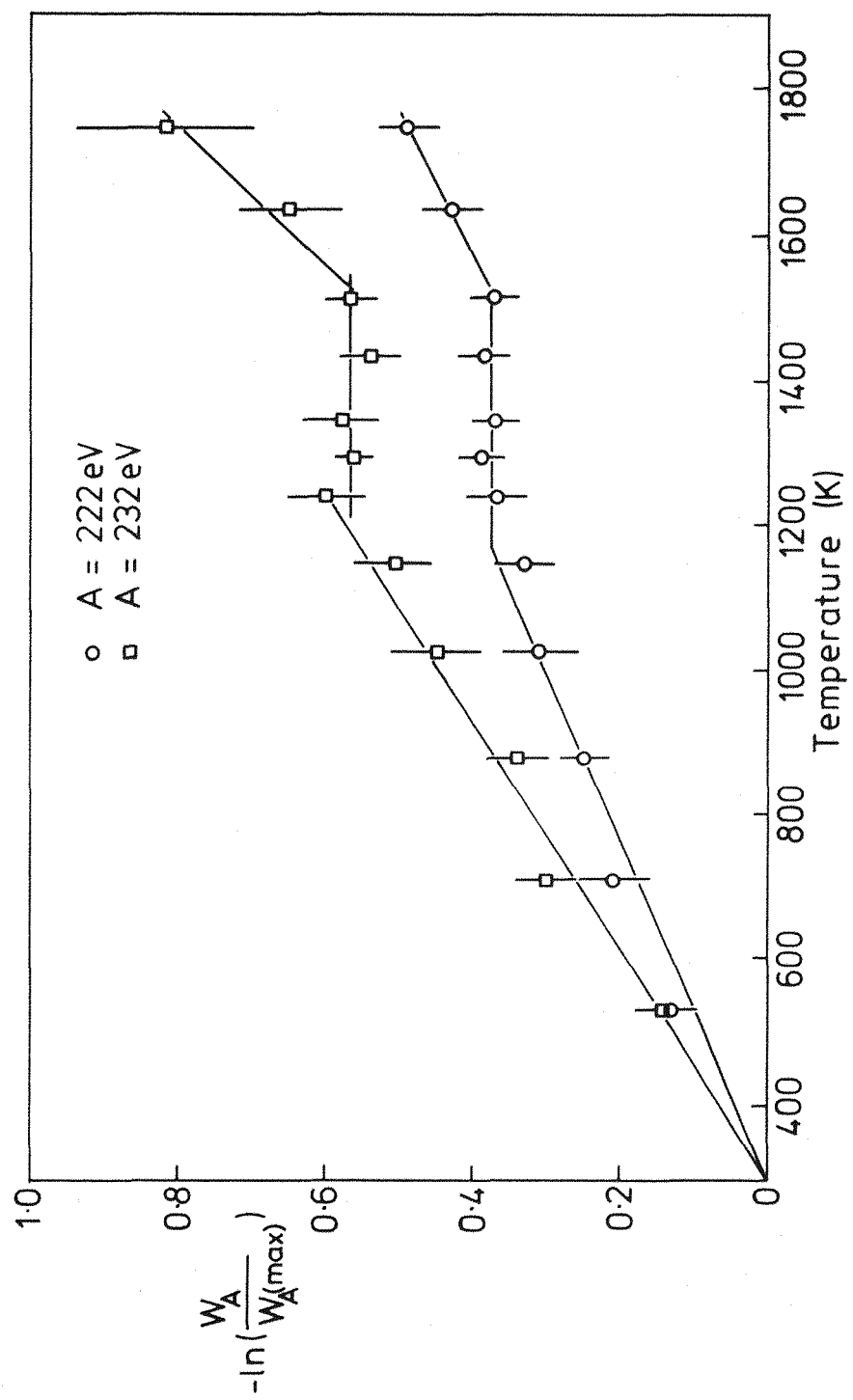


Figure 5.2 Temperature dependence of tungsten 222eV and 232eV peaks - logarithmic scale.

This thesis builds on the detailed work already done by looking at the little-studied rhenium spectrum. Preliminary results are also presented for tantalum and gold. Though gold has already been studied by two groups, their opposite conclusions show that the metal requires more investigation.

The present and previous results are then compared with each other and with the theories to draw final conclusions on the Auger peaks in the low energy spectrum of the 5d transition metals.

## CHAPTER 6

### THE RHENIUM AUGER TRANSITIONS: 150-200eV

This chapter discusses the origins of the most intense peaks in the low energy (150-200eV) rhenium secondary electron emission spectrum.

The theoretically predicted Auger line energies (Larkins, 1977) and intensities (McGuire, 1974) do not agree with the experimental spectrum. If Larkins' line energies are correct then McGuire's calculations must be wrong, and vice versa.

#### 6.1 Results

Figures 6.1 and 6.2 show the low energy first derivative spectra induced by primary beams of 1400eV and 400eV respectively from a clean rhenium polycrystalline surface. A primary beam of energy 400eV is only sufficient to ionise the  $N_4$  level and levels above (Sevier, 1972). The 1400eV beam can also ionise the  $N_1, N_2$  and  $N_3$  levels. A positive slope has been subtracted from the 400eV derivative spectrum to make it horizontal. The integrals of the first derivative spectra are also shown in figures 6.1 and 6.2: these have been subjected to second-order polynomial background correction. The probable remaining background has been dotted in the diagrams.

The most intense electron emissions, those lying between 150eV and 200eV, are shown in figure 6.3 in second derivative form. The method of detection eliminates a second-order background from the second derivative spectra. A first glance at these spectra suggest that there are just three peaks contributing to the spectrum. The best fit of three Lorentzian peaks to the spectrum in figure 6.3a is seen in figure 4.2a. This 'curve fitting' exercise, described in chapter 4, assumes that any losses from the

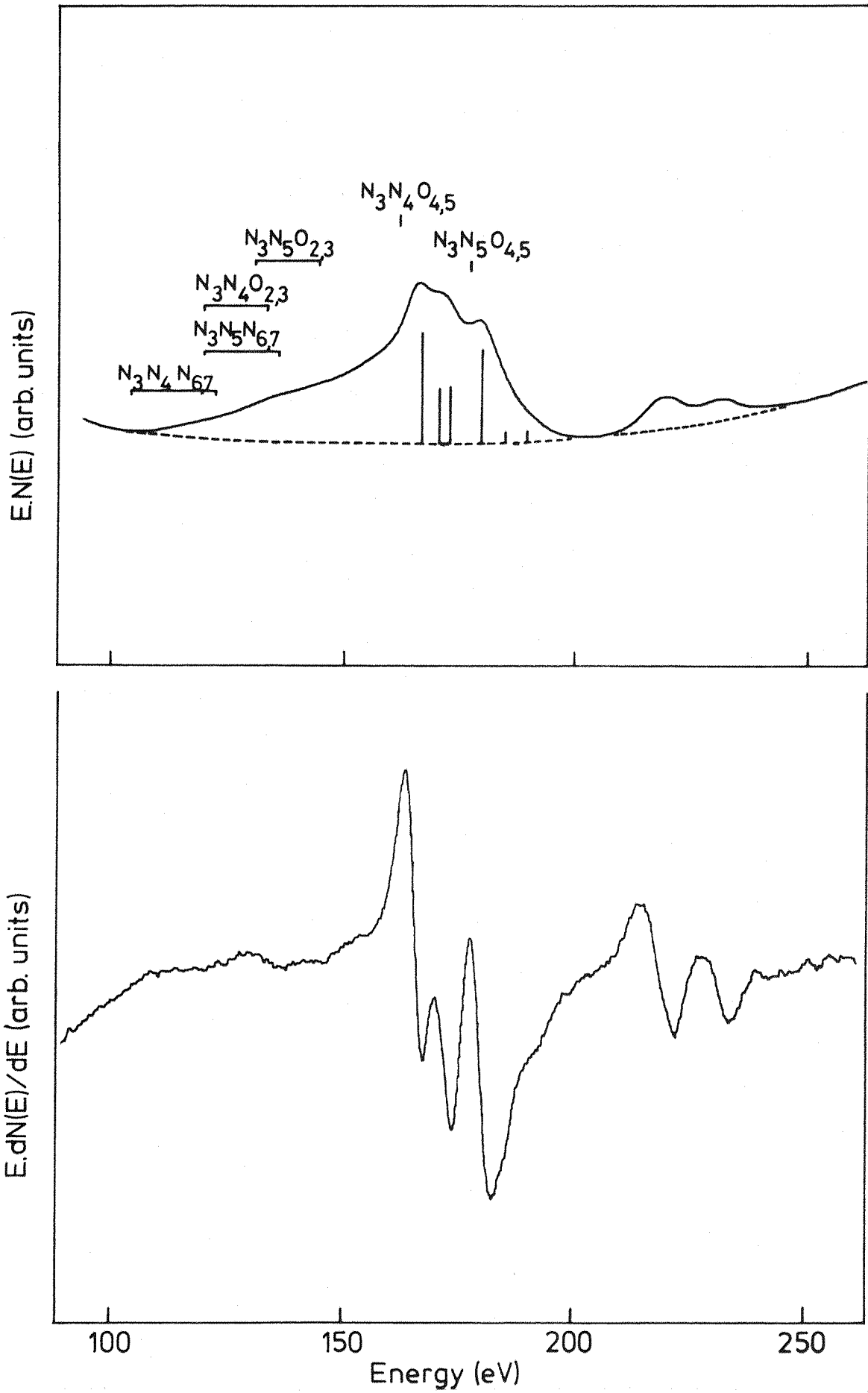


Figure 6.1 Rhenium secondary electron spectrum induced by 1400 eV primary electrons ( $I_b = 3 \mu A$ ,  $v_m = 3.3 V_{ptp}$ ,  $\tau = 0.3 s$ , scan  $1 eV \cdot s^{-1}$ ).

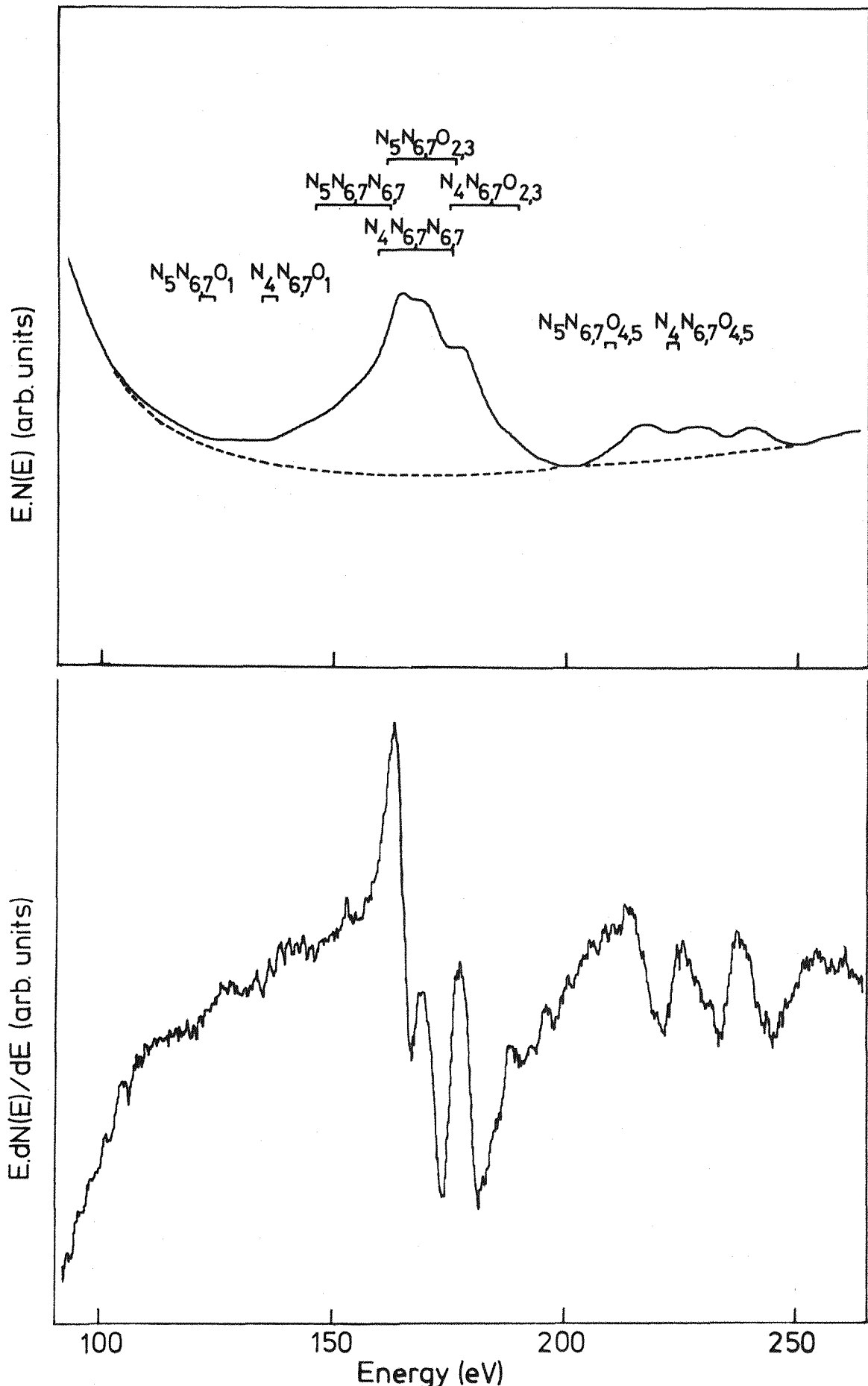


Figure 6.2 Rhenium secondary electron spectrum induced by 400eV primary electrons ( $I_b = 3\mu A$ ,  $v_m = 3.3V_{ptp}$ ,  $\tau = 0.3s$ , scan  $1eV.s^{-1}$ ).

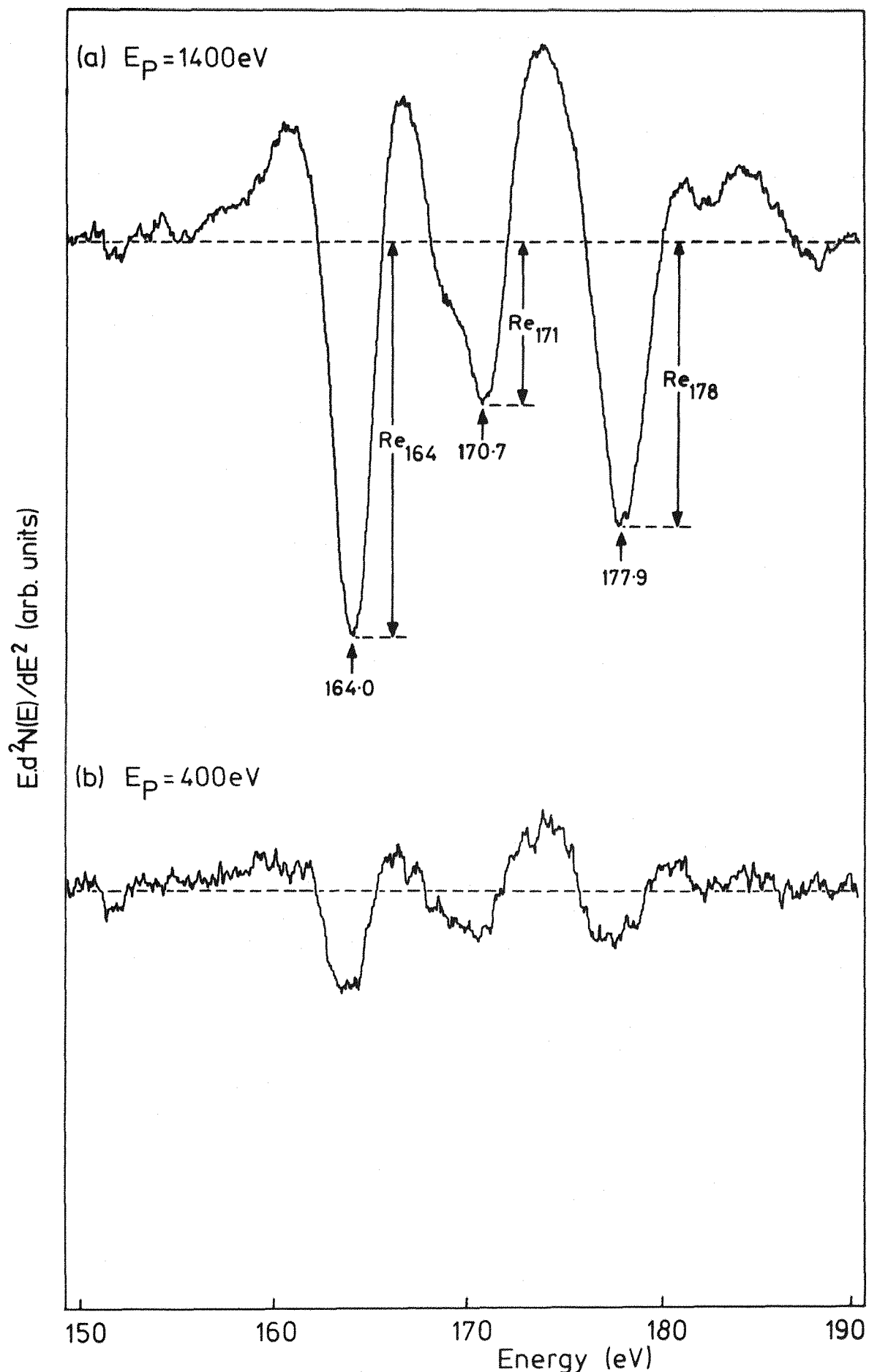


Figure 6.3 Second derivative rhenium secondary electron spectrum ( $I_b = 5\mu\text{A}$ ,  $v_m = 2.1\text{V}_{\text{ptp}}$ ,  $\tau = 0.3\text{s}$ , scan  $0.5\text{eV.s}^{-1}$ ).

intense emissions in this region have negligible intensity. This assumption is supported by the lack of intensity on the low energy side of a 177eV elastic peak (figure 6.4) which falls in the same energy window. From the three peak fit it is obvious that there are several more peaks in the spectrum. Six peaks are necessary to simulate adequately the experimental spectrum. Figure 4.2b shows six Lorentzian peaks fitted to the spectrum and figure 4.8 the fit of six broadened Lorentzian peaks. There may be several more peaks in this region but with low intensities compared to the peaks already considered. The energy positions and relative intensities of the six peaks from figure 4.8 are shown under the  $N(E)$  curve in figure 6.1.

Yield curves (figure 6.5) for the three obvious peaks were plotted by measuring their peak to background heights (as shown in figure 6.3) as a function of primary beam energy. Measurements were not taken for values of primary beam energy between 400 and 550eV as losses from the elastic peak overlapped the spectrum. For comparison a normalised theoretical cross-section (equation 2.5) of a 270eV deep core level is included in figure 6.5. This lies in the region to which the experimental yield curves show threshold behaviour. The energy positions of the rhenium inner shells to which the primary exciting electron beam has access are also shown (Sevier, 1972).

The yields for primary beams of 400eV and 1400eV were measured 32 times to give the normalised yields for each peak at 400eV as

$$R_{164} = Re_{164}(400) / Re_{164}(1400) = 0.272 \pm 0.002$$

$$R_{171} = Re_{171}(400) / Re_{171}(1400) = 0.311 \pm 0.004$$

$$R_{178} = Re_{178}(400) / Re_{178}(1400) = 0.232 \pm 0.002.$$

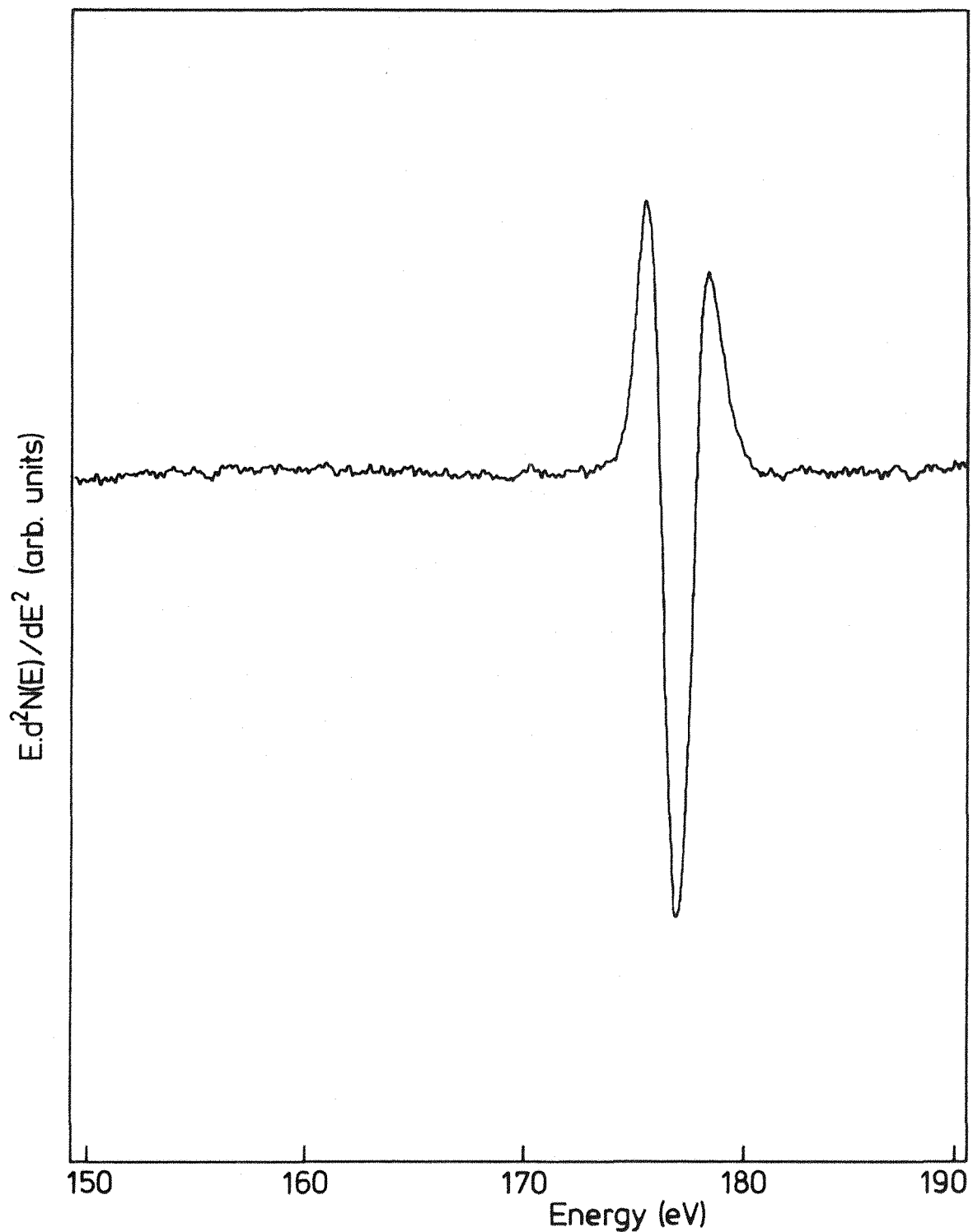


Figure 6.4 Second derivative spectrum of a 177 eV elastic peak from a rhenium surface ( $I_b = 5 \mu A$ ,  $v_m = 2.5 V_{ptp}$ ,  $\tau = 0.3 s$ , scan  $1 eV \cdot s^{-1}$ ).

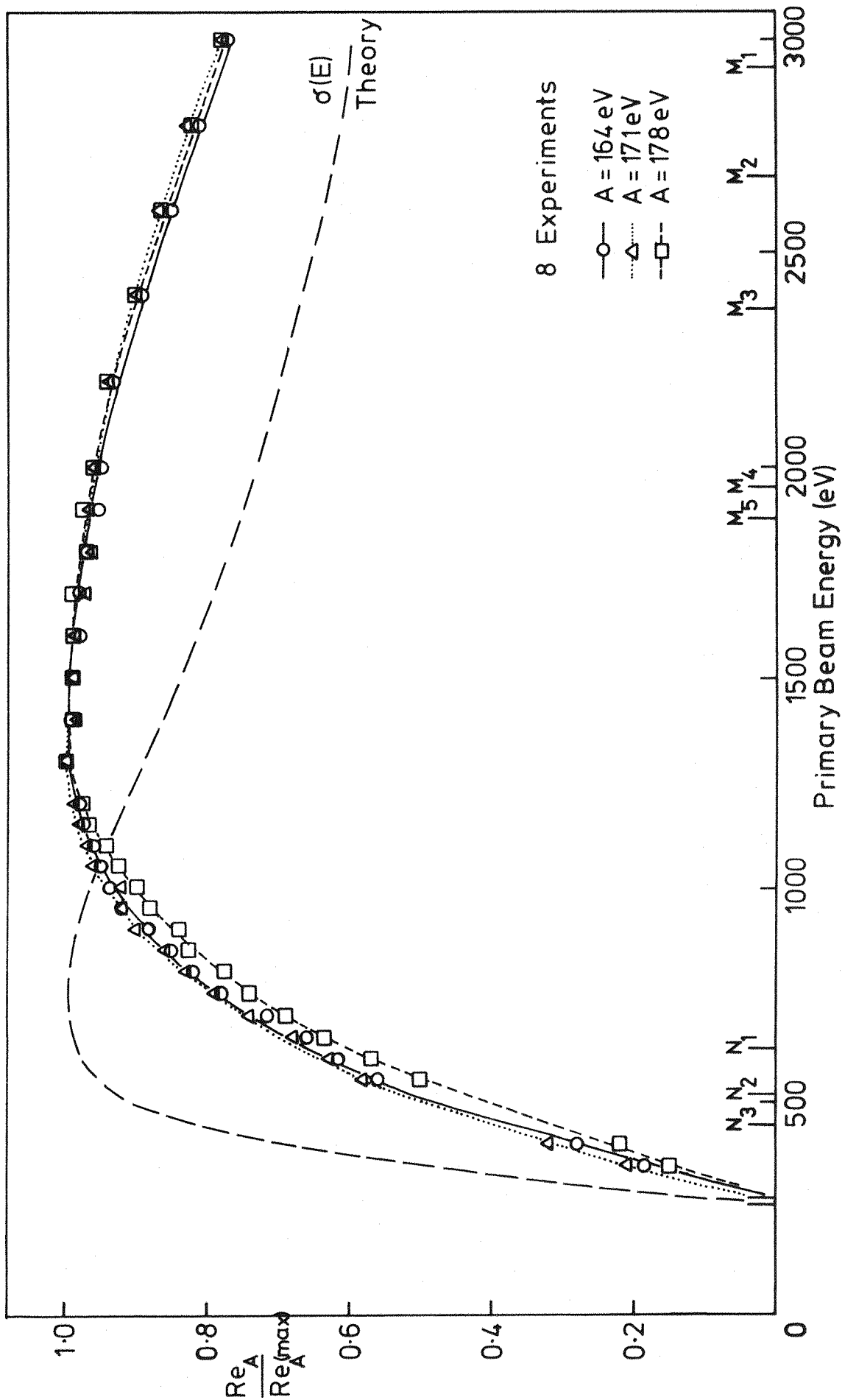


Figure 6.5 Yield curves for rhenium peaks at 164, 171 and 178 eV.

Normalising to  $R_{171}$  gives  $R_{164}=0.88$ ,  $R_{171}=1$ ,  $R_{178}=0.75$ . As the peak at 171eV is a doublet its ratio will be from the sum of two overlapping peaks. For comparison with these ratios several curve fits of six broadened and unbroadened Lorentzian peaks were performed on spectra at primary beam energies of 400 and 1400eV. The normalised yield ratios, average widths and energy positions of the six peaks are shown in table 6.1. As the yield of a peak is proportional to its area, the yield was calculated as the height of a peak multiplied by its f.w.h.m.

The errors in the position of the peaks are about  $\pm 0.1$ eV in table 6.1. This refers to the accuracy of a peak relative to the other peaks. The error (from the calibration of the energy scale) in the energy positions relative to the Fermi energy are  $\pm 0.5$ eV. The scale on the first derivative spectra (figures 6.1 and 6.2) is about 5eV different to that for rhenium in the Handbook of Auger Electron Spectroscopy (1976). As the handbook's energies are relative to the vacuum level, 5eV is the difference between the Fermi level and vacuum level. This is a reasonable value and supports the energy scale used in the present work.

The peak at 350eV, shown in figures 3.6 and 3.7, has a yield curve with an  $N_3$  level threshold. This curve was plotted by measuring the peak to base height in the second derivative spectrum and the peak to peak height in the first derivative spectrum (after subtracting a slope to make the spectrum flat where necessary) as a function of primary beam energy. Both methods gave the same results and figure 6.6 shows the average of all results taken.

The yields of the peaks at 164.0, 168.6, 171.0, 177.8, 182.0 and 350.2eV did not vary as the temperature of the rhenium sample was altered. The 187.8eV peak, which was temperature dependent, will be discussed in chapter 7.

Energy position w.r.t. Fermi level (eV) (average of 10 experiments)	Yield Ratio $Re_{E(400)}/Re_{E(1400)}$ (normalised) (average of 4 experiments)
164.0 <u>±</u> 0.04	0.92 <u>±</u> 0.05
168.6 <u>±</u> 0.1	1.01 <u>±</u> 0.07
171.0 <u>±</u> 0.06	1.0 <u>±</u> 0.1
177.8 <u>±</u> 0.09	0.79 <u>±</u> 0.04
182.0 <u>±</u> 0.2	1.2 <u>±</u> 0.4
187.8 <u>±</u> 0.1	1.8 <u>±</u> 0.8

Table 6.1a Results from fit of 6 Lorentzian peaks to rhenium spectrum, figure 4.2b.

Energy Position w.r.t. Fermi level (eV) (average of 10 experiments)	f.w.h.m. (eV) (average of 10 experiments)	Yield Ratio $Re_{E(400)}/Re_{E(1400)}$ (normalised) (average of 4 experiments)
164.0 <u>±</u> 0.04	6.5 <u>±</u> 0.1	0.87 <u>±</u> 0.03
168.6 <u>±</u> 0.1	6.0 <u>±</u> 0.2	1.1 <u>±</u> 0.3
171.0 <u>±</u> 0.06	5.6 <u>±</u> 0.2	0.9 <u>±</u> 0.1
177.8 <u>±</u> 0.09	7.6 <u>±</u> 0.1	0.75 <u>±</u> 0.02
182.0 <u>±</u> 0.2	5.2 <u>±</u> 0.3	1.2 <u>±</u> 0.2
187.8 <u>±</u> 0.1	8.4 <u>±</u> 0.6	2.4 <u>±</u> 0.7

Table 6.1b Results from fit of 6 broadened Lorentzian peaks to rhenium spectrum, figure 4.8.

4 Experiments

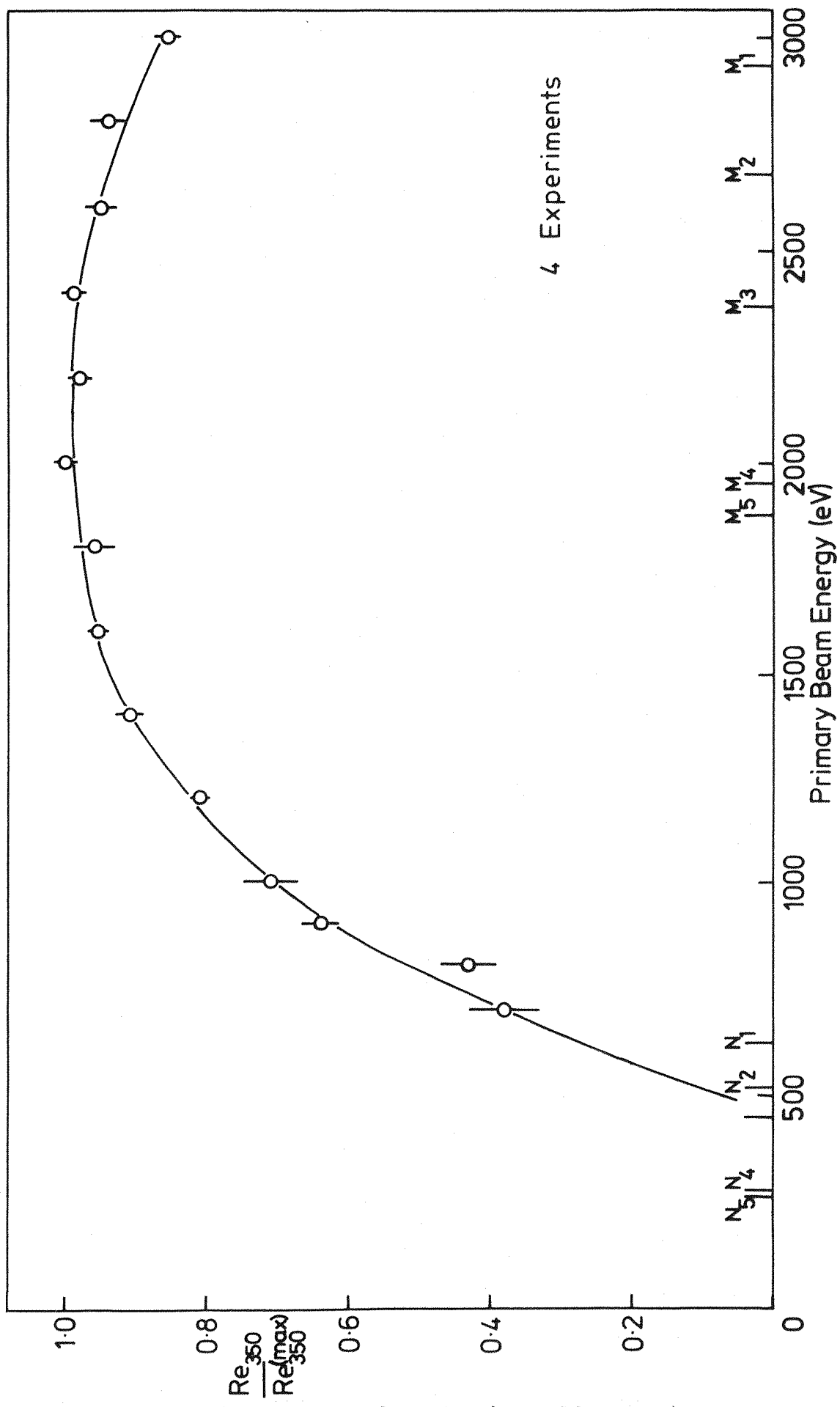


Figure 6.6 Yield curve for rhenium 350 eV peak.

## 6.2 Discussion

When trying to determine the origin of peaks in a secondary electron spectrum it is important to look at the spectrum induced by primary beams of different energies. There may be several contributions to what is apparently one peak and some of these contributions may be eliminated by reducing the primary beam energy. In figure 6.1, the beam of 1400eV was able to ionise levels down to the  $N_1$  level: the 400eV beam in figure 6.2 however can only ionise the  $N_4$  level and above. The theoretically predicted Coster-Kronig and super Coster-Kronig line energies in this region are shown in both figures and in table 6.2 which also includes ordinary Auger transitions. The close similarity between the spectra in figures 6.1 and 6.2, and figures 6.3a and b show that most of the intensity between 150 and 200eV in the spectrum arises from the decay of  $N_4$  and  $N_5$  single hole states as the 400eV primary beam can only lead to  $N_4$  and  $N_5$  initial state Auger transitions. The yield curves (figure 6.5) agree with this suggestion as they show threshold behaviour toward the  $N_4$  and  $N_5$  levels and are smooth curves with no obvious 'kink' to suggest a large contribution from another initial hole.

The results of the six peak curve fitting exercise in table 6.1 confirm the assumption that the two peaks contributing to the 171eV peak have similar yield behaviour ( $R_{168.6} \approx R_{171.0}$ ) and can therefore be analysed together. The small peak at 182.0eV will have some influence on the large peak at 177.8eV. Its yield ratio of about 1.2 has a large error because the yield is so small (about 10% of the intensity of the 177.8eV peak in figure 6.1).  $R_{177.8} \approx R_{182.0}$  within the errors and so it is assumed that the small peak either has the same yield behaviour or, if not, is small and will not influence the larger peak significantly.

From the theoretical prediction of the line energies, the  $N_5$  initial state Auger transitions occur at a lower energy than the  $N_4$  based transitions for the same final

Transition	Energy range w.r.t. Fermi level (eV) (error <u>±5</u> eV)
$N_1 N_3 N_{6,7}$	116.5 - 124.9
$N_1 N_3 O_{2,3}$	129.1 - 141.1
$N_1 N_4 O_1$	259.4 - 259.8
$N_2 N_4 N_{6,7}$	176.8 - 195.6
$N_2 N_4 O_1$	152.3 - 152.7
$N_2 N_4 O_{2,3}$	192.5 - 206.6
$N_2 N_5 N_{6,7}$	193.1 - 209.2
$N_2 N_5 O_1$	165.6 - 166.2
$N_2 N_5 O_{2,3}$	203.5 - 217.9
$N_3 N_4 N_{6,7}$	103.3 - 122.1
$N_3 N_4 O_{2,3}$	119.0 - 133.1
$N_3 N_5 N_{6,7}$	119.6 - 135.7
$N_3 N_5 O_{2,3}$	130.0 - 144.4
$N_4 N_{6,7} N_{6,7}$	159.1 - 175.1
$N_4 N_{6,7} O_1$	134.2 - 137.3
$N_4 N_{6,7} O_{2,3}$	174.3 - 188.8
$N_5 N_{6,7} N_{6,7}$	145.6 - 161.6
$N_5 N_{6,7} O_1$	120.7 - 123.8
$N_5 N_{6,7} O_{2,3}$	160.8 - 175.3

Table 6.2a Theoretical Coster-Kronig and super Coster-Kronig line energies for rhenium in the region 90eV-260eV (Larkins, 1977).

Transition	Energy Range (eV)
$N_1 N_3^0 4, 5$	166.95
$N_2 N_4^0 4, 5$	234.6
$N_2 N_5^0 4, 5$	249.7
$N_3 N_4^0 4, 5$	161.1
$N_3 N_5^0 4, 5$	176.2
$N_4 N_6, 7^0 4, 5$	221.0 - 223.6
$N_5 N_6, 7^0 4, 5$	207.5 - 210.1

Table 6.2b Theoretical Coster-Kronig and super Coster-Kronig line energies for rhenium in the region 90eV-260eV (using equation 2.4 and binding energies from Sevier (1972)).

Transition Energy Range (eV)

$N_4^0 1^0 1$	107.2
$N_4^0 1^0 2, 3$	138.7 - 150.5
$N_4^0 1^0 4, 5$	188.7
$N_4^0 2, 3^0 2, 3$	170.1 - 193.7
$N_4^0 2, 3^0 4, 5$	220.2 - 232.0
$N_4^0 4, 5^0 4, 5$	270.3
$N_5^0 1^0 2, 3$	125.2 - 137.0
$N_5^0 1^0 4, 5$	175.2
$N_5^0 2, 3^0 2, 3$	156.6 - 180.2
$N_5^0 2, 3^0 4, 5$	206.7 - 218.5
$N_5^0 4, 5^0 4, 5$	256.8

Table 6.2c Theoretical Auger line energies for rhenium in the region 90eV-260eV (using equation 2.4 and binding energies from Sevier (1972)).

states. It would therefore seem a reasonable hypothesis to assign the 164eV peak to an  $N_5$  based transition, the 178eV peak to an  $N_4$  based transition and the 171eV peak to a mixture of the two. This hypothesis is supported by looking at the energy separation between the  $N_3$  based peak at 350eV and the 164eV and 178eV peaks:  $350.2-177.9=172.3$ eV and  $350.2-164.0=186.2$ eV. The difference between the  $N_3$  and  $N_4$  binding energies is 170.7eV and the  $N_3$  and  $N_5$  difference is 184.2eV. Bearing in mind that the error on both the experimental line energies and binding energies is  $\pm 0.5$ eV, these calculations suggest that the 164, 178 and 350eV peaks are  $N_5$ ,  $N_4$  and  $N_3$  initial hole transitions respectively with the same final state.

With the 164eV peak being  $N_5$  based, the 178eV peak being  $N_4$  based and the 171eV peak being a mixture of the two the ratios of yields at 400 and 1400eV primary beam energies would be in the order  $R_{164} > R_{171} > R_{178}$  ( $R_{N_5} > R_{N_4}$ ). However,  $R_{171}$  is greater than  $R_{164}$  suggesting that the 171eV peak is  $N_5$  based and the 164eV peak is  $N_5$  plus a contribution from an initial hole in a deeper level. According to McGuire (1974) an  $N_3$  based contribution should be the most intense. In figure 6.1 the  $N_3N_4O_{4,5}$  Auger emission occurs at  $\sim 161$ eV. Assuming that this produces intensity in the 164eV peak the  $N_3$  contribution can be estimated by finding the proportions of the  $N_5$  and  $N_3$  yield curves that best fit the yield curve for the 164eV peak. This calculation was performed using a regression method. The  $N_3$  yield curve was taken to be that from the peak at 150eV (figure 6.6). If the 171eV peak's yield curve is shifted to the  $N_3$  threshold level and expanded by  $\sim 40\%$  it has the same shape as the 150eV curve. This lends confidence to the assumption that they are both yield curves from just one level. The yield curve fit for the 164eV peak is shown in figure 6.7 and the best fit gives the 164eV peak as  $N_5 + 0.05N_3$  based.

As  $R_{178}$  is the lowest of the three ratios the 178eV peak could be just  $N_4$  based ( $R_{N_5} > R_{N_4}$ ). However, from the

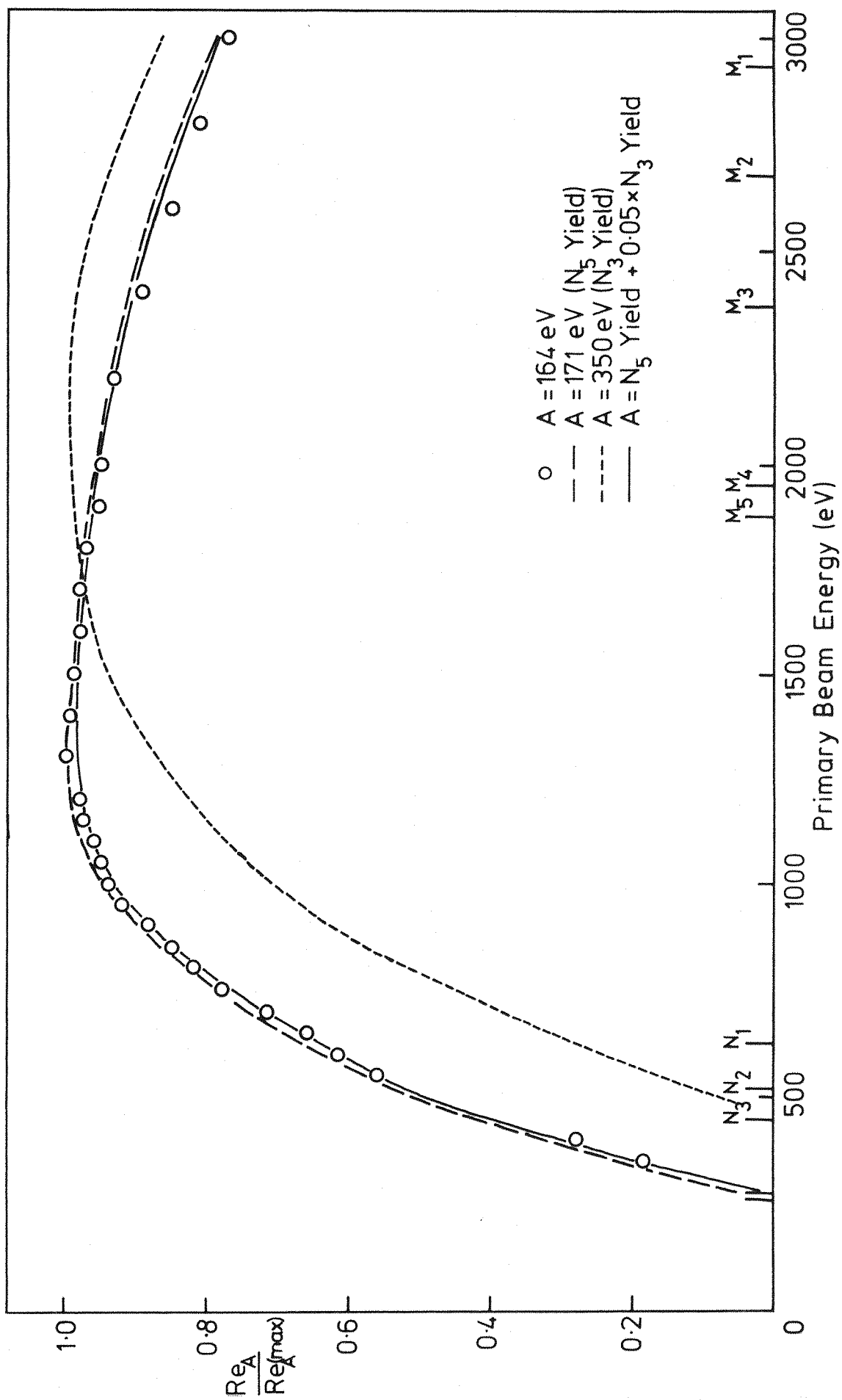


Figure 6.7 Best fit of  $N_5$  and  $N_3$  yield curves to the rhenium 164 eV peak's yield curve.

theoretical cross section ratio of  $\sigma_{N_4}/\sigma_{N_5} = 0.84$  (equation 2.5) for rhenium with a primary beam of 400eV, the ratio  $R_{178}/R_{171}$  should be 0.84 for the 178eV peak to be pure  $N_4$  based if the 171eV peak is  $N_5$  based. This relies on the relevance of the theoretical ratio  $\sigma_{N_4}/\sigma_{N_5}$  in this case. The theoretical cross section shown in figure 6.5 does not agree with the experimental curves. This is because the experimental result is from a solid surface which not only reflects the cross section of an isolated core level within the escape depth of the Auger electron, but also the influence of the scattered electrons still having sufficient energy to ionise that level. The ratio of cross sections,  $\sigma_{N_4}/\sigma_{N_5}$ , however should be very similar in both the theoretical and experimental cases. The experimental ratio  $R_{178}/R_{171} = 0.75$  is much lower than the theoretical ratio of 0.84. The  $N_3N_4O_{4,5}$  Auger emission occurs at  $\sim 176$ eV (figure 6.1) and could be a significant contribution to the 178eV peak, accounting for the low value of 0.75. As there is no pure  $N_4$  experimental yield curve the 171eV yield curve was shifted 13.5eV (the difference between the  $N_4$  and  $N_5$  binding energies (Sevier, 1972)) to give it  $N_4$  threshold behaviour. The fit of this  $N_4$  curve and the  $N_3$  curve to the 178eV yield curve is shown in figure 6.8. This calculated that the 178eV peak is  $N_4 + 0.13N_3$  based.

According to McGuire (1974), the intensity of the  $N_3N_4O_{4,5}$  emission should be about 20% of that due to  $N_3N_5O_{4,5}$ . If the areas of the  $N_3$  contributions to the 164 and 178eV peaks are calculated using area = height  $\times$  f.w.h.m. for the peaks from the curve fitting exercise, the  $N_3N_4O_{4,5}$  is  $\sim 35\%$  of the  $N_3N_5O_{4,5}$  intensity. McGuire's calculations refer to a free atom and so may not describe the solid state situation well when a conduction band electron ( $O_{4,5}$ ) is involved as in this case.

The final states of these  $N_4$  and  $N_5$  initial hole transitions are difficult to assign as Larkins (1977) predicted that the  $N_{4,5}N_{6,7}N_{6,7}$  super Coster-Kronig and  $N_{4,5}N_{6,7}O_{2,3}$  Coster-Kronig transitions overlap considerably

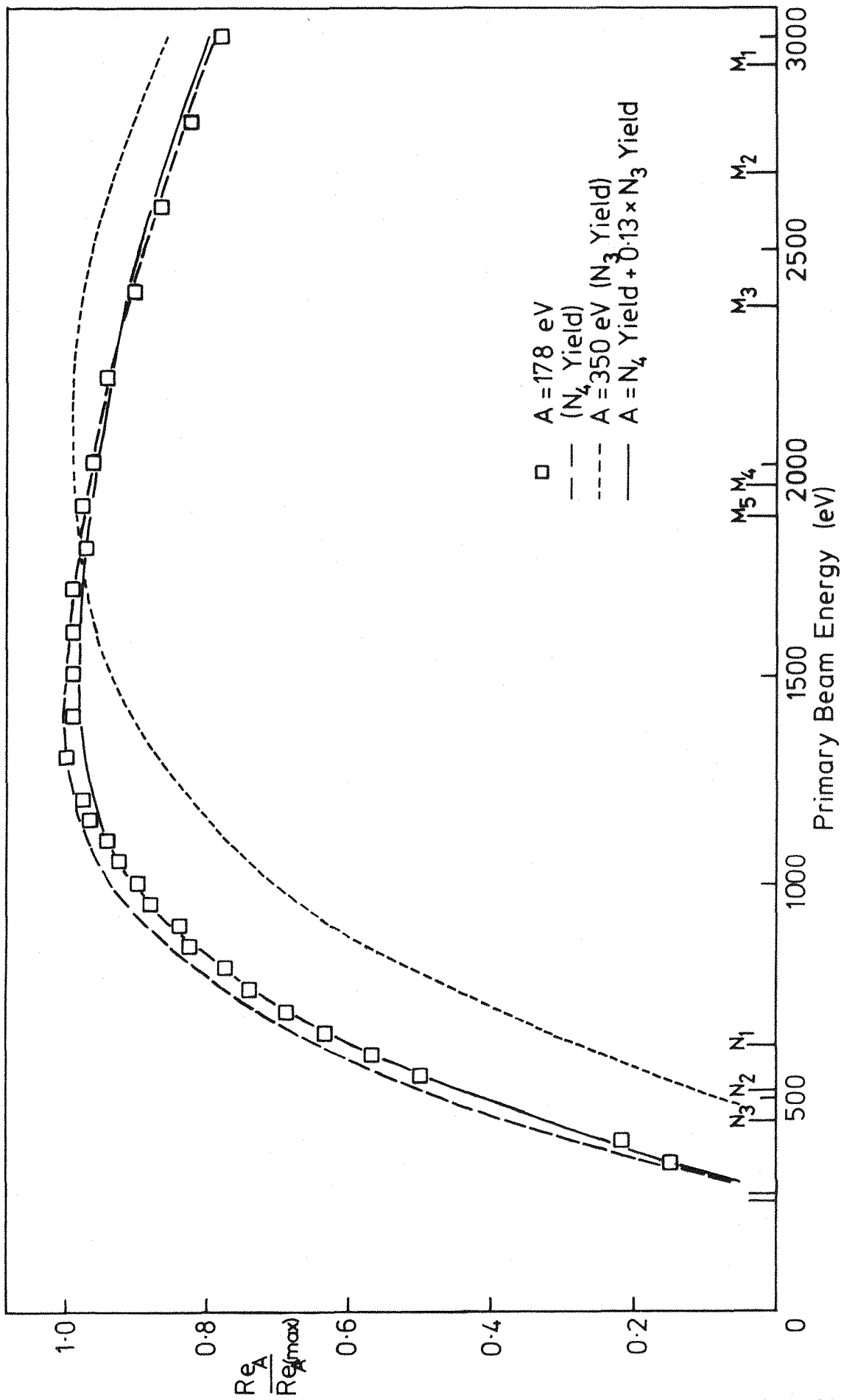


Figure 6.8 Best fit of  $N_4$  and  $N_3$  yield curves to the rhenium 178 eV peak's yield curve.

(figure 6.2). Larkins' line energies and the energies of the first five peaks in table 6.1 (the sixth peak is temperature dependent and will be discussed later) are shown in table 6.3 and figure 6.9. Matthew (1980) and Rawlings et al. (1980a) have noted that the low angular momentum terms tend to contribute least to the observed spectra. The experimental peaks in figure 6.9 do not line up well with either the  $N_{4,5}N_{6,7}N_{6,7}$ ,  $N_{4,5}N_{6,7}O_{2,3}$  or both series together! The  $N_{4,5}N_{6,7}O_{2,3}$  series lie in the right energy region but the energy gaps between the lines prevent a good match to the five experimental peaks. For the experimental energies to satisfactorily be  $N_{4,5}N_{6,7}N_{6,7}$  transitions the spectrum has to be shifted  $\sim 10$  eV. Larkins (1977) notes that he expects his energies to be generally within 2 eV of the experimental values with the maximum discrepancies near 5 eV. McGuire (1974) expects the  $N_{4,5}N_{6,7}N_{6,7}$  series to dominate the  $N_{4,5}N_{6,7}O_{2,3}$  transitions.

From table 6.1 the full width at half maximum for the experimental peaks range from 5.2 eV to 7.6 eV. These are lower than those predicted by McGuire who calculates that the widths should be almost 8 eV.

Finally, the possibility of an  $N_4N_5V$  Coster-Kronig transition can be considered. If there is no  $N_4 \rightarrow N_5$  rate, the  $N_5$  to  $N_4$  single hole ratio for  $N_5$  and  $N_{4,5}N_{6,7}X$  (where  $X=N_{6,7}$  or  $O_{2,3}$ ) processes are expected to be 3:2 for an excitation energy well above threshold. This is deduced from the multiplicity of the  $N_4$  and  $N_5$  levels. The  $N_4$  level is denoted  $4d_{3/2}$  and so has  $2S+1 = 2 \times 3/2 + 1 = 4$  different levels. Similarly the  $N_5$  level ( $4d_{5/2}$ ) has 6 levels. Assuming that all the levels have the same probability of ionisation under a high energy beam, one would expect the ratio of areas under the  $N_5$  peaks to the ratio of the areas under the  $N_4$  peaks to be 6:4 or 3:2. Adding up the areas of the  $N_5$  and  $N_4$  based peaks, taken as height  $\times$  f.w.h.m. for the curve fitting of  $E_p = 400$  eV spectra (where there is no  $N_3$  contribution), the ratio turns out to be  $\sim 2.4:1$  (3:1.25). Thus there is another decay route for  $N_4$  initial holes

Transition	Term	Energy w.r.t. Fermi level (eV)
$N_4 N_6 N_6$	$^1S_0$	159.1
	$^3P_2$	166.4
$N_4 N_6 N_7$	$^3P_1$	167.0
	$^3P_0$	167.4
	$^1I_6$	167.7
	$^1D_2$	168.9
$N_4 N_6 N_6$	$^1G_4$	170.0
$N_4 N_6 N_7$	$^3F_3$	171.7
$N_4 N_7 N_7$	$^3F_2$	171.8
$N_4 N_6 N_7$	$^3H_4$	172.0
	$^3H_5$	172.9
$N_4 N_7 N_7$	$^3F_4$	174.1
	$^3H_6$	175.1
$N_5 N_6 N_6$	$^1S_0$	145.6
	$^3P_2$	152.9
$N_5 N_6 N_7$	$^3P_1$	153.5
	$^3P_0$	153.9
	$^1I_6$	154.2
	$^1D_2$	155.4
$N_5 N_6 N_6$	$^1G_4$	156.5
$N_5 N_6 N_7$	$^3F_3$	158.2
$N_5 N_7 N_7$	$^3F_2$	158.3
$N_5 N_6 N_7$	$^3H_4$	158.5
	$^3H_5$	159.4
$N_5 N_7 N_7$	$^3F_4$	160.6
	$^3H_6$	161.6

Table 6.3a Theoretical super Coster-Kronig line energies for rhenium (Larkins, 1977).

Transition	Term	Energy w.r.t. Fermi level (eV).
$N_4 N_6 O_2$	$^1D_2$	174.3
	$^3G_3$	175.2
$N_4 N_7 O_2$	$^1G_4$	176.9
	$^3D_3$	177.2
$N_4 N_6 O_3$	$^3D_1$	185.0
	$^3G_4$	185.2
	$^3F_2$	185.9
	$^3F_3$	186.7
$N_4 N_7 O_3$	$^3D_2$	186.9
	$^3G_5$	188.3
	$^1F_3$	188.8
	$^3F_4$	188.8
$N_5 N_6 O_2$	$^1D_2$	160.8
	$^3G_3$	161.7
$N_5 N_7 O_2$	$^1G_4$	163.4
	$^3D_3$	163.7
$N_5 N_6 O_3$	$^3D_1$	171.5
	$^3G_4$	171.7
	$^3F_2$	172.4
	$^3F_3$	173.2
$N_5 N_7 O_3$	$^3D_2$	173.4
	$^3G_5$	174.8
	$^1F_3$	175.3
	$^3F_4$	175.3

Table 6.3b Theoretical Coster-Kronig line energies for rhenium (Larkins, 1977).

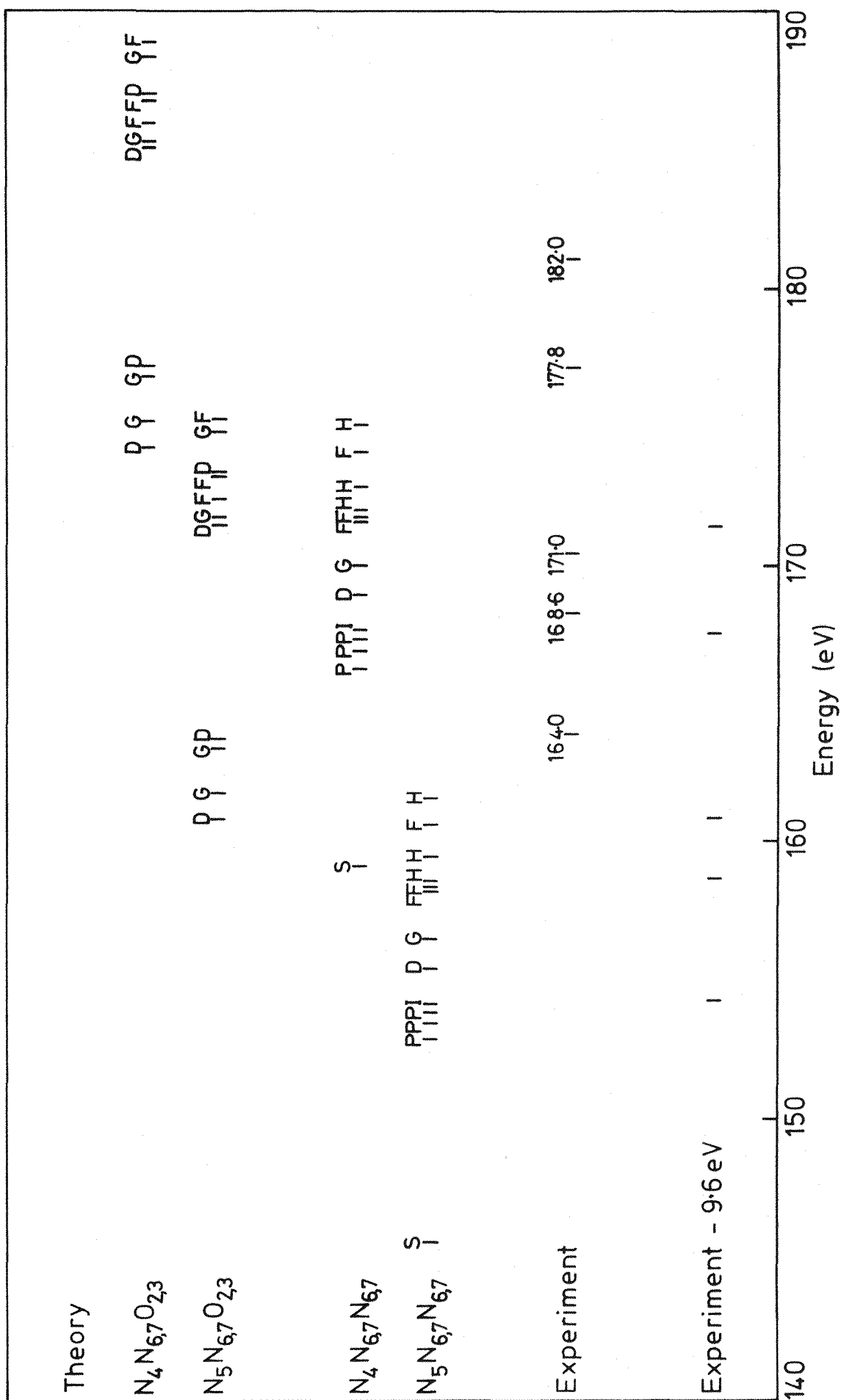


Figure 6.9 Comparison of Larkins' theoretical line energies and rhenium experimental line energies.

taking ~38% of the  $N_4$  initial holes. The only possibility is into  $N_5V$  final states. These are predicted to occur at ~6eV above the Fermi level using the semi-empirical formula in equation 2.4 (Chung and Jenkins, 1970). McGuire's rate calculations suggest that only 1.2% of  $N_4$  states decay via the  $N_5$  level compared to  $N_4$  decay via the  $N_{6,7}$  levels by Coster-Kronig decay. As mentioned before, the calculations refer to a free-atom and so may be different to the rate in this case where in  $N_4N_5V$  transitions a conduction band electron is involved. There may also be errors from the semi-empirical estimate of the Auger line energy used by McGuire (equation 2.4) as the calculated transition rates are strongly dependent on this energy. Rawlings et al. (1980a) also predicted the presence of the  $N_4N_5V$  emission in tungsten with the  $N_5$  to  $N_4$  single hole ratio for  $N_5$  and  $N_4N_{6,7}X$  processes as 2.4:1.

### 6.3 Conclusions

The rhenium secondary electron spectrum between 150 and 200eV is dominated by the decay of  $N_4$  and  $N_5$  single hole states via the  $N_{4,5}N_{6,7}O_{2,3}$  Coster-Kronig and/or  $N_{4,5}N_{6,7}N_{6,7}$  superCoster-Kronig processes. The rate calculations suggest that the  $N_{4,5}N_{6,7}N_{6,7}$  transitions dominate but the spectrum has to be shifted about 10eV for these to match up with the experimental results. The  $N_{4,5}N_{6,7}O_{2,3}$  transitions are in the correct region but the line energies do not agree well. If Larkins' (1977) line energies are correct then McGuire's (1974) rate calculations must be wrong, and vice versa.

The  $N_3N_4V$  and  $N_3N_5V$  emissions are both significant: the ratio of their intensities  $N_3N_4V:N_3N_5V$  being 1:3 compared to the ratio 1:5 predicted by the rate calculations.

The  $N_4N_5V$  transition appears to occur at a sufficient rate to change the expected rates predicted by McGuire for the  $N_4N_{6,7}X$  and  $N_5N_{6,7}X$  processes (where  $X = N_{6,7}$  or  $O_{2,3}$ ).

## CHAPTER 7

### MINOR PEAKS IN THE RHENIUM SECONDARY ELECTRON SPECTRUM

This chapter is concerned with the origins of several low intensity peaks in the low energy rhenium secondary electron spectrum. Specifically those occurring at 216, 229, 241, 187.8, 350 and 361eV.

#### 7.1 The Peaks at 216eV and 229eV

##### 7.1.1 Results

These peaks are on the high energy side of the intense Auger peaks (150-200eV) and can be seen in figures 6.1 and 6.2 in first derivative and  $N(E)$  form for primary beam energies of 1400eV and 400eV respectively. They are also shown in figure 3.6 in second derivative mode for a primary beam of 2500eV. Their yield curves (figure 7.1) were plotted by measuring their peak to peak heights from the first derivative spectra as a function of primary beam energy and at constant beam current. At low primary beam energies, where the derivative spectrum lies on a significant positive slope, the slope was subtracted before the peak to peak height was measured. Measurements were only taken at primary beam energies which did not produce losses in the region of the peaks. The yield curve for the 241eV peak was measured in the same way and will be discussed later.

The 216 and 229eV peaks were not noticeably temperature dependent.

##### 7.1.2 Discussion

Both the yield curves in figure 7.1 shows threshold behaviour toward the  $N_4$  and  $N_5$  levels indicating that there is an  $N_4$  and/or  $N_5$  initial hole contribution to both the 216eV and 229eV peaks. The difference between the positions

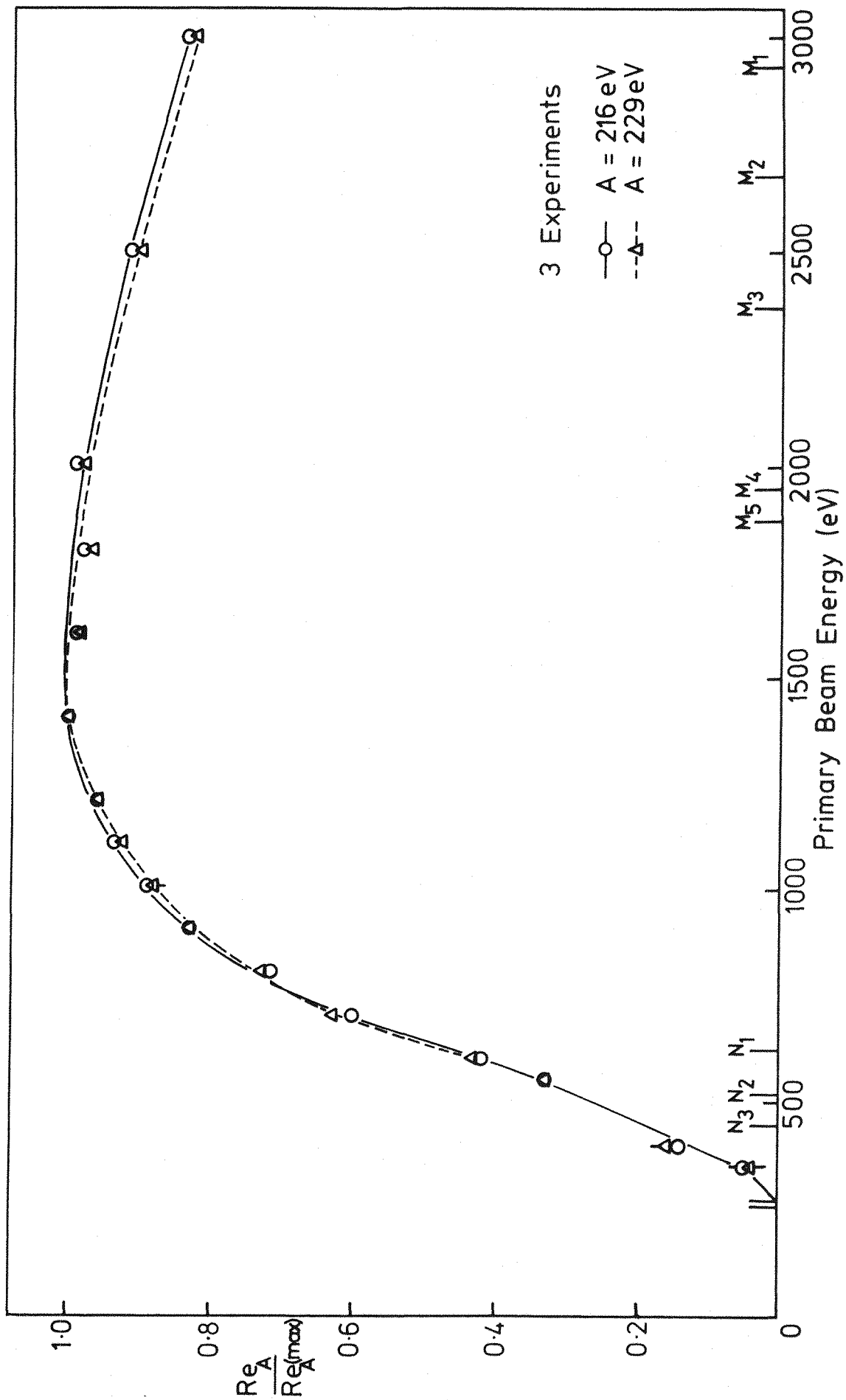


Figure 7.1 Yield curves for rhenium peaks at 216 eV and 229 eV.

of these peaks is  $228.9 - 215.6 = 13.3\text{eV}$  which, when compared with the difference in the binding energies (from Sevier (1972))  $E(N_4) - E(N_5) = 13.5\text{eV}$ , suggests that one peak decays from an  $N_4$  initial hole and the other from an  $N_5$  initial hole to the same final state. The predicted positions of the  $N_4 N_{6,7}^0$  and  $N_5 N_{6,7}^0$  emissions, calculated from a semi-empirical formula (equation 2.4), are shown in figure 6.2 and table 6.2. These are the only  $N_{4,5}$  based transitions in this region and therefore the  $216\text{eV}$  peak is assumed to have an  $N_5 N_{6,7}^0$  contribution and the  $229\text{eV}$  peak an  $N_4 N_{6,7}^0$  contribution.

The curvature on the yield curves (figure 7.1) as they near threshold indicate that the yields are not pure  $N_4$  and  $N_5$  but have an additional yield from a transition based on a deeper level. The most likely contribution will be decay from an  $N_3$  initial state (McGuire, 1974). In figure 7.2 the experimental results for the  $216\text{eV}$  peak, the  $N_5$  yield (from the  $171\text{eV}$  peak) and the  $N_3$  yield (from the  $350\text{eV}$  peak) are plotted. The use of the  $171\text{eV}$  peak's yield as  $N_5$  and  $350\text{eV}$  peak's yield as  $N_3$  has already been discussed in chapter 6. The yield curve for the  $216\text{eV}$  peak is obviously not pure  $N_5$  or pure  $N_3$ . A best fit of the  $N_5$  and  $N_3$  yields to the data produces the curve in figure 7.2 with the  $216\text{eV}$  peak as  $N_5 + N_3$  based. If a similar analysis is applied to the  $229\text{eV}$  peak, as in figure 7.3, using an  $N_4$  yield (the  $N_5$  yield shifted  $13.5\text{eV}$ ) and the  $N_3$  yield, the best fit is  $N_4 + 0.7N_3$ . About half of the intensity of both peaks is thus by decay from an initial hole in the  $N_3$  level.

There are, however, no  $N_3$  initial hole Auger transitions in this region (figure 6.1 and table 6.2)! Rawlings et al. (1979) came across the same problem with the  $210\text{eV}$  peak in the tungsten secondary electron spectrum. They identified the  $N_3$  contribution to the peak as coming from the second step in an Auger cascade. The  $210\text{eV}$  peak in tungsten and the  $216$  and  $229\text{eV}$  peaks in rhenium are in similar positions relative to the high intensity peaks in the spectra. The two materials, being adjacent in the

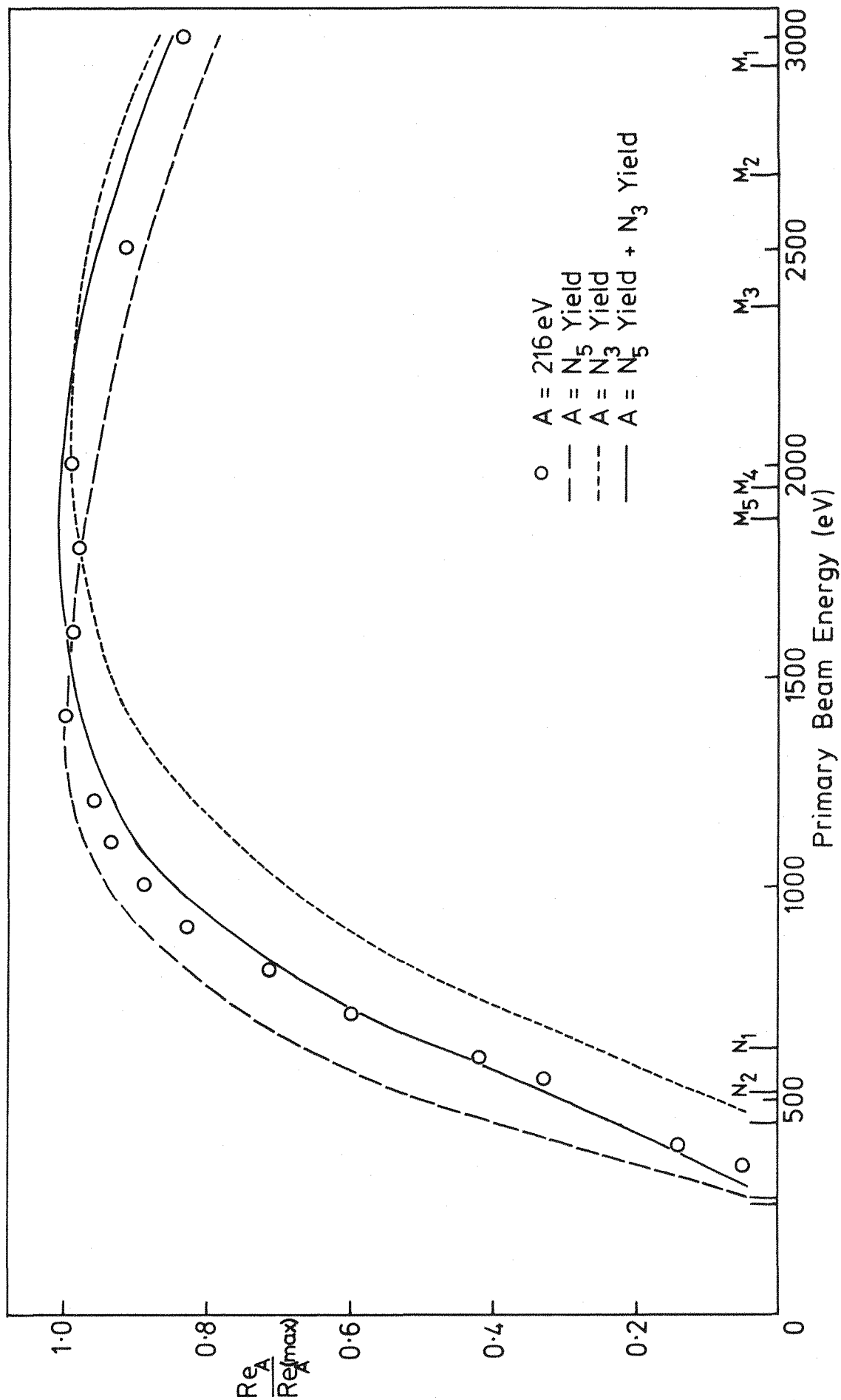


Figure 7.2 Best fit of  $N_5$  and  $N_3$  yield curves to the rhenium 216 eV peak's yield.

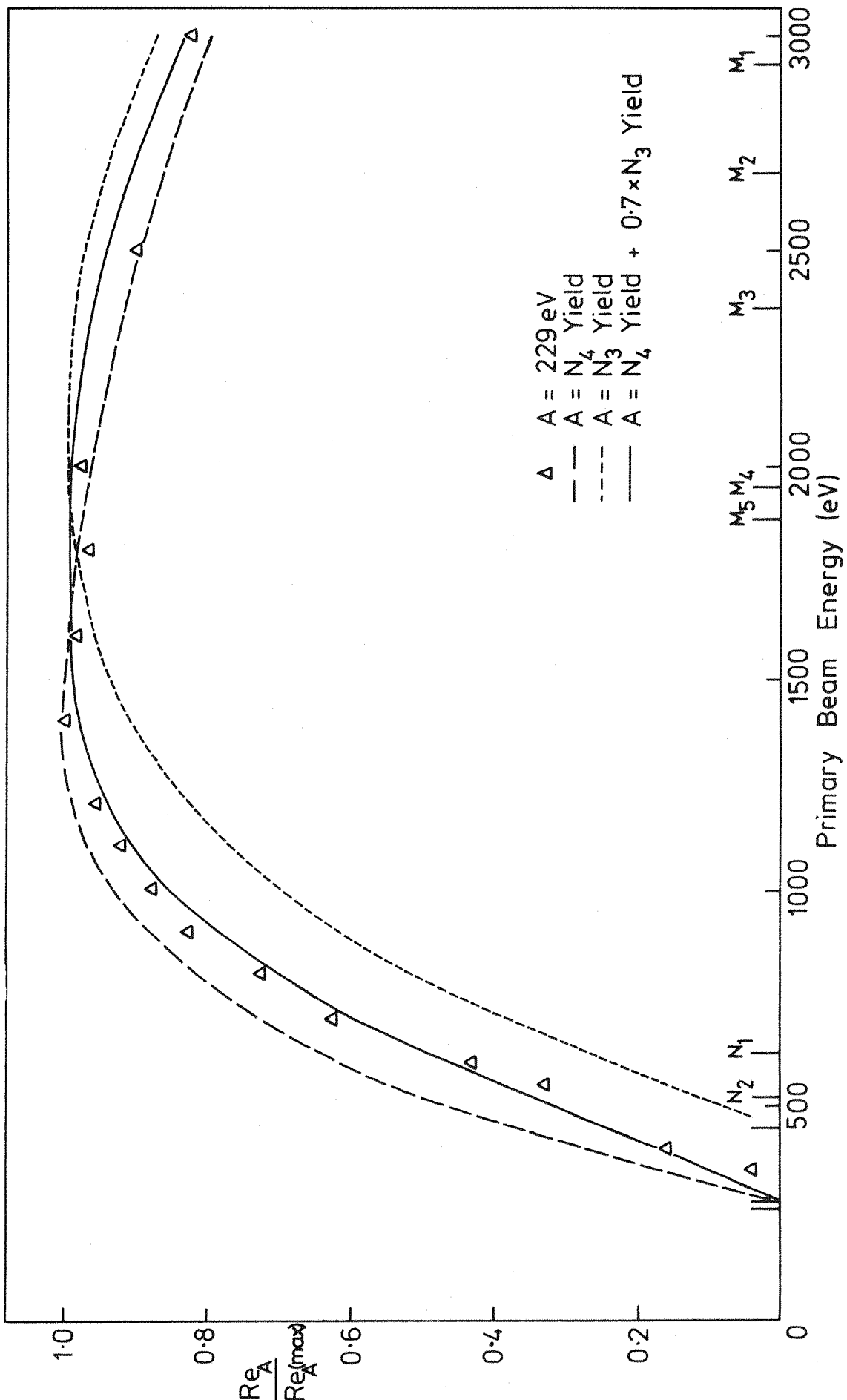


Figure 7.3 Best fit of  $N_4$  and  $N_3$  yield curves to the rhenium 229 eV peak's yield.

periodic table, are expected to produce peaks with similar origins in the secondary electron spectra. Rawlings' analysis for the tungsten 210eV peak was therefore applied to the rhenium 216 and 229eV peaks.

The cascade begins with an initial hole decaying to a two hole final state as in a normal Auger process. This two hole final state then becomes the initial state of a second decay to a three hole final state. The problem is to look for decay from a two hole to three hole state which produces intensity in the 216 and 229eV peaks, and where the first decay from a one hole to two hole state has the initial hole in the  $N_3$  level as the yield will be controlled by the first process. Of course there has to be sufficient two hole states produced, and therefore a significant intensity of Auger electrons ejected from the first decay, to give rise to the observed intensity of secondary electrons from the second decay.

In chapter 6 two  $N_3$  initial hole transitions were found to produce intensity in the 164eV and 178eV peaks. These were the  $N_3N_4V$  and  $N_3N_5V$  Auger processes and are candidates for the first decay in a cascade. The  $N_3N_4V$  transition leaves an  $N_4V$  two hole final state and the  $N_3N_5V$  transition leaves an  $N_5V$  final state. Dealing with the  $N_4V$  state first: the energy of the  $N_4V$  state can be calculated from the relation

$$E(N_3N_4V) = E(N_3) - E(N_4V) = 164.0\text{eV}$$

(from the experimental position of the peak).

If  $E(N_3) = 444.4\text{eV}$  (Sevier, 1972) then  $E(N_4V) = 280.4\text{eV}$ . This number can be compared with that from a semi-empirical formula (equation 2.4)

$$E_{75}(N_4V) = \frac{1}{2}(E_{75}(N_4) + E_{76}(N_4) + E_{75}(O_{4,5}) + E_{76}(O_{4,5})) = 283.3\text{eV}.$$

These are in reasonable agreement bearing in mind that valence levels are involved. Rawlings et al. (1979) extended

the semi-empirical formula to cope with the second decay process as follows

$$E_{75}(N_4^0 4,5 \rightarrow N_6^0 4,5 0_{4,5}) = 280.4 - \frac{1}{3}(E_{75}(N_6) + E_{76}(N_6) + E_{77}(N_6) + 2E_{75}(0_{4,5}) + 2E_{76}(0_{4,5}) + 2E_{77}(0_{4,5})) = 220.2 \text{ eV.}$$

If this calculation is repeated for all possible final states, there are only four final three hole states emitting an electron in the correct energy region. These are

$$E_{75}(N_4^0 4,5 \rightarrow N_6^0 4,5 0_{4,5}) = 220.2 \text{ eV}$$

$$E_{75}(N_4^0 4,5 \rightarrow N_7^0 4,5 0_{4,5}) = 223.0 \text{ eV}$$

$$E_{75}(N_4^0 4,5 \rightarrow 0_2^0 4,5 0_{4,5}) = 220.0 \text{ eV}$$

$$E_{75}(N_4^0 4,5 \rightarrow 0_3^0 4,5 0_{4,5}) = 232.0 \text{ eV}$$

Repeating this calculation for the  $N_5^V$  two hole state:

$$E(N_3^V N_5^V) = E(N_3) - E(N_5^V) = 177.9 \text{ eV}$$

(from the experimental energy).

With  $E(N_3) = 444.4 \text{ eV}$ ;  $E(N_5^V) = 266.5 \text{ eV}$ . The semi-empirical formula gives  $E(N_5^V) = 268.3 \text{ eV}$  which compares well with  $266.5 \text{ eV}$ . Finally Rawlings' extended formula gives

$$E_{75}(N_5^0 4,5 \rightarrow N_6^0 4,5 0_{4,5}) = 206.3 \text{ eV}$$

$$E_{75}(N_5^0 4,5 \rightarrow N_7^0 4,5 0_{4,5}) = 209.1 \text{ eV}$$

$$E_{75}(N_5^0 4,5 \rightarrow 0_2^0 4,5 0_{4,5}) = 206.1 \text{ eV}$$

$$E_{75}(N_5^0 4,5 \rightarrow 0_3^0 4,5 0_{4,5}) = 218.1 \text{ eV}$$

These results suggest that the  $N_4^V$  state decays to an  $XVV$  (where  $X = N_{6,7}$  and/or  $0_{2,3}$ ) state to produce intensity in the  $229 \text{ eV}$  peak with  $N_3$  threshold yield behaviour, and the  $N_5^V$  state decays similarly to produce intensity in the  $216 \text{ eV}$  peak.

A rough calculation of the areas ( $\propto$ intensity) of these  $N_3$  based peaks gives the relative intensities of the  $N_3$

based emissions at 164eV and 229eV as 1.4:1, and the relative intensities of the  $N_3$  based emissions at 178eV and 216eV as 1.4:1. So there are enough  $N_4V$  and  $N_5V$  states to account for the intensity at 216eV and 229eV. Also, roughly the same proportion of initial two hole states decay to the three hole final states in both peaks.

Both yield curve fits in figures 7.2 and 7.3 have regions where several points of the raw data are to one side of the best fit. This may indicate that there is another small contribution to the yield.  $N_2$  and  $N_1$  yield curves (estimated by shifting and expanding the  $N_3$  curve) were added but did not produce a better fit than shown. The only possibility seems to be a curve shaped similar to that in figure 7.4 for the 241eV peak but with a deeper level threshold. A fit with a peak of this shape was not attempted as it was difficult to predict the shape for a different threshold level. Also the 241eV peak is temperature dependent and the 216 and 229eV peaks were not found to have any noticeable temperature dependence.

## 7.2 The 241eV Peak

### 7.2.1 Results

The 241eV peak can be seen in figure 6.2. With a primary beam energy of 400eV the 216, 229 and 241eV peaks have about the same intensity. As the primary beam energy is increased, the intensity of the 241eV peak decreases with respect to the others until at 1400eV beam energy it is very small (figure 6.1). This yield behaviour is shown in figure 7.4. The yield curve shows threshold behaviour towards the  $N_4$  and  $N_5$  levels but the shape is very different to typical Auger emission yield curves. This peak was found to be temperature dependent and the variation of yield with temperature is shown in figure 7.5. The peak to peak height of the 241eV peak from a first derivative spectrum was normalised with the peak to peak height of the 216eV peak as



### 3 Experiments

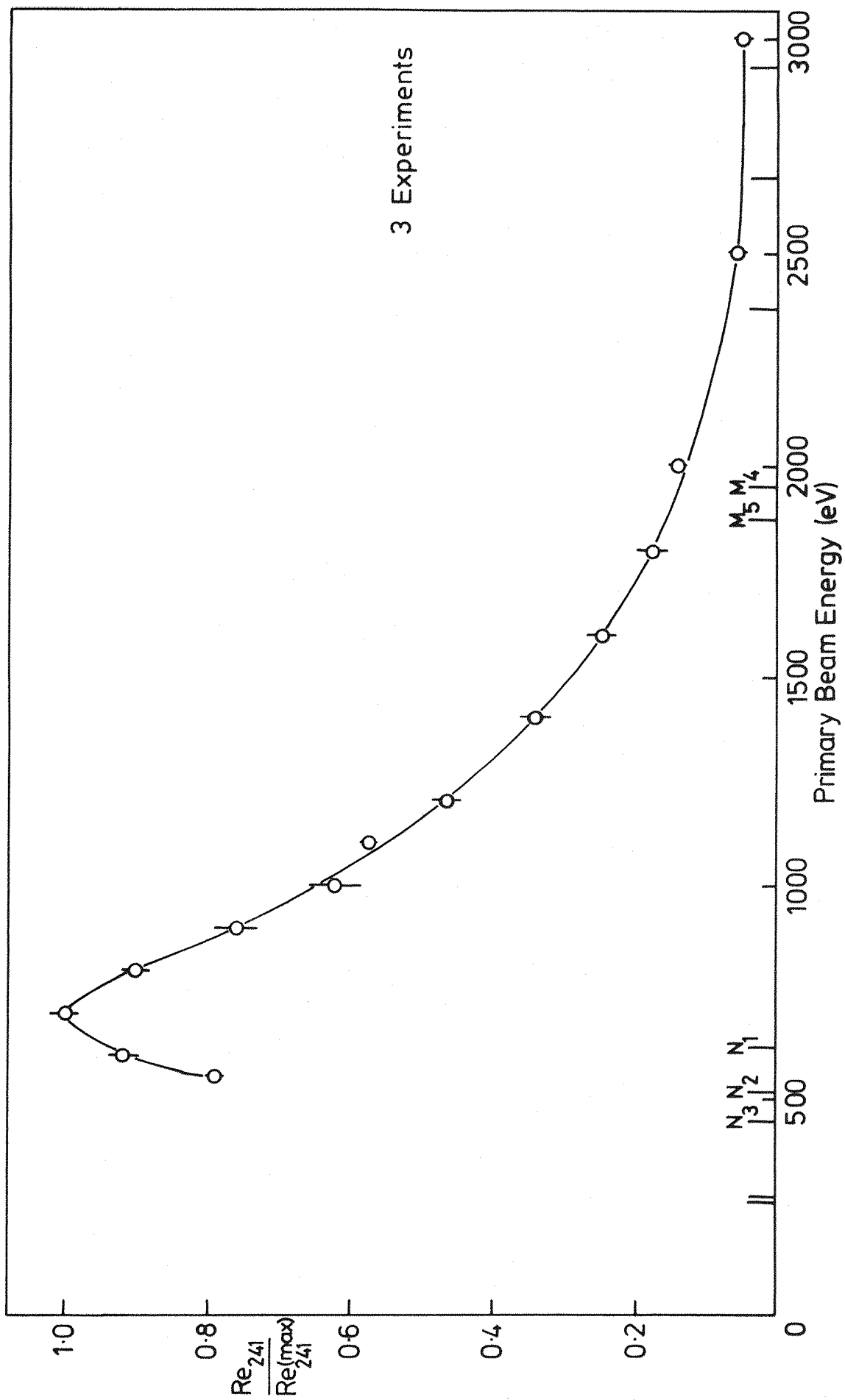


Figure 7.4 Yield curve for rhenium 241 eV peak.

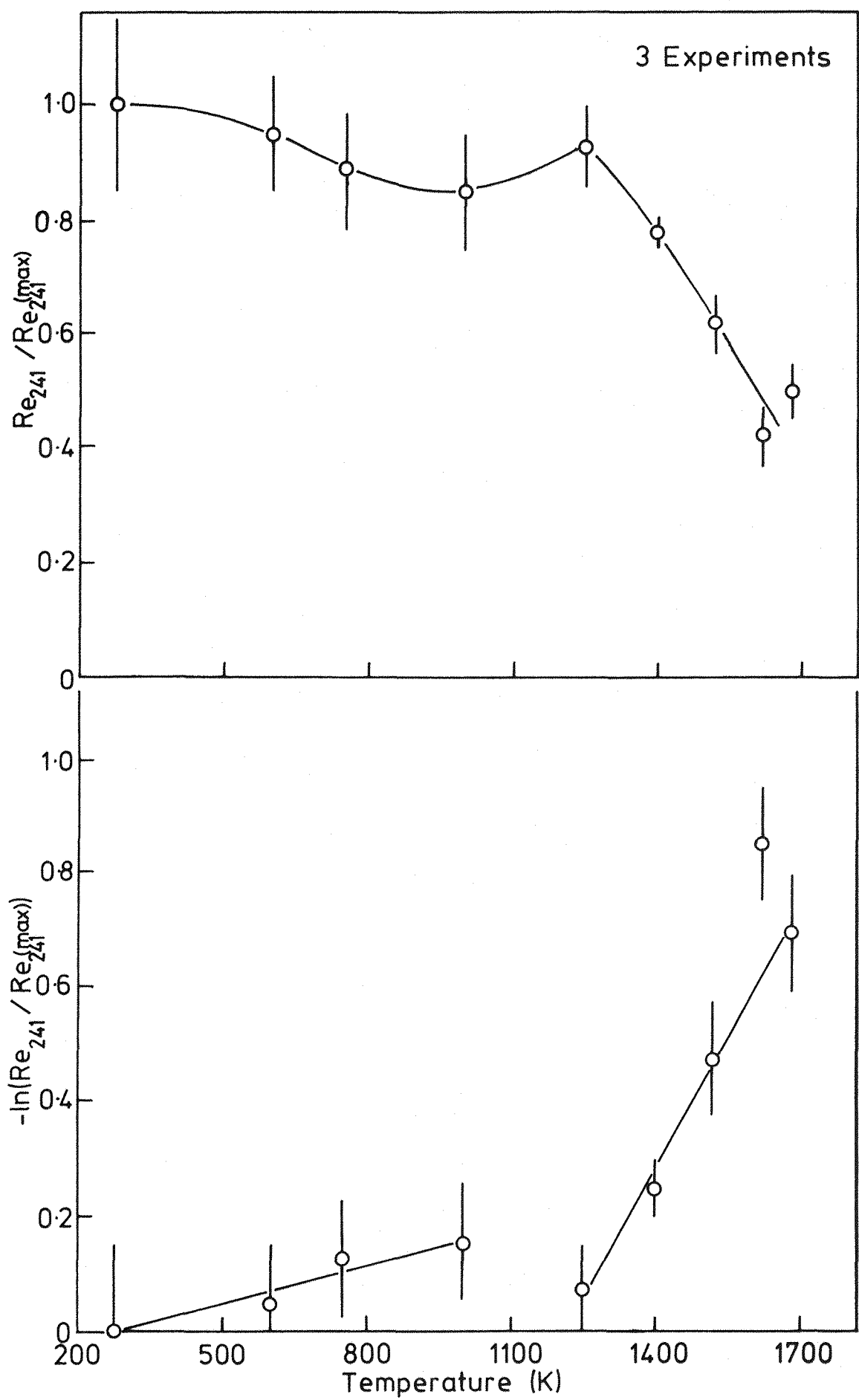


Figure 7.5 Temperature dependence of rhenium 241 eV peak.

there was some variation in the intensities of all peaks, presumed to be due to movement of the sample with respect to the analyser, at high temperatures.

### 7.2.2 Discussion

This peak has a very similar yield curve to that of the tungsten 229eV peak (Rawlings et al., 1980b) discussed in chapter 5. The temperature dependence in figure 7.5 is also similar to that in figures 5.1 and 5.2, though the reliability of drawing straight lines through the data in the logarithmic scale graph is dubious. Diffraction, occurring during the escape of secondary electrons, is often assumed to be responsible for temperature dependent peaks. The diffraction explanation is supported if the peak to peak intensities decrease exponentially with temperature as in a Debye-Waller effect (Thapliyal and Unertl, 1979). A Kikuchi mechanism (chapter 5) has been suggested to account for the 229eV tungsten temperature dependent peak based on the data up to 1250K. The equivalent data for the rhenium peak is up to 1000K. The gradient of a straight line through this data is  $-4300 \pm 1000 \text{ } \text{K}^{-1}$ . The data from 1200K to 1700K follows a separate straight line of gradient  $-480 \pm 50 \text{ } \text{K}^{-1}$ . A similar analysis to that for tungsten could not be applied to the rhenium surface as the calculations require the Miller indices of the surface producing the diffraction, and these were not determined. The break in the logarithmic graph may be due to reversible reordering in the surface.

## 7.3 The 187.8eV Peak

### 7.3.1 Results

This peak is the sixth peak in the curve fitting exercise of chapter 6. It is best seen in the second derivative spectra of figure 6.3. The three peak curve fit in figure 4.2 proves that the 187.8eV peak does exist even

though it has low intensity compared with the major peaks next to it. Its yield curve could not be measured directly as its intensity was overshadowed by the large negative wing of the 177.8eV peak. It was impractical to do curve fits on a large number of points in order to produce a yield curve for the peak. However, the ratio of yields at 400 and 1400eV primary beam energies was found to be approximately twice the same ratios for the major peaks (table 6.1) from the curve fitting exercise. The intensity of this peak decreased, with respect to the intensity of the major transitions, with increasing temperature.

Finally, as the crystal was moved slightly relative to the analyser, the 187.8eV peak was seen to become more intense. At one position it was as large as the major peaks.

### 7.3.2 Discussion

If the yield curve from the 241eV temperature dependent peak (figure 7.4) is compared with those from Auger peaks (figure 6.5) it is obvious that the ratio of yields at 400 and 1400eV primary beam energies will be highest for the temperature dependent feature. This suggests that the 187.8eV peak has similar yield behaviour to the 241eV peak. This evidence, plus the facts that both peaks are temperature dependent and the intensity of the 187.8eV peak changes with movement, suggest that the 187.8eV peak originates as a result of the diffraction of secondary electrons emerging from the sample.

## 7.4 The 350eV and 361eV Peaks.

### 7.4.1 Results

These peaks can be seen in figures 3.6 and 3.7. Their yield curves were plotted as described in section 6.1. The 350eV yield curve is shown in figure 6.6 and was deduced to be due to  $N_3N_{6,7}X$  ( $X=N_{6,7}$  and  $O_{2,3}$ ) Auger processes to fit

in with the analysis of the major rhenium peaks in chapter 6. The experimental data for the 361eV peak and the  $N_3$  yield curve (from the 350eV peak) are plotted in figure 7.6.

#### 7.4.2 Discussion

The data for the 361eV peak falls below the  $N_3$  yield curve up to a primary beam energy of 1500eV indicating that there is also a contribution from an initial hole in a deeper level. This must be either an  $N_2$  or  $N_1$  level. There are no  $N_2$  initial hole Auger transitions within 10eV; the nearest being the  $N_2O_1O_1$  emission at 351.4eV (using equation 2.4). The only  $N_1$  based transition in the region is the  $N_1N_5O_{4,5}$  at 356.8eV (again using equation 2.4). If this transition produces intensity in the 361eV peak, the yield curve should be the sum of a fraction of the  $N_3$  yield curve plus a fraction of an  $N_1$  yield curve. In chapter 6 the  $N_3$  yield curve was found to be the same as the  $N_5$  yield curve shifted to the  $N_3$  threshold level and expanded 40%. Assuming that all the yield curves have the same shape, if the  $N_3$  yield curve is shifted to have  $N_1$  threshold behaviour and expanded 35% it should be a good approximation to an  $N_1$  yield curve. 35% was chosen because the difference between the  $N_1$  and  $N_3$  binding energies (180.6eV) is less than that between the  $N_3$  and  $N_5$  binding energies (184.2eV), and the  $N_5$  yield curve had to be expanded by 40% to coincide with the  $N_3$  curve. The  $N_1$  curve is dotted in figure 7.6. The best fit of the  $N_3$  and  $N_1$  yield curves to the experimental yield data gave the 361eV peak as  $N_3+0.26N_1$  based.

#### 7.5 Conclusion

The 216eV peak is composed of about equal intensities of an  $N_5N_{6,7}V$  emission and emission from the second step in the Auger cascade  $N_3 \rightarrow N_5V \rightarrow XVV$  (where  $X=N_{6,7}$  and  $O_{2,3}$ ). Similarly the 229eV peak has intensity from the  $N_4N_{6,7}V$  Auger transition and the cascade  $N_3 \rightarrow N_4V \rightarrow XVV$ . There may be

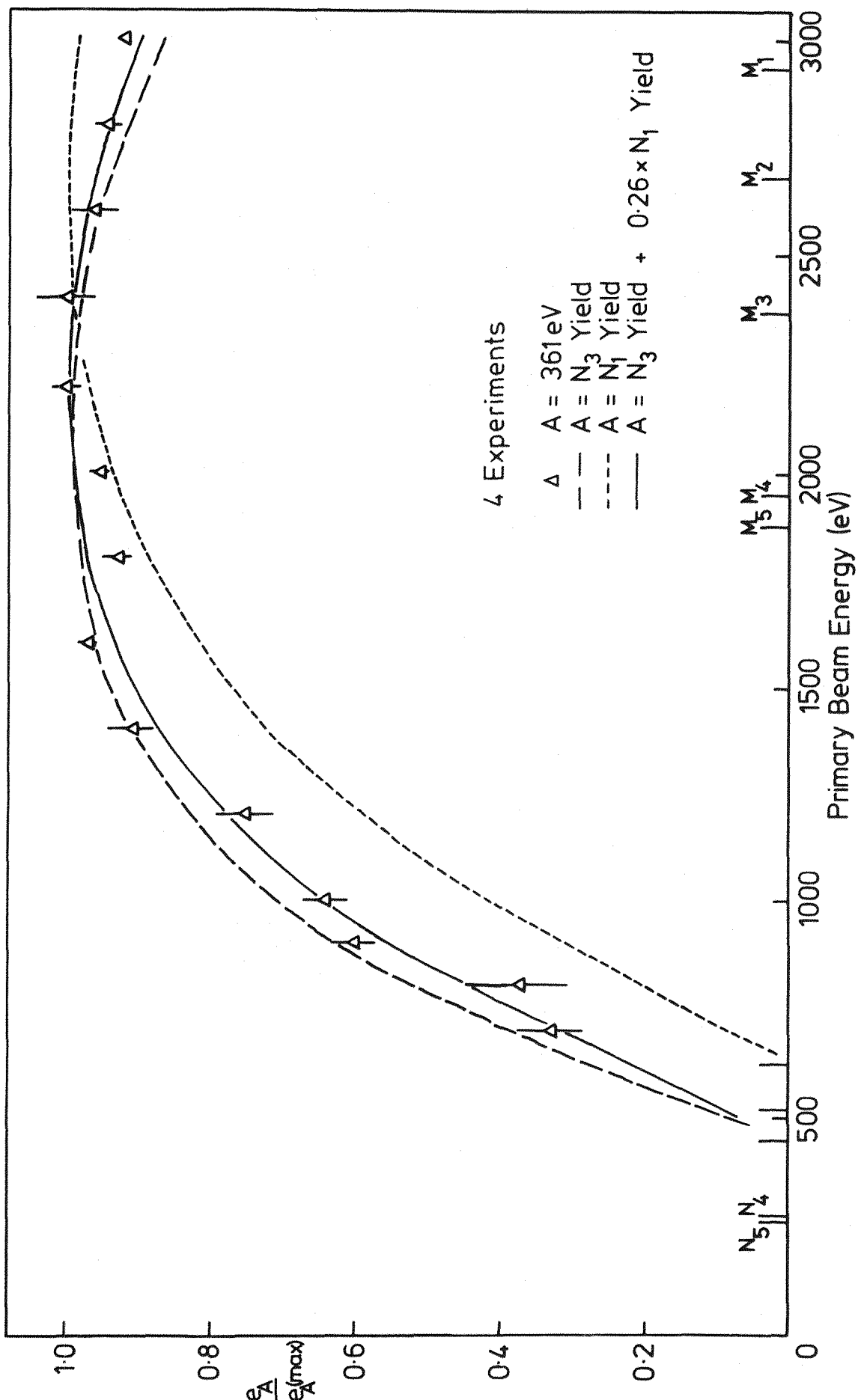


Figure 7.6 Best fit of  $N_3$  and  $N_1$  yield curves to the rhenium 361 eV peak's yield.

another small contribution in both peaks to account for the systematic differences between the experimental data and best fits in figures 7.2 and 7.3. The temperature dependent peaks at 241eV and 187.8eV are a result of the diffraction of secondary electrons emerging from the sample. The 350eV peak is due to  $N_3N_{6,7}^X$  transitions, and the 361eV peak has about 80% of its intensity from the  $N_3N_{6,7}^X$  emissions and 20% from  $N_1N_5O_{4,5}$  emissions.

## CHAPTER 8

### PRELIMINARY RESULTS FROM TANTALUM AND GOLD

This chapter presents a preliminary investigation into the origins of peaks in the low energy secondary electron spectra of tantalum and gold. Both samples used in the study were polycrystalline foils.

#### 8.1 Tantalum

The tantalum surface used was part of the sample support and could not be heated sufficiently to clean it because of its large cross sectional area (see chapter 3). There was thus a significant amount of sulphur and oxygen present on this surface during the experiments.

##### 8.1.1 Results

The low energy secondary electron spectrum induced by a primary beam of 2500eV is shown in figure 8.1 in first derivative form and figure 8.2 in second derivative form. These spectra show the tantalum surface at its cleanest. The carbon Auger signal around 270eV is comparable with the noise but there is a very large sulphur peak at 149eV from the  $L_{2,3}M_{2,3}M_{2,3}$  transitions, and significant oxygen KLL emissions from 490 to 520eV.

The energy axes were calibrated as for tungsten and rhenium spectra with the elastic peak (as described in chapter 3). The main effects of the contaminants on the surface will be to shift (Sickafus, 1974) and attenuate the substrate peaks. The core-core-core Auger emissions are expected to be affected similarly but transitions involving the valance band, which is involved in bonding, may be more seriously altered. To determine the clean surface positions of the substrate peaks, in order to compare experimental and theoretical peak positions, the contaminated spectrum in

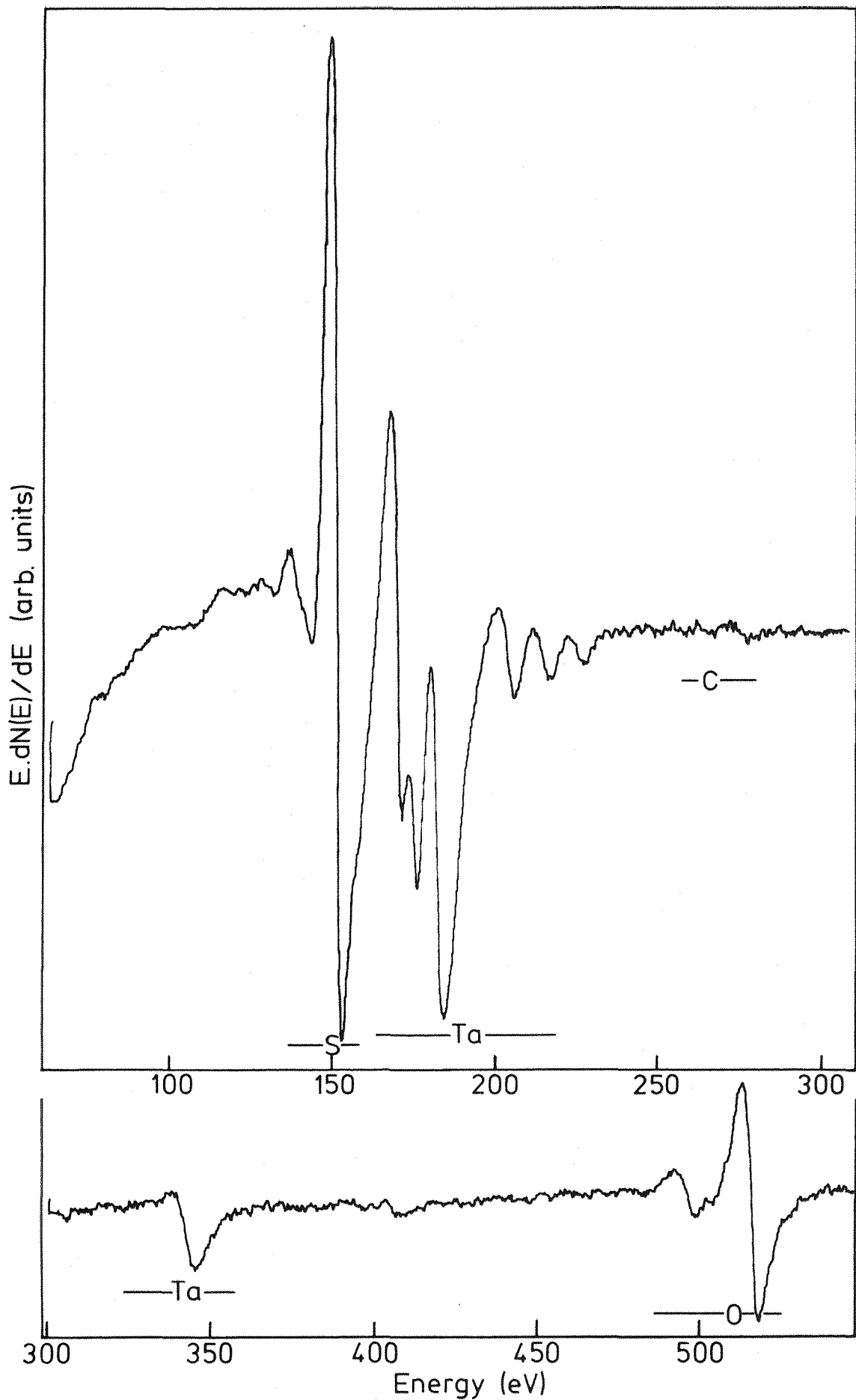


Figure 8.1 First derivative tantalum secondary electron spectrum induced by 2500 eV primary electrons ( $I_b = 3 \mu A$ ,  $v_m = 3.2 V_{ptp}$ ,  $\tau = 0.3 s$ , scan  $1 eV.s^{-1}$ ).

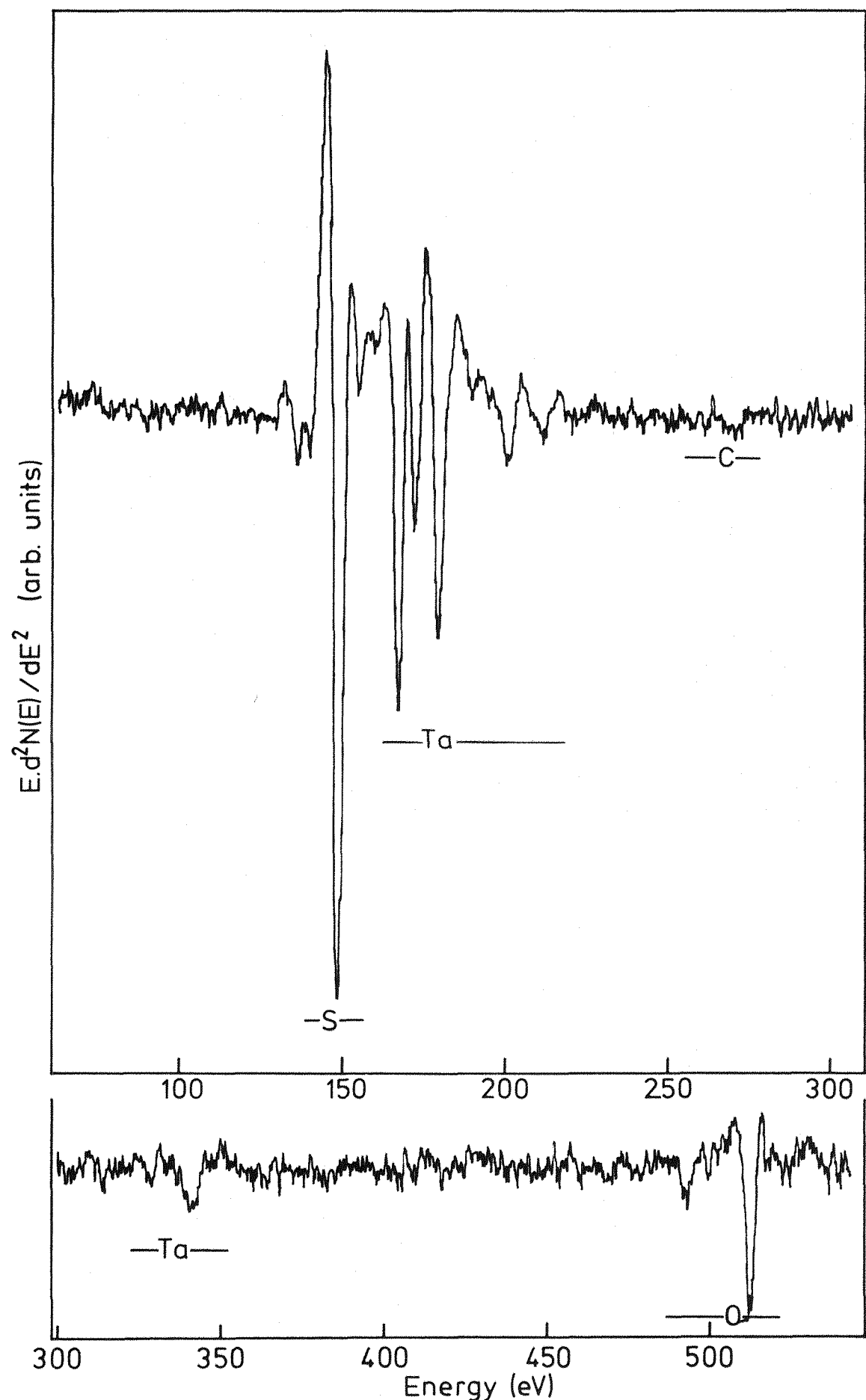


Figure 8.2 Second derivative tantalum secondary electron spectrum induced by 2500 eV primary electrons ( $I_b = 5 \mu A$ ,  $v_m = 2.8 V_{ptp}$ ,  $\tau = 0.3 s$ , scan  $1 eV \cdot s^{-1}$ ).

figure 8.1 was compared to the 'clean' surface spectrum from the Handbook of Auger Electron Spectroscopy (1976) (there are (unfortunately) small carbon and oxygen signals on the spectrum in the handbook). The spectra in the handbook are referenced to the vacuum level and energies are only quoted to the nearest eV. The negative dip of the peak at 182.0eV in figure 8.1 is marked as 179eV in the handbook. Bearing in mind that the handbook's energy scale for the rhenium spectrum was ~5eV below that of the present work (due to the difference in vacuum and Fermi level references) the tantalum peaks must be shifted ~2eV higher for their experimental energies to be equivalent. With a 2eV correction the energy positions of the peaks are expected to have an error of  $\pm 1$ eV. The energies marked in the remainder of the diagrams include this correction.

The tantalum transitions between 160 and 230eV are shown in figure 8.3 for primary beam energies of 1100eV and 350eV. A beam of 1100eV produces the maximum yield of the major peaks between 160 and 190eV, whilst the 350eV beam is not sufficient to ionise the  $N_3$  level at 404.5eV (Sevier, 1972). The theoretically predicted Coster-Kronig and super Coster-Kronig line energies (Larkins, 1977 and equation 2.4 for transitions involving the conduction band) are also indicated in figure 8.3 and table 8.1. The major peaks are shown expanded in figure 8.4 again for primary beam energies of 1100 and 350eV. Both spectra are very similar except for the peak at 192eV which is much larger with respect to the major peaks at 350eV than at 1100eV primary beam energy.

Yield curves were not plotted for these peaks but the ratio of the yields with 350 and 1100eV beam energies was taken for the three peaks as shown in figure 8.4. The average of 32 experiments gave

$$R_{169} = Ta_{169(350)}/Ta_{169(1100)} = 0.279 \pm 0.002$$

$$R_{174} = Ta_{174(350)}/Ta_{174(1100)} = 0.259 \pm 0.004$$

$$R_{182} = Ta_{182(350)}/Ta_{182(1100)} = 0.250 \pm 0.002.$$

Note that these are in the order  $R_{169} > R_{174} > R_{182}$ .

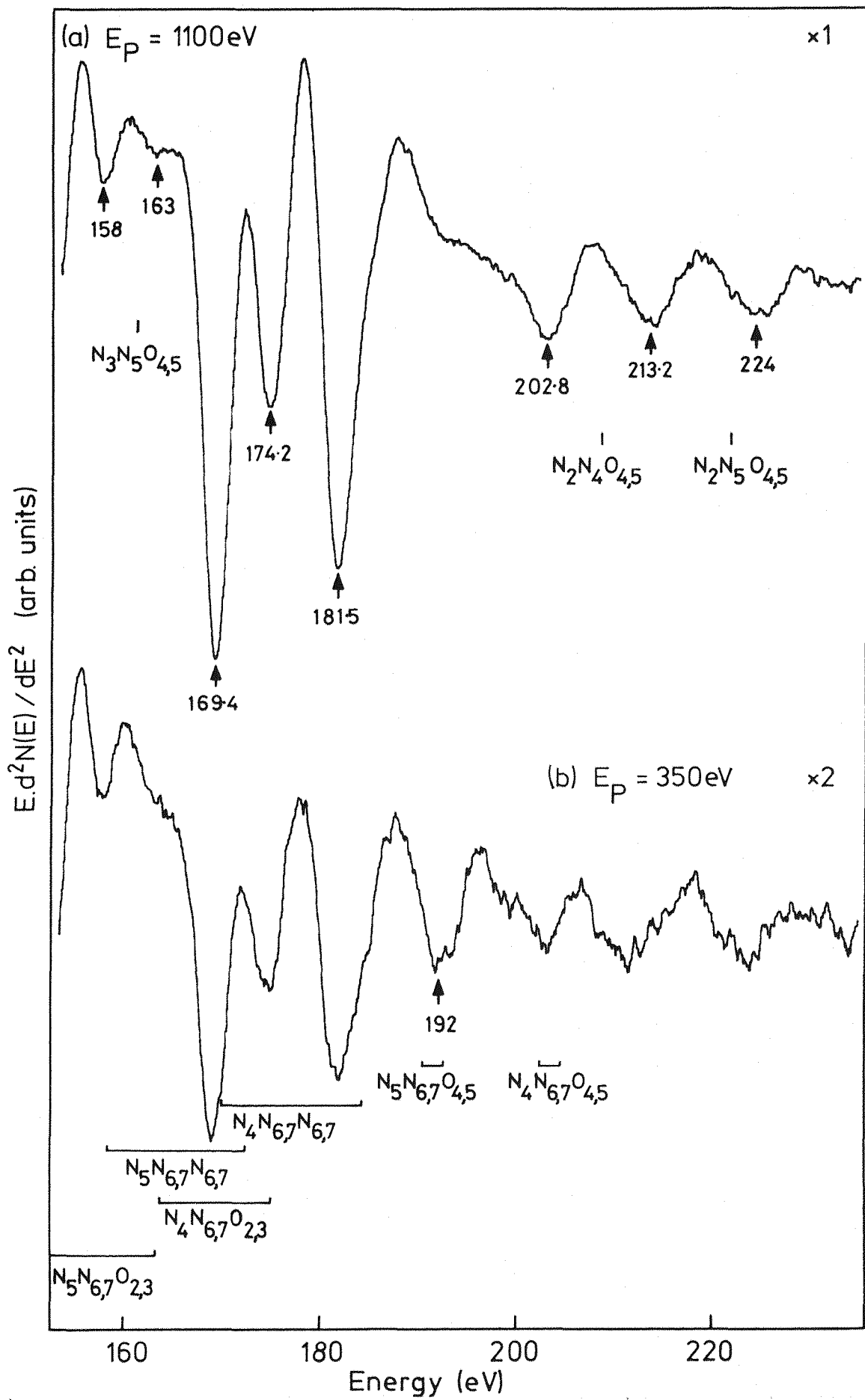


Figure 8.3 Second derivative tantalum secondary electron spectrum ( $I_b = 5\mu A$ ,  $v_m = 3.8 V_{ptp}$ ,  $\tau = 0.3 s$ , scan  $1 \text{ eV.s}^{-1}$ ).

Transition	Energy range w.r.t. Fermi level (eV). (error $\pm 5$ eV)
$N_1 N_3 N_{6,7}$	118.8 - 126.3
$N_1 N_3 O_{2,3}$	110.5 - 120.0
$N_1 N_4 O_1$	244.2 - 244.6
$N_2 N_4 N_{6,7}$	178.3 - 195.7
$N_2 N_4 O_1$	143.5 - 143.9
$N_2 N_4 O_{2,3}$	172.8 - 185.3
$N_2 N_5 N_{6,7}$	192.7 - 206.2
$N_2 N_5 O_1$	155.3 - 155.9
$N_2 N_5 O_{2,3}$	181.4 - 194.2
$N_3 N_4 N_{6,7}$	118.0 - 135.4
$N_3 N_4 O_{2,3}$	112.5 - 125.0
$N_3 N_5 N_{6,7}$	132.4 - 147.3
$N_3 N_5 O_{2,3}$	121.1 - 132.2
$N_4 N_{6,7} N_{6,7}$	170.2 - 184.4
$N_4 N_{6,7} O_1$	134.6 - 137.2
$N_4 N_{6,7} O_{2,3}$	163.6 - 175.1
$N_5 N_{6,7} N_{6,7}$	158.2 - 172.4
$N_5 N_{6,7} O_1$	122.6 - 125.2
$N_5 N_{6,7} O_{2,3}$	151.6 - 163.1

Table 8.1a Theoretical Coster-Kronig and super Coster-Kronig line energies for tantalum in the region 100eV - 260eV (Larkins, 1977).

Transition Energy Range (eV)

$N_1 N_3^0 4,5$	144.7
$N_2 N_4^0 4,5$	208.9
$N_2 N_5^0 4,5$	221.6
$N_3 N_4^0 4,5$	148.6
$N_3 N_5^0 4,5$	161.3
$N_4 N_6,7^0 4,5$	202.7 - 204.7
$N_5 N_6,7^0 4,5$	190.7 - 192.7

Table 8.1b Theoretical Coster-Kronig and super Coster-Kronig line energies for tantalum in the region 100eV - 260eV (using equation 2.4 and binding energies from Sevier (1972)).

Transition Energy Range (eV)

$N_4^0 1^0 1$	93.1
$N_4^0 1^0 2,3$	121.4 - 131.2
$N_4^0 1^0 4,5$	161.3
$N_4^0 2,3^0 2,3$	149.6 - 169.3
$N_4^0 2,3^0 4,5$	190.0 - 199.4
$N_4^0 4,5^0 4,5$	229.5
$N_5^0 1^0 2,3$	109.4 - 119.2
$N_5^0 1^0 4,5$	149.3
$N_5^0 2,3^0 2,3$	137.6 - 157.3
$N_5^0 2,3^0 4,5$	178.0 - 187.4
$N_5^0 4,5^0 4,5$	217.5

Table 8.1c Theoretical Auger line energies for tantalum in the region 100eV - 260eV (using equation 2.4 and binding energies from Sevier (1972)).

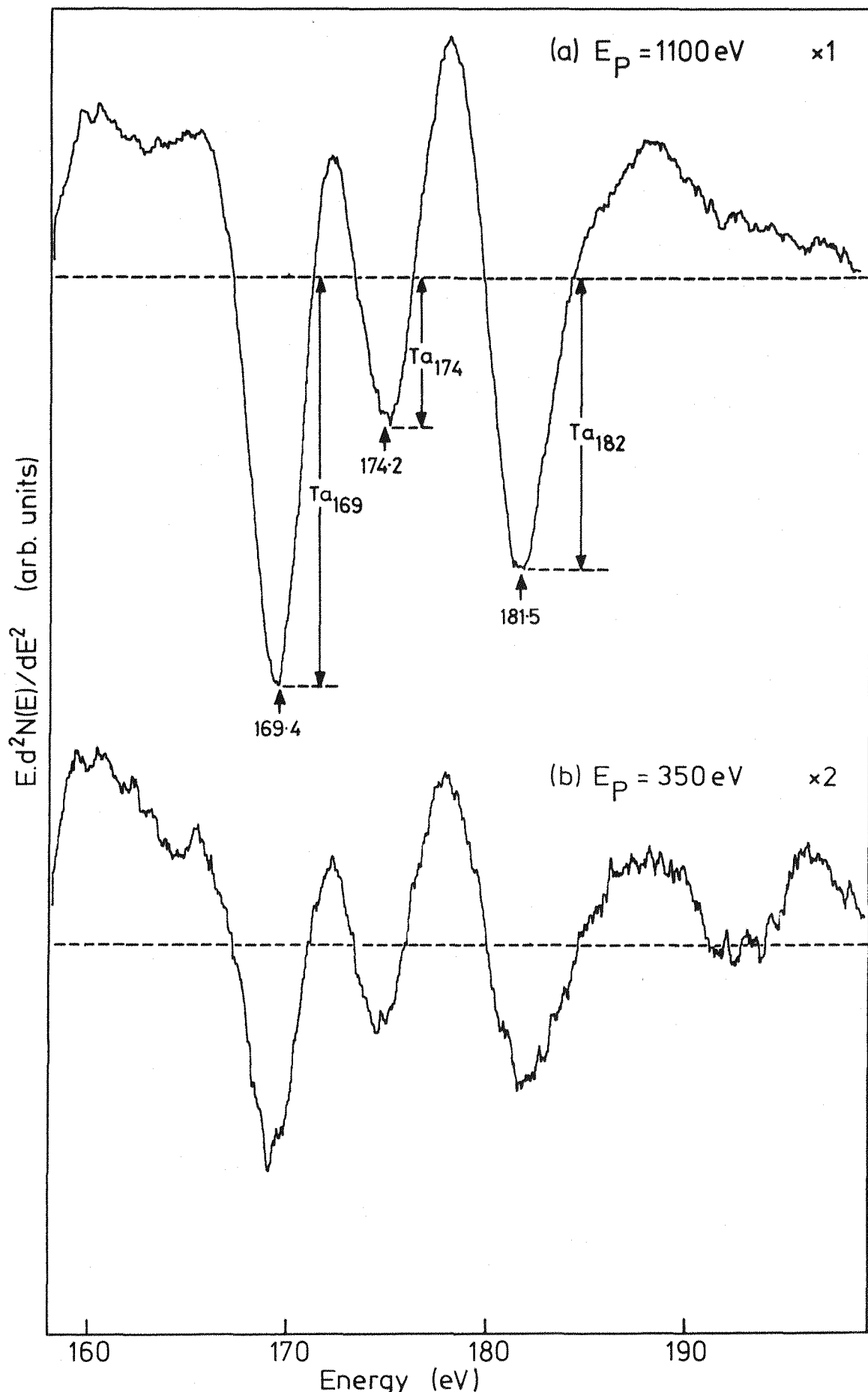


Figure 8.4 Second derivative tantalum secondary electron spectrum ( $I_b = 5 \mu\text{A}$ ,  $v_m = 2.8 \text{ V}_{\text{ptp}}$ ,  $\tau = 0.3 \text{ s}$ , scan  $\text{eV} \cdot \text{s}^{-1}$ ).

To gain some idea of the number of peaks in this region of the spectrum some curve fitting was attempted. This was difficult because, to take account of the large sulphur peak which will obviously affect the smaller substrate peaks, the spectrum could not be expanded as much as desired. Figure 8.5 shows a fit of four Lorentzian peaks to a spectrum induced by a primary beam of 2500eV. From this there are at least three extra peaks required and seven peaks (figure 8.6) fit the tantalum intensity reasonably well though several more peaks are obviously necessary to simulate the area around the sulphur peak. The peak fitting does not indicate the presence of two peaks in the 174eV peaks as found for the equivalent peaks in rhenium (chapter 6) and tungsten (chapter 5) spectra. In figure 8.4 however this peak does look asymmetric though not as obviously as the 171eV rhenium peak in figure 6.3. The asymmetry could be misleading and due to overlapping of the side wings of the adjacent peaks. The 174eV peak in figure 8.6 is not expanded enough for the curve fitting to distinguish two peaks and unfortunately a curve fit could not be successfully applied to the spectra in figure 8.4 because of the presence of the sulphur peak.

The temperature of the tantalum sample could not be raised sufficiently to test for temperature dependent peaks.

Finally, it was noted that the intensity of the peak at 224eV (figure 8.3) changed considerably with respect to the other peaks as the sample was moved relative to the analyser.

#### 8.1.2 Discussion

Despite the high contamination of the tantalum surface, several conclusions can be drawn from these results.

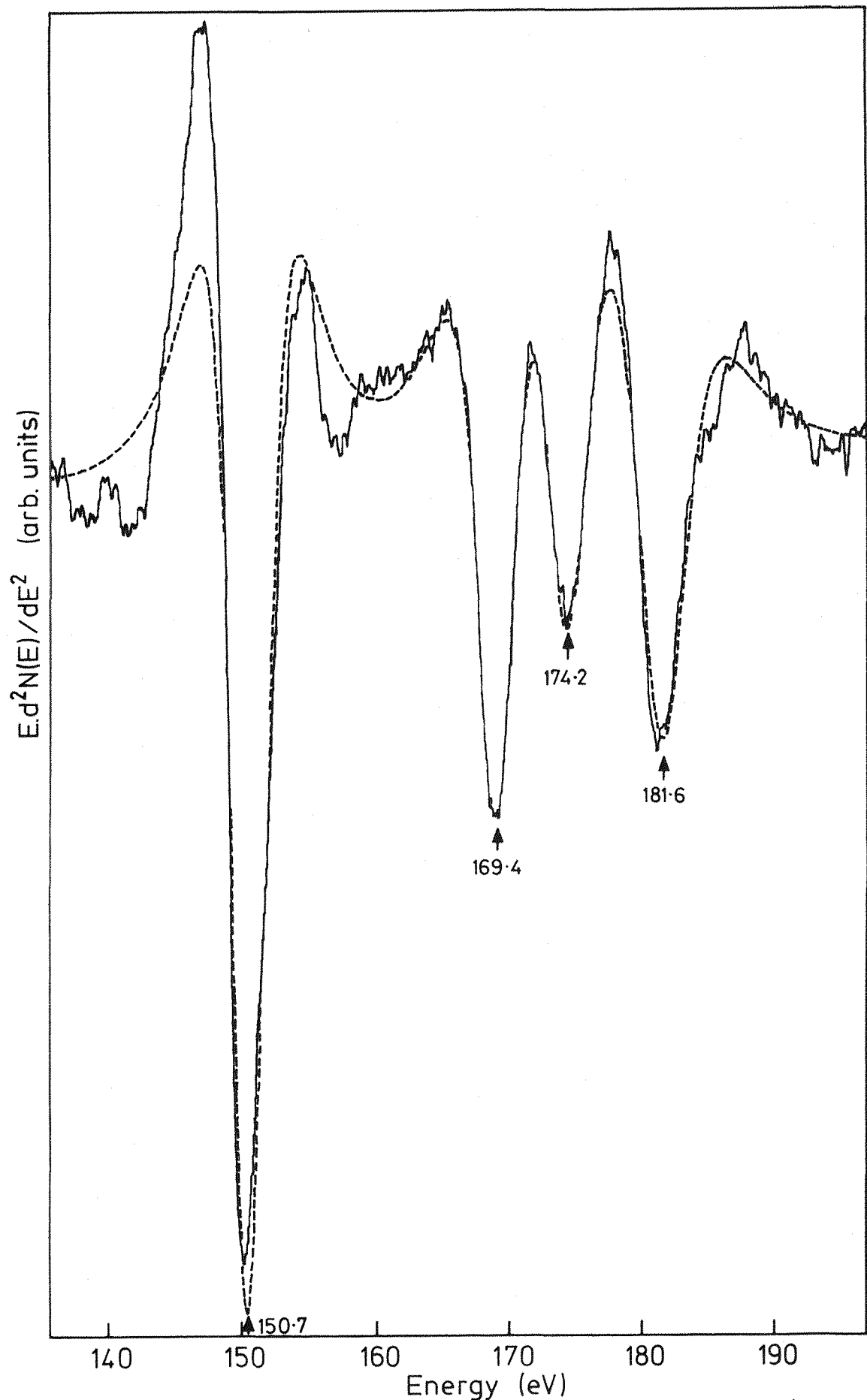


Figure 8.5 Simulation of tantalum spectrum by 4 Lorentzian peaks ( $E_p = 2500$  eV,  $I_b = 5 \mu\text{A}$ ,  $v_m = 2.8 V_{\text{ptp}}$ ,  $\tau = 0.3$  s, scan  $1 \text{ eV} \cdot \text{s}^{-1}$ ).

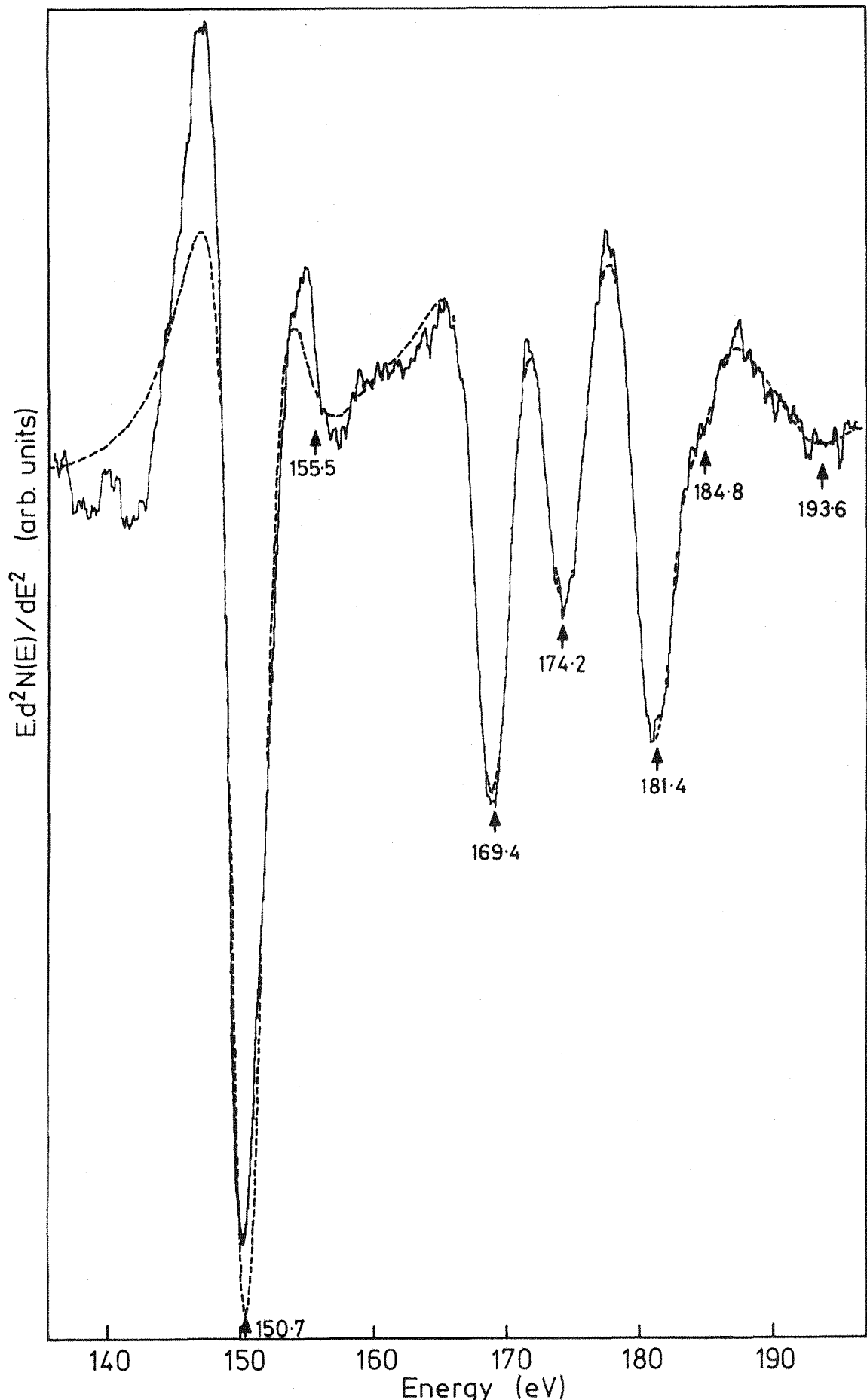


Figure 8.6 Simulation of tantalum spectrum (shown in figure 8.5) by 7 Lorentzian peaks ( $E_0 = 2500$  eV,  $I_b = 5 \mu\text{A}$ ,  $v_m = 2.8 \text{ V}_{\text{ptp}}$ ,  $\tau = 0.3 \text{ s}$ , scan  $1 \text{ eV} \cdot \text{s}^{-1}$ ).

### 8.1.2.1 160eV to 190eV

First, the spectra in figures 8.3a and b, and 8.4a and b are very similar indicating that most of the intensity in this region is due to  $N_4$  or  $N_5$  initial vacancies. There are no new peaks appearing in the 1100eV spectra which are not already present in the 350eV spectra. The only part of the spectrum taken at 1100eV which suggests an increase in intensity with respect to the 350eV spectrum is at 163eV. Looking at the differences in the energy positions of the 169eV, 182eV and 343eV peaks gives:

$$\begin{aligned}343.1 - 181.5 &= 161.6\text{eV} \\343.1 - 169.4 &= 173.7\text{eV} \text{ and} \\181.5 - 169.4 &= 12.1\text{eV.}\end{aligned}$$

Comparison with the differences in electron binding energies of the levels involved (Sevier, 1972):

$$\begin{aligned}E(N_3) - E(N_4) &= 163.2\text{eV} \\E(N_3) - E(N_5) &= 175.2\text{eV} \\E(N_4) - E(N_5) &= 12.0\text{eV}\end{aligned}$$

suggests that the 169, 182 and 343eV peaks are a result of initial holes in the  $N_5$ ,  $N_4$  and  $N_3$  levels respectively decaying to the same final state. This is supported by considering the ratios of yields at 350 and 1100eV primary beam energies for the major peaks. The order of the ratios is  $R_{169} > R_{174} > R_{182}$ . Remembering that  $\sigma_{N_5} > \sigma_{N_4}$ , the 169eV peak can be attributed to  $N_5$  initial hole transitions, the 182eV peak to  $N_4$  initial hole transitions, and the 174eV peak to a mixture of the two. Larkins' theoretical predictions of the  $N_{4,5}N_{6,7}N_{6,7}$  and  $N_{4,5}N_{6,7}O_{2,3}$  line energies for tantalum are compared to the experimental line energies derived from the curve fitting in figure 8.7. The experimental peaks do not line up well with either theoretical series bearing in mind the above constraints. To

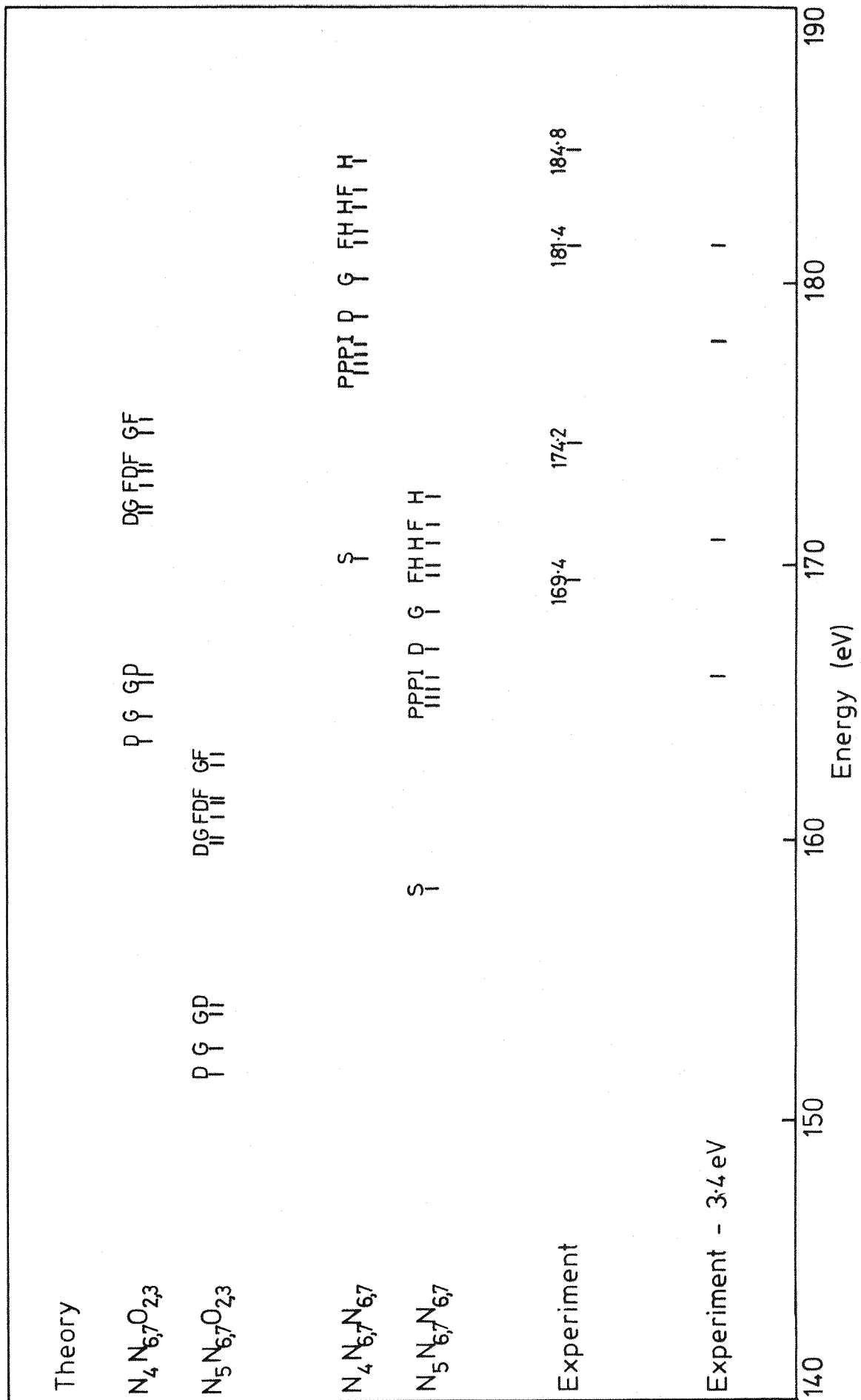


Figure 8.7 Comparison of Larkins' theoretical line energies and tantalum experimental line energies.

give any reasonable match with the  $N_{4,5}N_{6,7}O_{2,3}$  series the line energies have to be shifted  $\sim 11\text{eV}$ , though two of the experimental line energies still lie over  $1\text{eV}$  from a theoretical line. The best fit to the  $N_{4,5}N_{6,7}N_{6,7}$  series, remembering that high angular momentum terms are expected to dominate, is achieved by shifting the line energies  $3.4\text{eV}$ . This is shown in figure 8.7. With this  $3.4\text{eV}$  shift the  $N_4$  based contribution to the  $174\text{eV}$  peak can come from the  $N_{4,5}N_{6,7}O_{2,3}$  series.

#### 8.1.2.2 190eV to 200eV

The region on the high energy side of the major tantalum peaks is expected to have significant intensity from the  $N_{4,5}N_{6,7}O_{4,5}$  Coster-Kronig transitions. As these involve the valance band they are likely to be affected more than the transitions already discussed by the contamination on the surface. However some conclusions can still be drawn. Whilst no yield curves were plotted, an idea of the variation of intensity with primary beam energy can be formed by looking at the spectra in figures 8.3b, 8.3a and 8.2. The most obvious change is in the  $192\text{eV}$  peak which is much larger with respect to the other peaks for  $350\text{eV}$  than for  $1100\text{eV}$  or  $2500\text{eV}$  primary beam energies. This sort of yield behaviour was seen for the rhenium  $240\text{eV}$  peak (figure 7.4) and tungsten  $229\text{eV}$  peak (Rawlings et al., 1980b). These peaks were found to be temperature dependent and thus due to diffraction of secondary electrons but unfortunately the temperature dependence could not be determined for the tantalum peak. The tantalum  $192\text{eV}$  peak also falls within the predicted positions of the  $N_{5}N_{6,7}O_{4,5}$  emissions (figure 8.3). A third possible contribution to this peak could come from the second step of the cascade  $N_3 \rightarrow N_5 V \rightarrow XVV$  (where  $X = N_{6,7}$  and  $O_{2,3}$ ). This has been discussed in detail by Rawlings et al. (1979) for tungsten and in chapter 7 for rhenium. The first step in the cascade is the  $N_3N_5V$  Coster-Kronig transition. By equation 2.4 this produces

intensity at 161.3eV. There is an increase in intensity at 163eV in figure 8.3a compared to figure 8.3b which can be accounted for by  $N_3N_5V$  emission. Thus there are sufficient final two hole states to provide significant intensity from a second decay. From the relation

$$E(N_3N_5V) = E(N_3) - E(N_5V) = 163\text{eV}$$

with  $E(N_3) = 404.5\text{eV}$  the final state  $E(N_5V) = 241.5\text{eV}$ . This compares well with a semi empirical calculation (similar to equation 7.1) giving  $E(N_5V) = 243.3\text{eV}$ . Now using an equation equivalent to equation 7.2 for tantalum, the transitions giving emission around 192eV are

$$\begin{aligned} E_{73}(N_5V \rightarrow N_6VV) &= 193.5\text{eV} \\ E_{73}(N_5V \rightarrow N_7VV) &= 195.6\text{eV} \\ E_{73}(N_5V \rightarrow O_2VV) &= 185.5\text{eV} \\ E_{73}(N_5V \rightarrow O_3VV) &= 195.8\text{eV} \end{aligned}$$

Thus there are three possible contributions to the 192eV peak:  $N_5N_6,7O_4,5$  Coster-Kronig emission, intensity from the second step in the cascade  $N_3 \rightarrow N_5V \rightarrow XVV$  and a diffraction effect.

#### 8.1.2.3 200eV to 215eV

In rhenium the cascade  $N_3 \rightarrow N_4V \rightarrow XVV$  was also found to produce significant intensity (section 7.1.2). In tantalum the first step in this cascade should produce intensity around 149eV but could not be seen because of the large sulphur peak though this does not prove that it does not exist. The calculations for the second step give

$$\begin{aligned} E_{73}(N_4V \rightarrow N_6VV) &\sim 208\text{eV} \\ E_{73}(N_4V \rightarrow N_7VV) &\sim 210\text{eV} \\ E_{73}(N_4V \rightarrow O_2VV) &\sim 200\text{eV} \\ E_{73}(N_4V \rightarrow O_3VV) &\sim 210\text{eV} \end{aligned}$$

These may therefore produce intensity in the 203eV and/or 213eV peaks. The 203eV peak also falls in the predicted region of the  $N_4N_6,7^0N_4,5$  emissions (figure 8.3). Though there appear to be no predicted  $N_4$  or  $N_5$  initial hole transitions in the 213eV peak it must be remembered that the semi empirical formula used for the calculations involving the valance band does not take account of the hole-hole interaction. When Larkins includes this for the  $N_4,5N_6,7N_6,7$  and  $N_4,5N_6,7^0N_2,3$  transitions, the range of emissions for each series covers  $\sim 12$ eV (figure 8.7). If the  $N_4N_6,7^0N_4,5$  emissions also have this range they may well produce intensity over the range 180eV to 215eV.

#### 8.1.2.4 215eV to 230eV

Finally, the 224eV peak was found to vary significantly in intensity with respect to the other peaks as the sample was moved relative to the analyser. This behaviour was seen for the 188eV rhenium peak which was attributed to a diffraction effect. The yield of the 224eV peak also decreases with respect to the other peaks as the primary beam energy is increased (compare figures 8.3 and 8.2) which is consistent with it being a diffraction feature.

#### 8.1.3 Conclusion

Though the tantalum surface was highly contaminated several 'clean surface' conclusions can be drawn from the experimental data.

The most intense emissions between 160 and 190eV are a result of  $N_4,5N_6,7N_6,7$  and/or  $N_4,5N_6,7^0N_2,3$  transitions. The most intensity appears to come from the  $N_4,5N_6,7N_6,7$  series with the theoretical line energies shifted  $\sim 3.4$ eV to agree best with the experimental energies.

The 192, 203 and 213eV peaks have significant intensity from the  $N_4,5N_6,7^0N_4,5$  emissions and may have contributions from the cascades  $N_3 \rightarrow N_4,5 \rightarrow XVV$  (where  $X = N_{6,7}$  and  $O_{2,3}$ ).

There is evidence to suggest that the 192 and 224eV peaks are at least partly due to diffraction of secondary electrons.

## 8.2 Gold

The gold sample was a polycrystalline ribbon. Heating at 800K for 5 minutes reduced all contaminants on the surface apart from carbon to an acceptable level. The carbon could not be removed by heating the surface in vacuum, oxygen or hydrogen. There was therefore a layer of carbon on the surface during the experiments.

### 8.2.1 Results

The first derivative low energy secondary electron spectrum induced by a primary beam of 2500eV is shown in figure 8.8. This 'cleanest' spectrum has a large carbon Auger peak and a small oxygen peak.

The energy axis was calibrated with the elastic peak as for the other metals. To estimate the effect of the surface contamination on the energy positions of the peaks, figure 8.8 was compared with the gold spectrum in the Handbook of Auger Electron Spectroscopy (1976). Using the same reasoning that was outlined for tantalum in section 8.1.1 the gold peaks must be shifted  $\sim$ 1 eV higher than their experimentally measured values to correct for the effect of contamination. With this correction the energy positions of the peaks have an estimated error of  $\pm$ 0.5eV. The energies marked in the remainder of the diagrams include this 1eV correction shift.

Only the section of the spectrum where  $N_{4,5}N_{6,7}X$  ( $X = N_{6,7}$ ,  $O_{2,3}$  and  $O_{4,5}$ ) transitions are expected were studied here. The theoretically predicted positions of these peaks are given in table 8.2. For comparison they are also shown on the spectrum in figure 8.9. The spectrum is presented in second derivative form so that the centre of each peak is clear. A primary beam energy of 1700eV was found to give the

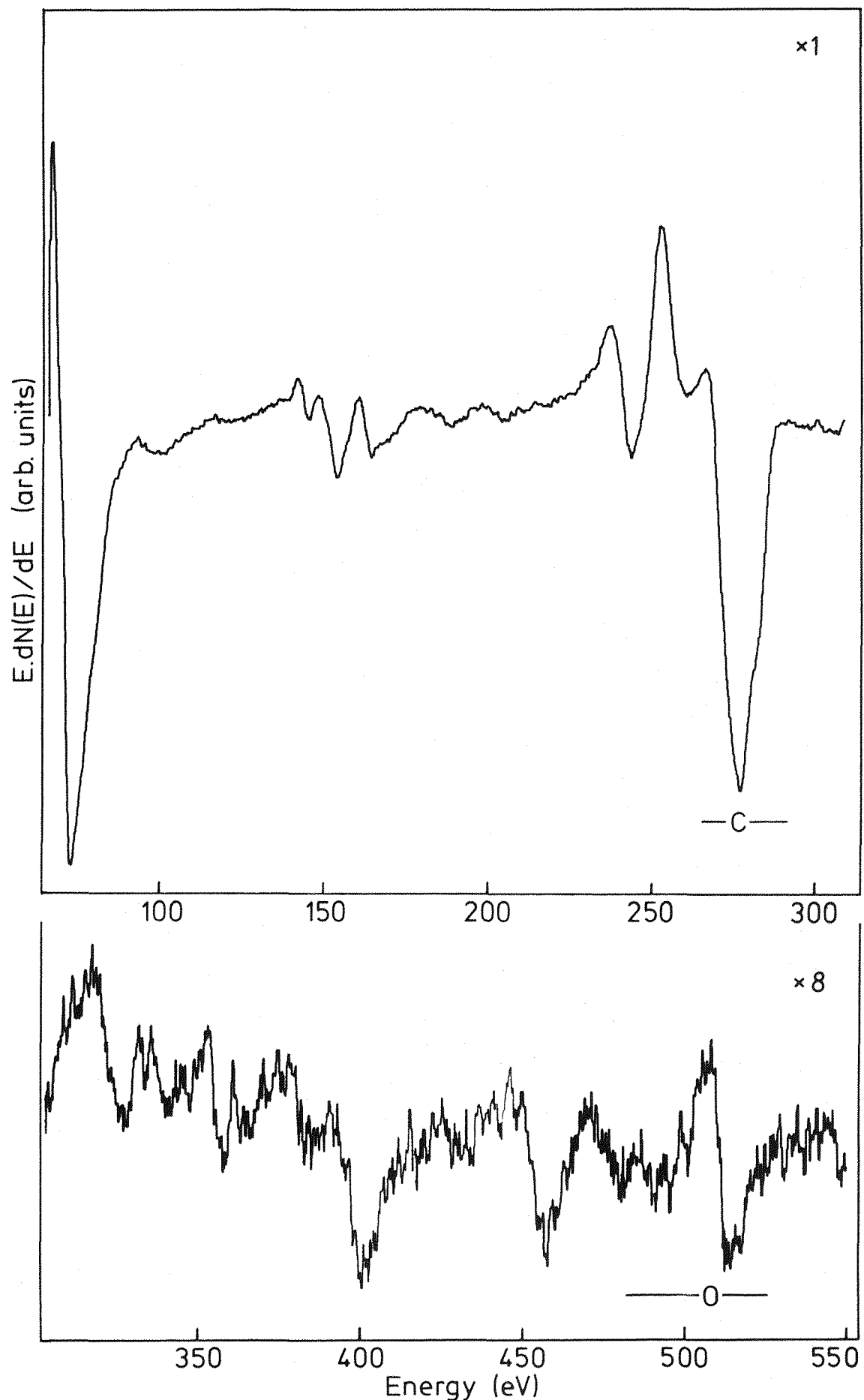


Figure 8.8 First derivative gold secondary electron spectrum induced by 2500 eV primary electrons ( $I_b = 5 \mu A$ ,  $v_m = 3.1 V_{ptp}$ ,  $\tau = 0.3 s$ , scan  $1 eV.s^{-1}$ ).

Transition	Energy Range w.r.t. Fermi level (eV) (error $\pm 5$ eV)
$N_1^N N_3^N 6,7$	106.8 - 117.1
$N_1^N N_3^O 2,3$	134.6 - 148.9
$N_1^N N_4^O 1$	288.9 - 289.4
$N_2^N N_4^N 6,7$	181.2 - 203.1
$N_2^N N_4^O 1$	173.8 - 174.3
$N_2^N N_4^O 2,3$	212.7 - 231.4
$N_2^N N_5^N 6,7$	202.7 - 221.2
$N_2^N N_5^O 1$	191.7 - 192.4
$N_2^N N_5^O 2,3$	225.7 - 244.8
$N_3^N N_4^O 2,3$	114.4 - 133.1
$N_3^N N_5^N 6,7$	104.4 - 122.9
$N_3^N N_5^O 2,3$	127.4 - 146.5
$N_4^N N_6,7^N 6,7$	153.2 - 173.3
$N_4^N N_6,7^O 1$	146.5 - 150.8
$N_4^N N_6,7^O 2,3$	185.6 - 203.5
$N_5^N N_6,7^N 6,7$	134.9 - 155.0
$N_5^N N_6,7^O 1$	128.4 - 132.7
$N_5^N N_6,7^O 2,3$	167.3 - 185.2

Table 8.2a Theoretical Coster-Kronig and super Coster-Kronig line energies for gold in the region 110eV - 290eV (Larkins, 1977).

Transition	Energy range (eV)
$N_1 N_2^0 4,5$	113.1 - 113.6
$N_1 N_3^0 4,5$	210.8 - 212.2
$N_2 N_4^0 4,5$	288.0 - 290.8
$N_3 N_4^0 4,5$	189.7 - 192.5
$N_3 N_5^0 4,5$	207.5 - 210.9
$N_4 N_6,7^0 4,5$	250.5 - 254.4
$N_5 N_6,7^0 4,5$	232.4 - 236.3

Table 8.2b Theoretical Coster-Kronig and super Coster-Kronig line energies for gold in the region 110eV - 290eV (using equation 2.4 and binding energies from Sevier (1972)).

Transition	Energy Range (eV)
$N_4^0 1^0 1$	127.0
$N_4^0 1^0 2,3$	164.4 - 183.3
$N_4^0 1^0 4,5$	237.9 - 240.7
$N_4^0 2,3^0 2,3$	201.9 - 230.0
$N_4^0 2,3^0 4,5$	274.9 - 292.9
$N_5^0 1^0 2,3$	146.3 - 165.2
$N_5^0 1^0 4,5$	219.8 - 222.6
$N_5^0 2,3^0 2,3$	183.8 - 211.9
$N_5^0 2,3^0 4,5$	256.5 - 274.8

Table 8.2c Theoretical Auger line energies for gold in the region 110eV - 290eV (using equation 2.4 and binding energies from Sevier (1972)).

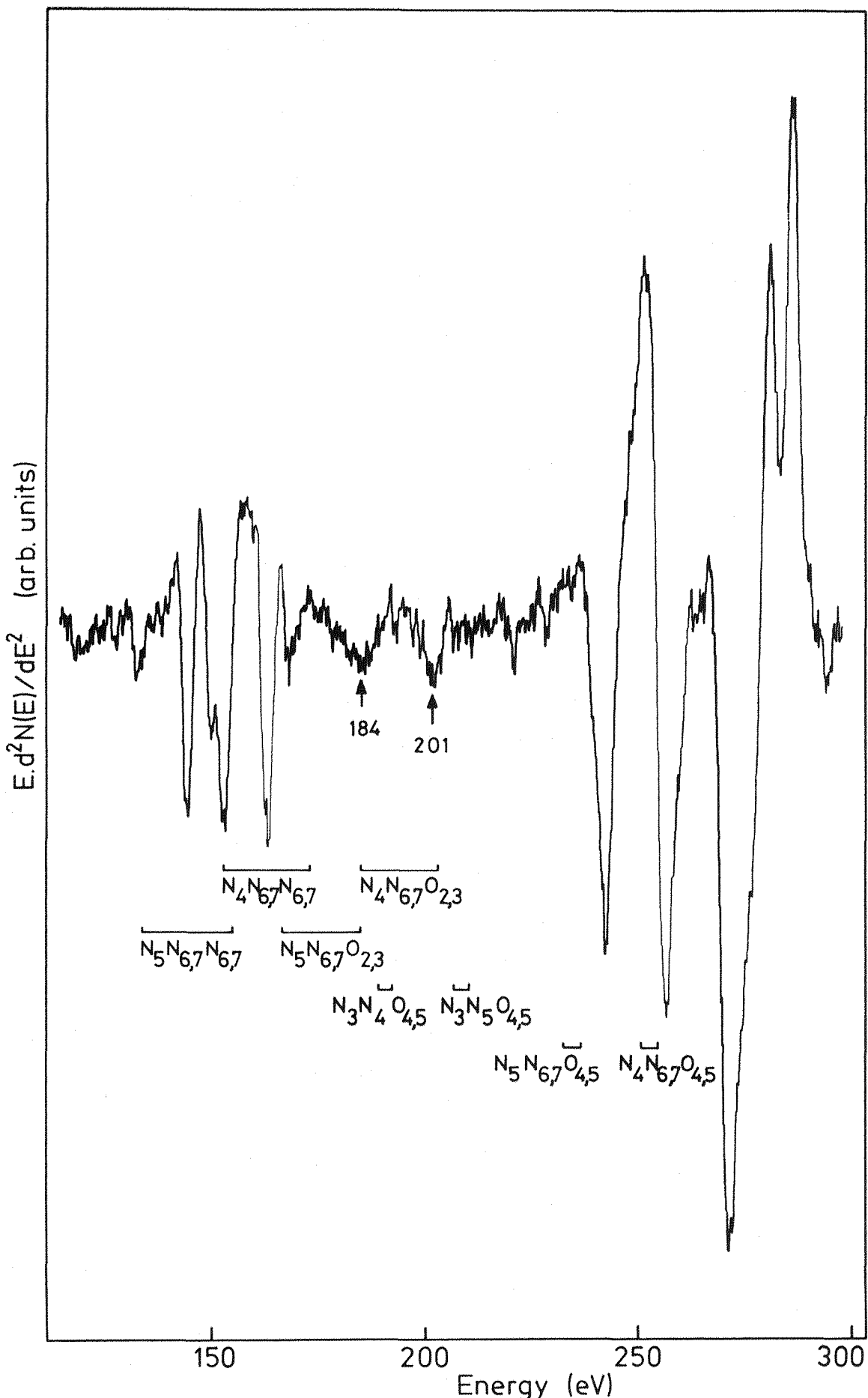


Figure 8.9 Second derivative gold secondary electron spectrum induced by 1700 eV primary electrons ( $I_b = 6 \mu A$ ,  $v_m = 3.8 V_{ptp}$ ,  $\tau = 0.3 s$ , scan  $1 eV \cdot s^{-1}$ ).

most intense peaks. Unfortunately this primary beam is sufficient to ionise the gold  $N_1$  level at 758.8eV (Sevier, 1972) and lower energy levels.

The two major areas of intensity in figure 8.9, 140eV to 170eV and 220eV to 290eV were studied more closely in the hope of identifying the  $N_{4,5}N_{6,7}X$  peaks. Both these areas were recorded at 1700eV and also at 480eV primary beam energies (figures 8.10 and 8.11). 480eV is insufficient to ionise the  $N_3$  level (at 545.4eV (Sevier, 1972)); thus any gold Auger peaks that do occur in the 1700eV spectra but are not present in the 480eV spectra must result from  $N_3$ ,  $N_2$  and/or  $N_1$  initial vacancies.

The only way in which figure 8.10b (primary beam energy 480eV) differs significantly from figure 8.10a (primary beam energy 1700eV) is that there is an extra peak between the two peaks of the  $\sim 152$ eV doublet. Further investigation revealed that the peak became noticeable at a primary beam energy of 600eV and grew gradually with respect to the other peaks as the primary beam energy decreased. The  $L_{2,3}M_{2,3}M_{2,3}$  sulphur Auger peak occurs at  $\sim 152$ eV so this was considered as a possible explanation for the peak. The binding energy for the  $L_{2,3}$  sulphur levels is  $\sim 165$ eV compared to the binding energy of the gold  $N_{4,5}$  levels at  $\sim 340$ eV (Sevier, 1972): if both sulphur  $L_{2,3}$  and gold  $N_{4,5}$  initial holes have similar normalised yield curves (figure 8.12), then at 480eV primary beam energy the sulphur transition would have approximately twice the normalised yield of the gold transition. Figure 8.12 shows how the yield of the sulphur peak increases with respect to the gold yield as the primary beam falls below  $\sim 1000$ eV. Thus the presence of sulphur could account for the appearance of a peak in figure 8.10b but not in figure 8.10a.

It is difficult to estimate the relative contributions of sulphur and gold to the 152eV peak in figure 8.10b. However by considering the position of the shoulder on the high energy side of the peak, and the height of the peak relative to its neighbours, the sulphur could account for at

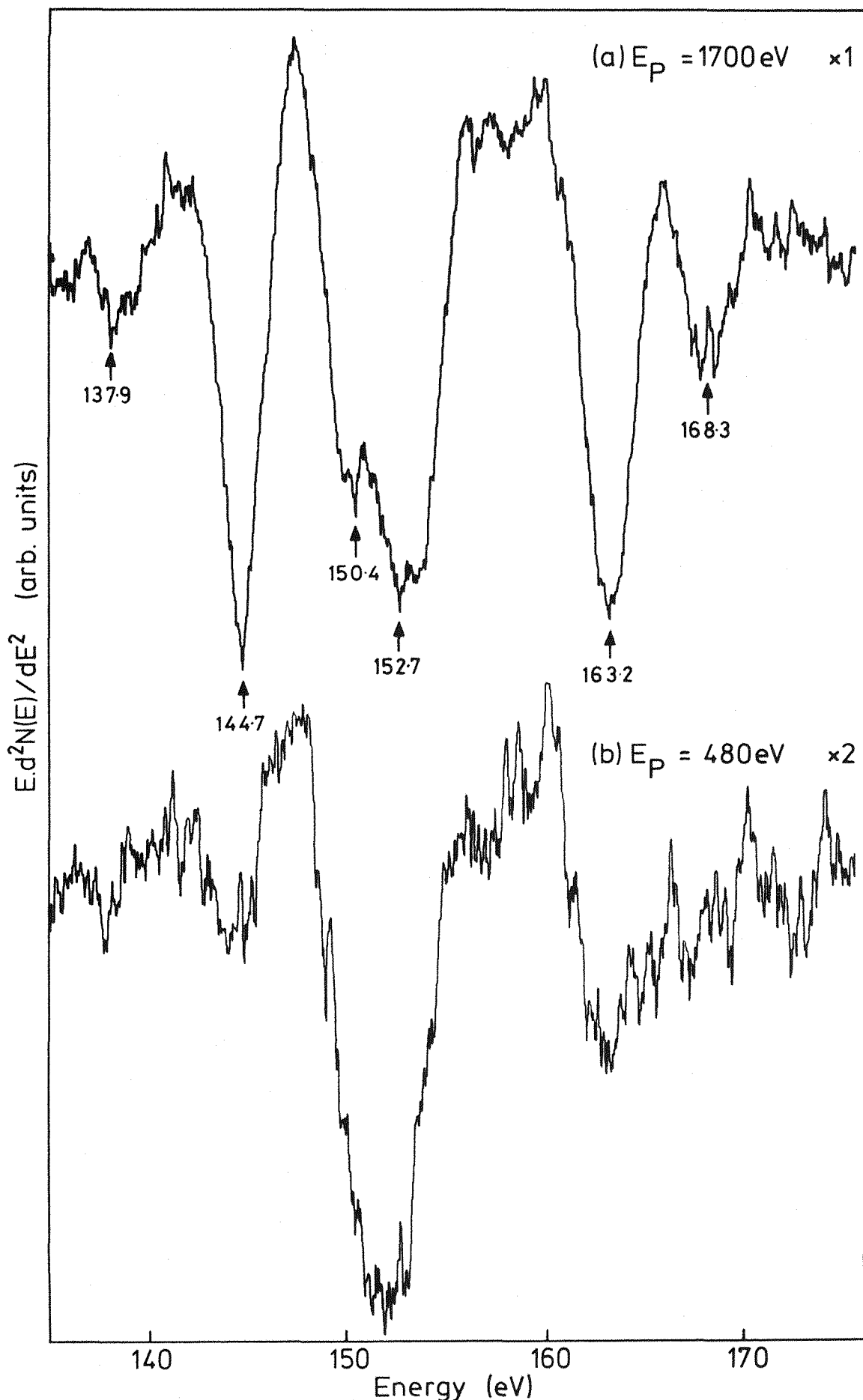


Figure 8.10 Second derivative gold secondary electron spectrum 140 to 170 eV ( $I_b = 6 \mu A$ ,  $v_m = 3.8 V_{ptp}$ ,  $\tau = 0.3 s$ , scan  $1 eV.s^{-1}$ ).

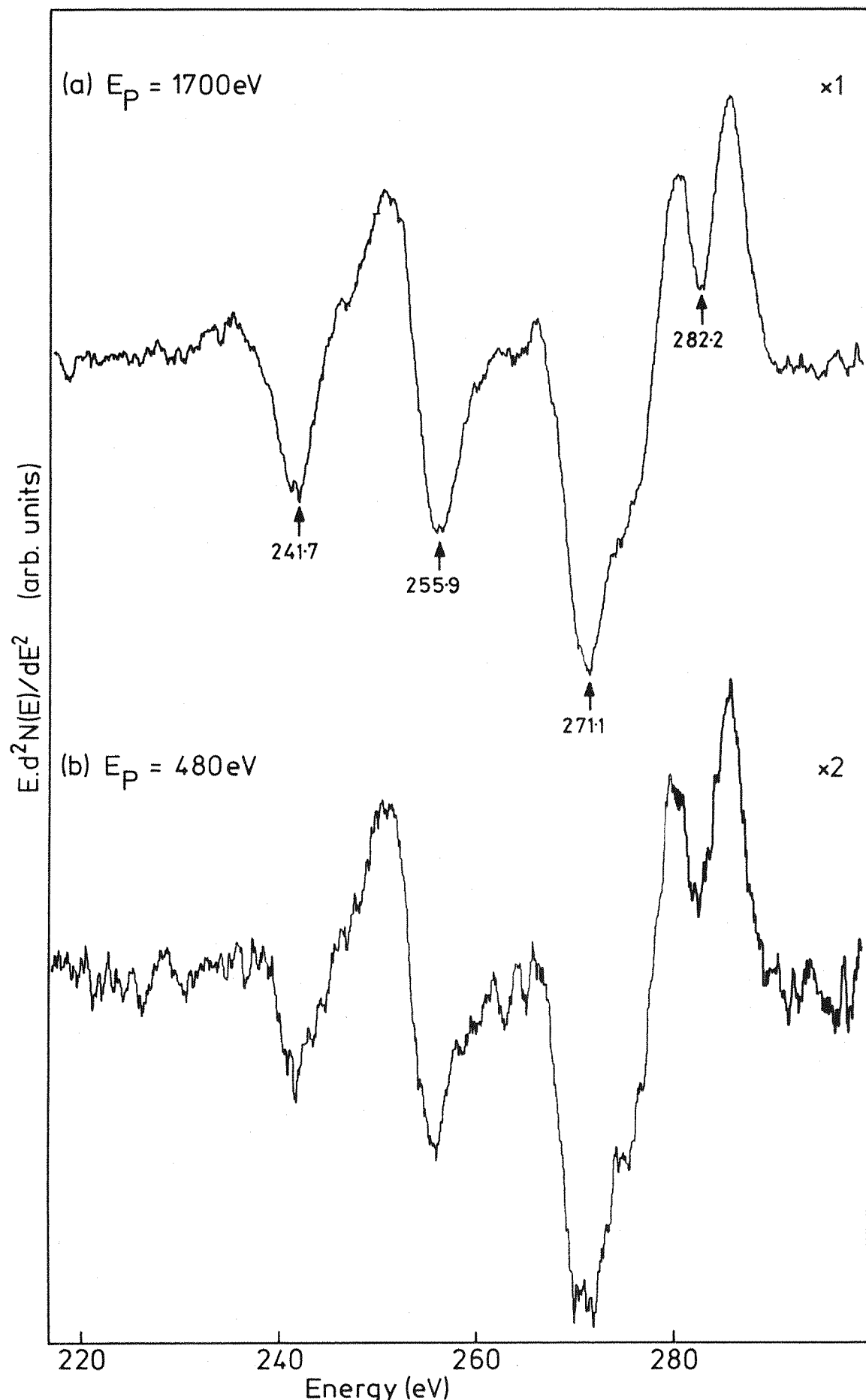


Figure 8.11 Second derivative gold secondary electron spectrum 220 to 290eV ( $I_b=6\mu\text{A}$ ,  $v_m=3.8\text{V}_{\text{ptp}}$ ,  $\tau=0.3\text{s}$ , scan  $1\text{eV.s}^{-1}$ ).

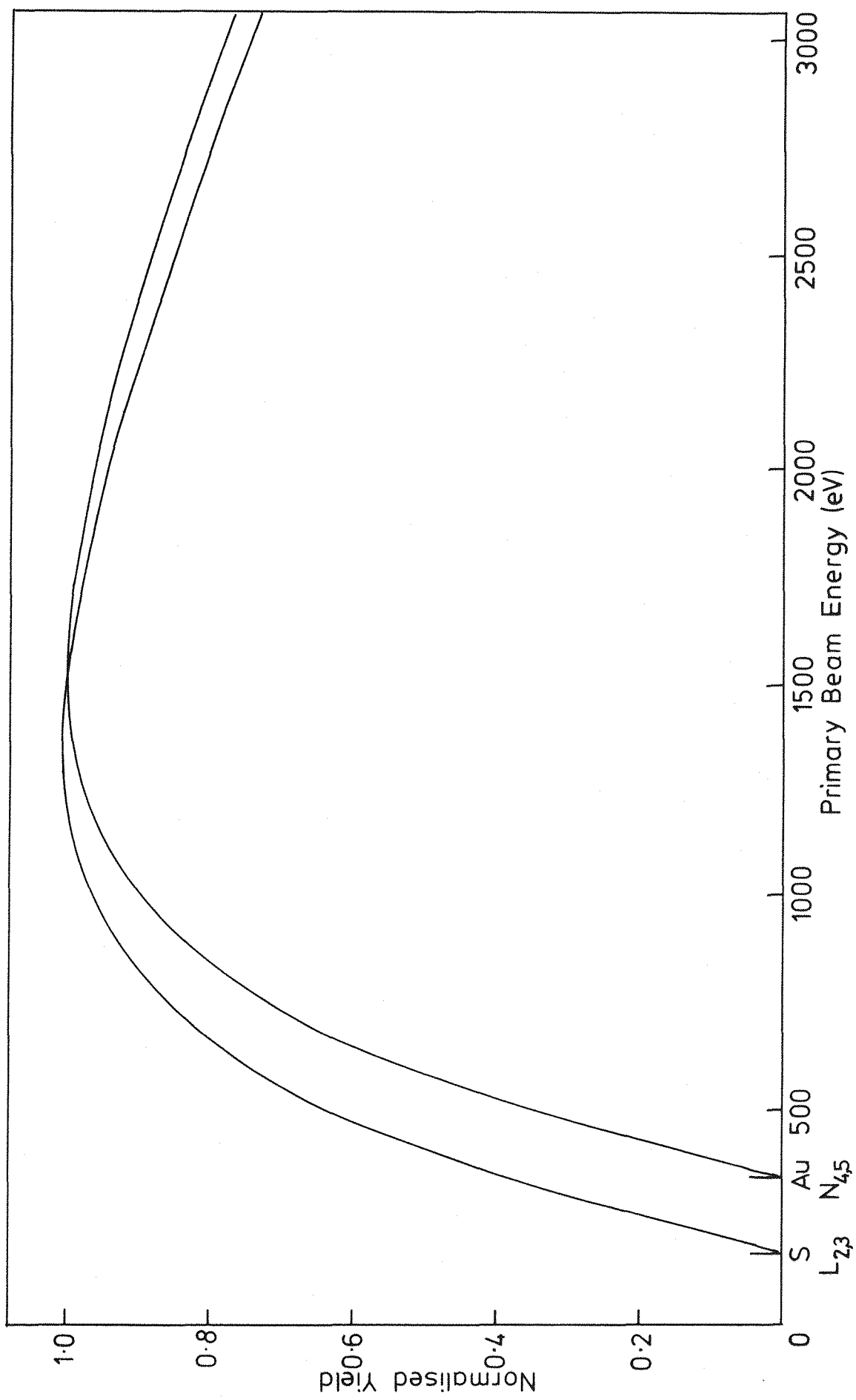


Figure 8.12 Approximate comparison of sulphur  $L_{2,3}$  and gold  $N_{4,5}$  yield curves (yield curves approximated by rhenium yield curve in figure 6.5).

most half of the total height of the peak. If this is so, because of the yield curve for each peak, the sulphur could be responsible for as much as one third of the intensity in the 152eV doublet in figure 8.10a. An extra peak at ~152eV in figure 8.10a would increase the total intensity of the experimental peak and bring the apparent positions of the two gold peaks (the doublet) closer together.

Because the effect of the sulphur peak was difficult to quantify no attempt was made to plot yield curves nor to synthesise the spectrum.

Finally, several spectra were recorded at temperatures up to 1000K. No significant changes in the spectra were seen.

### 8.2.2 Discussion

The contamination on the gold surface prevented many useful experiments and analyses such as curve synthesis. However some useful conclusions can still be drawn by comparing the experimental line energies with theoretical line energies (figure 8.9 and table 8.2).

#### 8.2.2.1 140eV to 170eV

The 145eV, 150eV and 153eV peaks are in the  $N_5N_6,7N_6,7$  super Coster-Kronig region, and the 163eV and 168eV peaks are in the  $N_4N_6,7N_6,7$  region. These assignments are supported by looking at the differences in energy positions of some of the peaks:

$$168.3 - 150.4 = 17.9\text{eV}$$

and  $163.2 - 144.7 = 18.5\text{eV}$ .

Comparison with the difference in electron binding energies of the gold  $N_4$  and  $N_5$  levels (Sevier, 1972) ( $E(N_4) - E(N_5) = 18.1\text{eV}$ ) suggests that the 168eV and 163eV peaks result from initial holes in the  $N_4$  level and the

150eV and 145eV peaks result from initial  $N_5$  holes. Larkins' (1977) theoretical predictions of the  $N_{4,5}N_{6,7}N_{6,7}$  and  $N_{4,5}N_{6,7}O_{2,3}$  line energies for gold are compared with the experimental line energies (figure 8.10a) in figure 8.13. Remembering that high angular momentum terms are expected to dominate the spectrum, the best fit to the  $N_{4,5}N_{6,7}N_{6,7}$  series is achieved by shifting the line energies just 1eV.

#### 8.2.2.2 170eV to 220eV

Looking again at figure 8.9 the  $N_5N_{6,7}O_{2,3}$  and  $N_4N_{6,7}O_{2,3}$  transitions line up with the 184eV and 201eV experimental peaks.

#### 8.2.2.3 220eV to 290eV

The large carbon peak at 271eV has a significant effect on the gold spectrum in that region. The presence of contamination on the surface also has a much greater effect on Auger transitions involving the conduction band (expected in this region) than on core-core-core transitions. Despite these problems it is reasonable to assign the 242eV peak to  $N_5N_{6,7}O_{4,5}$  Coster-Kronig transitions and the 256eV peak to  $N_4N_{6,7}O_{4,5}$  transitions as these peaks still appear in the spectrum with a primary beam energy below the gold  $N_3$  binding energy (figure 8.11).

#### 8.2.2.4 A cascade process

In the tungsten, rhenium and tantalum spectra some peaks were assigned, at least partly, to a cascade process of the form  $N_3 \rightarrow N_5 V \rightarrow XVV$  or  $N_3 \rightarrow N_4 V \rightarrow XVV$  (where  $X = N_{6,7}$  and  $O_{2,3}$ ). Using the method described in chapter 7.1.2 to calculate the positions of the peaks, the second steps of the cascades would produce intensity in the region 230eV to 290eV. This is the same region as the  $N_4N_{6,7}O_{4,5}$  and  $N_5N_{6,7}O_{4,5}$  peaks. For the second step of the  $N_3 \rightarrow N_5 V \rightarrow XVV$

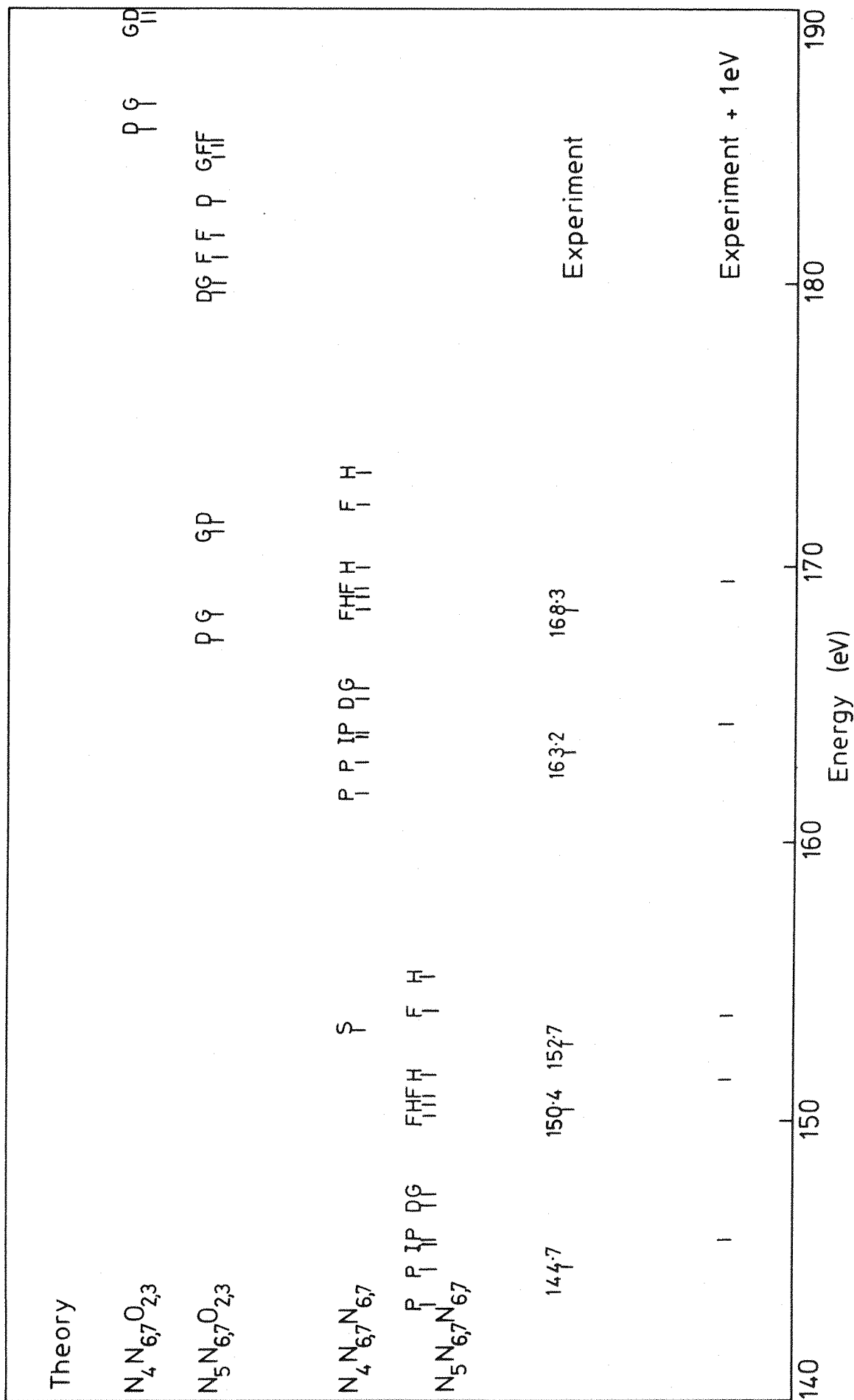


Figure 8.13 Comparison of Larkins' theoretical line energies and gold experimental line energies.

cascade to occur there must be some  $N_3N_5O_{4,5}$  Coster-Kronig intensity. Similarly for the  $N_3N_4O_{4,5}$  transition. In figure 8.9 the expected positions of the  $N_3N_5O_{4,5}$  and  $N_3N_4O_{4,5}$  transitions are marked but no experimental peaks correspond! However it is possible that they contribute intensity to the small peaks at 184eV and 201eV. Even so, the intensity resulting from the second step of a cascade could only be a small percentage of the large peaks at 242eV and 256eV. Therefore these cascade processes cannot be observed.

### 8.2.3 Conclusion

Some 'clean surface' conclusions can be drawn from these results despite the high level of contamination. The peak assignments that follow are in agreement with those of both Larkins and Lubenfeld (1977) and Matthew et al. (1980).

The intensity between 140 and 170eV is a results of  $N_{4,5}N_{6,7}N_{6,7}$  super Coster-Kronig transitions. For the best fit to the experimental line energies the theoretical line energies must be shifted 1eV which is within the error in the energy positions.

The large peaks at 242 and 256eV are due to  $N_{4,5}N_{6,7}O_{4,5}$  Coster-Kronig transitions. The small peaks at 184 and 201eV are due to  $N_{4,5}N_{6,7}O_{2,3}$  transitions.

Larkins and Lubenfeld (1977) and Matthew et al. (1980) disagreed on the relative intensities of the  $N_{4,5}N_{6,7}N_{6,7}$  and  $N_{4,5}N_{6,7}O_{4,5}$  series. Unfortunately the results presented in this chapter cannot be used to resolve this conflict because of the surface contamination.

## CHAPTER 9

### COMPARISON OF RESULTS

In this chapter the authors results (from chapters 6,7 and 8) are compared with the work of other authors (discussed in chapter 5) to get a complete picture of the 5d transition metals. A comparison of the spectra from several transition metals answers questions that were left unanswered after analysis of each metal individually.

The low energy secondary electron spectra from the metals of the 5d series form a 'family' of similarly shaped spectra. These similarities can be seen in the standard reference spectra (e.g. the Handbook of Auger Electron Spectroscopy (1976) and McGuire (1979)). Haas et al. (1970) concluded that the equivalent peaks in each spectra must have the same physical origin. The next section compares these equivalent peaks to resolve the major problem remaining at the end of chapter 6: Are the peaks between 150 and 185eV in the rhenium spectrum mainly due to  $N_{4,5}N_{6,7}N_{6,7}$  super Coster-Kronig transitions or  $N_{4,5}N_{6,7}O_{2,3}$  Coster-Kronig transitions?

#### 9.1 The $N_{4,5}N_{6,7}N_{6,7}$ Super Coster-Kronig Transitions?

This section discusses the origin of five Auger peaks lying between 150 and 185eV in the rhenium spectrum. The experimental positions of these peaks were found by curve synthesis (table 6.1). A comparison of the five peak positions with Larkins' (1977) theoretical  $N_{4,5}N_{6,7}N_{6,7}$  and  $N_{4,5}N_{6,7}O_{2,3}$  line energies (figure 6.9) suggests that the experimental peaks are due to  $N_{4,5}N_{6,7}O_{2,3}$  transitions. However McGuire's (1974) calculations suggest that these experimental peaks should be attributed to  $N_{4,5}N_{6,7}N_{6,7}$  transitions. Rawlings et al. (1980a) found the same disagreement between the theories when analysing their tungsten spectrum.

The two theories are in better agreement, however, for the metals tantalum and gold (chapter 8). The equivalent peaks to the five rhenium peaks between 150 and 185eV are closer to Larkins'  $N_{4,5}N_{6,7}N_{6,7}$  line energies than the  $N_{4,5}N_{6,7}O_{2,3}$  line energies. The theories also agree for Larkins and Lubenfeld's (1977) results for gold, and Matthew et al.'s (1980) results for gold, platinum and iridium.

#### 9.1.1 Change in Peak Position with Atomic Number

The problem of assigning the rhenium and tungsten experimental peaks can be resolved by looking at the change in peak position with atomic number. Table 9.1 is a compilation of the positions of the equivalent experimental peaks from tantalum (figure 8.6), tungsten (Rawlings et al., 1980a), rhenium (figure 4.2), iridium (Matthew et al., 1980), platinum (Matthew et al., 1980) and gold (figure 8.10; Matthew et al., 1980; Larkins and Lubenfeld, 1977). The peak energies from this thesis and for tungsten were determined by curve synthesis (chapter 4) of second derivative spectra. However, Matthew et al.'s (1980) and Larkins and Lubenfeld's (1977) energies are measured directly from their  $N(E)$  spectra; hence the gaps in table 9.1 (Matthew et al. only marked the energies of the two most intense peaks in their spectra. Larkins and Lubenfeld did not quote peak energies; the values in table 9.1 were estimated from figure 2 in their paper).

The results in table 9.1 are presented graphically in figure 9.1. It is immediately obvious from both the table and graph that the energy position of a peak decreases monotonically with increasing atomic number. It is also apparent that the experimental shift in peak energy with atomic number is largest for the elements with higher atomic numbers. Haas et al. (1970) noted these trends in the position of the three major peaks in their first derivative spectra. The following sections compare figure 9.1 with similar plots of theoretical line energies.

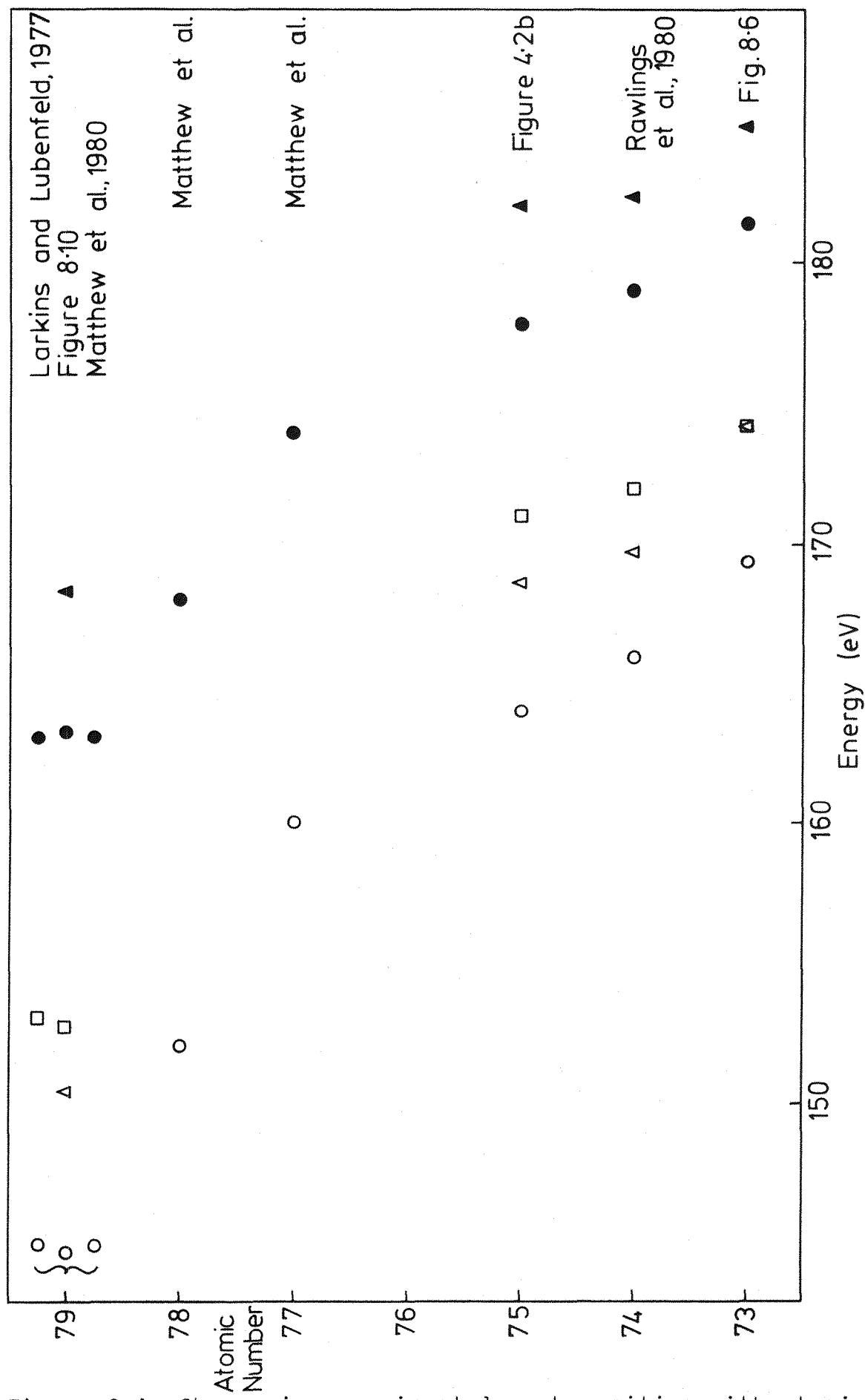
<u>Atomic Number</u>	<u>Peak positions (w.r.t. the Fermi level)</u>				
----------------------	--	--	--	--	--

73	169.4	174.2	174.2	181.4	184.8
74	166.0	169.7	172.0	179.0	182.3
75	164.0	168.6	171.0	177.8	182.0
76	-	-	-	-	-
77	160	-	-	174	-
78	152	-	-	168	-
79	145	-	-	163	-
79	~145	-	~153	~163	-
79	144.7	150.4	152.7	163.2	168.3

References

73 Figure 8.6  
74 Rawlings et al., 1980a  
75 Figure 4.2  
77 Matthew et al., 1980  
78 Matthew et al., 1980  
79 Matthew et al., 1980  
79 Larkins and Lubenfeld, 1977  
79 figure 8.10

Table 9.1 Comparison of the positions of equivalent experimental peaks.



### 9.1.2 Comparison with Larkins' Theoretical Line Energies

Figure 9.2a shows Larkins' (1977) prediction for the  $N_4N_6N_6^1S_0$  super Coster-Kronig line energy with respect to atomic number. For comparison figure 9.2b shows the  $N_4N_6O_2^1D_2$  Coster-Kronig line energy. To avoid cluttering the diagram the rest of the terms in the  $N_{4,5}N_{6,7}N_{6,7}$  and  $N_{4,5}N_{6,7}O_{2,3}$  series are omitted. Since the terms in each series show very similar trends in energy this omission does not affect the conclusions. Absolute energies will be discussed later.

Neither figure 9.2a or 9.2b shows the monotonic decrease in energy with atomic number seen in figure 9.1. However figure 9.2a shows the right general trend; figure 9.2b being completely opposite. On this basis it is reasonable to conclude that the peaks between 150 and 185eV in the rhenium secondary electron spectrum are due to  $N_{4,5}N_{6,7}N_{6,7}$  super Coster-Kronig transitions. Similarly, Rawlings et al.'s (1980a) tungsten peaks can be assigned to  $N_{4,5}N_{6,7}N_{6,7}$  transitions.

Assuming that all the peaks in figure 9.1 are due to  $N_{4,5}N_{6,7}N_{6,7}$  transitions, the disagreement between the experimental peak energies and theoretical line energies is now explored. Chapter 6 concluded that the theoretical line energies had to be shifted up 10eV to fit the rhenium experimental peaks best. Larkins (1977) states that the accuracy of his results depends largely on the accuracy of the binding energies (Sevier, 1972) used in his calculations. Where the binding energies are known to a high accuracy he suggests that his Auger electron energies should be within 1 to 2eV of the experimental values with the maximum discrepancies near 5eV. The difference of 10eV for the rhenium peaks therefore casts doubt on the accuracy of Sevier's (1972) binding energies.

Sevier indicates the expected error in the binding energies that he quotes. The  $O_2$  level in rhenium has the

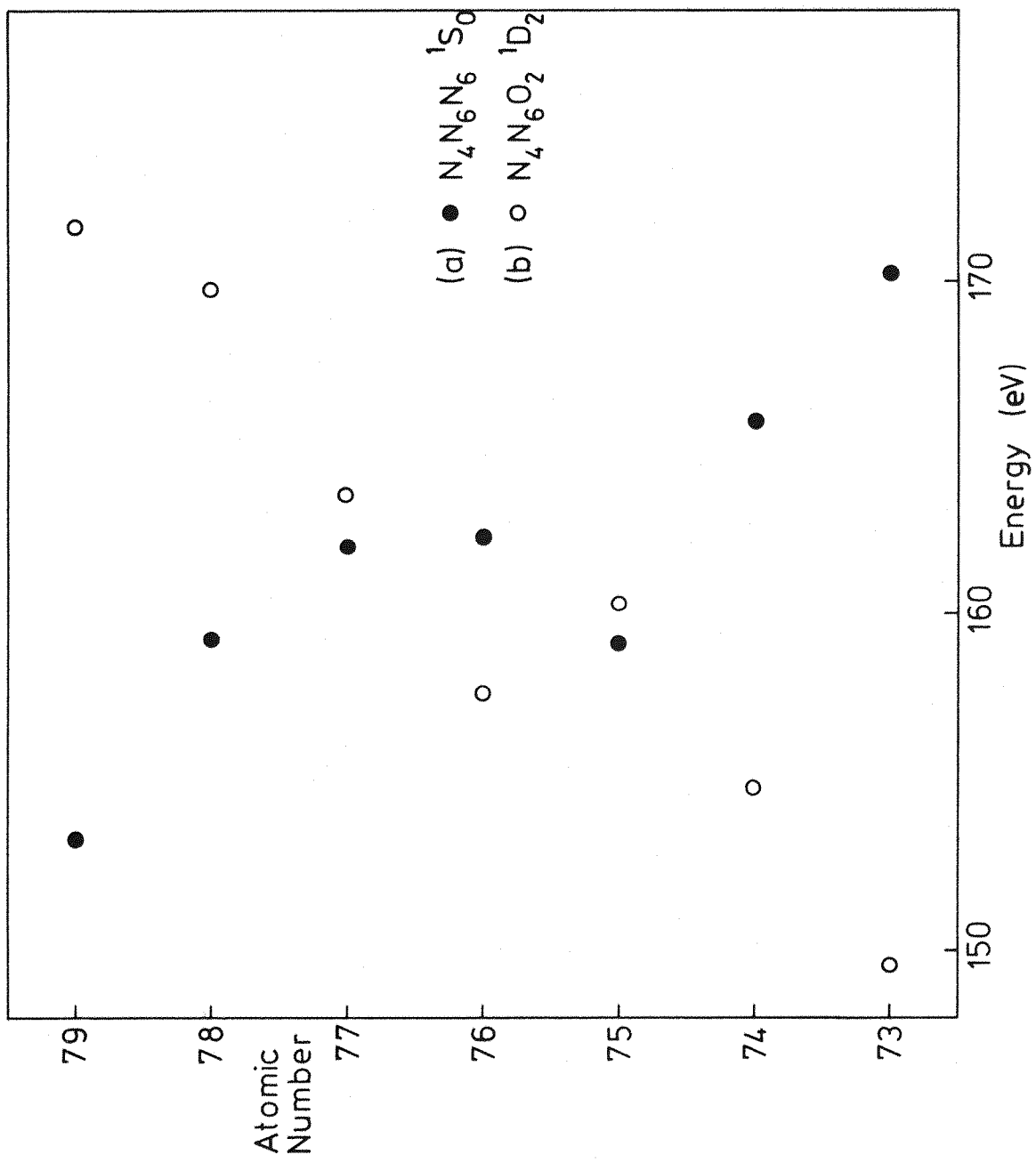


Figure 9.2 Examples of Larkins' theoretical line energies v. atomic number.

largest error; 0.7eV. If all three levels had this error, the maximum error in the Auger line energy would be only 2.1eV. It is therefore unlikely that the 10eV discrepancy for the  $N_{4,5}N_{6,7}N_{6,7}$  rhenium peaks can be entirely blamed on errors in the binding energies.

Figure 9.3 plots the discrepancy between experimental and theoretical line energies with respect to atomic number. { In this figure the values for tantalum, rhenium and gold are taken from chapters 6 and 8. The value for tungsten is from Rawlings et al. (1980a). Values for iridium and platinum are estimated from spectra in Matthew et al. (1980) using the same criteria as for the other metals; that high angular momentum terms are expected to dominate the spectrum. } The graph shows that the discrepancy between experiment and theory increases as the 5d shell fills, reaching a maximum when the 5d shell is half full and decreasing as the 5d shell completes.

#### 9.1.3 Comparison with Empirical Line Energy Calculations

Having shown the inaccuracy in Larkins' (1977) predictions the question arises: Do the empirical methods of calculating line energies agree better with the experimental results?

Haas et al. (1970) used the empirical equation

$$E_Z(WXY) = E_Z(W) - E_Z(X) - E_{Z+1}(Y)$$

to calculate Auger line energies. They only found one group, the  $N_5N_{6,7}N_{6,7}$  transitions, that decreased monotonically in energy with increasing atomic number. They therefore assigned their three first derivative peaks to these transitions. Significantly they used an earlier compilation of binding energies (Siegbahn et al., 1968) than in the present work, and did not quote the calculations for osmium as they did not consider it experimentally.

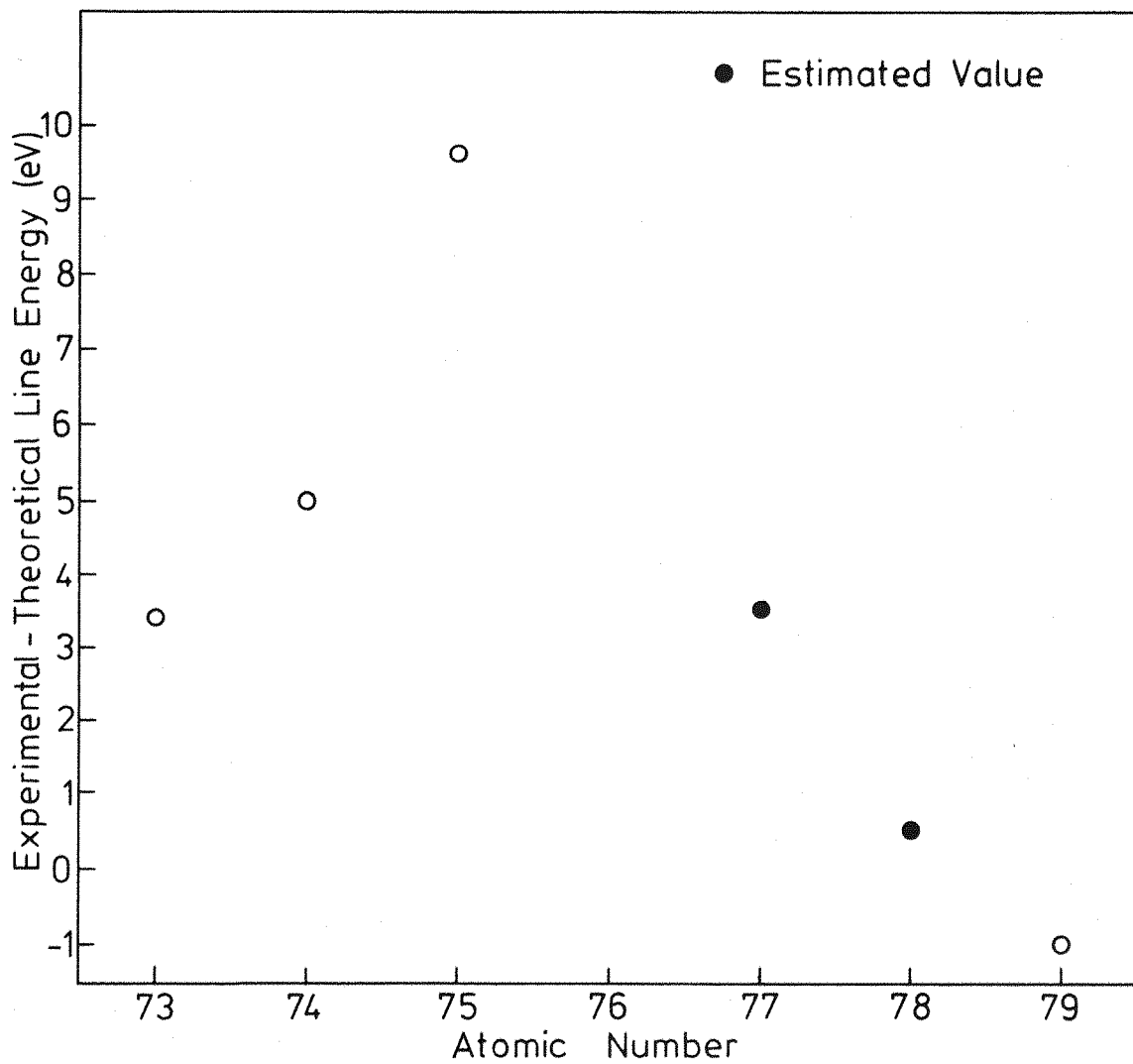


Figure 9.3 Discrepancy between experimental and Larkins' theoretical line energies v. atomic number.

Chung and Jenkins (1970) considered that the empirical equation 2.4 gives a more accurate prediction of line energies than the equation used by Haas et al. They felt that Haas et al.'s peaks should be attributed to  $N_{4,5}N_{6,7}N_{6,7}$  as well as  $N_{5,6}N_{6,7}N_{6,7}$  transitions because the range of experimental peak energies overlapped both series.

Figure 9.4 shows the  $N_{4,5}N_{6,7}N_{6,7}$  line energies predicted by equation 2.4 (using Sevier's (1972) binding energies). These values are within a mere 0.2eV of the energies predicted by the equation used by Haas et al. The  $N_{5,6}N_{6,7}N_{6,7}$  series (excluding osmium) still shows the monotonic decrease in energy with atomic number. The  $N_{4,5}N_{6,7}N_{6,7}$  series does not have the same decrease in energy. Both series, however, show the larger change in energy with atomic number for the elements with higher atomic numbers. This agrees with the trend in experimental energies; Larkins' theory does not follow this trend (figure 9.2a).

The experimental energies are shown alongside the theoretical energies in figure 9.4. The theory is ~6eV lower than the Ta, W and Re experimental energies, and ~3eV lower than the Ir, Pt and Au energies. There is no tendency to the increasing discrepancy shown in figure 9.3 for Larkins' theory. A comparison of both theories (figures 9.2a and 9.4) suggests that the 'kink' appearing in figure 9.2a must be partly due to the values of binding energies used in the equation as the energies in figure 9.4 are calculated entirely from binding energies. Any extra discrepancy shown in figure 9.3 must therefore be a result of Larkins' calculations.

#### 9.1.4 Widths of Peaks

McGuire (1974) calculated the width of transitions with  $N_4$  and  $N_5$  initial holes for atomic numbers 73, 74, 77 and 79 as follows:

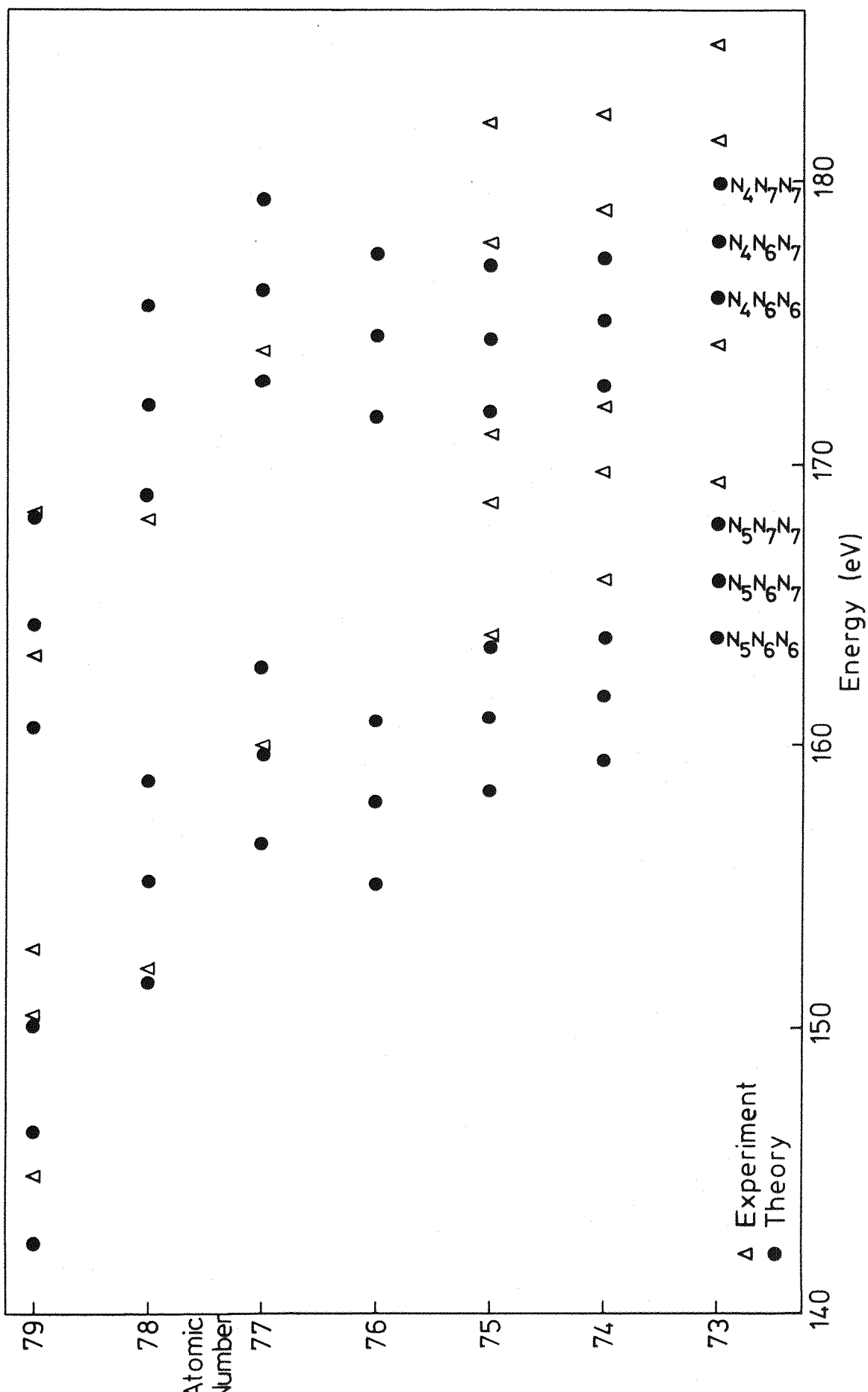


Figure 9.4 Comparison of experimental peak positions with theoretical line energies calculated using an empirical equation (equation 2.4).

Element	Atomic Number	$\Gamma(\text{eV}), N_4$	$\Gamma(\text{eV}), N_5$
Ta	73	7.73	7.61
W	74	7.89	7.72
Ir	77	8.63	8.34
Au	79	8.83	8.40

The only experimental widths that can be directly compared to the theory are in table 6.1. These are the widths of the  $N_{4,5}N_{6,7}N_{6,7}$  peaks found from a broadened Lorentzian fit of the rhenium spectrum. The experimental widths of the  $N_{4,5}N_{6,7}N_{6,7}$  peaks vary from 5.0 to 7.6 eV. By interpolation of the theoretical results in the table, the width of the rhenium  $N_{4,5}$  initial hole transitions may be estimated at  $\sim 8$  eV. Thus the experimental peaks are all narrower than predicted.

## 9.2 The $N_{4,5}N_{6,7}O_{2,3}$ Coster-Kronig Transitions

Sometimes it is difficult to estimate the intensity of a peak when it is masked by another larger peak with almost equal line energy. This occurs with the  $N_{4,5}N_{6,7}O_{2,3}$  Coster-Kronig transitions which are buried beneath the more intense  $N_{4,5}N_{6,7}N_{6,7}$  transitions in spectra from tantalum (chapter 8.1), tungsten (Rawlings et al., 1980a) and rhenium (chapter 6). However an estimate of the intensity of the  $N_{4,5}N_{6,7}O_{2,3}$  transitions to these spectra can be made by looking at the spectra from gold, platinum and iridium (Matthew et al., 1980). The  $N_{4,5}N_{6,7}O_{2,3}$  peaks are well resolved from the  $N_{4,5}N_{6,7}N_{6,7}$  peaks in the gold spectra, in platinum there is some overlap of the  $N_{5}N_{6,7}O_{2,3}$  peak with the  $N_{4}N_{6,7}N_{6,7}$  peak, while in iridium the  $N_{5}N_{6,7}O_{2,3}$  peak is buried in the  $N_{4,5}N_{6,7}N_{6,7}$  intensity. In Matthew et al.'s gold spectrum the area under the  $N_{4,5}N_{6,7}O_{2,3}$  peaks is approximately 10% of the total  $N_{4,5}N_{6,7}N_{6,7}$  peak area. Whilst accurate measurements of peak areas are not possible from the

platinum and iridium spectra, the  $N_{4,5}N_{6,7}O_{2,3}$  peak is also approximately 10% of the  $N_{4,5}N_{6,7}N_{6,7}$  peak area in both spectra. Thus a tentative estimate of the  $N_{4,5}N_{6,7}O_{2,3}$  contribution to the tantalum, tungsten and rhenium spectra is about 10% of the  $N_{4,5}N_{6,7}N_{6,7}$  intensity. In fact the  $N_{4,5}N_{6,7}O_{2,3}$  series explains the  $N_4$  initial hole contribution to the 174eV peak in the tantalum spectrum (chapter 8.1).

### 9.3 The $N_{4,5}N_{6,7}O_{4,5}$ Coster-Kronig Transitions

The present work on gold (chapter 8.2) was unable to resolve the conflict between Matthew et al. (1980) and Larkins and Lubenfeld (1977): Larkins and Lubenfeld's gold spectrum showed the  $N_{4,5}N_{6,7}O_{4,5}$  intensity about seven times as great as the  $N_{4,5}N_{6,7}N_{6,7}$  intensity, whereas in Matthew et al.'s gold spectrum the  $N_{4,5}N_{6,7}O_{4,5}$  intensity was lower than the  $N_{4,5}N_{6,7}N_{6,7}$  intensity. McGuire's (1974) theory is in better agreement with Matthew et al.'s results.

A look at other metals in the 5d series suggests that the  $N_{4,5}N_{6,7}O_{4,5}$  transitions are always less intense than the  $N_{4,5}N_{6,7}N_{6,7}$  transitions: The studies of tantalum (chapter 8.1), tungsten (Rawlings et al., 1980a) and rhenium (chapter 7) showed that the peaks in the expected  $N_{4,5}N_{6,7}O_{4,5}$  region had a much lower intensity than the peaks deduced to be due to  $N_{4,5}N_{6,7}N_{6,7}$  transitions. Moreover, for all three metals,  $N_{4,5}N_{6,7}O_{4,5}$  transitions were found to be only one of several processes contributing intensity in that region. Thus the  $N_{4,5}N_{6,7}O_{4,5}$  contribution is even less than it appears at first from the spectra.

Matthew et al. (1980) studied iridium and platinum as well as gold. A comparison of their spectra with the tantalum, tungsten and rhenium spectra show the intensity of the  $N_{4,5}N_{6,7}O_{4,5}$  peaks increasing with respect to the  $N_{4,5}N_{6,7}N_{6,7}$  intensity with increasing atomic number. Matthew et al. found that the intensities of the iridium, platinum and gold  $N_{4,5}N_{6,7}O_{4,5}$  transitions were greater than the intensities predicted by McGuire's theory but always

lower than the  $N_{4,5}N_{6,7}N_{6,7}$  intensity. Their measured  $N_{4,5}N_{6,7}O_{4,5}$  intensity is probably higher than it should be as they did not look for other contributions in this area of the spectrum such as cascades or diffraction peaks.

Thus a comparison across the 5d transition metals suggests that McGuire's theory correctly predicts that the  $N_{4,5}N_{6,7}N_{6,7}$  super Coster-Kronig transitions are more intense than the  $N_{4,5}N_{6,7}O_{4,5}$  Coster-Kronig transitions.

#### 9.4 Conclusion

The following conclusions have been reached by comparing the low energy secondary electron spectra from 5d transition metal surfaces. The most intense peaks in the spectra are due to  $N_{4,5}N_{6,7}N_{6,7}$  transitions. The  $N_{4,5}N_{6,7}O_{2,3}$  intensity is about 10% of the  $N_{4,5}N_{6,7}N_{6,7}$  intensity. Though the  $N_{4,5}N_{6,7}O_{4,5}$  intensity increases with respect to the  $N_{4,5}N_{6,7}N_{6,7}$  intensity with increasing atomic number, the  $N_{4,5}N_{6,7}N_{6,7}$  intensity is always greater.

## CHAPTER 10

### SUMMARY AND CONCLUSIONS

This thesis has reported an investigation into the origins of peaks in the low energy secondary electron spectra of 5d transition metal surfaces. The rhenium spectrum was studied in detail, followed by a preliminary study of tantalum and gold.

Spectra were detected using a cylindrical mirror analyser. Initially data was logged by a Nicolet signal averager. This was replaced by a Cromemco microcomputer which made data analysis much easier. The variation of a peak's intensity with primary beam energy was plotted to indentify the initial state of the process giving rise to the peak. The shape of this yield curve was used to identify the process or processes contributing to the peak. The variation of a peak's yield with temperature was investigated using a pulsed heater. This helped to distinguish between diffraction peaks which vary with temperature and Auger peaks which do not. Computer programs were written to analyse the yield curves and also to simulate parts of the experimental spectrum. This 'curve fitting' was used to determine how many peaks there were in an area of overlapping peaks. The relative intensities of the peaks could thus be calculated. All these experimental results and analyses were compared with current theories of Auger line energies and intensities. Finally the results were compared with previous work to answer the remaining questions.

The 'curve fitting' technique, developed to fit a simulated spectrum to an experimental second derivative spectrum, was very successful. It identified peaks in areas of overlapping peaks that could not be resolved by eye. Initially spectra were simulated by several second derivative Lorentzian shaped peaks. The technique was extended to fit Lorentzian peaks broadened by the voltage

modulation method used to collect the experimental second derivative spectra. A best fit of either Lorentzian peaks or 'broadened' Lorentzian peaks to the same experimental spectrum gives virtually the same energy positions for the peaks and similar relative intensities. However, the broadened peaks mimic the experimental situation better and also give a value for the width of a peak which is consistent, independent of the modulation voltage used to detect the spectrum.

The most intense group of peaks in the rhenium spectrum, 150eV to 185eV, were identified as mainly due to  $N_{4,5}N_{6,7}X$  Auger transitions ( $X=N_{6,7}, O_{2,3}$ ) from analysis of the yield curves and comparison with Larkins' (1977) theoretical line energies. There was also a contribution from  $N_3N_{4,5}O_{4,5}$  and  $N_3N_{5,4}O_{4,5}$  transitions when the primary beam energy was above the  $N_3$  binding energy. From the curve fitting exercise the ratio of  $N_3N_{4,5}O_{4,5}$  to  $N_3N_{5,4}O_{4,5}$  intensity was ~1:3 whereas McGuire (1974) suggests it should be ~1:5. However McGuire's calculations are for a free atom and so may not describe the solid state situation accurately. The assignment of X for the  $N_{4,5}N_{6,7}X$  transitions was difficult as the theoretical line energies for  $N_{4,5}N_{6,7}N_{6,7}$  super Coster-Kronig and  $N_{4,5}N_{6,7}O_{2,3}$  Coster-Kronig transitions overlap considerably. The  $N_{4,5}N_{6,7}O_{2,3}$  line energies are closest to the experimental peaks but do not fit well with the pattern of peak energies found from the curve fitting. However the  $N_{4,5}N_{6,7}N_{6,7}$  line energies line up well with these same experimental peaks after being shifted up 10eV. McGuire expected these  $N_{4,5}N_{6,7}N_{6,7}$  super Coster-Kronig transitions to be more intense than the  $N_{4,5}N_{6,7}O_{2,3}$  Coster-Kronig transitions.

Analysis of the equivalent area of peaks in the tantalum spectrum, 160eV to 190eV, showed that the  $N_{4,5}N_{6,7}O_{2,3}$  line energies would have to be shifted ~11eV to (poorly) fit the experimental line energies. The better fit of the  $N_{4,5}N_{6,7}N_{6,7}$  line energies was achieved with a shift of 3.4eV.

The equivalent area in the gold spectrum is from 140eV to 170eV. The theoretical  $N_{4,5}N_{6,7}O_{2,3}$  line energies are ~20eV from the experimental line energies whereas the  $N_{4,5}N_{6,7}N_{6,7}$  line energies give a good fit with a shift of just 1eV.

Comparison of these results with previous work showed that this area of intensity must be the result of  $N_{4,5}N_{6,7}N_{6,7}$  super Coster-Kronig transitions in agreement with McGuire (1974). However the discrepancy of 10eV between Larkins' (1977) theoretical  $N_{4,5}N_{6,7}N_{6,7}$  line energies and the rhenium experimental peak energies is not within the maximum error of 5eV that he quotes. Analysis showed that the discrepancy between experiment and theory was smallest at each end of the 5d transition metal series and increased to a maximum at the middle, where rhenium has a half full 5d shell. The discrepancy could only be partly due to errors in the binding energies Larkins used in the calculations.

From the curve simulation of the rhenium spectrum, the ratio of intensity from  $N_5$  initial holes to that from  $N_4$  initial holes was calculated as 2.4:1. Comparison with the expected ratio of 3:2 for decay to the same final state shows that ~30% of  $N_4$  initial holes decay to an  $N_5V$  final state. McGuire suggests that only 1.2% of  $N_4$  initial holes decay via the  $N_5$  level compared to decay via the  $N_{6,7}$  levels. McGuire's calculations may again be in error because conduction electrons are involved. Rawlings et al. (1980a) found the same proportion of  $N_4$  initial states in tungsten decaying to the  $N_5V$  state.

Another measurement from the simulated spectrum was of the widths of peaks contributing to the rhenium spectrum between 150eV and 185eV. These varied from 5.0eV to 7.6eV which is below the value of ~8eV calculated by McGuire.

From comparison with previous spectra of gold and platinum the  $N_{4,5}N_{6,7}O_{2,3}$  transitions have around 10% of the  $N_{4,5}N_{6,7}N_{6,7}$  intensity in the spectra from the 5d transition metal surfaces.

The intensity of the  $N_{4,5}N_{6,7}O_{4,5}$  transitions increases with respect to the  $N_{4,5}N_{6,7}N_{6,7}$  transitions with increasing atomic number. In rhenium the 216eV peak had equal intensities of  $N_{5}N_{6,7}O_{4,5}$  and the second step of the cascade  $N_3 \rightarrow N_5 V \rightarrow XVV$ . The 229eV peak was  $N_{4}N_{6,7}O_{4,5}$  plus 0.7 times the second step of  $N_3 \rightarrow N_4 V \rightarrow XVV$ . The  $N_3 \rightarrow N_5 V \rightarrow XVV$  cascade was identified in the tungsten spectrum (Rawlings et al., 1979). The  $N_3 \rightarrow N_{4,5} V \rightarrow XVV$  cascade could contribute to the tantalum spectrum but no yield curves were plotted so this cannot be proved.

Temperature and/or position dependent peaks were found in both the rhenium and tantalum spectra. In rhenium at 188eV and 241eV and in tantalum at 192eV and 224eV. Comparison with similar peaks in the tungsten spectrum (Rawlings et al., 1980b) led to the conclusion that all these peaks were due to the diffraction of secondary electrons.

The present study has shown that it is not enough just to compare experimental spectra with theoretical calculations in order to identify Auger transitions. Careful experimental research is necessary to understand all the contributions to a spectrum. Then those who use Auger Electron Spectroscopy as a tool in other analyses or experiments can rely on their results.

Detailed studies of the spectra from a tungsten surface (Rawlings et al., 1980a, 1979, 1980b) and a rhenium surface have been completed. Similarly detailed studies of spectra from surfaces of the remaining 5d transition metals would give a fuller understanding of the changes across the series. Possible variations in the secondary electron spectrum between different crystal faces of the same metal would also be of interest.

APPENDIX I Experimental Control Language Interpreter  
(E.C.L.I.)

I.a. Energy window calculations.

1024 points are stored per sweep of the energy window (there are 1023 gaps between points). The user inputs the required low and high energy limits for the energy window, El and Eh. The energy step between two adjacent points is:

$$\delta E = ((Eh \times 80) - (El \times 80) + (1023 \text{ div } 2)) \text{ div } 1023$$

Where div is defined as the integer after truncation of the real number after a division. Eh is then adjusted to give an equal number of points for each input at one energy:

$$(Eh \times 80) = (El \times 80) + (\delta E \times 1023).$$

The energy for the ramp is output to the 12-bit board starting from Energy = (El  $\times$  80) and incrementing by  $\delta E$  as

output (Energy + 8 div 2) div 8.

Thus the value of Eh is adjusted by the computer and may not be exactly that specified by the user. This was never found to be a problem in practice.

I.b. How E.C.L.I. works.

In common with many BASIC interpreters the users commands are lexically analysed (Welsh and McKeag, 1980) by E.C.L.I. when typed in to translate them into an internal form. In this form a single word (e.g. GOTO) is held as a number instead of a string of four characters. Similarly the number 1234 is held as a binary number instead of the four characters '1', '2', '3', and '4'. This translation process is one-to-one and hence is reversible. Thus when the user

is one-to-one and hence is reversible. Thus when the user types LIST his program is translated back and typed in a form close to that which he typed in (spacing information being lost).

The user program is translated and stored in ascending order of line numbers in an array. Each line has its length stored with it so that lines can be easily skipped. When a single command or one for a user program is typed in it is checked for validity. The computer types warning or error messages immediately if a mistake is detected. For example if the user types:-

```
20 LET @2 = INTEGRAL (@1+
```

the computer responds with the message:-

```
ERROR 19: WRONG SYMBOL AT LINE 20- '+' FOUND BUT ')' EXPECTED.
```

I.c. Summary of all possible user commands.

I.c.1. Commands for both immediate mode and user programs.

SET  
STATUS  
SWEEP  
DISPLAY  
LET with INTEGRAL, SMOOTH, DIVE, +, -, etc.  
GOTO  
PRINT  
PAUSE

I.c.2. Commands only allowed in user program.

STOP  
END

I.c.3. Commands only allowed in immediate mode.

LIST  
RUN  
SAVE } (User programs on disk)  
LOAD }  
GET } (Spectra on disk)  
PUT }  
DELETE  
SCRATCH  
BYE  
TRACE  
NOTRACE  
DEBUG  
NODEBUG  
DUMP  
DIR (directory of files on disk)

## APPENDIX II

The Newton-Raphson method can be used to solve equations of the form  $f(x)=0$ .

If  $f(x)$  crosses zero, and  $x^{(1)}$  is a first guess at the root, figure II.1 shows the next two approximations to the root  $x^{(2)}$  and  $x^{(3)}$  found by the Newton-Raphson method. The method will obviously iterate to the correct solution.

If, however,  $f(x)$  does not reach zero,  $x^{(2)}$  and  $x^{(3)}$  are as shown in figure II.2. Further iterations 'bounce' the best guess for the root either side of the correct root and never reach the correct value.

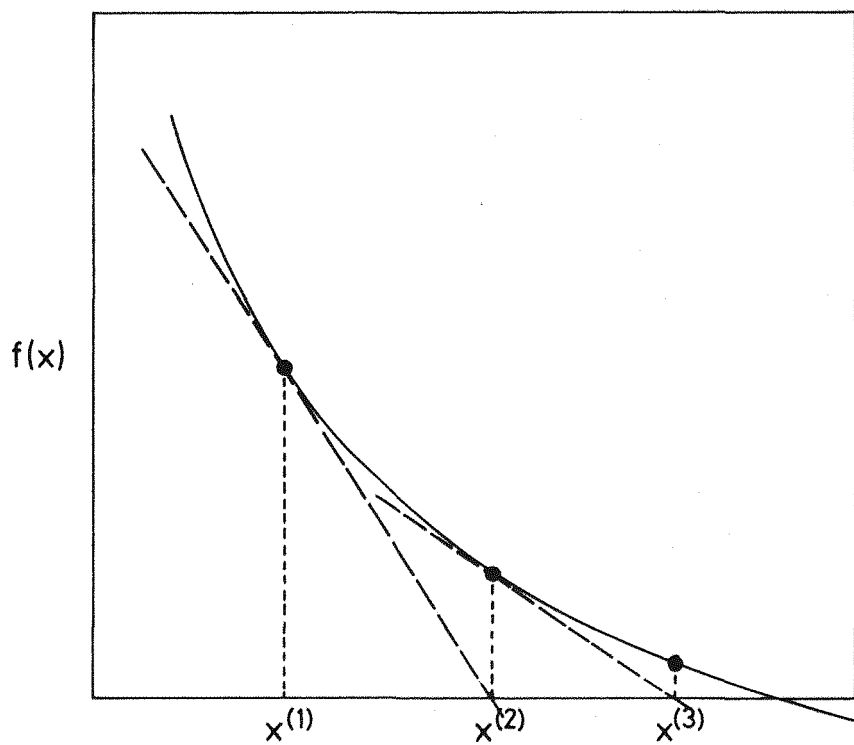


Figure II.1 The Newton-Raphson method for  $f(x)=0$  when  $f(x)$  crosses zero.

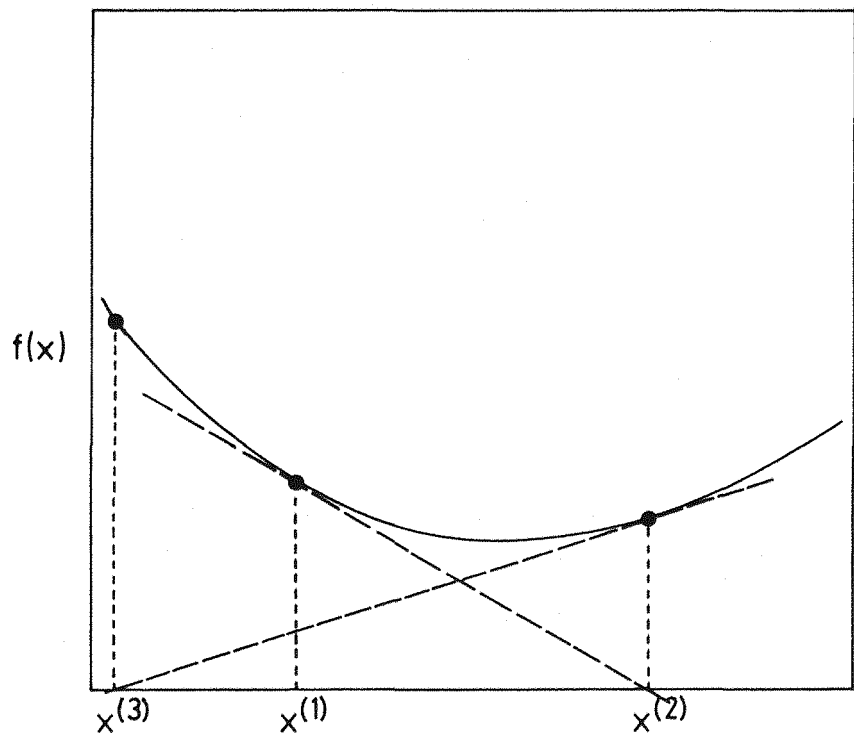


Figure II.2 The Newton-Raphson method for  $f(x)=0$  when  $f(x)$  does not reach zero.

## REFERENCES

Albridge R.G. and Hollander J.M. (1961)  
Nucl. Phys. 27 554

Alnot M., Weber B., Ehrhardt J.J. and Cassuto A. (1979)  
Appl. of Surf. Sci. 2 578

Antonides E., Janse E.C. and Sawatzky G.A. (1977)  
Phys. Rev. B. 15 1669

Auger P. (1923)  
Compt. Rend. 177 169

Bauer E. (1975)  
'Topics in Applied Physics, Vol 4, Interactions on Metal Surfaces' Ed. R. Gomer, Ch. 6.

Becker G.E. and Hagstrum H.D. (1974)  
J. Vac. Sci. Tech. 11 284

Bergström I. and Hill R.D. (1954)  
Ark. Fys. 8 21

Bishop H.E. and Rivière J.C. (1969)  
J. Appl. Phys. 40 1740

Burton J.J., Helms C.R. and Polizzotti R.S. (1976)  
J. Vac. Sci. Technol. 13 204

Chattarji D. (1976)  
'The Theory of Auger Transitions' Academic Press

Chesters M.A., Hopkins B.J. and Leggett M.R. (1974)  
Surf. Sci. 43 1

Chung M.F. and Jenkins L.H. (1970)

Surf. Sci. 22 479

Condon E.U. and Shortley G.H. (1935)

'The Theory of Atomic Spectra' Cambridge Univ. Press, London and N.Y., Ch 7-11

Coster D. and Kronig R. De L. (1935)

Physica 2 13

Dooley III G.J. and Haas T.W. (1970)

Surf. Sci. 19 1

Dushman S. and Lafferty J.M. (1962)

'Scientific Foundations of Vacuum Technology' John Wiley

Erman P., Bergström I., Chu Y.Y. and Emery G.T. (1965)

Nucl. Phys. 62 401

Fock V. (1930a)

Z. Phys. 61 126

Fock V. (1930b)

Z. Phys. 62 795

Foulais S.D. (1982)

Ph.D. Thesis, Southampton University

Froitzheim H., Ibach H. and Lehwald S. (1975)

Rev. Sci. Instrum. 46 1325

Gallon T.E. and Nuttall J.D. (1975)

Surf. Sci. 53 698

Haas T.W., Grant J.T. and Dooley G.J. (1970)

Phys. Rev. B. 1 1449

Hamilton J.C. (1978)

J. Phys. E. 11 399

'Handbook of Auger Electron Spectroscopy' (1976)

Davis L.E., MacDonald N.C., Palmberg P.W., Riach G.E. and  
Weber R.E. Physical Electronics Industries Inc., Minnesota

Hartree D.R. (1927)

Proc. Cambridge Phil. Soc. 24 89

Henrich V.E. (1980)

Appl. of Surf. Sci. 6 87

Houston J.E. and Park R.L. (1972)

Rev. Sci. Instr. 43 1437

Hoyt F. (1930)

Phys. Rev. 36 860

Hoyt. A. (1932)

Phys. Rev. 40 477

Jones A.R. (1976)

Ph.D. Thesis, Southampton University

Knowles S., Croxall R.J. and Hopkins B.J. (1982)

J. Phys. E. 15 719

Kowalczyk S.P., Ley L., McFeely F.R., Pollak R.A. and

Shirley D.A. (1974)

Phys. Rev. B. 9 381

Kowalczyk S.P., Pollak R.A., McFeely F.R., Ley L. and

Shirley D.A. (1973)

Phys. Rev. B. 8 2387

Kowalik J. and Osborne M.R. (1968)

'Methods for Unconstrained Optimization Problems', American Elsevier, N.Y.

Krause M.O. (1975)

'Atomic Inner-Shell Processes', Vol 2, Ed. B. Crasemann, Academic Press, Ch 2

Kirschner J. (1977)

'Topics in Current Physics, Electron Spectroscopy for Surface Analysis', Ed. H. Ibach, Springer-Verlag, N.Y.

Larkins F.P. (1975)

'Atomic Inner-Shell Processes', Vol 1, Ed. B. Crasemann, Academic Press, Ch 10

Larkins F.P. (1976)

J. Phys. B: Atom. Molec. Phys. 9 47

Larkins F.P. (1977)

Atomic Data and Nuclear Data Tables 20 311

Larkins F.P. and Lubenfeld A. (1977)

J. Electron Spec. and Rel. Phen. 12 111

Martin J. (1973)

'Design of Man-Computer Dialogues', Englewood Cliffs, N.J.: Prentice Hall

Matthew J.A.D. (1973)

Surf. Sci. 40 451

Matthew J.A.D. and Komninos Y. (1975)

Surf. Sci. 53 716

Matthew J.A.D. (1980)

Private Communication in Rawlings K.J. et al. (1980a) J. Electr. Spectr. 18 213

Matthew J.A.D., Netzer F.P. and Bertel E. (1980)  
J. Electron Spec. and Rel. Phen. 20 1

McDonnell L., Powell B.D. and Woodruff D.P. (1973)  
Surf. Sci. 40 669

McGuire E.J. (1969)  
Phys. Rev. 185 1

McGuire E.J. (1972)  
Phys. Rev. A. 5 1043

McGuire E.J. (1974)  
Phys. Rev. A. 9 1840

McGuire E.J. (1975a)  
'Atomic Inner-Shell Processes' Vol 1, Ed. B. Crasemann,  
Academic Press, Ch 7

McGuire E.J. (1975b)  
Sandia Report No. RS 5211/001 (unpublished)

McGuire G.E. (1979)  
'Auger Electron Spectroscopy Reference Manual' Plenum Press,  
N.Y.

Møller C. (1931)  
Z. Phys. 70 786

Mott N.F. and Massey H.S.W. (1965)  
'The Theory of Atomic Collisions' Oxford Univ. Press

Nathan R. and Hopkins B.J. (1973)  
J. Phys. E. 6 1040

Palmberg P.W., Bohn G.K. and Tracy J.C. (1969)  
Appl. Phys. Lett. 15 254

Palmberg P.W. (1976)  
J. Vac. Sci. Tech. 13 214

Rawlings K.J., Hopkins B.J. and Foulis S.D. (1978)  
Surf. Sci. 77 561

Rawlings K.J., Hopkins B.J. and Foulis S.D. (1979)  
Solid State Commun. 31 393

Rawlings K.J., Hopkins B.J. and Foulis S.D. (1980a)  
J. Electr. Spectr. 18 213

Rawlings K.J., Foulis S.D., Hopkins B.J. and Knowles S.  
(1980b)  
Solid State Commun. 35 643

Red'kin V.S., Zashkvara V.V., Korsunskii M.I. and Tsveiman  
E.V. (1971)  
Soviet Phys.-solid state, 13 1269

Rosseland S. (1923)  
Z. Phys. 14 173

Sevier K.D. (1972)  
'Low Energy Electron Spectrometry' Wiley-Interscience

Shaw Jr R.W. and Thomas T.D. (1972)  
Phys. Rev. Lett. 29 689

Shelton J.C., Patil H.R. and Blakely J.M. (1974)  
Surf. Sci. 43 493

Shirley D.A. (1973)  
Phys. Rev. A. 7 1520

Shneiderman B. (1980)  
'Software Psychology' Cambridge, Mass.: Winthrop, pp 238-241

Sickafus E.N. (1974)  
J. Vac. Sci. Technol. 11 299

Siegbahn K. et al. (1968)  
Air Force Materials Laboratory Technical Report No.  
AFML-TR-68-189 (unpublished)

Slater J.C. (1960)  
'Quantum Theory of Atomic Structure' Vols 1 and 2, McGraw  
Hill, N.Y.

Thapliyal H.V. and Unertl W.N. (1979)  
J. Vac. Sci. Tech. 16 523

Tu Y.Y. and Blakely J.M. (1976)  
Rev. Sci. Instrum., 47 1554

Weisskopf V. and Wigner E. (1930)  
Z. Phys. 63 54

Weightman P., McGilp J.F. and Johnson C.E. (1976)  
J. Phys. C. 9 L585

Welsh J. and McKeag M. (1980)  
'Structured System Programming' Englewood Cliffs, N.J.:  
Prentice-Hall, pp 64-81

Wentzel G. (1927)  
Z. Phys. 43 524

### ACKNOWLEDGEMENTS

I would like to thank my supervisor Dr. B.J. Hopkins for his help during this work and his patience during the writing of this thesis. Thanks also to Dr. K.J. Rawlings for his guidance and encouragement especially in the early stages of the work.

Many thanks to R.J. Croxall for developing the 'E.C.L.I.' software and for advice in computing matters.

I would also like to thank all the members of the Surface Physics Group for their help and willingness to discuss ideas.

I am grateful to the Science Research Council for financial assistance.

Thanks to Cerberus for the production of this thesis.

And last, but not least, many thanks to my long suffering husband who read the draft of this thesis and will be glad to see the back of it!

Removed due to copyright:

1. Rawlings, K.J., Foulias, S.D., Hopkins, B.J., and Knowle, S., 'Temperature dependent and other features in electron emission from W(110)' in *Solid State Communications*, 35, 9 (1980), pp. 643-648.

DOI 10.1016/0038-1098(80)90865-0

2. Knowles, S., Croxall, R.J., and Hopkins, B.J., 'Efficient use of a microcomputer-based data-logging system using a special-purpose control language interpreter' in *Journal of Physics E: Scientific Instruments*, 15 (1982), pp. 719-721.

DOI 10.1088/0022-3735/15/7/007